A MICROTEXTURE BASED ANALYSIS OF SURFACE ROUGHENING IN DUCTILE METALS DURING TENSILE DEFORMATION.

BY

NICOLA JANETTE WITTRIDGE

A thesis submitted to the Faculty of Engineering of the University of Cape Town in fulfilment of the requirements for the degree of Doctor of Philosophy.

Department of Materials Engineering
University of Cape Town

January 1998

ABSTRACT

AN ANALYSIS OF THE SURFACE ROUGHENING BEHAVIOUR OF DUCTILE METALS DURING TENSILE DEFORMATION.

By: Nicola Wittridge, Materials Engineering, University Private Bag, Rondebosch, 7700.

January 1998

This thesis examines the cause and mechanism for the occurrence of parallel surface ridges during the deformation of two specific ductile metal alloys, namely AISI 430 ferritic stainless steel and an aluminium alloy designated AA3002. The investigation considers, in particular, the development of parallel ridges during uniaxial tension, and their effect on the overall surface roughening of the sheet material.

A detailed account of the microstructure and texture of the individual sample sheet materials is presented and proposals for the mechanisms of surface roughening are based on plasticity analysis of the actual material data. Both the microstructural characterisation and the texture determination was carried out using mainly electron microscopy techniques. Electron backscattered diffraction techniques were used to measure the microtexture, and analysis of this data allowed the calculation of the plastic flow behaviour of discrete volumes of the sample material. The yield behaviour was implemented in a finite element model to simulate the material behaviour under uniaxial tensile conditions.

Analysis of microtexture results has indicated that elongated texture clusters are visible in the aluminium sample material which exhibits severe surface roughening during elongation in the rolling direction. It is proposed that initially surface roughening is the result of a variation in plastic flow of the surface grains due to the local texture clustering. With continued straining, the condition described by the MK analysis[11] for strain localisation is able to arise and this leads to through-thickness strain localisation and necking, and so results in the formation of a ribbed profile. Ridging in stainless steel on the other hand can be attributed to an asymmetric distribution of texture components or plastic flow properties about the mid-plane of the material. An asymmetric arrangement yield properties initiates the development of differential transverse strains about the mid-plane of the material. The variation in transverse strain in turn results in a series of localised bending events which, on a macroscopic level, produces longitudinal corrugations and an overall ridged surface morphology.

ACKNOWLEDGEMENTS

I wish to thank all those who have assisted me throughout this project, but in particular:

Professor R.D. Knutsen, my supervisor, for the years of assistance and encouragement.

The Council for Mineral Technology (MINTEK) are greatly acknowledged for their financial support, as well as for the provision of the bulk texture measurements.

The Foundation for Research and Development for their financial assistance.

The Department of Materials Engineering at Carnegie Mellon University, Pittsburgh, in particular Professor H.R. Piehler, for discussions and the provision of facilities for microtexture research.

Hulett Aluminium for their financial contribution.

Columbus Stainless Steel for the provision of sample material.

Mr HC Bowles for advice and assistance with the FEM.

The staff and students in the Department of Materials Engineering for their assistance and motivation.

My friends and family for their endless support and encouragement.

Dedicated to my Mom.

TABLE OF CONTENTS

LIST OF ABBREVIATIONS

AISI	American Iron and Steel Institute
ECC	Electron Channelling Contrast
EBSD	Electron Backscattered Diffraction Pattern
SEM	Scanning Electron Microscope
TEM	Transmission Electron Microscope
TMP	Thermomechanical Process
RD	Rolling Direction
TD	Transverse Direction
ND	Normal Direction
ODF	Orientation Distribution Function
GL	Gauge Length
Ra	Average Roughness Value
PV	Peak-to-Valley Measurement
BCC	Body Centred Cubic
FCC	Face Centred Cubic
M	Taylor Factor
r-value	Lankford Strain Ratio
r_{RD}	Strain Ratio for elongation in the RD
r_{TD}	Strain Ratio for elongation in the TD
FEM	Finite Element Modelling
S_{22}	Stress in the Transverse Direction
U3	Displacement in the Normal Direction
MK	Marciniak and Kuczynski

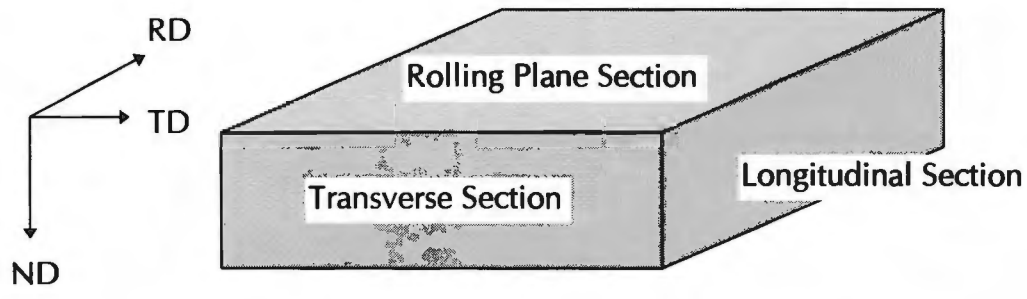

Reference diagram indicating the naming convection used throughout the document.

CHAPTER 1

INTRODUCTION

The development of surface roughening during the forming operations of sheet metal is a well known phenomenon and has been reported in alloys of copper, aluminium and stainless steel[1,2,4]. Many of the applications of these metallic materials require a good surface finish of the final product and thus any form of surface roughening is undesirable, for example, in the automotive industry for automotive trim or in the food industry for holloware components. In certain alloys surface roughening during forming appears as continuous parallel ridges extending across the material surface. The ridges destroy the smooth appearance and surface shine of the product and thereby reduce the quality of the formed article. Physical removal of the ridges requires time consuming and costly grinding and polishing operations which are unacceptable to the manufacturer. Two such metals which show this surface roughening effect are ferritic stainless steel (AISI 430) and an Al-Mn alloy (AA3002).

In the case of the ferritic stainless steel, the ridges can be characterised by narrow parallel undulations extending for a few millimetres in the rolling direction of the sheet. Extensive investigation has been done in an attempt to characterise and explain the origin of this unfavourable defect, which has been termed ridging, roping and also wrinkling. By far the most interest has been in the texture related origins of ridging and the majority of proposals attempting to explain the mechanism of ridging are based on an inhomogeneous texture distribution and related crystal plasticity anisotropy. In particular, mechanisms have been based on directionality of plastic strain ratio[32], shear strain variation according to grain orientation[38], bending due to an asymmetric distribution of texture clusters about the centre plane[37], and transverse buckling associated with longitudinal bands of preferred orientations[34]. More recently an investigation involving microscopic local orientation measurements has precluded ridging behaviour as being attributed to texture heterogeneity alone[36]. Instead it has been proposed that the macroscopic deformation of the

cross-section plane, obtained as a sum of the (microscopic) deformations of the individual grains of even very different orientations, can be shown to be responsible for the ridging profile. Although texture distribution is a common factor in the majority of suggested mechanisms of ridging, several disagreements and contradictions exist concerning the exact mechanism responsible for ridging.

In contrast to the extensive investigation of ridging in stainless steel, few papers have been published which deal directly with the development of parallel ridges on the surface of aluminium and its alloys. The development of surface roughening during deformation of aluminium alloys has in general been attributed to grain rotations of certain texture components near the surface of the sheet[1]. In some cases, alignment of the texture components is suggested to cause elongated bands of roughness which appear as ridges on the sheet surface[2]. In addition, a notable amount of research dealing with the effect of surface roughness on the evolution of strain localisation and necking has been published, which incorporates the development of ridges on the sheet surface. In most cases, the phenomenon of parallel ridges in aluminium alloys has been termed ribbing or roping[77]. Despite the proposed mechanisms for ridging in stainless steel and aluminium, it is the view of the present author that there is still no definitive understanding of ridging behaviour.

An interesting difference in the occurrence of ridging in stainless steel and aluminium is that during uniaxial tension, ridging occurs in steel when the major tensile axis is parallel to the rolling direction, whereas a similar surface effect only occurs in aluminium when the metal is elongated in the transverse direction. However, it must be emphasised that in both cases the ridges occur parallel to the rolling direction.

The objective of the present study is to characterise the ridging phenomenon in a ferritic stainless steel AISI 430 and an aluminium alloy AA3002, with the aim of providing an explanation for the ridging mechanism occurring during deformation. A detailed investigation of the microstructural and texture properties of sample material of the abovementioned alloys has been

undertaken, as well as an examination of the deformation behaviour under various tensile conditions. Since the synergism of applied tensile load and crystal orientation is critical for any form of plasticity analysis, this investigation concentrates on microtexture characterisation determined by electron backscattered diffraction techniques. The following approach to the investigation has been adopted:

i) Characterisation of the surface roughening behaviour of several samples during uniaxial tension.

ii) Acquisition of spatially related texture data using the electron backscattered diffraction technique.

iii) Calculation of the plastic flow behaviour of the polycrystalline metals based on the discrete microtexture data.

iv) Suggestion of a mechanism of surface roughening based on the plastic analysis.

CHAPTER 2

LITERATURE REVIEW

2.1 Surface Roughening of Metallic Materials

2.1.1 Introduction

The development of parallel ridges on the surface of sheet metals during tensile deformation can be described as a peculiar form of surface roughness. Although several published research papers address the specific phenomenon of ridging in stainless steels, there are very few papers which deal explicitly with the development of parallel ridges on the surface of aluminium and its alloys. However, a significant amount of research dealing with strain localisation and limit strains in aluminium has been presented, which includes some reference to the development of parallel grooves on the metal surface. Since the underlying feature of ridging in both ferritic stainless steel AISI 430 and aluminium alloy AA3002 is the formation of a roughened surface, it is pertinent to review the basic causes of surface roughening in ductile metallic materials. This theme is followed by consideration of the relationship between surface roughness and the development of plastic instability during tensile straining. Thirdly, some aspects of strain localisation in aluminium and the development of parallel ridges are presented. Finally, considerable attention is given to a review of the ridging phenomenon in ferritic stainless steels.

2.1.2 General Surface Roughness Development in Polycrystalline Metals

Due to its industrial significance, the surface roughening of sheet metals during forming operations has been the topic of extensive investigation. Surface roughening during deformation is common in a number of metallic materials including alloys of steel, copper and aluminium. Appearing on the surface in several different forms, it destroys the shiny lustre and smooth appearance of the

formed component and is therefore undesirable in almost all applications. The origins of surface roughening have been linked to individual grain rotations[1], crystallographic texture[2] and an inhomogeneous microstructure[3]. The effects of microstructural properties, for example grain size[6] and crystallographic texture[4,6], on the rate of roughening have been well established, as well as the influence of test conditions, such as strain state and applied strain[5].

From the many investigations, the development of surface roughening has been found to depend on factors such as initial roughness[1], grain size[1,6,7], grain anisotropy[2,4], crystal structure [8], strain state[1] and crystallographic texture[2,4]. The most significant source of roughening has thus far been attributed to ***individual crystal rotations*** of the surface grains[1,9]. Lattice rotations and inhomogeneous deformation are most favourable for grains near a free surface in which the effects of mutual constraint are partially relaxed. At a free surface the compatibility requirement normal to the surface is relaxed, so fewer slip system need operate in these grains and this allows the crystals to rotate and deform more easily. The stress for yielding decreases in these surface grains resulting in inhomogeneous deformation between the surface and centre regions, which could make an important contribution to the overall flow stress of the material if the grain size is large[10]. The fact that surface roughness increases linearly with grain size has been well established[6,7] and can be easily understood in terms of the above individual grain rotation theory. Many attempts to reduce surface roughening during deformation therefore concentrate on a reduction in the average grain size. Yamaguchi and Mellor[7] researched the roughening behaviour of steel sheets and found that the surface roughness of the material is directly dependant on the average grain size and the magnitude of the equivalent strain. The roughening of a sheet on the scale of the grain size is commonly termed the orange peel effect.

2.1.3 Relationship between Surface Roughness and Plastic Instability

An in-depth study of the effects of grain anisotropy on surface roughness and the resultant strain inhomogeneities developed during biaxial stretching on brass

and steel sheet metal was conducted by Wilson, Roberts and Rodrigues[4]. It was found that the formation of surface roughness and the subsequent development of localised areas of strain during biaxial stretching, of metal sheets possessing a *weak crystallographic texture*, depends heavily on the ratio of sheet thickness to grain diameter, t_0/d_0. The amount of strain experienced by the sheet, before failure at regions of intense localised necking, decreases sharply with a decreasing ratio of t_0/d_0, provided that plastic anisotropy of individual grains is the dominant source of strain inhomogeneity. Thus, for commercially produced metal sheets grain size plays a vital role in determining the surface roughness of the sheet and the quality of the final product.

In the investigation, during the first stages of roughening, Wilson *et al*[4] concluded that strain inhomogeneities are the result of grain anisotropy of individual grains and are therefore initiated on a scale of the microstructure. Hence, for the samples used in the investigation, no long wavelength variations in flow stress on a scale greater than the grain size were found, which meant that no coherent regions of strain concentration could develop across the sheet thickness. This was termed the **microstructural phase** of strain localisation. During this phase the rate at which surface roughness develops is dependent on grain size and the effective applied strain, and is independent of sheet thickness and the applied ratio of principal strains. At a certain applied strain the rate of surface roughening, $dR/d\varepsilon$, starts to accelerate. This is accompanied by an increase in the growth of thickness inhomogeneity or strain localisation and continues until the point of fracture by localised necking. The increase in roughening rate is said to indicate the start of the **macroscopic phase** of the process and can be described as the point at which variations in strain rate evolve across the sheet thickness. Considering geometrical aspects, Wilson *et al*[4] suggested that the most appropriate quantitative mechanism to describe the macroscopic phase is the model developed by Marciniak and Kuczynski [MK theory][11], discussed in the following section.

As a second stage in the investigation, surface roughening and strain localisation effects were studied in a sheet metal which possessed a *well-developed*

texture[2]. The general conclusion was that preferred orientations in a material can have a major influence on the effect of grain size and sheet thickness on the limit strains or fracture point during biaxial stretching. In other words, deformation behaviour leading to strain localisation and necking can be significantly altered by the textures present in the sheet. In a material of a certain grain size, preferred orientations can lead to an increase in the rate at which thickness inhomogeneities form and thus can expedite strain localisation and necking. Furthermore, the distribution of different texture components within the sheet can influence the development of strain inhomogeneity. In particular, the separation of texture components into elongated colonies of similar preferred orientations can dramatically reduce the biaxial stretching limits. This effect will be further concentrated if the two textures have distinctly differing Taylor factors. According to Wilson and Rodrigues[3] alignment of texture components in the RD (rolling direction), also called mechanical fibering, occurs fairly frequently in aluminium alloys. It has been suggested that when a material containing mechanical fibering, such that the bands of material possess different flow stresses, is subjected to biaxial stretching, surface grooves will form parallel to the RD which will eventually lead to failure.

It is evident from the abovementioned research that strain localisation can occur at certain areas of severe roughness, which can in turn lead to plastic instability and ductile failure. In uniaxial tensile testing, strain localisation or necking begins at a maximum value of stress when the work hardening of the material becomes insufficient to compensate for the reduction in cross section. In the last few decades numerous models (including many adaptations and improvements) have been published in an attempt to simulate deformation behaviour and strain localisation[9,11-21,106]. Models dealing with strain localisation leading to failure can be divided into two main categories. Firstly, material behaviour models which extend the very first ideas of bifurcation of strain state using deformation theory of plasticity, and secondly, models which involve the assumption of defects in the sheet which disturb the strain state.

Material behaviour models incorporating plastic deformation theory generally utilise the constitutive equations for yielding in terms of total strain experienced

by the sheet, as opposed to incremental strain used in flow theories of deformation. Hutchinson and Neal[21] and Storen and Rice[20] used this approach to formulate a deformation model, known as the J_2 theory, using effective measures of stress and strain, equivalent to the von Mises yield criterion. The J_2 theory provides solutions which can be considered vertices on the plastic potential surface, equivalent to corners of a yield surface in flow theory. Despite the fact that most predictions from deformation theories are in good agreement with measured results, the models have received some criticism[22].

The original continuum model which incorporated a material defect was proposed by Marciniak and Kuczynski[11] in 1967 and since then a number of mechanisms based on this idea have been suggested[9,18,19]. The defect took the form of an infinitely long shallow groove in which local strain concentration increased during deformation. Deepening of the groove occurs followed by strain localisation with gradual fading of strain concentration in the region surrounding the groove, until this reduced strain reaches a limiting strain. The Marciniak and Kuczynski model[11] is summarised in the section below.

The Marciniak and Kuczynski model

The original MK theory[11] made use of the anisotropic yield function by Hill[23], as well as an assumption of planar isotropy and isotropic hardening. The model analysed the loss of stability of a sheet metal subjected to biaxial tension when the ratio of principal stresses σ_2/σ_1 is between 0.5 and 1. In order to realistically describe the failure of a sheet, a new approach to the local loss of stability was applied. Instead of defining loss of stability as a certain end or fracture point, it was analysed as a process which takes root from an initial inhomogeneity of the sheet metal. It was suggested that this inhomogeneity could take the form of a groove or reduced through-thickness of material and would run in a direction perpendicular to the larger principal stress. A defect coefficient, f, was defined as the ratio of the material thickness in the groove to the thickness of the surrounding material, i.e. $f = t_B/t_A$. Gradually as deformation proceeds, strain concentrates in the groove with a corresponding reduction in thickness. This concentration in local strain is accompanied by a decrease in strain in the area

around the groove, until eventually a certain limiting value of strain, ε^*, is reached. At this point the remaining areas outside the groove undergo unloading and revert back to the elastic state, implying complete loss of stability and failure. For a particular stress state the strain inside the groove is greater than the surrounding material, therefore the material within the groove must possess a lower strain hardening rate. A system of equations was derived based on anisotropic plasticity theory which enabled the limiting strain of the sheet metal to be determined. Consideration was given to the fact that this value is dependent on a number of material properties including i) initial inhomogeneity of the sheet, ii) coefficient of normal anisotropy, iii) initial plastic strain, iv) fracture strain and v) coefficient of normal anisotropy. In addition, the influence of the ratio of the applied stresses and the loading procedure of the sheet on the final value was taken into account. Marciniak and Kuczynski[11] concluded that the parameter which exerts the greatest influence on the limiting strain is the initial inhomogeneity or material defect. Only geometrical aspects of the defect were taken into account such as defect size and changes in its thickness, while any variations in plastic properties were neglected. Furthermore, it was stated that a similar result could be derived if the inhomogeneity resulted from other material property variations such as non-uniform texture, varying distribution of impurities and grain size variations. These physical inhomogeneities could then be manipulated into the equivalent geometrical inhomogeneity.

2.1.4 Strain Localisation and Ridge Development in Aluminium

Work done by P.S. Bate[24] on aluminium sheet revealed that surface roughening in the form of grooves and subsequent local necking could be the result of spatial segregation of preferred orientations. As a first stage of the study, colonies of texture components were identified using anodising techniques and polarised light imaging. Long ribbons of R texture $\{123\}<634>$ were identified running in the RD within a matrix of mainly cube orientated grains. Secondly, Bate[24] assumed that for ductile localised failure, the wavelength of the critical property variation must be more than double the thickness of the sheet[25]. A

random simulation was then conducted, using metallographic information, with the aim of predicting whether or not the bands of R texture present in the material were appropriately distributed to exert an influence on strain localisation. The result of the simulation was a long wavelength variation of 0.08 for the thickness-averaged R texture colonies, which was greater than twice the sheet thickness. This favourable result, coupled with the fact that the difference in strain ratios (r-values) between the R and cube texture is about 20%, enabled Bate[24] to conclude that there is a strong possibility that textural variations found in commercially pure aluminium will promote the development of surface roughness during straining. It was suggested that roughening would take the form of elongated grooves in the RD associated with the as-rolled grain structure. Continued straining would then promote strain localisation and necking of the form represented in the MK analysis[11].

Tadros and Mellor[5] also examined the effect of strain on the surface roughness of steel, aluminium and brass and concluded that, although the surface roughness of each alloy increases with continued straining until the point of fracture, failure does not necessarily occur at a trough of surface roughness. Nevertheless, the surface roughness does contribute to the overall thickness variations of the sheet metal, and therefore must play a role in the initiation of plastic instability, as well as influencing the point at which fracture occurs. These results support the theory that severe surface roughening, leading to a non-uniform sheet thickness, can result in strain localisation, tensile instability and eventual ductile failure.

Recently Becker[26] performed a detailed investigation on the development of surface roughness using a finite element modelling (FEM) approach. A number of numerical simulations were performed in order to determine the influence of microstructure and mechanical properties on the deformation behaviour of a sheet metal. A model was devised in which each of the surface grains was represented explicitly in a mesh, and thus detailed information regarding deformation of these grains could be captured. To provide a realistic simulation, details of grain structure, texture and strain hardening behaviour were measured from an Al-6111 recrystallised aluminium sheet and used as

input for the simulation. Both crystallographic slip and lattice rotations were taken into account by the crystal plasticity model used in the simulation. As the control of grain size and strain on roughness has already been well reported, Becker[26] concentrated on the influences that are not easily measured through experimentation, for example, the effect of strain hardening, strain rate sensitivity, grain misorientations and crystal structure.

The results showed that altering the strain rate sensitivity parameters had almost no effect on the surface roughness, while increasing the strain hardening factors decreased the roughening significantly. The decrease in roughness in this case could be attributed to the decrease in strain localisation which was visible from the contour plots of strain distribution. Although the initial simulation was based on data measured from an aluminium alloy, the model was expanded to simulate the deformation behaviour of any face centred cubic (FCC) or body centred cubic (BCC) polycrystalline material. The variation in roughness with crystallographic texture was investigated by comparing the behaviour of a set of measured orientations to that of three sets of random orientations. The average roughness for the random textures was similar and unexpectedly higher than that for the measured texture, suggesting the presence of a recrystallisation texture in the measured sample.

As expected, the results indicated a steady increase in roughness with increased strain, as well as a higher rate of roughness development for a compression test compared to a tensile test. Distribution of strain after deformation was analysed via contour plots of the maximum principal strain in the four tensile strain paths, namely in-plane shear, uniaxial tension, plane strain tension and biaxial tension. Strain localisation was evident in all cases but had the greatest effect during plane strain tension. At the regions where the bands of local strain intersected the model surface, additional strain inhomogeneities were formed and valleys appeared in these regions. Corresponding peaks were evident in the regions surrounding these areas where the strain concentration was relatively lower. Strain localisation therefore appeared to be the cause of the valleys and peaks across the surface profile. It was concluded that all factors influencing strain

localisation, such as strain hardening and texture, will have a significant effect on the final surface roughening behaviour of the sheet.

2.1.5 Ridging Phenomenon in Ferritic Stainless Steels

Since the late 1950s much research has been published on the ridging phenomenon in ferritic stainless steel. Many suggestions have been given as to the origin of this surface defect, including columnar grains in the cast ingot[27], grain morphology due to certain deformation processes[28] and the distribution of the hard martensitic phase originating from the hot roll stage[29]. Ridging has also been attributed to elemental partitioning between the α and γ phases[30,31] and to thermomechanical process parameters such as annealing and rolling temperatures. Yet the theories that have received by far the most interest and support, have been those based on texture distribution within the metal sheet and related anisotropic plastic flow behaviour[32-40,47].

The first proposals for the ridging mechanism involving textural arguments were published in 1967 by Chao[32] and Takechi *et al*[38] and in both cases their theories were based on the presence of local texture banding, identified using an etch pitting technique. In 1972, Wright[34] proposed an alternative "buckling mechanism" for the development of corrugations in ferritic stainless steel. This theory also relied on the existence of texture colonies found by etch pitting methods. However, the etching techniques used in these three experiments were neither very reliable nor did they give very accurate results, which meant that correct identification of texture distributions within the sheet was exceedingly difficult. Almost twenty years later with the advent of the Electron Backscattered Diffraction (EBSD) pattern technique, the ability to easily identify local texture distribution or microtexture distribution within a material was made possible[41]. Combining texture information provided by this technique and detailed microstuctural analysis, Harase *et al*[37] were able to formulate the first ridging mechanism based on large scale maps showing local microtexture variations. Microtexture surveys over large areas utilising an EBSD system were also used by Bethke *et al*[36] in their recent investigations on the origin of ridging.

In this investigation, no colonies of similar orientations were detected, which cast doubt on all previous models, and instead a new "stochastic" mechanism for ridging was suggested. In the section below the five ridging mechanisms based on texture related properties mentioned above are summarised and critically compared. Results of an investigation of the relationship between fibre textures and ridging, conducted by Salsgiver *et al*[39] are also presented. In section 2.1.5.3 the non-texture related explanations for ridging are outlined, while in section 2.1.5.4 the many suggestions given for the elimination of ridging are discussed. Finally an investigation by Nagashima *et al*[113], in which the deformation behaviour of a ferritic stainless steel possessing an inhomogeneous texture distribution is simulated using finite element modelling, is briefly summarised.

2.1.5.1 Texture Related Ridging Mechanisms

Ridging Mechanism after Takechi et al (1967)

Takechi *et al*[38] characterised the ridging profile of a 17%-chromium stainless steel sheet as a true corrugation, where the peaks and troughs of the upper surface corrugations correspond directly with the peaks and troughs on the lower surface, as indicated in figure 2.1. At the time no theory for the ridging mechanism existed, though Appel *et al*[43] had put forward the idea that ridging could be the result of a difference in yielding behaviour between the matrix and the transformed phase. Takechi *et al*[38] made some assumptions based on the fact that ridging occurs only in ferritic stainless steels and therefore must originate from properties particular to these steels. One such characteristic identified was the absence of the ferrite-austenite transformation during hot rolling, and another was the presence of many precipitates with a high dissolution temperature in the material. For these reasons, it was surmised that firstly no randomisation of texture occurs during annealing, and secondly, that the extensive precipitation prevents grain boundary migration. Thus the rolling textures would be retained even after final annealing. This prompted the

authors to use ferritic stainless steel in the cold rolled condition in the investigation rather than going to the extent of annealing the material.

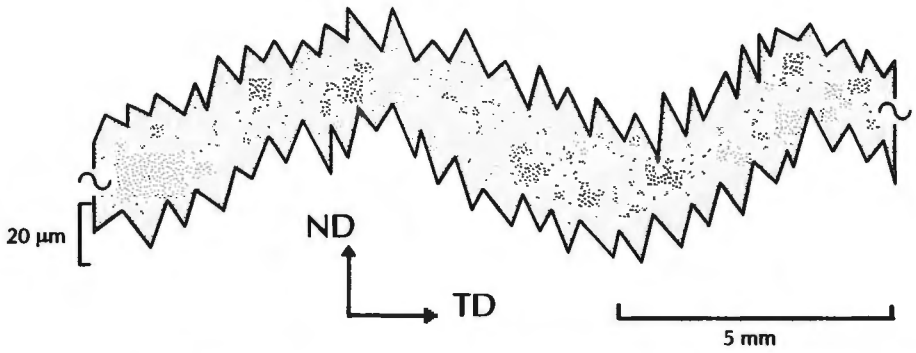

Figure 2.1: Ridging profile according to Takechi *et al*[38].

As a first stage in the investigation the plastic behaviour of the identified principal texture components, namely <011>//RD or partial α-fibre texture, was examined in uniaxial tension with the tensile axis parallel to the <011> direction. Unlike the model by Chao[32], which was presented at about the same time, both lattice rotations and shape changes resulting from slip were considered. To calculate the shape change for a BCC crystal, a cartesian coordinate system 0-xyz was introduced where x, y and z are parallel to RD, TD (transverse direction) and ND (normal direction) respectively. Strain due to slip, E, could then be represented by considering a strain tensor that takes into account the direction cosines of slip directions and of directions normal to slip planes about the coordinate axes x, y and z. For the case where the texture is described as $(\bar{1}00)[011]$, then the most stressed slip planes are $(\bar{2}11)$ and (211), and the total strain, E, is given as:

$$E = E_{(\bar{2}11)} + E_{(211)} = E_x \begin{pmatrix} 1 & 0 & 0 \\ 0 & 0 & 0 \\ 0 & 0 & -1 \end{pmatrix}$$

where E_x = elongation in the x direction. The resultant shape change is shown in the figure below and the strain matrix indicates that no shear strain occurs (i.e. ε_{23} and ε_{32} are zero).

In considering other members of the <011>//RD fibre, Takechi *et al*[38] stated that any orientation along this fibre can be characterised by an angle θ, which is defined as the rotation angle from $(\bar{1}00)[011]$ around the [011] axis. E_θ can then be described as the strain of the crystal with a [011]//RD orientation characterised by θ under [011] tensile deformation.

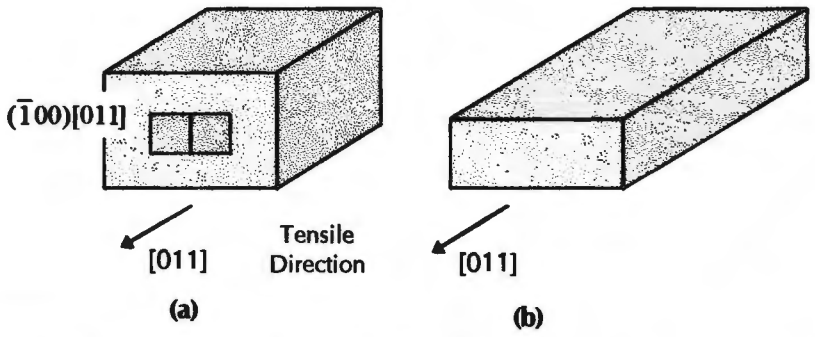

Figure 2.2: Shape change of a $(\bar{1}00)[011]$ orientated crystal deformed under [011] tensile conditions. (a) Before and (b) after deformation[38].

To calculate E_θ a new Cartesian co-ordinate system 0-xy'z' was introduced (figure 2.3).

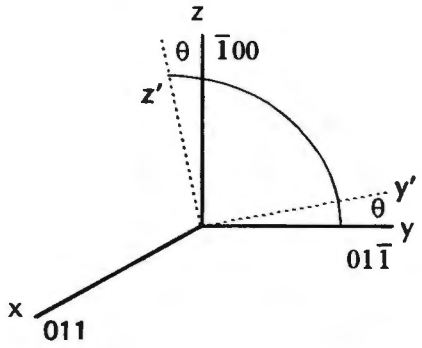

Figure 2.3: Relationship between the 0-xyz and the 0-xy'z' systems[38].

If T is the co-ordinate transformation matrix, E_θ is given as:

$$E_\theta = T E T^{-1}$$

where T^{-1} is the reciprocal matrix of T. Substitution of the new direction cosine values yields E_θ as follows:

$$E_\theta = E_x \begin{pmatrix} 1 & 0 & 0 \\ 0 & -\sin^2\theta & -\frac{1}{2}\sin^2\theta \\ 0 & -\frac{1}{2}\sin^2\theta & -\cos^2\theta \end{pmatrix}$$

where:

θ = Angle of rotation of any crystal from $(\bar{1}00)[011]$ about the [011] axis.

E_θ = Strain experienced by the crystal under [011] tensile condition.

E_x = Elongation along the [011] tensile axis.

From this matrix Takechi *et al*[38] was able to identify a shear component of strain, $-\frac{1}{2}\sin 2\theta$ in the 23 direction (i.e. ε_{23}). The maximum value of this shear strain corresponded to θ values of $\pm 45°$, resulting in a shape change as shown in figure 2.4.

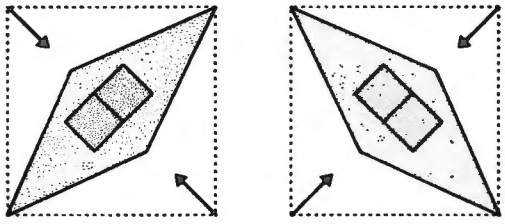

(a) θ = -45° (b) θ = 45°

Figure 2.4: Shape change due to deformation of a crystal with an [011] orientation[38].

Thus it was concluded that if a sample with a banded crystallographic orientation configuration as shown in figure 2.5 is elongated in the [011] direction, each band of the sample will deform under shear conditions as shown in figure 2.4, thus providing an undulating profile across the sample.

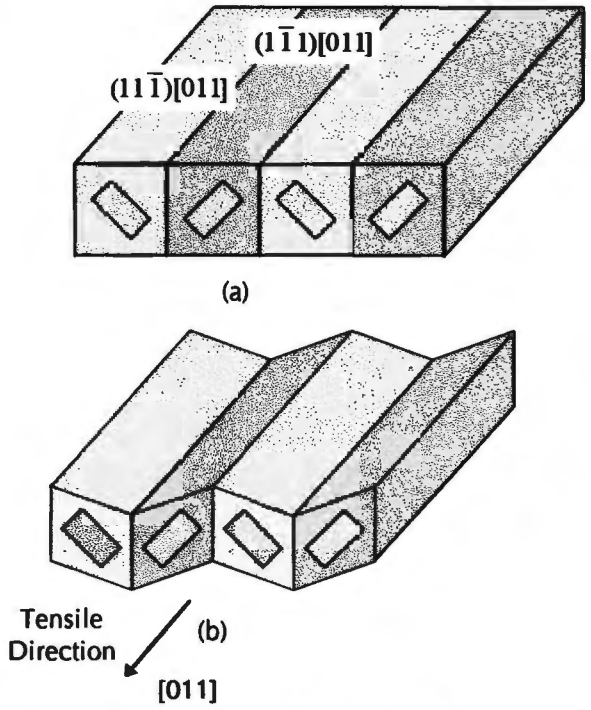

Figure 2.5: Banded configuration of texture.

Note: Each band contains many crystals of similar orientations[38].

The final stage in the investigation was to verify that such local texture variations do actually exist in the material. Mico-etch pitting techniques were used for this purpose and bands of orientations of the $<011>$//RD fibre texture were found, extending in the rolling direction.

Ridging Mechanism after Chao (1967)

The first assumption made by Chao[32,47] was that the appearance of a ridged sheet after forming can be characterised by differences in sheet thickness in adjacent areas. It was postulated that such differences could arise if the areas differed in crystallographic texture. The plastic strain ratio, r, where $r = d\varepsilon_{TD}/d\varepsilon_{ND}$ is highly orientation dependent and it was therefore suggested that texture variations could lead to anisotropic plastic flow during deformation, resulting in variations in sheet thickness. This prompted Chao[32] to investigate the r-values and slip behaviour of various BCC textures, with the aim of discovering whether plastic strain ratio characteristics could account for ridging. The major texture groups found in ferritic stainless steels were identified as:

Cube-on-corner (CC)	$\{111\}<011>, \{111\}<112>$
Cube-on-edge (CE)	$\{110\}<001>$
Cube-on-face (CF)	$\{100\}<011>$
	(including other similar orientations.)

The deformation behaviour of these textures was predicted using crystal plasticity theory. From Schmids Law it is possible to calculate the normal strain resulting from slip along any set of reference axes and thus the strain relationships in the rolling, normal and transverse directions of a rolled sheet can be found. When the tensile axis is parallel to the RD, and the $\{011\}<111>$ slip system is considered, the following strain ratios were calculated for the different texture groups:

Cube-on-corner group:

If (110) and $(\bar{1}01)$ slip planes are favoured

$$\varepsilon_{ND} = \tfrac{1}{2}\varepsilon_{TD} = -\tfrac{1}{3}\,\varepsilon_{RD}, \quad r = \varepsilon_{TD}/\varepsilon_{ND} = 2$$

If $(10\bar{1})$ and $(\bar{1}10)$ slip planes are favoured

$$\varepsilon_{ND} = 0, \varepsilon_{TD} = -\varepsilon_{RD}, \quad r = \infty$$

These are the limiting deformation modes, therefore r varies between 2 and infinity. When $r = \infty$ no thinning occurs in the normal direction.

Cube-on-edge group:

Isotropic flow $\varepsilon_{ND} = \varepsilon_{TD} = -\tfrac{1}{2}\,\varepsilon_{RD}, \quad r = 1$

Cube-on-face group:

Anisotropic flow $\varepsilon_{ND} = -\varepsilon_{RD}, \varepsilon_{TD} = 0, \quad r = 0$

No thinning in the transverse direction.

Chao[32] also considered the yield stress relationships of the various textures. Due to their orientation, one texture may yield appreciably before the yield stress of another is reached. From the strain ratio calculations it was possible to conclude that anisotropic plastic flow and thus ridging could occur in a sheet in which these texture combinations and distributions were present.

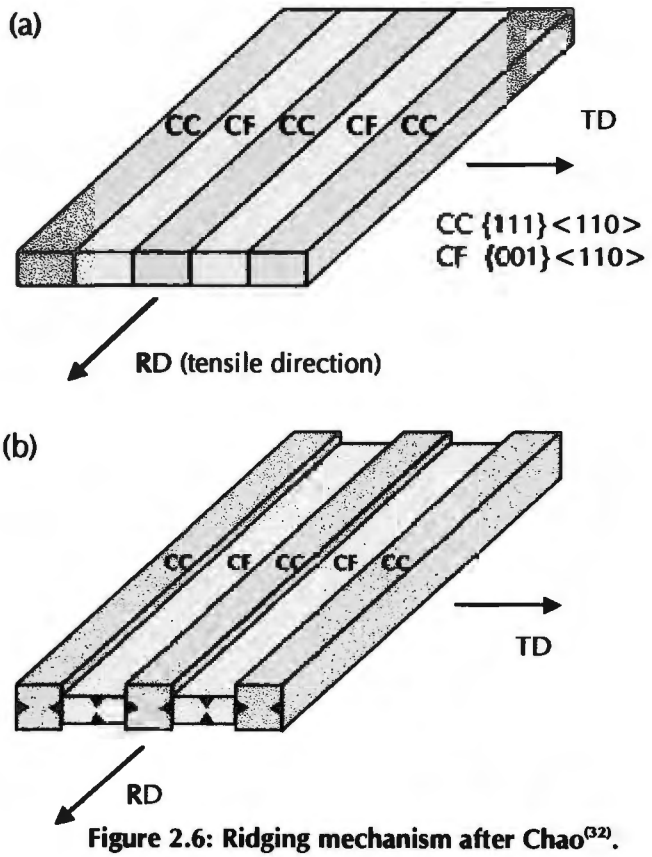

Figure 2.6: Ridging mechanism after Chao[32].

It was postulated that whenever a cube-on-face or cube-on-edge texture exists as a banded component in a cube-on-corner matrix, ridging results from differences in anisotropic yielding of the varying texture components (figure 2.6). Due to the work hardening effects of the cube-on-edge texture only slight ridging occurs when bands of this orientation are dominant, as opposed to more severe ridging when cube-on-face textures are prevalent. Furthermore, it was suggested that the development of the corrugations is restricted to the early stages of deformation when the applied stress is lower than the stress necessary to cause isotropic flow in all the grains.

Micro-etch pitting was also used in this investigation to discover texture composition and distribution in order to verify the mechanism. Small clusters of cube-on-face orientations were identified in a matrix of cube-on-corner orientations, however the accuracy of the results was again limited by the technique.

Ridging Mechanism after Wright (1972)

Unlike previous models, Wright[34] was determined to formulate a ridging mechanism that was consistent with both the ridging morphology and the observed textures in the ferritic stainless steel. It was suggested that, although there are a number of orientations found in these steels, almost all have the rolling direction near the [110] or [11$\bar{2}$] directions. Previous research had been done on the plasticity behaviour of the [110] texture[32,38], but no results for the behaviour of the [11$\bar{2}$] texture had thus far been published. This led to the decision to calculate the strain matrix for crystals orientated with their [11$\bar{2}$] directions parallel to the rolling direction. Similar mathematical methods used by Takechi *et al*[38] were employed, including lattice rotations and shape changes. Again the shear component ε_{23} was examined and found to correspond to the presence of severe ridging.

As a first step in the analysis by Wright[34], conclusions were drawn from data published by Chao[32] and Takechi *et al*[38] on the yielding behaviour of the [110]

texture. These conclusions were in agreement with the ideas of the original authors and can be summarised in the following two statements:

i) Elongation in the RD produces contraction in the ND for the (001)[110] cube-on-face texture, and contraction in the transverse direction for the $(\bar{1}10)[110]$ cube-on-edge texture.

ii) Shear strain ε_{23} in the transverse cross section of the sheet is near maximum for the $(\bar{1}11)[110]$ cube-on-corner and $(\bar{1}12)[110]$ textures.

Wright[34] was able to simplify the analysis of the $[11\bar{2}]$ component because, of the five pairs of slip systems having the highest Schmid factor, all of them were either of the form (hkl)[111] or $(hkl)[1\bar{1}1]$, making a general analysis feasible. The textures which underwent contraction in the normal direction ($\varepsilon_{z'z'}$), contraction in the transverse direction ($\varepsilon_{y'y'}$) and shearing in the transverse cross section of the sheet ($\varepsilon_{y'z'}$ or $\varepsilon_{z'y'}$), were calculated. The terms y′ and z′ are used to denote a coordinate system that takes into account rotations about the x axis. The results are summarised in Table 2.1.

Table 2.1: Textures associated with various transverse strains.

	Maximum εy′y′	Maximum εz′z′	Near max εy′z′, εz′y′
[110]//RD	$(\bar{1}10)[110]$	(001)[110]	$(\bar{1}11)[110]$ $(1\bar{2}1)[110]$
$[11\bar{2}]$//RD	$(111)[11\bar{2}]$	$(\bar{1}10)[11\bar{2}]$	$(021)[11\bar{2}]$

The information was used to evaluate texture data presented by Chao[32] and Eichen (unpublished data) in which the degree of ridging was correlated with the textures present in the material. In each case, the sheet exhibiting severe ridging included textures such that some produced contraction in the normal direction, $\varepsilon_{z'z'}$, while others produced yielding in the transverse direction, $\varepsilon_{y'y'}$, when elongated in the RD. Also, for three severely ridged cases, textures were present in the sheet which had maximum $\varepsilon_{y'z'}$ and $\varepsilon_{z'y'}$ shear strain components.

A model for ridging was subsequently proposed utilising the yield behaviour of the non-random textures and a plastic instability mechanism. The requirements for the model are longitudinal through-the-thickness bands of similarly

orientated grains contracting in the ND upon loading in the RD. These bands should be surrounded by matrix material having predominantly cube-on-corner orientations which will experience less or no contraction in the TD when subjected to the same stresses. During loading, the failure of the band to contract in the plane of the sheet will result in compressive stresses being generated across the band width and the ultimate buckling of the band across its width, as illustrated in figure 2.7. A series of localised buckling events would result in a sheet profile consistent with the ridging morphology.

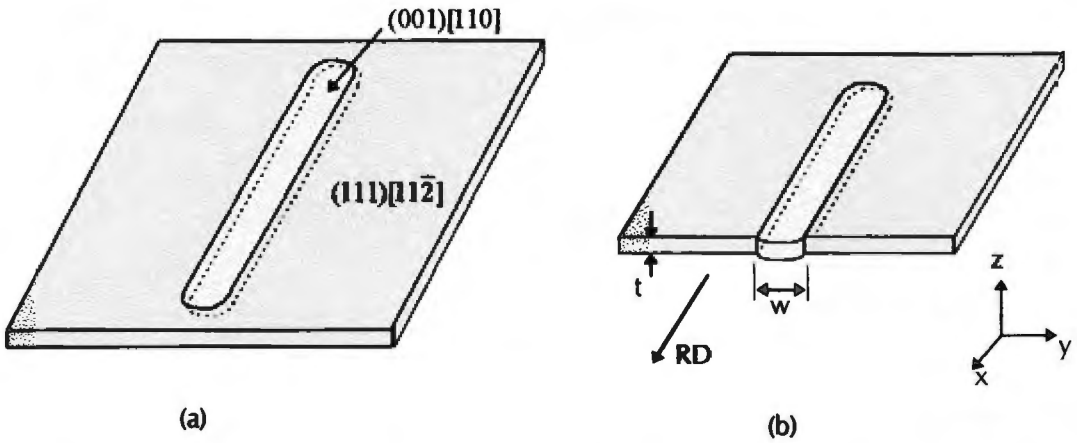

Figure 2.7: Buckling mechanism after Wright[34] (a) Before deformation (b) After deformation.

As an extension to the mechanism, Wright[34] considered how the mechanical properties of the sheet would affect the buckling behaviour of the unstable band. It was suggested that the material dictates a maximum thickness-to-width ratio, (t/w), for such a plastically unstable situation. A simple Euler buckling formula for clamped ends was used in the analysis. The critical buckling stress was defined as:

$$\sigma_{critical} = \frac{3.29 E_t t^2}{w^2}$$

where $\sigma_{critical}$ = buckling stress
E_t = tangent modulus
w = band width
t = sheet thickness

The formula can be rearranged to express the thickness-to-width ratio as a function of stress and modulus:

$$\frac{t}{w} = 0.55\left(\frac{\sigma_{critical}}{E_t}\right)^{1/2}$$

After yielding at approximately 415 MPa, the tangent modulus of annealed AISI 430 stainless steel was estimated to be roughly $7x10^5$ MPa, which produces a maximum thickness-to-width ratio of 0.43 for buckling. Investigation of actual ridging profiles of alloys AISI 430 and AISI 434 indicated that, while most bands have a thickness-to-width ratio of below 0.4, there are a few which exceed this figure. This was thought to be partly due to the fact that the assumption of clamped ends for the buckling model may be inaccurate and that an improved model could be somewhere between the case for clamped ends and hinged ends. Nevertheless, the ridging morphology of the sample is consistent with the quantitative predictions of the mechanism.

Furthermore, the calculations suggested that if the crystal plasticity behaviour of these textures is considered, ridging should not occur before 0.4% strain when elongated in the RD. From tensile tests, the onset of ridging was found to coincide with a tensile strain of 2.0%. This inconsistency was explained by the fact that in real materials bands of pure (001)[110] texture in a $(111)[11\bar{2}]$ matrix do not exist, but rather areas rich in (001)[110] texture in a matrix with appreciable $(111)[11\bar{2}]$ orientations are found. Thus the minimum RD tensile strain could be much higher than 0.4% and possibly in the region of 2.0%.

Ridging Mechanism after Harase et al (1990).

Harase *et al*[37] examined the ridging phenomenon in 17%-chromium stainless steel alloyed with 0.17% aluminium, with emphasis on the effect of rough rolling interpass time on ridging severity. For probably the first time, single grain orientation measurements were recorded, using scanning electron microscopy and electron channelling pattern (SEM-ECP) techniques, in order to characterise orientation distribution in both the transverse and longitudinal sections.

Sample material for comparative purposes was prepared by rough rolling in six passes to 12 mm. Interpass times were varied from 10 s (sample A) to 30 s

(sample B), while rough rolling finish temperatures were decreased from 1080°C (A) to 1021°C (B). Samples were further hot rolled to 3.7 mm, finishing at 570°C to prevent recrystallisation, and finally cold rolled to 0.74 mm both with and without annealing before cold rolling. Tensile tests in the RD indicated that extensive ridging occurred in sample A compared to mild ridging in sample B.

The following conclusions were drawn as to the effect of increasing the interpass time during rough rolling from 10 s (sample A) to 30 s (sample B):

i) There is an overall decrease in grain size.

ii) Although the principal texture components present are similar, a randomisation of the texture occurs.

iii) Regions of γ phase which are not elongated in the rolling direction are present in sample A (and not sample B), suggesting that nucleation occurred after rough rolling.

iv) Colonisation of grains of similar orientation decreased in both the TD and RD sections.

v) The fraction of large {100} < 011 > colonies decreased.

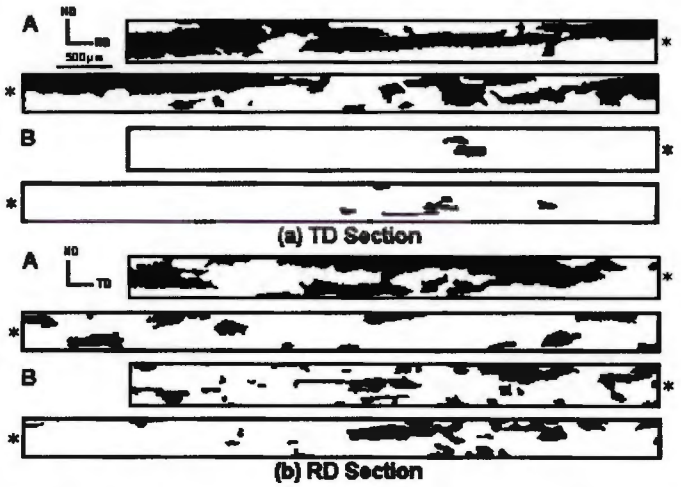

Figure2.8: Distribution of {100} < 011 > colonies in the central portion of rough rolled bar. A: Interpass time 10s, B: Interpass time 30s [37].

Precipitation of the γ phase during hot rolling has the effect of suppressing static recrystallisation when transformation and recrystallisation occur simultaneously. The presence therefore, of the large {100} < 011 > colonies in sample A was attributed to limited static recrystallisation due to the short interpass time, and

the suppression of recrystallisation by γ phase precipitation. Figure 2.8 illustrates the distribution of the {100}<011> colonies across the TD and RD sections of samples A and B. Sample A demonstrates an increase in the size and number of colonies across both sections. Therefore, based on this result and the result of the tensile tests, ridging was attributed to the distribution of {100}<011> colonies within the sheet. Harase *et al*[37] suggested that the colonies formed during rough rolling are inherited in the final annealed sheets because the {100}<011> texture is stable and persists even after cold rolling and annealing. The <111>//ND texture important to the mechanisms of Chao[32] and Wright[34], was largely absent.

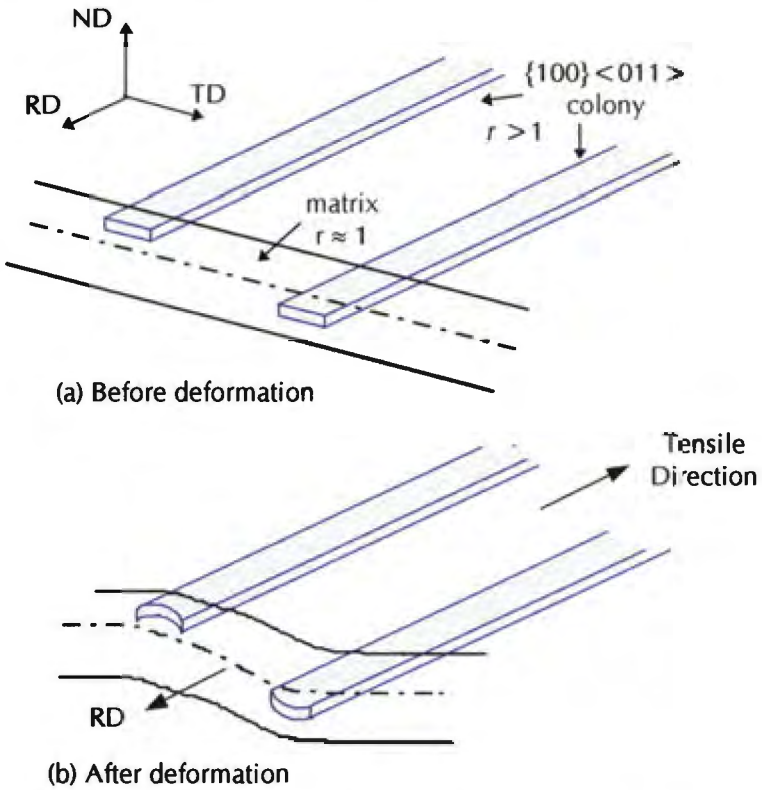

Figure 2.9: Ridging mechanism after Harase *et al*[37].

Although the authors did not consider plasticity analysis in any detail, a mechanism of ridging was proposed which suggests that when the {100}<011> colonies are distributed asymmetrically about the mid-plane of the sample, a bending moment will be generated which will result in the formation of the ridged profile (figure 2.9).

Ridging Mechanism after Salsgiver et al (1990)

Fibre texture analysis and strain ratio calculations were the focus of the investigation of the ridging phenomenon by Salsgiver et *al*[39]. A primary recrystallised strongly textured 3%-silicon steel was used to model the ridging behaviour in the more commonly researched 17%-chromium stainless steel. In an attempt to correlate fibre textures with ridging height, two samples, namely high permeability grain orientated (HGO) 3%Si-Fe and the conventional grain orientated (CGO) 3%Si-Fe steels, were examined.

A strong Goss texture $\{110\}<100>$ or η-fibre texture $<100>$//RD is expected from the CGO sample, as the secondary recrystallised grains are small and equiaxed. This is in contrast to the HGO steels which normally have a weaker η-fibre and strong γ-fibre texture $<111>$//ND in the primary recrystallised strip. Bulk texture measurements carried out by Salsgiver et *al*[39] confirmed these expectations. A strong γ-fibre and weak η-fibre was detected in the HGO alloy, while a strong η-fibre and weaker γ-fibre texture was evident in the CGO alloy. Examination of the ridged surface after 15% elongation of these samples revealed that CGO samples (possessing strong Goss) ridged severely, while HGO samples (possessing weak Goss) indicated essentially no ridging. These results suggested a correlation between ridging behaviour and the percentage of Goss or η-fibre texture.

In an attempt to validate these results, texture measurements through-the-thickness of the sheet were performed on both samples. It was found that the specimens which ridge (CGO), also have a Goss texture component which varies through-the-thickness, with the greatest intensity near the surface. But in non-ridging specimens (HGO), Goss orientations are largely absent and texture gradients are small. Thus the expectation of a correlation between Goss texture and ridging was confirmed. Furthermore, strain ratios calculated from centre to surface confirmed the relationship between ridging height and a through-thickness texture gradient. Ridging steels exhibited a higher overall r-value and a significant difference in strain ratio from centre to surface, while non-ridging steels showed very little difference in strain ratio through the sheet thickness.

Therefore, during tensile elongation the surface and central layers of the non-ridging steel or HGO alloy will deform homogeneously, while those of the CGO alloy will behave inhomogeneously relative to each other, giving rise to a corrugated surface profile. The authors, however, did not go as far as proposing a ridging mechanism.

Ridging mechanism after Bethke et al (1994)

Bethke *et al*[36] used a single cast of 17%-chromium ferritic stainless steel in the cold rolled annealed condition to investigate ridging and its relationship to texture. Local orientation measurements were performed using a semi-automatic EBSD facility along two line scans (TD and RD) and one area scan (transverse plane) on a sample which was subsequently subjected to 7% elongation.

The results of the line scan exhibited the difference between orientations along a line with respect to a reference direction $(001)[1\bar{1}0]$ (figure 2.10). These differences were represented by Rodrigues vectors, where the length describes the angle and the direction indicates the rotation axis in Rodrigues space. If the neighbouring points correspond to neighbouring grains, the differences between their vectors would describe the misorientation of the adjacent grains. For the transverse line scan, the vectors or orientations differed distinctly from point to point, whereas in the rolling direction the vectors showed two main preferred orientations, namely $(111)[1\bar{1}0]$ and $(11\bar{2})[1\bar{1}0]$. These vectors were also grouped in bundles of approximately 50 grains of similar orientation.

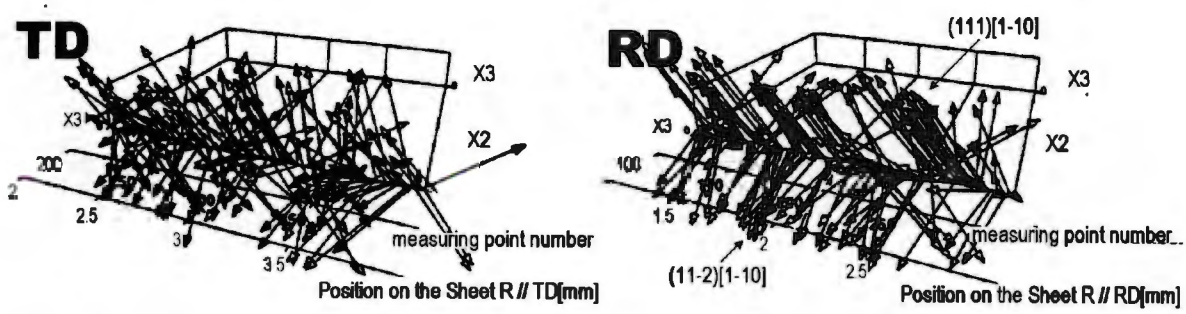

Figure 2.10: Orientation difference between measuring points given by Rodriques vectors for the (a) transverse direction and (b) rolling direction[36].

The distance between measuring points for the transverse plane area scan was set at 5μm which was slightly smaller than the average grain size. For evaluation purposes all orientation measurements were collected into classes within a misorientation angle of 10° relative to seven preferred ideal orientations and superimposed on the area scan. These seven ideals all fell on either the α or γ-fibre textures. Examination of the resultant orientation map showed *no distinct clustering of similar orientations* but rather a random distribution of texture.

These findings allowed for some important conclusions:

i) There is an anisotropic arrangement of orientations in the rolling plane, indicated by the line scan results.

ii) The concept that deformation of single grains of different orientation is the cause of ridging is ruled out by the fact that one ridge, of dimensions 1 mm x 0.5 mm, contains about 5000 grains all of varying orientation.

iii) The idea that ridging is the result of the deformation of clusters of similar grains cannot be correct, as the length of clustering in the RD is at least 500 times smaller than the actual length of the ridge.

These conclusions were confirmed by calculating the misorientation correlation index, MCI, of the orientation difference distribution function (ODDF). This function is equivalent to the texture index, J, of an ODF and describes the sharpness of the ODDF. (A purely random ODDF would produce an MCI of 1). The MCI value for the RD was > 1 for about 50 to 100 points (0.5 - 1.0 mm), whereas for the TD it was only >1 for one or two points. In addition, the strength of correlation for nearest neighbouring orientation differences was higher by a factor of five for the RD, agreeing well with the outcome of the line scans.

Consideration of the above information led to a proposal for the ridging mechanism based on the idea that ridging is caused by the superposition of the deformation of a great many grains. As in previous investigations, Bethke *et al*[36] evaluated the behaviour of the main slip systems in BCC materials, which again led to the conclusion that there exists a preference for the ε_{23} shear component

during straining. For two symmetrically equivalent orientations, this component would have the same magnitude but opposite sign. Using EBSD it was possible to map the spatial distribution of such symmetrically equivalent shears across the area scan, assigning the appropriate positive or negative sign to each shear. The results showed that a spatial coherency of similar sign was evident in this area scan which was larger than that found in the orientation map, while a preponderance for one sense of shear added to the results (figure 2.11).

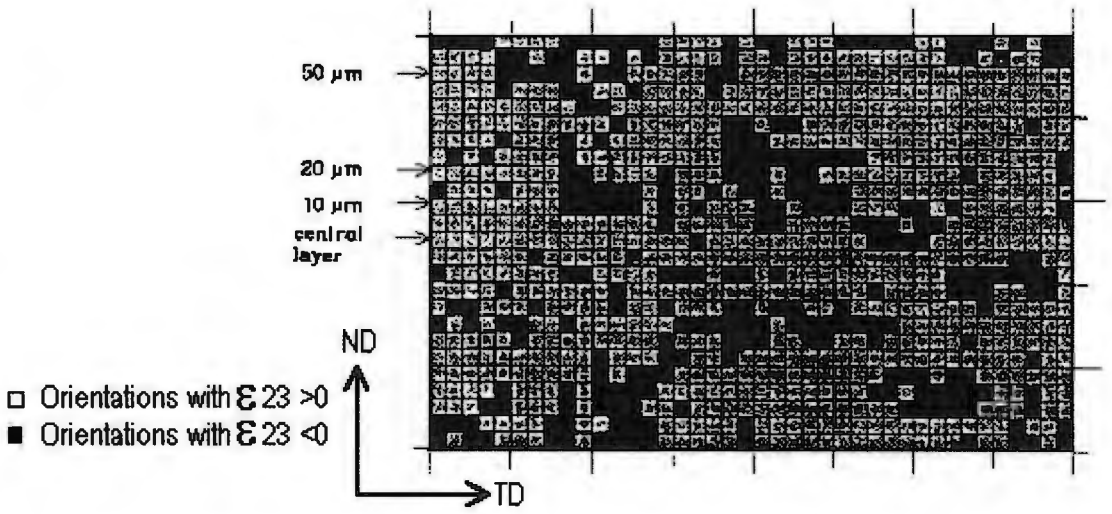

Figure 2.11: Orientation measurements collected into two classes of the shear component $\varepsilon_{23} > 0$ and $\varepsilon_{23} < 0$[36].

The model was expanded further in an attempt to quantify the explanation for ridging. It was surmised that for a linear row of points, the variation in sign (i.e. direction of ε_{23} shear) would lead to a zigzag line, where the sign for the nth grain is given by $\Delta h_n = 2\varepsilon_{23}(n)10$ µm, where 10 µm corresponds to the average grain size (figure 2.12). Thus, for a thin sheet the effect of deformation of grains lying on top of one another would superimpose, providing an average deformation through the sheet thickness. A bending of the sheet would follow which is observable as corrugations. As a first estimation in testing this hypothesis, the same magnitude of shear was assigned to each grain providing the same probability for positive or negative shear. The resultant non-periodic profile of hills and valleys was then suggested to be the result of a stochastic process analogous to the outcome of a coin tossing experiment. The curves for three such coin tossing experiments are indicated in figure 2.13. The plots form

peaks and troughs of differing amplitude and period as was observed for the ridging profile.

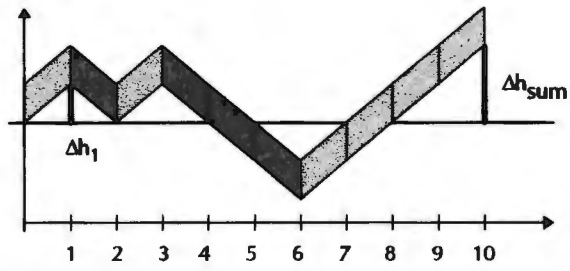

Figure 2.12: Shearings ε_{23} in the transverse section of the sheet[36].

Thus it was concluded that ridging is caused by the combination of deformation behaviours of many grains within a ridge of about 1mm. Most of the shear strains of the grains cancel each other out, but the remaining few yield to form corrugations. The stochastic approach used to quantify the model yields both the large undulations and the finer surface roughness observed on a ridged material.

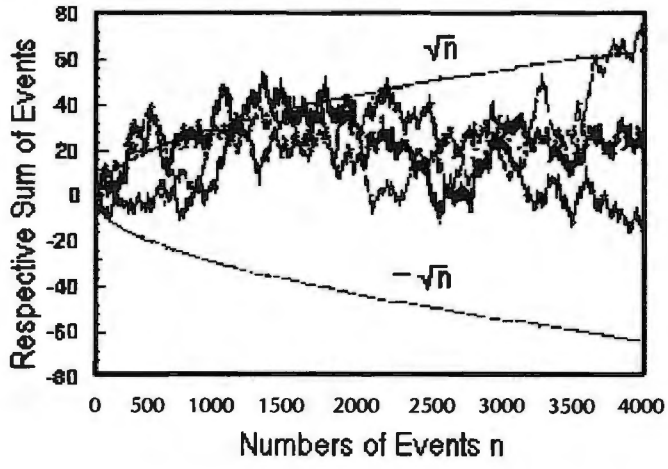

Figure 2.13: Results of three coin tossing experiments with ε_{23} set to ±1[36].

2.1.5.2 Discussion of the Texture Related Ridging Models

Although the textural ridging mechanisms presented in the last few decades clearly differ, they all share the one characteristic that the ridging phenomenon is linked to the anisotropic deformation behaviour of the texture components present in the material. The earlier models possess a number of shortcomings, due in part to the lack of a suitable technique for microtexture measurement, as

well as the lack of a method for accurate surface morphology characterisation. For example, the very well known mechanism proposed by Chao[32] is based on variations in sheet thickness across the transverse plane. It is now known that the ridging profile exhibits a true corrugation, maintaining sheet thickness across the transverse section, which naturally invalidates the mechanism by Chao[32].

Although Takechi *et al*[38] managed to characterise correctly the ridging profile, other factors cast doubt on the generality of this mechanism. Firstly, the model depends on the presence of either $\{111\}<011>$ or $\{211\}<011>$ texture clusters. Pole figures presented for samples after cold rolling show moderate evidence for the latter of these components; however, pole figures after annealing show little indication of either of these texture components, thus bringing the accuracy of the mechanism into question. Moreover, results of the etch pitting experiments, used to verify the mechanism, are insufficient to make accurate conclusions. In support of the model by Takechi *et al*[38], however, Bethke *et al*[36] in their recent analysis of ridging identified $\{111\}<011>$ and $\{211\}<011>$ orientations not only to be dominant, but also to be distributed in narrow clusters of each texture extending in the RD. Other researchers have also identified these orientations as contributing to the final texture present in the steel, but could find no clear correlation between the textures and the ridging characteristics of the sheet. For example, Salsgiver *et al*[39] states that the $\{111\}<011>$ component is of significant intensity in both the ridging and non-ridging steels.

In 1973, after Wright[34] published the 'plastic buckling mechanism' for ridging Chao[44] challenged this theory by publishing results that attempted to invalidate the model. Chao[44] produced evidence of ridging in samples elongated at tensile directions 0°, 30°, 45°, 60° and 90° from the RD. After deformation all ridges ran parallel to the RD. It was noted that the ridges on the transversely elongated samples could not be produced by the 'buckling mechanism'[45]. A tensile stress in the TD could not provide compressive stresses to cause buckling of the $\{001\}<110>$ texture in order to give rise to ridges along the rolling direction.

In reply Wright[46] performed similar investigations on samples with a tensile axis at various angles to the RD. It was found that the undulation was greatest for the samples elongated in the RD, and decreased as the tensile axis diverged from the RD to a point where no corrugations were visible for the specimens with a tensile axis at 90° to the RD. Light surface striations were visible on the latter samples, but when measured their out-of-plane displacement was found to be of an order of magnitude smaller than those for the RD elongated samples. Thus the deformation associated with the ridges or corrugations is on a much greater scale than the scale of the surface striations. It was thus concluded that no evidence existed which could call into question the acceptability of the buckling mechanism.

The investigation in 1994 by Bethke *et al*[36] cast doubt on all previous models, by concluding that the fundamental requirement of these models, i.e. the presence of texture clustering, does not actually exist. Nevertheless, the stochastic model proposed by Bethke *et al*[36] does seem to rely on specific texture clustering extending in the rolling direction. The reason given for the extension of the corrugations in the RD is the greater coherency length in that direction which relies directly on the alignment of similar orientations.

In addition, the ideal textures which experience ε_{23} shear during uniaxial tension are $\{111\}<110>$ and $\{112\}<110>$, while other ideals such as $\{111\}<112>$ and $\{100\}<011>$ will not shear in this direction. Naturally, if an orientation has a rotation slightly off the ideal it can produce a minor shear component in the ε_{23} direction. Bethke *et al*[36] classified all the orientations present in the area scan according to the direction of shear, while making no distinction between textures which produce small or large contributions of ε_{23} shear and thus the map of ε_{23} shear can be misleading.

2.1.5.3 Ridging Mechanisms Based on Non-textural Arguments

Ridging has been observed in ferritic stainless steels possessing almost exclusively a $\{111\}<112>$ texture and a very fine grain structure[40]. Conventionally this combination has been favourable for the elimination of

ridging[33], however the results of the abovementioned experiment suggest that origins of ridging are not limited to texture and grain size considerations. Suzuki *et al*[31] were motivated by these factors to investigate the relationship between the banded segregation of chromium and carbon in ferritic stainless steel and the ridging phenomenon. Elemental segregation was observed by way of a strip pattern which forms on the surface of the alloy during deep chemical etching. A ferritic stainless steel with 0.05 wt% carbon and therefore a $\alpha + \gamma$ dual phase structure in the range of 950°C and 1350°C was used in the study. During hot rolling, partitioning of the elements occurred due to solubility differences, resulting in the austenitic phase becoming enriched in carbon and iron and depleted in chromium. Variations in chromium content led to differences in corrosivity and thus during etching alternating light and dark regions appeared on the sheet surface parallel to the RD. Suzuki *et al*[31] identified a good correlation in terms of periodicity between the light and dark etched bands of the stripe pattern and the ridging profile and thus concluded that element partitioning could be a contributing factor to the ridging phenomenon.

The study conducted by Sheppard and Richards[28] into the ridging phenomenon in ferritic stainless steel also concluded with a non-texture related cause for the ridging phenomenon. The investigation examined in detail the effects of hot and cold process parameters on the structure, substructure and texture of the alloys, as well as the influence of these parameters on the mechanical properties of the material, such as formability and ridging behaviour. Results of hot rolling experiments indicated that deformation at low temperatures (825°C) followed by water quench prompted the formation of a non-favourable banded austenite/ferrite structure, while deformation at higher temperatures encouraged recrystallisation and grain growth. Results of a ridging test of recrystallised material showed a decrease in ridging height with an increase in hot roll temperature, suggesting that microstuctural banding could influence the ridging phenomenon. Thus Sheppard and Richards[28] suggested that the main cause of roping was the inhomogeneity of the developed structure and that the ridging mechanism was one of differential yielding under tension. It was also reported

in this investigation that the ridging profile did not extend through-the-thickness of the sheet to form a corrugation, but was rather a surface feature specific to each face.

Shortcomings of non-textural origins of ridging

Suzuki et al[31] in their investigation of the ridging phenomenon, provided conclusive correlation between the corrosive stripe pattern of the cold rolled annealed product and the ridging profile after tensile deformation. No actual mechanism however, is given for how the ridges arise during straining, or how the final microstructure and yielding properties are influenced by the banded segregation of the elements.

The explanation given by Sheppard and Richards[28] for ridging is based on the presence of an inhomogeneous microstructure in the form of bands of similarly sized grains running parallel to the RD. These bands form during hot rolling processes due to deformation in the $\alpha+\gamma$ dual phase region. Ridging however, has been observed in ferritic stainless steels that do not experience a phase transformation during hot rolling and where an equiaxed grain structure exists after annealing[211]. This suggests that grain size banding cannot be the principal cause of ridging and that other factors not related to grain morphology must be involved. Yet, the fact that phase banding has implications for texture distribution cannot be denied. Furthermore, the ridging profile in the study by Sheppard and Richards[28] was not characterised as a true corrugation, instead the surface features were found to be specific to each sheet face, which also casts doubt on these results.

2.1.5.4 Reduction of Ridging

As mentioned previously, the numerous proposals for the mechanism of ridging include mostly inhomogeneous texture distributions either through-the-thickness of the sheet or extending as bands in the RD of the material. It follows therefore, that the majority of the suggestions to control or eliminate ridging address ways in which to randomise the texture distribution through various

microstructural manipulations and control of the thermomechanical process. In the case where ridging is related to inhomogeneous microstructural features, such as grain size and precipitation distribution, similar methods to homogenise the structure are given as a means to control the ridging height.

It is commonly believed that ridging and non-ridging steels differ in γ-fibre intensity[32,33,49,50,51]. The $\{111\}<112>$ and $\{111\}<011>$ orientations, because of their high strain ratios, are known to encourage material flow in the width direction during forming operations. It has therefore been suggested that for deep drawing applications, it is beneficial for the sheet to possess a high intensity γ-fibre texture, providing a favourably high average r-value[33]. The γ-fibre texture is linked to recrystallisation and associated grain refinement processes which occur during annealing treatments, and thus by encouraging recrystallisation through manipulation of the thermomechanical process, the percentage γ-fibre texture can be increased.

Shindo *et al*[33] reported that ridging is most severe in steels where neighbouring bands of $\{100\}<011>$ and $\{111\}<011>$ textures are present in the hot rolled sheet. Texture inhomogeneity was found to persist through cold rolling and annealing until the final product, resulting in colonies of similar textures and the formation of ridges. The banded $<011>$//RD partial fibre texture supposedly results from insufficient recrystallisation due to a small reduction per pass during hot rolling. Indications are, therefore, that increased recrystallisation promotes the formation of the $\{111\}<112>$ texture at the expense of $<011>$//RD partial fibre texture, which corresponds to a reduction in ridging.

Alternatively, it has been suggested that ridging can be eliminated by the controlled distribution of a hard martensitic phase which forms upon rapid cooling from the α/γ dual phase region [52]. Dispersion of martensite introduces strain concentrations in the ferrite matrix during cold rolling, which produces a fine grain structure after final annealing and reduces the ridging height. This treatment, however, traditionally requires a time consuming and costly batch annealing process extending for about two hours after hot rolling. This prompted the investigation of an in-line or continuous annealing process which

would control ridging without the need for an additional heat treatment. For example, Koike *et al*[52] have developed a continuous annealing treatment of AISI 430 ferritic stainless steel to reduce ridging by controlling the hot roll coiling temperature. It was found that by rapid cooling from a coiling temperature of 400°C, bands of martensite are formed elongated in the rolling direction. These dispersions have the same effect as previously stated, to form strain concentrations during cold rolling and a fine grain structure which consequently reduces the ridging level. The percentage martensite was controlled by increasing the carbon content which acts as a grain refiner due to the increased number of particles present in the microstructure. Alloying with carbon however, has a detrimental effect on other physical properties such as formability, thus other austenite forming elements such as manganese and nitrogen were introduced instead. In this way Koike *et al*[52] was able to produce a low carbon steel with good formability and a low level of ridging during forming.

The addition of minor alloying elements, such as niobium, titanium and aluminium have also been reported to reduce the ridging phenomenon in ferritic stainless steel[28,49,53,54,55]. Niobium carbides and titanium carbonitrides which do not dissolve during recrystallisation effect both the grain size and the final textures of the sheet. The texture of a niobium or titanium alloyed steel revealed a deviation from the commonly encountered $\{111\}<112>$ recrystallisation texture towards an $\{557\}<583>$ orientation. This texture has been explained by Raabe and Lücke[56] to be the result of particle induced growth selection. Lee *et al*[55] reported that recrystallisation during hot rolling is suppressed by alloying and that the temperature of recrystallisation can be reduced by up to 100°C. Fine equiaxed microstructures are formed after such annealing treatments, which contribute towards the reduction of ridging in the sheet.

Alloying with aluminium (0.10-0.15 wt%) has a similar grain refining effect on the microstructure, as investigated by Sawatani *et al*[54]. In an investigation to develop a continuous annealing process for 17 wt% chromium stainless steel,

the addition of aluminium was found to improve the r-value, toughness, corrosion resistance and the ridging height of the material. Fine AlN precipitates, formed during slab heating between 1000°C and 1100°C, were shown to affect both texture and microstructure. The increased number of AlN precipitates resulted in an increase in the <111>//ND fibre texture in the centre layer of the microstructure, and consequently led to an improved r-value. By lowering the hot roll finish temperatures to 900°C and continuously annealing between 950°C and 1000°C, a fine equiaxed grain structure developed, as opposed to a retained elongated structure formed by the conventional batch annealing process. Thus it was possible to define a thermomechanical process, including a continuous anneal, for the production of a ferritic stainless steel containing 0.12% aluminium, which shows very little ridging during forming.

2.1.5.5 Simulation of the Ridging Phenomenon

The study of ridging by Nagashima *et al*[113] is the only published research sourced in the current investigation in which the deformation behaviour of a ferritic stainless steel is simulated using finite element modelling. A finite element model was set-up in which narrow fibres of cube-on-face texture were aligned parallel to the RD in a matrix of cube-on-corner orientations. The aim of the simulation was to establish whether or not FEM could be used to reproduce the form of the ridging profile in a SUS 430 steel. As an initial step in the investigation, the bulk texture of sample material which exhibited severe ridging was measured in order to identify the principal orientations. These orientations, namely (001)[110] and (554)[22$\bar{5}$] were then assigned to the fibres and matrix of the model respectively. Tensile tests were also performed on the sample material at 0°, 45° and 90° to the RD and the upper and lower surface profiles examined. After elongation, the tensile samples indicated a fine surface roughening effect superimposed on larger undulations, where the profiles of the upper surfaces matched those of the lower surfaces to produce a corrugated profile. Also, the corrugations were found to become smoother as the tensile axis was rotated away from the RD. The bulk texture before and after

elongation showed little variation in major orientations and therefore crystal rotation due to deformation was not considered in the FEM model.

A two dimensional finite element model (50 x 25 x 0.7 mm^3) containing 400 triangular elements was devised. Strain was applied in the lengthwise direction to 20% elongation and the displacements in the thickness and width directions were measured. The narrow fibres of (001)[110] orientations were arranged in the model parallel to the RD as indicated in figure 2.14. A rotation of the tensile axis was simulated by rearrangement of the (001)[110] orientation fibres at 0°, 45° and 90° to the tensile axis. During deformation, the number of active slip systems and the value of strain in the thickness direction (ε_z) and width direction (ε_x) were calculated for each element.

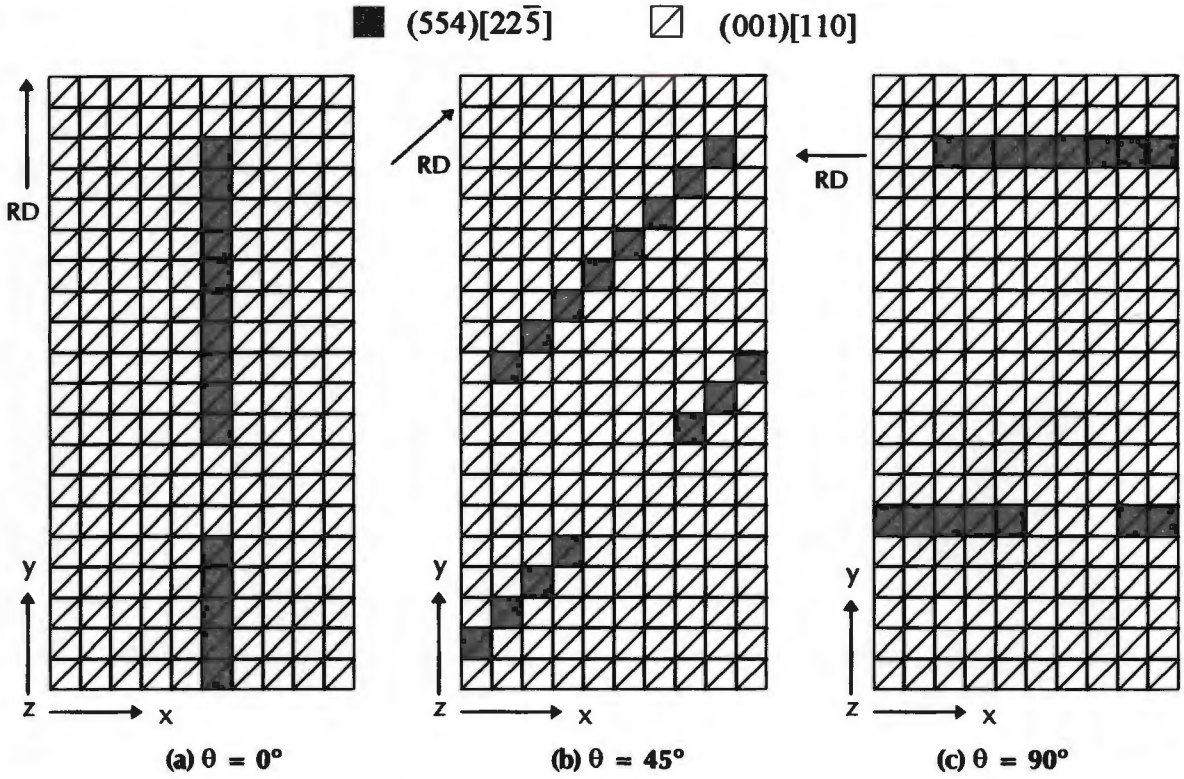

Figure 2.14: Arrangement of grains for finite element models. θ is the angle between the RD and the tensile axis[113].

The results of the simulation indicated that the (001)[110] fibres thinned more in the z direction during deformation compared to the surrounding matrix, but reduced significantly less in the width or x direction. In other words, the thickness strain in the fibres was larger than in the matrix, while the width strain

was relatively smaller. It was suggested that this gives rise to compressive stresses in the fibres in the width direction and consequently to a bending of the specimen in this region. By rotating the tensile axis away from the RD, it was established that a reduction in overall strain is experienced by the fibres and the matrix elements. The strain levels were higher than 0.0039% for the simulation in which deformation was applied in the RD and only just above 0.0017% for the simulation at 90° to the RD. This agreed well with the results of actual tensile tests performed on sample material. Although this model demonstrated the plastic behaviour of the two orientations coupled together, the actual ridging profile was not modelled, and the idea that compressive stresses can arise in the width direction was only surmised.

2.2 Constitution, Microstructure and Texture of Sample Material

2.2.1 Ferritic Stainless Steel

Ferritic stainless steels possess good formability and are used in many applications where press forming operations such as deep drawing are required. Their main advantages over the more popular austenitic stainless steels are their low susceptibility to stress corrosion cracking and their lower cost. They have a body-centred cubic structure, a low carbon content (less than 0.1 wt%) and a chromium content of between 11% and 30%. The conventional process route for the manufacture of ferritic stainless steel begins with a continuously cast slab, which is subsequently hot rolled into strip possessing a thickness of between 4 mm and 6 mm. This is followed by either a long term batch anneal process or a continuous line anneal process at around 820°C, and then a further reduction to about 1 mm by cold rolling. The sheet is subjected to a final annealing and pickling process before the product is complete. At each stage in the thermomechanical process (TMP), the specific parameters which have been applied in terms of temperature, strain, strain rate and interpass time, play a vital role in determining the properties and performance of the final sheet. Extensive research has gone into investigating the influence of the thermomechanical process parameters on the microstructural evolution of these steels, in an attempt to optimise their physical properties. More recently, a continuous annealing process, which does away with the costly conventional batch annealing process, has been used to treat the material before cold rolling[52].

2.2.1.1 Microstructural Evolution During the Thermomechanical Process

In addition to chromium, other alloying additions include austenite stabilising elements such as nickel and manganese, as well as molybdenum, aluminium, titanium and niobium, each added to improve specific physical properties. For example, molybdenum added to AISI 434 improves passivation and pitting corrosion resistance, while aluminium which is added to AISI 409 prevents

hardening of the alloy[57]. Aluminium is also added to AISI 430 to form fine dispersions of carbide and nitride precipitates which produce a uniform equiaxed grain structure. This improves the formability and deep drawing properties of the final sheet[53]. Niobium and titanium are often included in ferritic stainless steel to help prevent intergranular corrosion by "tying up" the carbon and nitrogen in the steel, thereby preventing the formation of chromium carbides and chromium nitrides at the grain boundaries[108]. The chemical compositions of the ferritic stainless steels are indicated in Table 2.2, including the alloy studied in the present investigation.

Table 2.2: Chemical composition of ferritic stainless steels according to the specifications of the American Iron and Steel Institute.

	C	Mn	P	S	Si	Ni	Mo	Cr	Other
AISI 405	0.08	1.00	0.040	0.030	1.00	0.60		11.5/14.5	0.1/0.3 Al
AISI 409	0.08	1.00	0.045	0.045	1.00	0.50		10.5/11.75	Ti0.75
AISI 429	0.12	1.00	0.040	0.030	1.00	0.75		14.0/16.0	
AISI 430	**0.12**	**1.00**	**0.040**	**0.030**	**1.00**			**16.0/18.0**	
AISI 434	0.12	1.00	0.040	0.030	1.00		0.75/1.25	16.0/18.0	
AISI 436	0.12	1.00	0.040	0.030	1.00		0.75/1.25	16.0/18.0	Cb0.7
AISI 442	0.20	1.00	0.040	0.030	1.00			18.0/23.0	
AISI 446	0.20	1.50	0.040	0.030	1.00			23.0/27.0	0.25 N

* All values quoted are maximums and in wt %.

Depending on the composition, ferritic stainless steel will undergo a phase transformation from ferrite to austenite at temperatures elevated above 800°C[108]. For simple ferritic grades with low carbon content and very minor austenite stabilising elements, no transformation occurs at high temperatures and the steel will remain fully ferritic during hot rolling. If however the carbon content is increased slightly, the austenite range will be expanded, and an austenitic phase will appear as elongated bands during hot rolling. For an alloy containing 16.5% chromium and 0.05% carbon, approximately 40% of the ferrite will transform to austenite during normal hot rolling procedures[58]. Figure 2.15 indicates the effect of increasing the percentage of carbon and nitrogen on the $\alpha/(\alpha+\gamma)$ boundary of the iron-chromium system. If sufficiently rapid, the austenitic bands are able to transform to cubic or relaxed martensite

on cooling. Thus at room temperature, the microstructure has a dual phase structure with hard martensitic regions dispersed within the elongated grains of ferrite matrix[59,58,28].

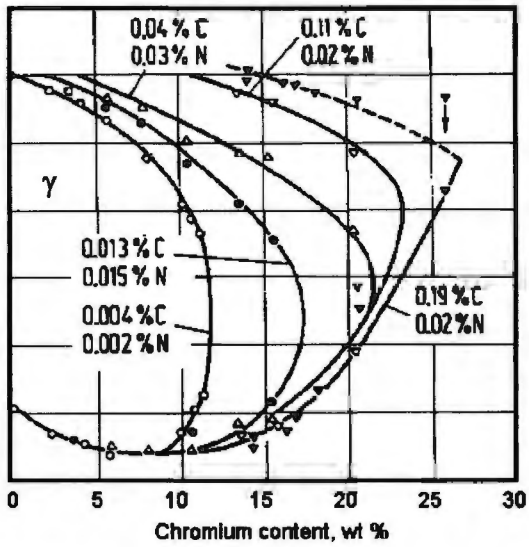

Figure 2.15: Effect of carbon and nitrogen on the iron/chromium system[57].

During subsequent annealing treatments the martensitic phase is able to transform into ferrite plus carbides. The size and distribution of the precipitates and grains after annealing is dependent on the prior hot rolling conditions, the percentage reduction imposed on the strip and the annealing time and temperature. Under certain conditions, hot rolling in the dual phase region produces a bimodal grain size, where the coarse and fine grains are distributed as bands within the microstucture and are elongated in the RD[52,53,28].

Cold rolling produces a highly deformed microstructure which generally completely recrystallises on annealing. The percentage cold rolling influences the strength and formability of the final annealed sheet. Any grain size banding formed during the hot rolling stage is preserved after cold rolling and annealing to produce a bimodal grain structure[28].

2.2.1.2 Deformation and Annealing Textures

Ferritic stainless steels, because of their low work hardening rate, are used in deep drawing applications where metal flow is required, rather than in stretch forming operations which require a high work hardening rate. Texture thus

plays a far more vital role in the fabrication of these alloys than, for example, in austenitic stainless steels which are more suitable for stretch forming. During deep drawing of ferritic stainless steels, material flow should occur in the sheet plane, as opposed to the thickness plane and should be equivalent in all directions. To ensure these properties, the material must possess a high strain ratio or Lankford r-value and a low Δr-value [$\Delta r = (r_0 + r_{90} - 2r_{45})/4$] to guarantee isotropic flow behaviour. This can be achieved through careful manipulation of the principal texture components by controlling the thermomechanical process parameters. Texture properties are thus fundamental in ensuring the quality of ferritic stainless steel sheet production, and a complete understanding of how the thermomechanical process affects the final texture, is essential.

The texture evolution during hot rolling, cold rolling and subsequent recrystallisation of 17%Cr ferritic stainless steel is reviewed in the following section. Orientation distribution functions (ODF) are used to provide an unambiguous representation of the principal texture components. Due to the cubic symmetry of the material and the orthorhombic symmetry of the rolled sheet, textures of ferritic stainless steel can be represented by three Euler angles (φ_1, ϕ, φ_2) in reduced Euler space ($0° \leq \varphi_1\ \phi\ \varphi_2 \leq 90°$). In addition, textures of BCC materials comprise almost entirely of a few orientation fibres, which can easily be represented by plotting the density of orientations along these fibres (fibre diagrams). An outline of the relevant fibres is given in Table 2.3, while a schematic of the fibres in reduced Euler space is shown in figure 2.16.

Table 2.3: Fibre textures found in ferritic stainless steel.

Fibre	Fibre Axis	Orientation on the Fibre
α	<110>//RD	{001}<110>–{112}<110> and {111}<110>
β	≈<111>//ND	{111}<110>, {557}<583> and {111}<112>
γ	<111>//ND	{111}<110>–{111}<112>
η	<100>//RD	{001}<100>–{011}<100>
ζ	<110>//ND	{011}<100>, {110}<112> and {110}<110>

Hot Rolling Textures

Due to the nature of the rolling procedure, regions near the surface will deform under shear conditions, while those closer to the centre will experience near

plane strain conditions[60-64]. This results in a marked texture gradient through-the-thickness of both the hot and cold rolled sheet. At the surface of the hot rolled plate, shear textures dominate including a strong Goss component $\{110\}<001>$ and minor components of $\{4\ 4\ 11\}<11\ 11\ 8>$ and $\{110\}<112>$ orientations (figure 2.17)[60,62-65].

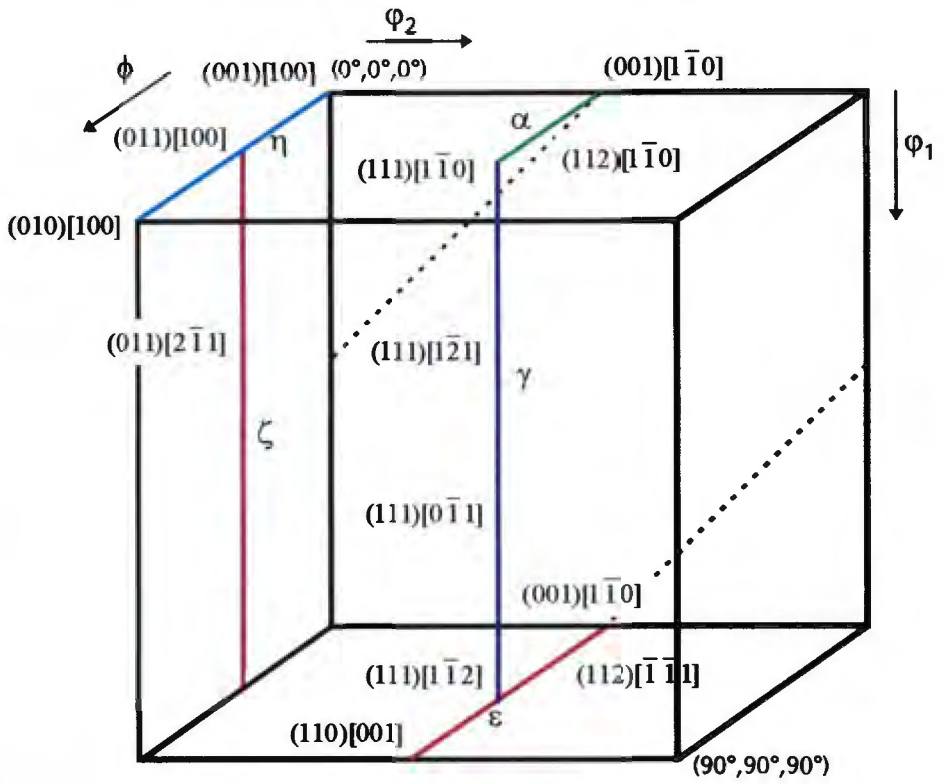

Figure 2.16: Reduced Euler space indicating fibre textures.

Raabe and Lücke[62] found that the intensity of the Goss texture is a maximum in the subsurface layers at a depth of s=0.8 (surface s=1.0 and centre s=0.0), (figure 2.18), which corresponds directly to the region of maximum shear strain, as well as to an increase in the Zener-Holloman parameter relative to the centre regions. The centre layers are characterised by an α-fibre texture with a maximum intensity at $\{001\}<110>$ and a secondary γ-fibre texture (figure 2.19)[60,62-65]. This typical "cold rolling" texture results from the combination of recovery of pancake shaped grains and plane strain deformation conditions. If temperatures in the centre layers remain high enough during hot rolling, dynamic recovery will occur and so nucleation and recrystallisation are

prevented. This leads to the characteristic pancake shaped grains and a strong α-fibre texture.

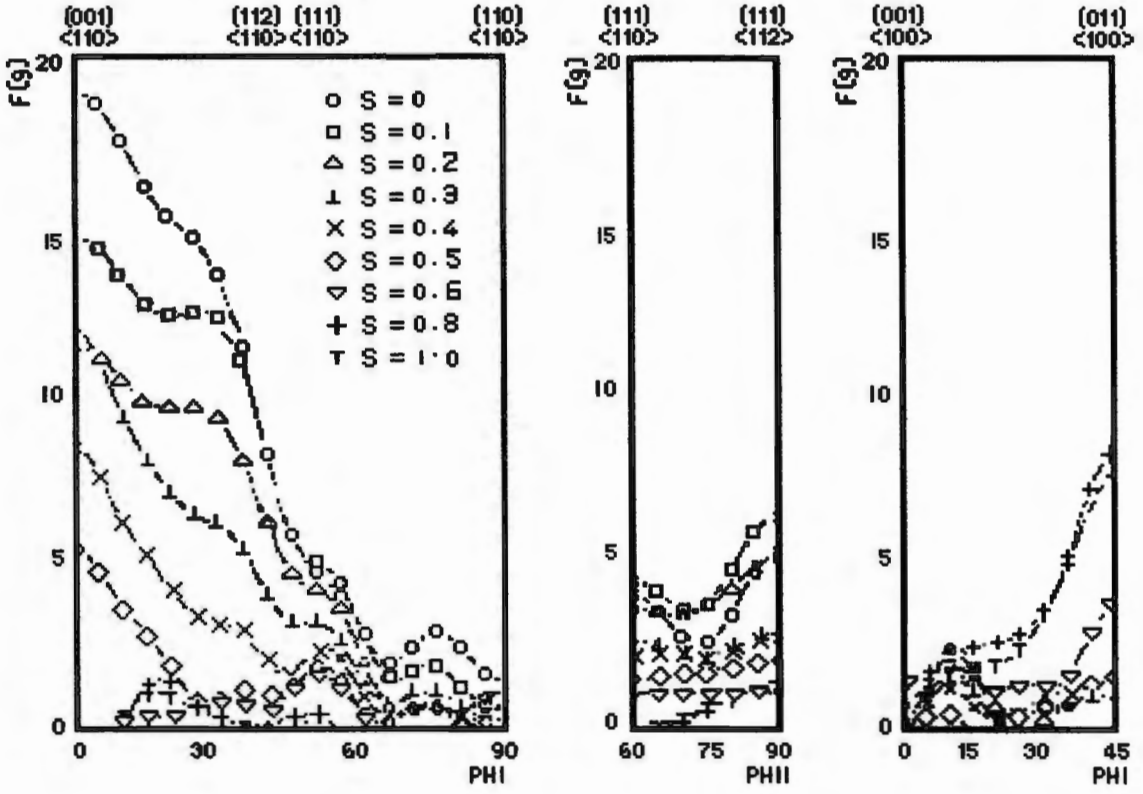

Figure 2.17: Fibre diagrams of hot-rolling textures through-the-thickness [63] (surface: s = 1.0, centre: s = 0).

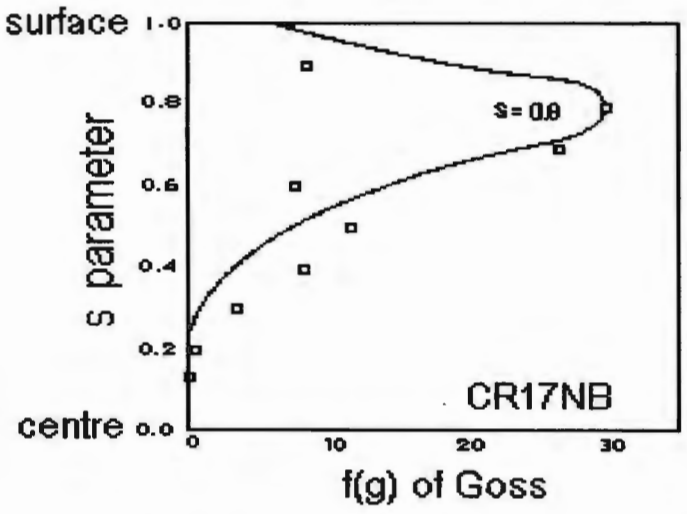

Figure 2.18: Profile of Goss texture through-the-thickness[62].

Cold Rolling Textures

Cold rolling of the hot band of ferritic stainless steel results in an overall sharpening of the hot-roll textures[60,62-65]. Textures remain inhomogeneous

through-the-thickness of the sheet until about 90% reduction of the hot rolled sheet. The primary component is once again the α-fibre while the secondary

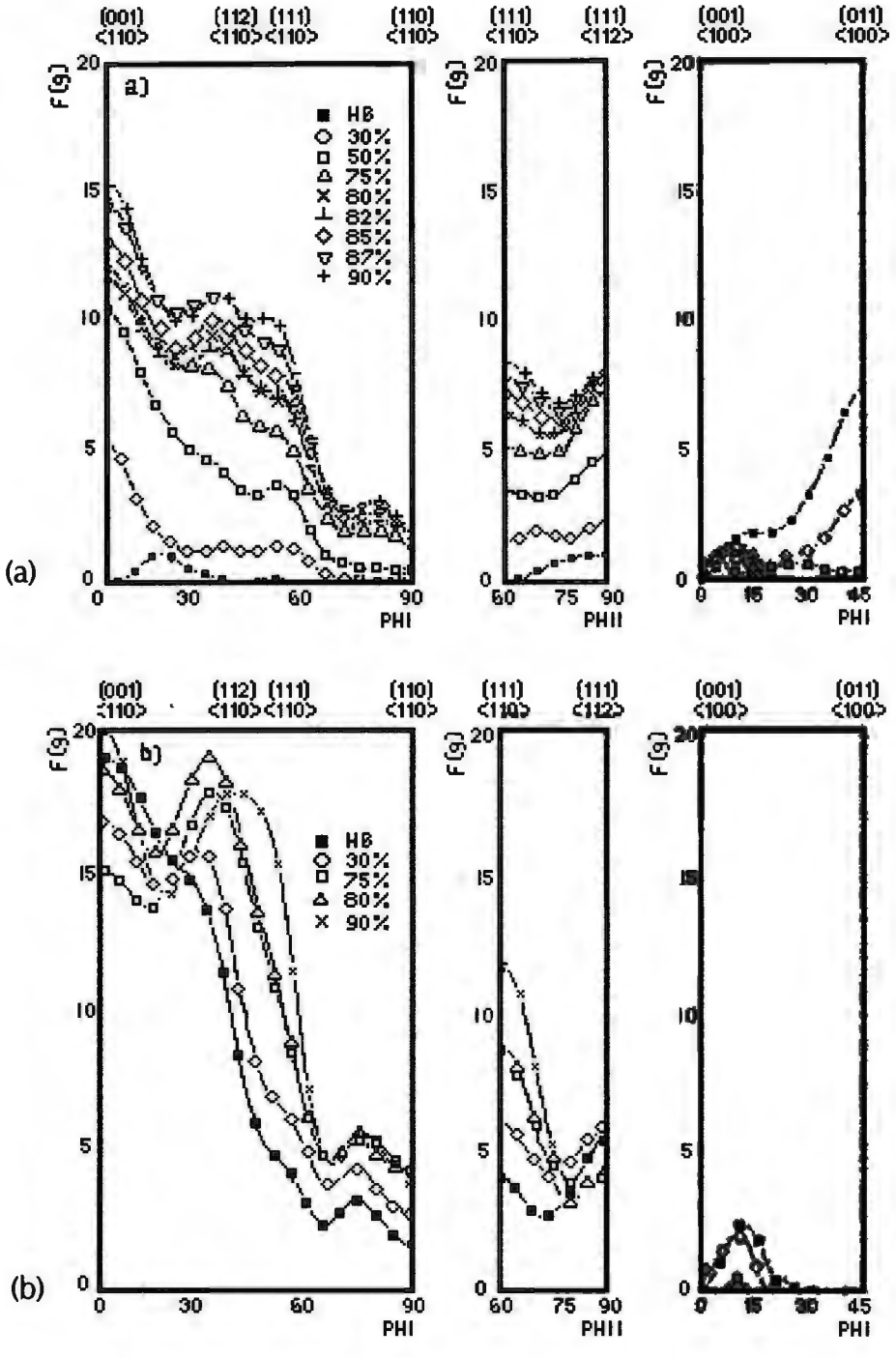

Figure 2.19: Cold-rolling textures of ferritic stainless steel. (a) Surface (b) Centre. The percentages indicate the amount of cold rolling reduction imposed on the sheet and HB = Hot band[63].

component incorporates the γ-fibre. Textures present in the central region are more intense due to stronger initial textures in the hot band. The Goss component at the sub-surface layer rotates simultaneously during cold rolling to both the $\{111\}<112>$ orientation on the γ-fibre and the $\{001\}<110>$ orientation on the α-fibre. This leads to the presence of transition bands within a single grain and to the preservation of the Goss texture between the rotated regions.

Annealing Textures

The most distinctive feature of the recrystallisation textures of ferritic stainless steels is the development of the $\{111\}<112>$ component at the expense of the $\{112\}<110>$ component (figure 2.20) [60,62-68]. The maximum at $\{111\}<112>$ can be explained by the $\approx 32°<110>$ rotational relationship between the $\{111\}<112>$ orientation and the $\{112\}<110>$ orientation of the rolling texture[69]. This relationship is near the ideal $27°<110>$ rotation found for high growth rates. The special grain boundaries of the new $\{111\}<112>$ grains can therefore grow selectively into the $\{112\}<110>$ rolling component, to form the primary recrystallisation component.

When annealing after approximately 70% prior cold rolling, the maximum intensity of the recrystallised Goss texture corresponds to a maximum in the $\{111\}<112>$ rolling texture component[60,62-67]. As mentioned previously, lattice rotations of the Goss texture during cold rolling result in regions between transition bands retaining their original orientation. It is suggested that during recrystallisation, new Goss grains nucleate and grow into these regions promoting the formation of a Goss texture in the cold-rolled and annealed sheet. Nucleation of new grains is favourable in these areas due to high local misorientations and fine cell structures. In alloys containing a large number of interstitials, for example Fe3%Si steels, Goss grains are able to nucleate in the many shear bands which form in these steels[70]. For 17%Cr stainless steel, shear banding is largely absent, and so nucleation in the transition bands is believed to be the dominant mechanism for the development of Goss texture[62].

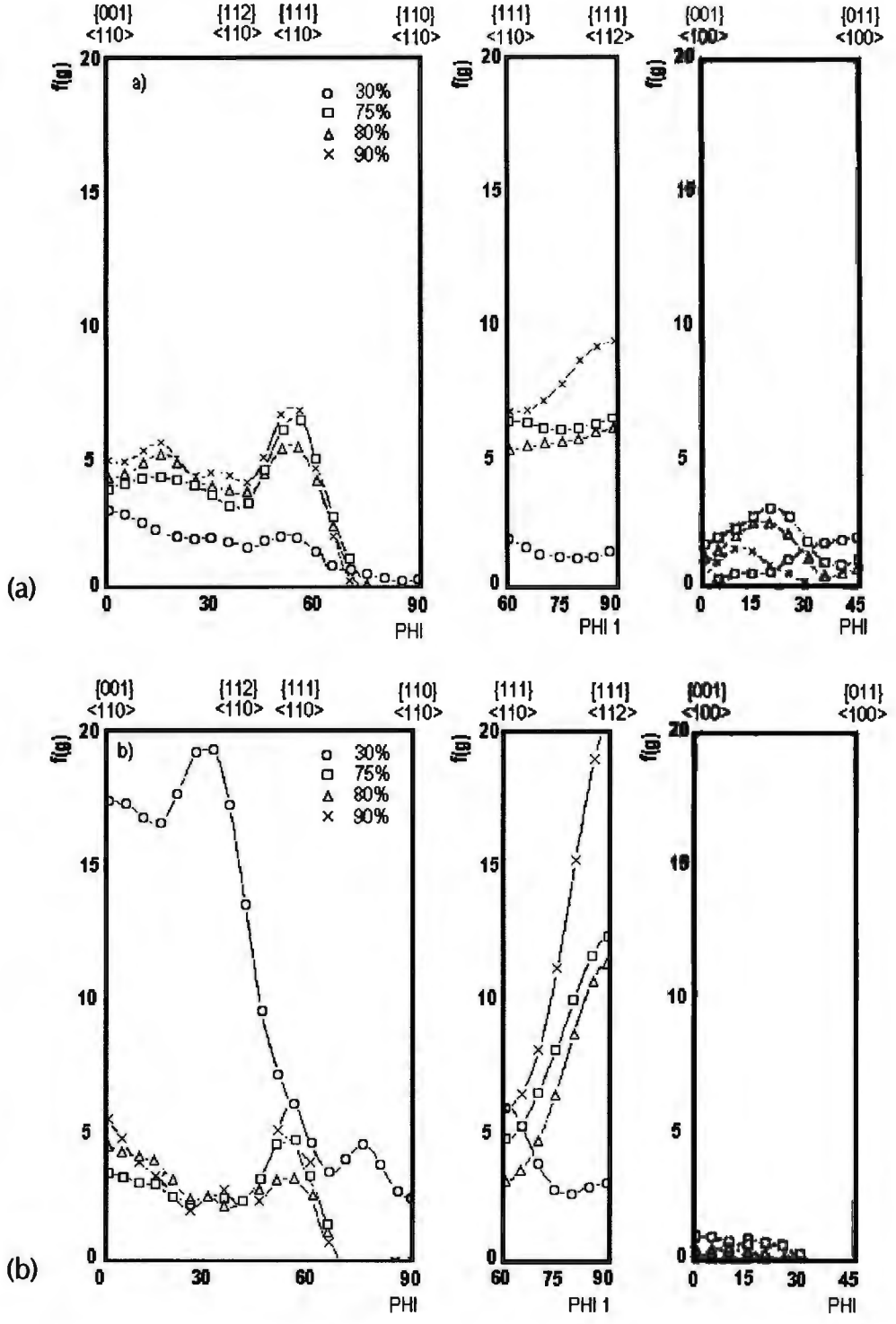

Figure 2.20: Annealing texture of ferritic stainless steel. (a) Surface (b) Centre. The percentages indicate the amount of prior cold rolling reduction imposed on the sheet [63].

2.2.2 Aluminium Alloys

Recrystallisation and deformation textures of aluminium alloys have been the topic of much research[71-76]. In FCC alloys it is the cube texture $\{100\}<001>$ which is often dominant[77,78] and which, in some cases, has a detrimental effect on the formability of the sheet[79]. Detailed analysis has therefore been done on all aspects of the formation and behaviour of the cube texture, with emphasis on how it influences flow properties such as earing behaviour[80,81] and resistance to thinning during deformation[79,82,83]. Other texture components, for example the R $\{124\}<211>$ orientation and the Goss $\{011\}<100>$ texture, also play a vital role in determining the mechanical properties of aluminium alloys and have been extensively characterised[75,78]. Evolution of texture depends on a number of factors including initial texture, mode of deformation, extent of precipitation, deformation temperature, and annealing times and temperatures[84-86]. Varying any one of these parameters will naturally influence the final microstructures and texture characteristics.

2.2.2.1 Textures of Aluminium Alloys

Aluminium alloys containing small additions of manganese and magnesium, such as AA3002 and AA3004, are used for sheet metal components where extreme formability is required. It is therefore important that the textures of these alloys are carefully controlled during the thermomechanical process to ensure mechanical properties of the highest standard. The principal rolling texture components of FCC metals, namely $\{225\}<554>$ copper and $\{011\}<211>$ brass textures, have been thoroughly characterised and the origins are well understood. The development of recrystallisation textures, namely cube and R $\{124\}<211>$, however, have only more recently been studied in detail.

Rolling Textures

In the deformed state aluminium alloys possess a strongly elongated band-like microstructure[87,88]. The texture at this stage can be described by the β-fibre

which extends from the copper orientation $\{112\}<111>$, through the S orientation $\{123\}<634>$ to the brass orientation $\{011\}<211>$[75,78]. A large number of cube and rotated cube (scatter about the RD and TD) orientations are also present, particularly within elongated bands extending through the microstructure. These bands have been termed cube bands or micro-bands.

Due to their high stacking fault energies, aluminium alloys are able to undergo recovery of the deformed structure during deformation (dynamic recovery) or during the first stages of annealing. The subgrain boundary energy will decrease during this process as the size of the subgrains within the bands increases. The misorientation between subgrains may also increase, however, no large angle subgrain boundaries are formed. Consequently, the β-fibre texture remains virtually unchanged during this extended recovery process, with possibly a slight increase in texture intensity[89].

Annealing Textures

Recrystallisation of aluminium alloys results mainly in two textures, namely the R texture $\{124\}<211>$ and the cube texture with some scattering about the RD[199]. The cube and rotated grains nucleate mostly in the cube bands of the deformed structure which comprise of many cube subgrains. Recovery of the subgrains leads to a size advantage of the cube nuclei which allows cube grains to grow and consume the surrounding matrix. These facts support orientated nucleation as the favoured mechanism for texture evolution in aluminium. Engler, Yang and Kong[89] in an investigation of the recrystallisation behaviour of an aluminium alloy possessing 1.3% Mn, found that after ageing for 170 hours at 400°C, all the potential nucleation sites lay within the cube bands. On the other hand, preferred growth of the cube grains has also been shown to contribute to the formation of this texture[91]. The cube texture possesses a $40°<111>$ orientation relationship with the S $\{123\}<634>$ texture, which is a major component of the rolling texture of aluminium[75,108]. Therefore, not only do the cube grains preferentially nucleate, but they are also able to grow rapidly into the surrounding matrix.

Recrystallisation textures also include as a major component the R orientation {124} <211>, which has a slight rotation from the rolling texture S orientation {123} <634> and is often grouped in the same category[75]. Nuclei possessing an R orientation nuclei are easily able to form in the deformed matrix, either within the S grains which are situated at the boundaries to different textures, or by extended recovery reactions of the S subgrains in which no large angle grain boundaries are created. In the latter situation, the absence of any high angle grain boundaries means that no orientation changes occur and the rolling texture will be retained. While in the former case, new R orientated grains will nucleate at the grain boundaries of S grains as this is where the strongest texture gradients exist. Recovery processes and subsequent successful nucleation of the R texture is thus most favourable at these sites.

Effect of particles on texture development

Large precipitates present in an aluminium alloy, for example Al_6Mn particles in an alloy containing 1.3%Mn, which are of a size greater than 1 μm, become important nucleation sites during recrystallisation[87,89,109]. During the initial stages of annealing, recovery occurs in the deformation zones surrounding the large precipitates and subgrain growth occurs until some large subgrain completely consumes the deformation zone. During subsequent annealing, rapid recovery allows the formation of fine subgrains within these zones, which are far smaller than those in the surrounding matrix. On further annealing, these subgrains grow until eventually the entire deformation zone is consumed. At this stage if a large angle grain boundary exists between the subgrain and the surrounding material and if the subgrain is of a sufficient size, it will grow out of the deformation zone and into the surrounding matrix to form a new grain. This mechanism is termed Particle Stimulated Nucleation (PSN). Therefore, in general, the presence of large particle in an aluminium alloy will promote the formation of a wide range of nuclei orientations, which will tend to randomise and weaken the textures present.

This is in contrast to what is known about the presence of small dispersoids within a material, which may severely inhibit the migration of low or high angle

grain boundaries during recrystallisation[78]. Also known as grain boundary pinning or Zener drag, it may a have a strong influence on the overall texture and microstructures in the final product. In the case of a strong Zener drag if the particles are non-deformable and very small, grain boundary pinning is very effective and recrystallisation can be suppressed. In this case no large angle grain boundaries are formed and the deformation textures are retained.

CHAPTER 3

EXPERIMENTAL APPROACH

3.1 Sample Material

3.1.1 Stainless Steel

For the investigation of the ridging phenomenon in the current project, sample material of a commercially produced AISI 430 stainless steel was sourced and given the designation C430. The sheet was provided in a cold-rolled annealed condition and has a through-thickness dimension of 0.7 mm. The material was chosen for its severe ridging behaviour during uniaxial tensile deformation. A full process history is unavailable but it is reasonable to assume that the material has undergone a standard hot rolling, anneal, cold rolling and final annealing procedure. The study of the C430 sample material constituted the first stage of the investigation into the ridging phenomenon in ferritic stainless steel. As a second stage the aim was to establish the effect of the TMP parameters on the ridging behaviour and for this reason a set of controlled rolled stainless samples were produced. In particular, the effect of hot roll finish temperature on ridging behaviour has been examined.

A single melt of ferritic grade AISI 430 stainless steel (Table 3.1) was cast to produce three heats (5kg) of identical composition. The heats were hot rolled after an homogenisation treatment (1100°C), and in each case the finish temperature was varied systematically to give three different hot rolling schedules terminating at 920°C, 785°C and 654°C. The total hot roll reduction was 83% and the alloy heats were labelled 1, 2 and 3 respectively according to the aforementioned finishing temperatures. The strip thickness at this stage was approximately 6 mm. Following a standard annealing treatment at 860°C for 10 minutes, the heats were cold rolled by 72% reduction to a sheet thickness of 1.6 mm, and finally annealed at 830°C for 8 minutes. Samples were cropped at the end of each process stage, namely hot roll (stage A), hot roll-anneal (stage B),

cold roll (stage C), and cold roll-anneal (stage D). Sample identification is facilitated by combining the alloy heat and the process stage designations (for example, D1 represents a cold roll-annealed sample that was hot roll finished at 920°C). A schematic of the laboratory rolling procedure is indicated in figure 3.1. The alloy compositions for the commercial stainless steel, as well as for the laboratory produced alloy are shown in Table 3.1.

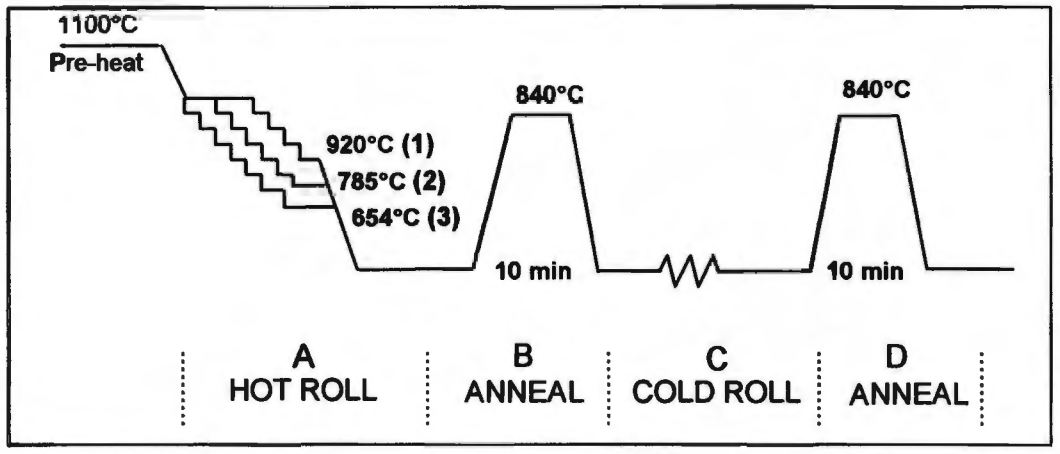

Figure 3.1: Process schedule for laboratory rolled stainless steel.

Table 3.1: Composition of the laboratory rolled heats and the commercially produced stainless steel C430. All values are given in weight percentages.

Sample	Cr	C	Mn	Si	Ni	N_2	S	P	Ti	Fe
C430	16.02	0.045	0.38	0.27	0.18	0.036	0.027	0.017	0.01	Bal.
Lab Heats	16.85	0.015	0.43	0.75	0.11	0.024	0.007	0.018	-	Bal.

3.1.2 Aluminium Alloys

Sample material of the aluminium alloy AA3002 was obtained from two separate suppliers and designated ALU1 and ALU2. The material was acquired in the cold rolled-annealed condition with a sheet thickness of 0.8 mm for sample ALU2 and 1.25 mm for sample ALU1. The TMP route for alloy ALU1 was provided by the manufacturer, but the details of the process route for the ALU2 material is unknown. Although the latter situation is unfortunate, the two samples were chosen for the extreme contrast in their roughening behaviour. The alloy compositions of the two materials are indicated in Table 3.2 below.

Table 3.2: Alloy compositions in weight percentages of sample material AA3002.

Sample	Si	Fe	Cu	Mn	Mg	Cr	Zn	Ti	Al
ALU1	0.069	0.05	0.054	0.12	0.051	0.001	0.004	0.009	Bal.
ALU2	0.061	0.07	0.14	0.17	0.061	0.002	0.004	0.030	Bal.

The thermomechanical process route for sample ALU1 can be summarised as follows:

(i) Ingot preheat at 530°C - 540°C followed by hot rolling in 15 passes from 490 mm to 7.1 mm. The hot roll start temperature was 520°C and the 7.1 mm gauge was coiled at 273°C and air cooled to room temperature.

(ii) Cold rolling was carried out in three passes, namely (7.1 mm - 3.5 mm), (3.5 mm - 2.0 mm) and (2.0 mm - 1.3 mm).

(iii) Final coil was batch annealed in an inert atmosphere at 310°C - 330°C for two hours.

It was assumed that AL2 was also manufactured via a hot roll/cold roll process, but the temperatures and deformation cycles could have varied quite significantly.

3.2 Ridging Analysis

The debate concerning the ridging phenomenon, its origin and physical characteristics, has been on-going for the last 40 years. In an attempt to fully characterise the physical aspects of the ridging phenomenon in ferritic stainless steel, a series of tensile tests were conducted on the commercial stainless steel as well as on the laboratory rolled heats. Ridging reportedly begins at plastic elongations of as low as 1.5%[34] and increases in severity until elongations of between 15% and 20%[31] are reached. For the current project, all ridging tests were conducted to a tensile strain of 20% and at a strain rate of $10^{-3}s^{-1}$ on specimens initially polished to a mirror finish.

Specimens were machined in such a way as to produce 0° tensile axis (parallel to the RD) and 90° tensile axis (parallel to the TD) orientations, and in the case of the laboratory heats, specimens were also prepared for 45° tensile axis (diagonal direction) testing. Since the materials were all tested in the cold

rolled-annealed condition, the standard tensile specimen thickness was always the final gauge thickness. Specimens of the commercial steel possess a width dimension of 12 mm and a maximum gauge length of 55 mm, while those of the laboratory rolled steel have a width of 20 mm and a gauge length of 60 mm.

Two further geometrical variations were considered for the commercial steel tested in the 0° tensile axis orientation. This included a systematic variation in the specimen gauge length (Table 3.3), whilst maintaining constant gauge width, and a specimen whose thickness had been reduced by machining a quarter-thickness off each surface. The former situation was devised to test the influence of constraint imposed by the gripped ends on the development of the ridging profile. The reduced thickness specimen was employed to establish if ridging is a "surface phenomenon", as indicated by some researchers, or whether it is a "bulk material phenomenon" depending instead on the entire average through-thickness properties of the sheet.

Ridging in the aluminium sample material was studied in a similar manner. Polished tensile samples, machined at 0° and 90° to the RD, were subjected to a 20% tensile elongation at a strain rate of $10^{-3}s^{-1}$. Also, a tensile specimen of sample ALU1 was machined down to almost half its original thickness from both surfaces, to establish if a change in ridging behaviour occurred. A list of the tensile tests conducted on the aluminium and the stainless steel samples is given in Table 3.3.

Table 3.3: Details of tensile tests conducted on steel and aluminium sample material.

	Commercial steel: C430 **AISI 430**	**Lab Heats: D1, D3** **AISI 430**	**Aluminium: ALU1, ALU2** **AA3002**
1	RD (0°)	RD (0°) [Also D2]	RD (0°)
2	—	Diagonal (45°)	—
3	TD (90°)	TD (90°)	TD (90°)
4	RD: Thickness halved, both sides removed.		RD: Thickness halved, both sides removed.
5	RD: Gauge length variation. (10,15,25,35,45,55mm)		

Surface Characterisation

In order to characterise the surface topography of the deformed tensile samples, the specimen gauge surfaces were examined using a non-contact optical profiler. The system combines phase-measuring interferometry and vertical scanning interference microscopy techniques to provide a complete 3D profile of the sample surface. The availability of instrumentation was optimised by engaging two commercially available systems, namely WYKO RST plus and ZYGO GP-maxim. Although the graphic formats may vary slightly, the output of the two instruments is essentially identical. An approximate surface area of 9 mm x 13 mm was measured on each stainless steel sample that exhibited ridges, while a smaller area was examined on the aluminium ridging samples and the steel samples that did not show ridging. Only samples with gauge lengths of 25 mm and 55 mm were analysed for the commercial steel specimens deformed in the RD. In view of the scan size limitations due to a minimum microscope magnification on the optical profiler, the measured areas of the ridged surfaces were divided into four equal quadrants, which could be combined at a later stage for graphical representation. Corresponding regions on both the upper and lower surfaces of each specimen were examined in order to characterise the sheet thickness variations occurring during ridging. Three dimensional surface profiles and two dimensional contour maps were plotted, and the average roughness (Ra) and peak-to-valley measurement (PV) was calculated, for each measured area. Ra is defined as the mean height, as calculated over the entire measured area, while PV is the vertical distance between the highest and lowest points on the surface. In addition, upper and lower surface profile measurements were recorded using a Surtronic 3P surface analyser in order to accurately characterise the thickness variations of the samples.

3.3 Microstructural Characterisation

Ridging in stainless steel has been attributed to inhomogeneous deformation due to variations in microstructural properties in more than one published investigation[28,29]. In contrast, it has also been clearly stated that no immediate differences in microstructure could be found between ridging and non-ridging

steels[32]. Therefore, to ensure a thorough investigation of ridging and its origins, it is essential that a careful microstructural characterisation be included in the investigation. Similarly, it is essential to understand the role that grain structure might play in the development of surface roughening in the aluminium samples.

3.3.1 Stainless Steel

In view of the intentional variation in the finish hot-roll temperatures to create diversity in the microstructures of the laboratory rolled material, a critical evaluation of the microstructure was carried out at each process stage to characterise the microstructural evolution[116]. Successful characterisation of the microstructure evolution during thermomechanical processing requires examination of the through-thickness variation in the grain structure. Since the thickness of the rolled product changes as a function of the process stage, it is most convenient to consider the examination of bulk samples in the longitudinal/through-thickness orientation, and for this reason light microscopy is an obvious approach.

Conventional metallographic techniques were employed to prepare stainless steel samples for light microscopy. Samples were mechanically polished using a 0.25 μm diamond paste before being given a final electrolytic polish to remove the deformed surface layers. A solution of 25g CrO_3 + 133ml acetic acid + 7ml H_2O at an applied potential of 20V was used in electrolytic polishing. Several etchants were considered for light microscopy, but the more successful results were obtained by electrolytically etching in the same solution mentioned above at a controlled current density of 25 mA/cm^2. Light microscopy was performed on a Reichert MeF3A metallograph using both bright field and Nomarski interference contrast techniques.

Although the ensuing analysis produced some reasonable images, in most instances the general grain structure remained undefined. Figure 3.2 represents the microstructure of sample A1 which exhibits martensite stringers in a ferrite matrix. Despite repeated attempts at etching, there is a noticeable absence of grain boundaries within the matrix. Sample B2, which was annealed after hot

rolling, displays more defined grain boundaries with evidence of veining associated with a recovered structure (figure 3.3). Better resolution of the grain boundaries was possible with sample B3 (figure 3.4), although complete delineation of the boundaries could still not be accomplished. A similar situation is represented in sample D1 which is reproduced in figure 3.5. Notwithstanding the fact that the grain size and grain shape can be discerned in some instances, it is generally not possible to obtain a clear image of the variation in grain structure through-the-thickness of the wrought material. This is obvious in figure 3.2, while even in figures 3.3 - 3.5 a critical assessment of the grain structure is prevented and meaningful comparisons cannot be made. The veining effect in figure 3.3 suggests the formation of a subgrain structure, but the absence of the same effect in figure 3.4 does not necessarily imply that sample B3 has fully recrystallised. The etching behaviour of the various sample conditions is not consistent and the presence of artefacts often hinder reliable interpretation. During chemical and electro-chemical etching, the high energy sites on the surface are preferentially attacked. For fully annealed metal where no interfaces other than grain-grain contacts exist, favoured attack will occur at grain boundaries only and the structure will be evenly contrasted. In the consideration of the present alloys, not only does the state of deformation vary, but numerous oxide inclusions occur within the microstructure which introduce additional interfaces. Furthermore, the occurrence of austenite in the ferrite matrix during hot rolling produces chemical micro-segregation as a result of the elemental partitioning between the two phases[31]. This leads to further localisation of attack during etching and exacerbates the problem of revealing the grain structure. In the case of sample D1, traces of the original martensite stringers are indicated by preferential micro-pitting which creates slightly darker streaks in figure 3.5. Thus the competing sites for attack that include grain boundaries, oxide inclusions, micro-segregation and dislocations, prevent uniform etching of the grain boundaries.

The difficulties experienced in etching the grain boundaries using light microscopy prompted the decision to employ the electron channelling contrast (ECC) technique in the scanning electron microscope (SEM). This technique permits examination of the microstructure of bulk samples in the polished condition. Electrolytic polishing techniques used for sample preparation were the same as those employed for light microscopy. The quality of ECC is critically dependent on the operating conditions of the microscope and on the integrity of the polished surface.

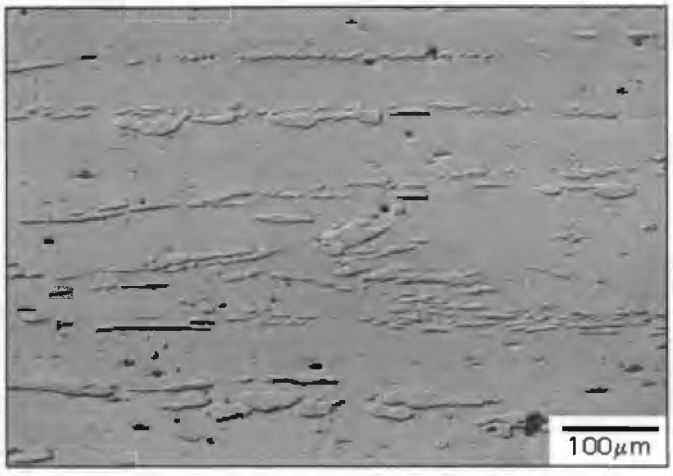

Figure 3.2: Martensite stringers visible in sample A1: hot roll finish 920°C.

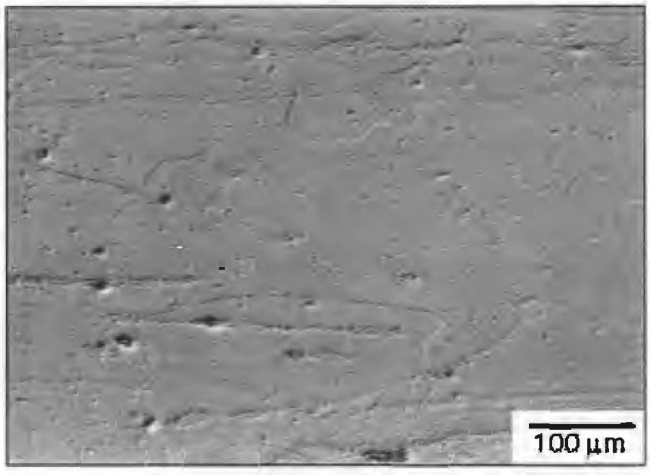

Figure 3.3:The veining effect demonstrates recovery in sample B2: hot roll finish 785°C.

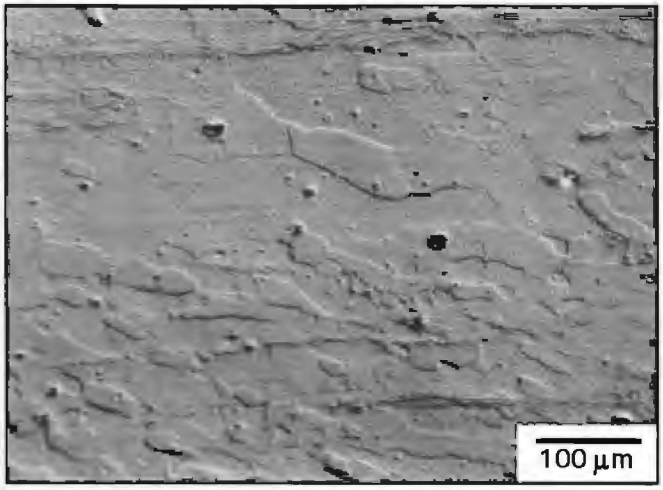

Figure 3.4: Uneven grain size in sample B3: hot roll finish at 654°C.

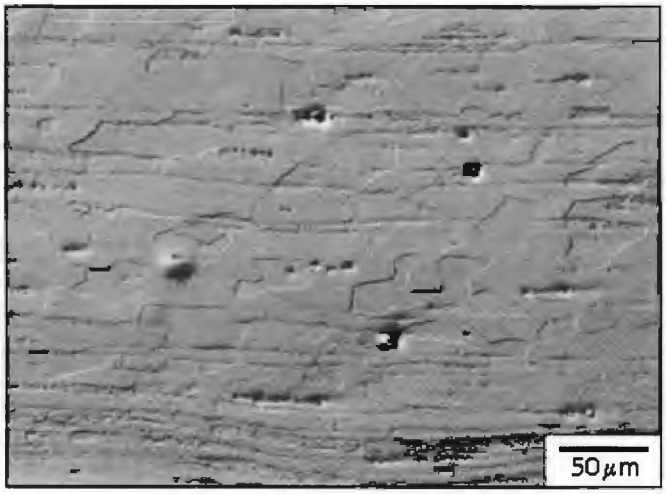

Figure 3.5: Limited grain boundary definition evident in sample D1 after electrolytic etching. Artefacts associated with the original martensite stringers are still visible in the form of micro-pits.

Several permutations of accelerating voltage and probe current were evaluated in an attempt to optimise the contrast of the image. Special attention was also given to minimising the sample working distance and to the selection of the final/objective aperture (50 μm diameter). Electron channelling contrast images were acquired via a solid state annular backscatter electron (BSE) detector (KE Developments Ltd) fitted to a Cambridge S200 SEM. Maximum contrast was provided by setting the operating conditions at an accelerating voltage of 20 kV and a probe current of 5.0 nA, while the sample-BSE detector distance was fixed at 7 mm. Samples of the commercial steel for microstructural analysis were also examined using ECC techniques in the SEM, across the longitudinal, transverse and rolling plane sections of the material. A LEICA 440 SEM was used to examine these samples and again images were acquired via a solid state annular backscatter electron (BSE) detector at an accelerating voltage of 20kV. Electrochemical polishing was carefully carried out to ensure the removal of the deformed layer associated with prior mechanical polishing, while at the same time it was necessary to avoid over-polishing which could introduce topographical effects.

Images produced via ECC techniques have the advantage of providing information regarding the structure and condition of the material. Figure 3.6 demonstrates clear grain contrast which indicates a fully recrystallised microstructure. Figure 3.7 on the other hand, presents a recovered structure indicated by the mottled effect of the ECC image. For confirmation of these results, the same samples were examined in the transmission electron microscope (TEM). TEM foils were prepared using a Struers twin jet electropolisher in a solution of 5% perchloric acid in methanol (35V at -15°C) and examined in a JEOL 200CX microscope at an accelerating voltage of 200kV. The fully recrystallised microstructure of the sample in figure 3.6 is verified by the dominance of high angle grain boundaries and few dislocations in figure 3.8, whereas a similar bright field TEM image of the sample in figure 3.9 displays a preponderance of subgrains which is characteristic of a recovered structure. In this way ECC can be reliably used to characterise the microstructural condition of a material.

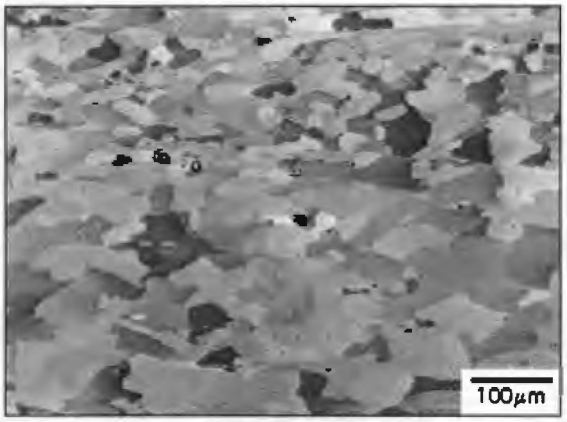

Figure 3.6: ECC image of a recrystallised grain structure.

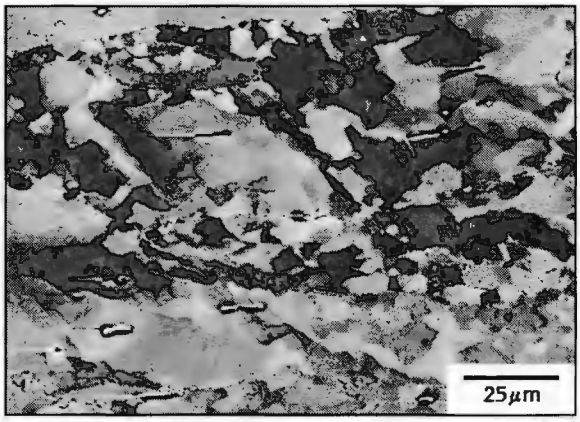

Figure 3.7: ECC image of a recovered grain structure.

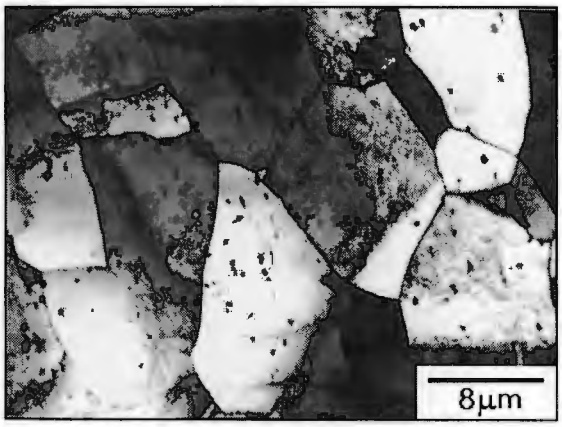

Figure 3.8: TEM image indicating the high angle grain boundaries of a recrystallised grain structure.

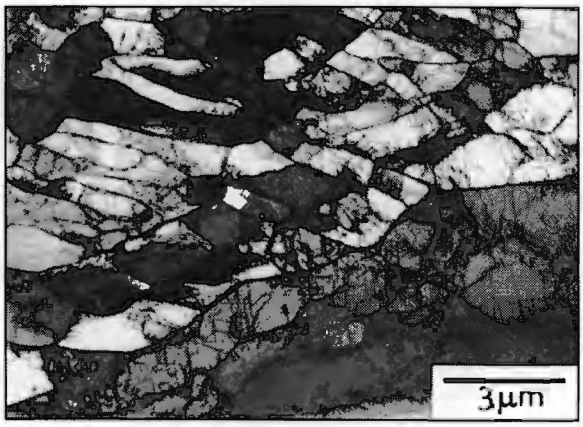

Figure 3.9: TEM image of a recovered subgrain structure.

3.3.2 Aluminium Alloys

The microstructures of the aluminium sample material were successfully revealed using conventional anodising methods for examination under the light microscope. Excellent grain contrast was obtained using both Nomarski interference and cross-polarised light in a Reichert MeF3A metallograph. An attempt was also made to use the anodically prepared samples and polarised light to reveal information regarding the orientations of the underlying grains. The background and methods used in this experiment are outlined in the section below.

Texture identification using polarised light:

The anodising technique incorporating polarised light has successfully been used to identify inhomogeneous textures present within pure aluminium sheet[24,92]. More commonly this approach has been used to reveal the grain and sub-grain structure of polycrystalline aluminium, however, a strong relationship between the optical properties of the anodic film and the crystallographic orientation of the underlying grain exists, which provides a means of obtaining information about the orientation of the surface grains.

Experiments employing this technique were conducted by P.S. Bate[24], in a commercial purity aluminium alloy (AA1100), in an attempt to characterise the relationship between mechanical inhomogeneity (or limit strains) exhibited during forming, and the spatial segregation of texture components within the rolled sheet. Bulk experiments on recrystallised sample material showed a well developed cube texture together with a secondary component centred on an orientation about 5° from {123} < 634 > S texture. Polarised light investigations on this material revealed the presence of bands of grains elongated in the rolling direction, which exhibited a high proportion of either light or dark orientation contrast. The dark regions were identified as grains having an <001> axis close to the sample normal, while the light areas corresponded to a higher concentration of grains of the R texture component. These conclusions were based upon the results of investigations by Saetre *et al*[92] in which the exact

relationship between crystallographic orientation and polarised light intensity, reflected from anodised grains, was established.

Considering the abovementioned experiments, a decision was taken to apply the anodising technique to the aluminium sample material, in an attempt to identify texture inhomogeneity. Rolling plane samples were mechanically polished using 0.25 μm diamond paste and given an electropolish in a 20% perchloric acid / 80% methanol electrolyte at 20V and -20°C. This ensured complete removal of the mechanically deformed layer produced during mechanical polishing. The samples were then anodised in a solution of 5% HBF / 95% H_2O at 30V and 20°C for approximately 45 seconds. A Reichert MeF3A metallograph, with the aperture diaphragm stopped down to approximately half its full opening, was used to examine the samples under polarised light conditions.

It was possible to confirm from the polarised light experiments that grains possessing a cube orientation are those which retain their contrast while rotating the sample around an axis normal to the surface. For example, the large central grain indicated in figures 3.10 to 3.12 does not vary in contrast during a 45° rotation and therefore must have a cube orientation. The surrounding smaller grains exhibit a contrast change from maximum intensity (bright) to minimum intensity (dark) within a 45° rotation of the sample and thus possess non-cube orientations. Examination of the microstructures at lower magnification for sample ALU1 alloy revealed a matrix of cube orientations incorporating a number of smaller non-cube grains (figure 3.13). The identification of extended clusters of non-cube grains was, however, hindered by the fact that many different secondary orientations occur in the aluminium rather than one secondary texture component, as indicated by the various shades of grey. A similar situation is evident for sample ALU2 shown in figure 3.14. Even a small rotation away from the ideal orientation would result in a contrast change making the identification of similar textures difficult. Thus, the technique of using polarised light to investigate texture inhomogeneity is only feasible if the material possesses a few texture components that are close to their ideal orientations.

Figure 3.10: Sample ALU2 showing large central cube grain within smaller non-cube grains.

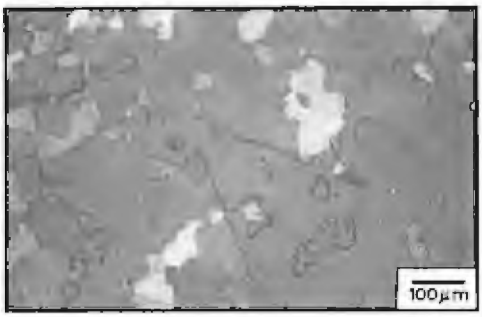

Figure 3.11: The same field of view, but the sample has been rotated by 45°. Cube grain remains grey but non-cube changes from black to white or visa versa.

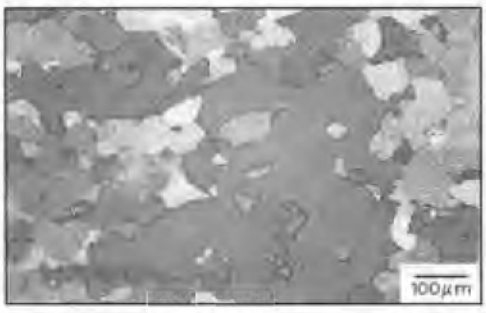

Figure 3.12: The same field of view but with the sample rotated by 90°. Cube grain again remains grey while the non-cube grains revert to white or black.

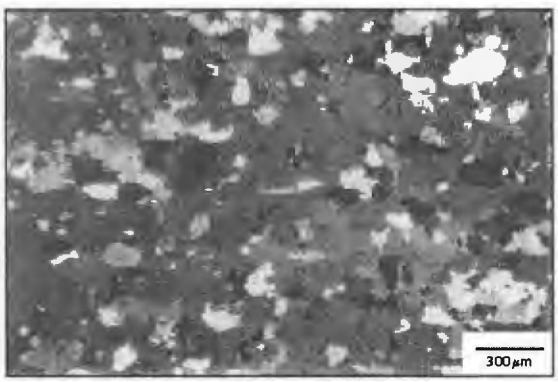

Figure 3.13: Sample ALU1 at 0°.

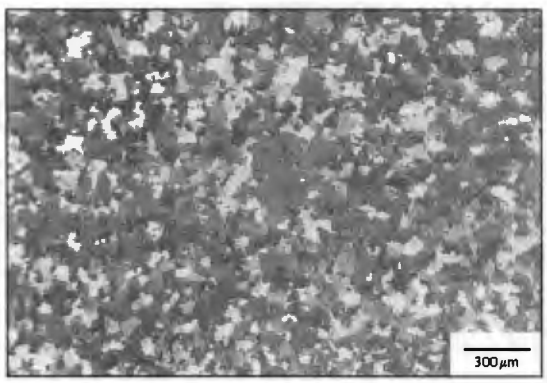

Figure 3.14: Sample ALU2 at 0°.

3.4 Texture Analysis

3.4.1 Introduction

Interest in the texture properties of polycrystalline materials has grown steadily in the last 30 years as the number of techniques for their measurement and analysis has increased. Texture has become an important physical attribute which is used to describe the microstructural condition of the material, as well as it being a useful tool to predict anisotropic properties during deformation.

The term bulk texture refers to the average preferred orientation of a material, and constitute a single statistical population without any regard to the spatial positioning of individual grains. Microtexture, on the other hand, describes the orientation of each grain within a material with reference to its location and relationship to adjacent neighbouring grains. For many years the vast majority of texture measurements were of the bulk category and thus methods of data representation were developed to deal with this kind of information. Due to the slow and labour intensive methods of single orientation measurement, very few studies of this nature were undertaken. In the mid 1980s a technique of single grain orientation measurement, based on the work of Venables *et al* [110], was developed by Dingley[41] where orientation measurements could be calculated in a relatively short time interval using EBSD patterns in the SEM. Since then the technique has been adapted and advanced to the point where now approximately 10 000 single grain orientation measurements can be recorded within one hour[42,112]. EBSD has allowed for a whole range of new investigations of material characteristics on a grain size scale, which were formerly too arduous to attempt. Coupled with these advances has been the development of new methods for the representation of texture data, which take into account the spatial properties of the microtexture information.

Although the microtexture characteristics of materials have received far more interest in the last decade, the bulk properties should not be discounted as they provide good opportunity for confirmation and comparison of the microtexture results.

The presentation of experimental details of the texture analysis commences with an outline of the various methods available for the definition of a crystal orientation in a material. This is to allow a clear understanding of the bulk texture and microtexture representations used in the present project. Similarly, the symmetry relationships present within a rolled cubic material are explained. A description of the texture experiments follows including the details of orientation measurements performed on the sample material and the methods used for the display of this data are presented. Considerably less emphasis, however, is placed on describing the methods of bulk texture analysis since the data is displayed using conventional fibre diagrams and ODFs plotted in Cartesian coordinates.

3.4.2 Orientation Representation and Symmetry Relationships

The orientation of a crystal, g, in a material can be defined by its orientation matrix. This 3 x 3 matrix specifies the exact crystal orientation using the position of the crystal axes (100, 010, 001) relative to the defined specimen reference axes. In the case of rolled materials it is logical to define the reference axes according to the RD, TD and ND, which form an orthogonal set of axes. The relationship between the crystal axes and specimen axes is illustrated in figure 3.15. The specimen axes are labelled X, Y and Z according to the RD, TD and ND of the rolled sheet. The cosine angular relationships between these two sets of axes constitute the elements of the orientation matrix and thus define the crystal orientation.

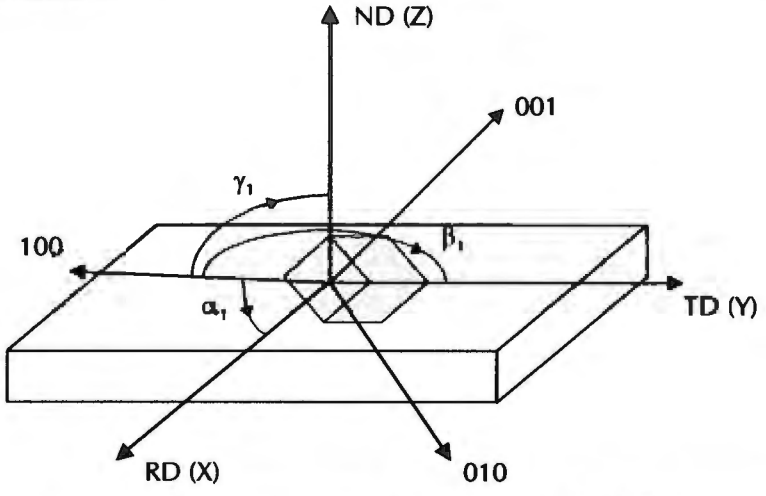

Figure 3.15: Crystal axes and specimen reference axes of a rolled material.

The components of the orientation matrix are:

$$g = \begin{pmatrix} \cos\alpha_1 & \cos\alpha_2 & \cos\alpha_3 \\ \cos\beta_1 & \cos\beta_2 & \cos\beta_3 \\ \cos\gamma_1 & \cos\gamma_2 & \cos\gamma_3 \end{pmatrix}$$

where α_1 is the angle between 100 and X, β_1 is the angle between 100 and Y, and γ_1 is the angle between 100 and Z, constituting the first column of the matrix. Similarly $\alpha_2\,\beta_2\,\gamma_2$ are the angles between 010 and the reference system, and $\alpha_3\,\beta_3\,\gamma_3$ are the angles between 001 and the reference axes, comprising the second and third columns. The matrix is therefore orthogonal and the elements within a row or column are perpendicular to each other. It is possible to convert this form of representation into the commonly used Miller index notation $\{hkl\}<uvw>$ where the orientation of a crystal is represented by the closest ideal orientation. If the orientation described in matrix form is represented by:

$$g = \begin{pmatrix} a_{11} & a_{12} & a_{13} \\ a_{21} & a_{22} & a_{23} \\ a_{31} & a_{32} & a_{33} \end{pmatrix}$$

then the formulae for calculating the Miller indices are:

$$a_{13} = h/C \qquad a_{23} = k/C \qquad a_{33} = l/C$$
$$a_{11} = u/D \qquad a_{21} = v/D \qquad a_{31} = w/D$$

where $D = \sqrt{u^2 + v^2 + w^2}$ and $C = \sqrt{h^2 + k^2 + l^2}$.

This method is convenient for the description of common textures such as the R texture $\{124\}<211>$ found in aluminium alloys.

Another useful method of expressing an orientation is using Euler angles. Assuming that the crystal axes and specimen axes are initially parallel, the Euler angles using Bunge notation are defined by the following clockwise rotations of the crystal axes (looking down the positive axis):

1) about the 001 axes through φ_1
2) about the 100 axes through ϕ
3) about the 001 axes through φ_2

The three Euler angles φ_1 ϕ φ_2 which are derived, express the final orientation of the crystal relative to the specimen coordinate system. Alternative definitions

have been suggested by Roe (Ψ,θ,ϕ), also known as Wenk, where $\varphi_1 = \Psi + 90°, \phi = \theta, \varphi_2 = \phi - 90°$, and Kocks which involve slightly different rotations but a similar principle. These angles can now be represented as Cartesian coordinates in three dimensional Euler space, where each orientation is expressed as a particular point in space. Euler space is therefore able to express all the orientations present within a sheet and so demonstrate the texture of a material. Unfortunately at ϕ = 0° Euler space degenerates. All points with $\varphi_1+\varphi_2$ equal to a certain value will represent the same orientation, thus making it impossible to differentiate between certain orientations when $\phi = 0°$. One method of avoiding this problem is to convert to polar coordinates defined by: $\varphi^+ = (\varphi_1+\varphi_2)/2$

$\varphi^- = (\varphi_1 - \varphi_2)/2$, while ϕ remains unchanged. The values φ^+, ϕ, φ^- can then be plotted as indicated in the adjacent diagram and graphically represented in φ^+ constant sections.

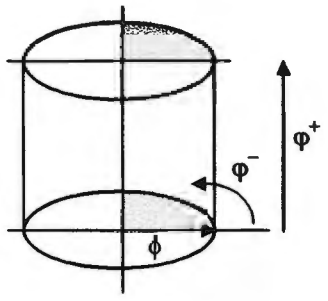

It is also possible to plot the sections of the 3D cylinder with the original Euler angles. For the current project φ_2 constant sections were employed to create discrete orientation plots. The misorientation between two orientations or between a set of orientations and a reference orientation can be calculated by multiplying the orientation matrix of the initial orientation with the inverse of the reference orientation matrix. In other words, the misorientation between two grains A and B is defined as: $M_{AB} = M_A^{-1} M_B$

where M_{AB} is the matrix that rotates orientation B onto orientation A, which is the reference orientation for this example. The misorientation between two grains is normally expressed as a set of Euler angles or an angle/axis pair. The latter representation is particularly useful as it has a direct physical relationship to the grain boundary geometry. For example, a high angle grain boundary can be recognised instantly from the angle/axis pair describing the misorientation between the two adjacent grains. The representation of an orientation using an

angle/axis pair and a Rodriques vector is explained in section 3.4.4.6, which describes the use of the definition to display microtexture measurements acquired during this investigation.

Crystals structures often possess structural symmetries which simplify the representation of their orientations, the most common being cubic crystal symmetry. Due to the nature of cubic symmetry, there are 24 equivalent ways of expressing any single orientation in the crystal. For example, if the S texture $(123)[63\bar{4}]$ is found within a cubic polycrystalline material, there will be 24 alternative ways of expressing that same orientation. Or rather, there are 24 symmetrically equivalent orientations for the $(123)[63\bar{4}]$ orientation in a cubic crystal structure. Furthermore, if the material has been rolled into sheet, an additional sample symmetry is introduced through the rolling process. A two fold rotational symmetry about the RD or orthogonal symmetry is set up within the sheet. The sample symmetry can thus be described as orthorhombic which introduces a further four symmetry elements.

If the cubic crystal and wrought sheet symmetries are combined to produce cubic-orthorhombic symmetry, the effects are multiplied and $24x4=96$ symmetrically equivalent ways of expressing the same orientation are generated. Symmetry relationships have an important influence on the graphical representation of the orientation data. Notwithstanding the usefulness of being able to reduce all 96 members of a given orientation class to a single representative orientation, careful separation of crystal and sample symmetry elements is important to be able to identify variants of a particular texture. A significant difference between bulk data and microtexture data is the ability of EBSD to distinguish between texture variants.

For example, the S texture $\{123\}<634>$ has four variants which are $(123)[63\bar{4}]$, $(123)[\bar{6}\bar{3}4]$, $(213)[36\bar{4}]$ and $(213)[\bar{3}\bar{6}4]$ which are **different orientations** and therefore produce four distinct EBSD patterns. If the generalised S texture is expressed as Euler angles $\varphi_1 = 59°$, $\phi = 33°$, $\varphi_2 = 65°$, the four texture variants are related by the following expressions:

(1)	$0° + \varphi_1$	$0° + \varphi_2$
(2)	$180° - \varphi_1$	$90° - \varphi_2$
(3)	$180° + \varphi_1$	$0° + \varphi_2$
(4)	$360° - \varphi_1$	$90° - \varphi_2$

and therefore the variants are:

	φ_1	ϕ	φ_2
(1)	59°	33°	65°
(2)	121°	33°	25°
(3)	239°	33°	65°
(4)	301°	33°	25°

Incorporating cubic symmetry for each of the orientations (1) to (4) listed above would produce four different sets of 24 symmetrically equivalent orientations. However, if cubic orthorhombic symmetry is specified, the same four sets of 96 symmetrically equivalent orientations would be generated and the variants would be indistinguishable. Thus only one member of the 96 possibilities is necessary to specify a generalised S texture component, and an angle set is chosen which falls within $0 \leq \varphi_1\ \phi\ \varphi_2 \leq 90°$. This is known as reduced Euler space. (A good explanation of texture variants and symmetries is given in reference 25).

3.4.3 Bulk Texture Analysis

3.4.3.1 Bulk Texture Measurements

Bulk texture measurements were performed by MINTEK[1] using a Siemens D500TT X-ray diffractomer fitted with a molybdenum anode tube and an Euler cradle. Textures were quantified via incomplete pole figures measured from an area of approximately 14 mm^2 using Mo$K\alpha_1$ radiation in back reflection mode. The laboratory rolled steel was examined after each stage in the TMP namely, hot roll (A), hot roll-anneal (B), cold roll (C) and final cold roll-anneal (D). All samples were analysed at the surface as well as at the mid-plane region. The aluminium samples were also subjected to a full bulk examination.

[1] Council for Mineral Technology, South Africa.

3.4.3.2 Bulk Texture Data Representation

Due to the cubic-orthorhombic sample symmetry of the stainless steel and aluminium samples, the volume of Euler space used for the ODF plots could be reduced to $0 \leq \varphi_1 \phi \varphi_2 \leq 90°$. ODFs were calculated from the four incomplete pole figures (111), (200), (220) and (311) for the aluminium samples and the (110), (200) and (211) pole figures for the stainless steel samples, using the series expansion method ($I_{max} = 22$)[93]. Both φ_1 and φ_2 constant sections (at intervals of 5°) were plotted for the stainless steel samples, while plots of φ_2 constant were constructed for the aluminium samples. Density contours are plotted at 15% intervals where the contour value represents a percentage of the maximum "times random" value. Fibre diagrams demonstrating the major texture components along the α and γ fibres were also constructed for the laboratory rolled samples at each stage in the TMP.

3.4.4 Microtexture Analysis

3.4.4.1 Microtexture Measurements

Methods currently available for the measurement of local textures of a material can be divided into four categories, namely optical techniques, X-ray methods, TEM and SEM procedures. Optical methods provide a fast visual assessment of the grain orientations over a fairly large area. Two commonly used methods include polarised light examination (described for aluminium in section 3.2.2) and etch pitting techniques. The second category, namely X-ray methods, includes Laue backscatter patterns, Kossel diffraction and synchrotron beam radiation, and is not currently used very frequently as it suffers from a number of disadvantages, including low resolution and the need for highly specialised equipment. By far the most popular are the electron beam techniques, which are the most suitable for microtexture measurements and offer advantages such as accurate high resolution orientation information and easy sample preparation. TEM based methods encompass both the evaluation of individual crystal diffraction patterns and the generation of direct microtexture pole figures. These techniques are suitable for very high resolution work in the order of 1 μm or

even 1 nm when using convergent beam electron diffraction. Of the two SEM based techniques, namely selected area channelling (SAC) and electron backscattered diffraction, it is the latter which has received by far the most interest in the last ten years and is now accepted as the optimum method for microtexture measurement.

The basic input for all electron beam techniques for microtexture measurement is the Kikuchi diffraction pattern. A Kikuchi pattern arises due to Bragg diffraction occurring for a number of crystal planes when the electron source for diffraction originates from a scattering centre within the crystal. In this way some electrons will naturally impinge on the crystal lattice planes at exactly the Bragg angle given by $2d\sin\theta_B = n\lambda$, (d = interplanar spacing, n = order of reflection, λ = electron wavelength, θ_B is the Bragg angle). When this happens the initially scattered electrons will be diffracted through the Bragg angle resulting in a set of cones radiating from a single set of planes (figure 3.16). Because the apex angle of the diffracting cones is so large the cones will appear as two parallel lines on an intersecting flat surface. Thus, a plane in the measured crystal will appear as a pair of straight lines in a Kikuchi pattern. The many lines seen in a Kikuchi pattern result therefore, from the multiple planes which constitute the crystal structure of the material. Directions within the crystal are defined by the intersection of these lines, which is called a zone axis, while the distance between two points of intersection on the pattern is equivalent to the angle between the respective directions. A Kikuchi pattern is thus able to give a highly accurate representation of the orientations within any crystalline material. EBSD techniques using Kikuchi pattern analysis are able to provide an orientation accuracy of about 1°, while spatial resolutions of 200 nm have been achieved[94]. The procedure to calculate a crystal orientation from a Kikuchi pattern is fairly straightforward and thus not included in this section. A good explanation is given in chapter 5 of reference 95.

Two main approaches were followed for determining the microtexture of samples in the present investigation. In the first instance, it was considered necessary to identify the level of local texture clustering or "texture colonisation". It was initially hoped that this approach would provide sufficient

insight concerning previously reported mechanisms of surface roughening. To this end, a reasonably low cost manual EBSD system was designed and built at the University of Cape Town and a brief description of the system follows.

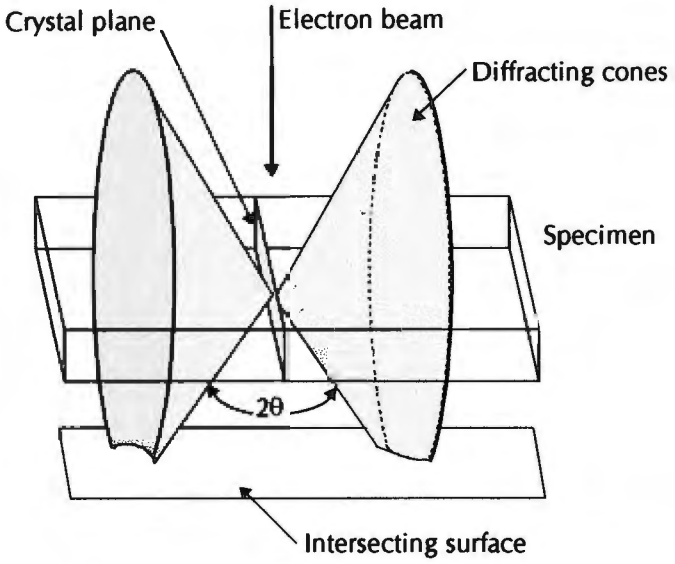

Figure 3.16: Interaction of the electron beam with a crystal plane forming two cones during electron diffraction.

The second approach for microtexture measurement involved the use of a fully automatic EBSD system developed by TexSEM laboratories in the USA. This was prompted by the fact that after several attempts at trying to identify texture colonisation, it became clear that much larger areas of individual grain measurements were required than that which is practically possible using the manual system. Details of the TexSEM system are also given below.

3.4.4.2 Manual EBSD System

An EBSD system for manual microtexture measurements was successfully installed on a LEICA 440 SEM at the Electron Microscope Unit at the University of Cape Town. The components of the system are presented schematically in figure 3.17. A purpose built specimen stage, which incorporates a silicon {001} calibration crystal, fixes the tilt angle at 70.5° with respect to the horizontal. The large tilt angle optimises the backscatter electron yield and the specific value of 70.5° provides a <114> pattern centre for the silicon crystal. The diffraction image on the phosphor screen is captured via a Hamamatsu C2400-

08 SIT video camera which is mounted externally, with a view through a lead glass window on one of the chamber quarter ports. Image enhancement is carried out via a MATROX IP-8 card which is incorporated within the SEM. At this point, pattern intersections (zone axes) are manually identified and the distances between the zone axes are calculated by the computer. This information is then transferred to a semi-automatic indexing software routine and the pattern is interpreted by the program. Based on the result, a computer simulation follows which generates a pattern overlay on the observed pattern and the operator is able to confirm the orientation result. The process allows approximately 60 orientations to be determined per hour. The region of interest on the sample is simultaneously imaged by the SEM via a back-scatter detector, which is mounted at the base of the phosphor screen to produce an ECC image. Scan rotation and tilt correction facilities allow the image to be seen without distortion.

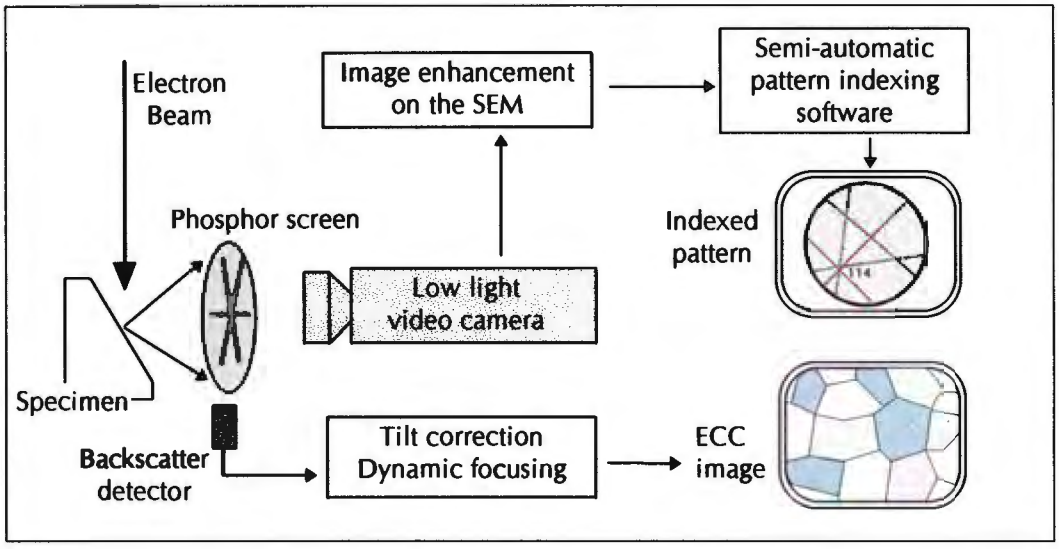

Figure 3.17: Schematic of manual EBSD system.

Individual grain orientations were measured on samples of the laboratory prepared stainless steel after the hot roll-anneal stage (B) and the cold roll-anneal stage (D). Measurements were recorded across the longitudinal section (RD-ND) over a maximum area of 0.3 mm^2 at the surface and the mid-plane areas. The surface of a sample for EBSD analysis should be unstrained, as even a small amount of surface deformation destroys the quality of the electron diffraction pattern. For this reason, the present samples were examined in the highly

polished condition using the electro-polishing techniques outlined in section 3.3.1.

Grain by grain orientations were measured by positioning the electron beam within individual grains, and the corresponding EBSD pattern was analysed after user identification of at least three zone axis positions on the computer display. The orientation data for each region of interest is stored in Miller index (hkl) < uvw > notation and Euler angle representations, thus facilitating a number of post processing routines that are described later.

3.4.4.3 Automatic EBSD System

Microtexture measurements were acquired on an Orientation Imaging Microscopy (**OIM™**)[2] system (TSL, TexSEM) at the Department of Materials Engineering, Carnegie Mellon University in Pittsburgh, USA. The fully automatic system is capable of analysing local texture on a grain or sub-grain level to provide information regarding orientation or grain boundary relationships. It comprises a low light level video camera attached to a Phillips 40XL FEG scanning electron microscope, an interface connecting the camera to the SEM, a Unix based workstation (Silicon Graphics Indy) and the **OIM** software (figure 3.18).

During operation, the EBSD patterns which radiate from the highly tilted (70°) sample are imaged on a phosphor screen placed at a distance of approximately 40 mm from the sample surface. These high quality EBSD patterns are imaged via a fibre optic bundle by a charge-coupled device (CCD) camera mounted on the side port of the SEM. The camera control unit is capable of averaging a variable number of video images (maximum 128 frames), with the extent of averaging dictated by the quality of the EBSD pattern. The quality in turn is determined by the atomic number, internal strain level and condition of the surface preparation of the sample. The averaged pattern can also be enhanced by subtracting a background image which is acquired by scanning over a large number of grains. Current spatial resolution of backscattered electron

[2] OIM is a trademark of TexSEM Laboratories Inc., Provo Utah USA.

diffraction is generally 0.2 μm; however, using a field emission SEM can reduce this to, for example, 0.04 μm when examining gold. A frame grabber card is installed in the computer which captures the enhanced image from the camera control unit and displays it in a video window of the Unix based workstation.

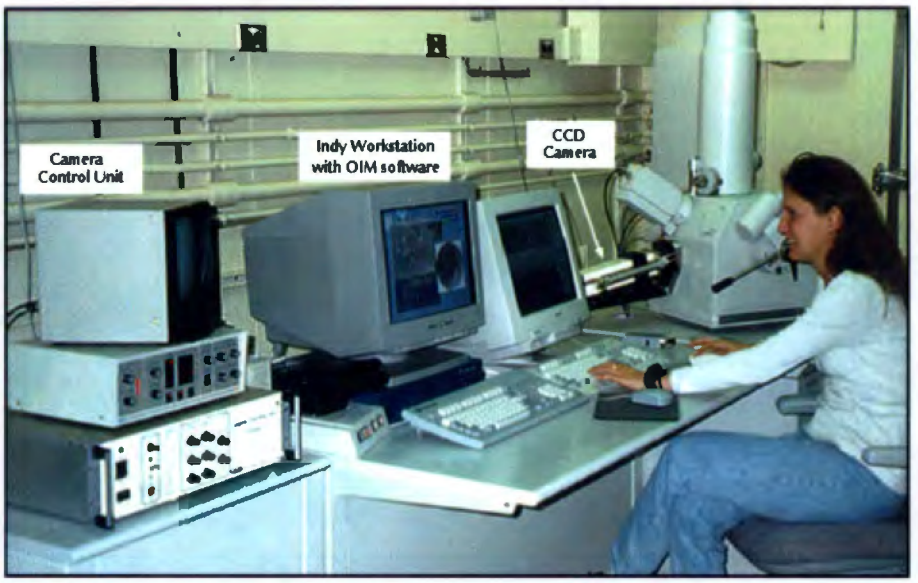

Figure 3.18: The Orientation Imaging Microscopy system at Carnegie Mellon University.

Complex crystallographic software indexes the pattern and calculates the five parameters, as follows:

- the orientation of the crystal in Euler angles (φ_1,ϕ,φ_2),
- the location of the data point on the sample in x-y coordinates,
- a quality index indicating the sharpness of the pattern,
- a confidence index indicating the level of confidence of the indexing

The electron beam is controlled automatically by the **OIM** software and scans across the area of interest in a raster formation, creating a grid of single orientation measurements. If the scan area is relatively large (i.e. 1mm x 1mm), then step size between measurements will be dictated by the grain size of sample. Depending on the required result, a minimum of two to three measurements should fall within a single grain. The indexing algorithms require a little over one second to identify a pattern, which means that about 3000 measurements could be recorded within one hour. To improve the accuracy of the pattern identification, a careful calibration procedure was carried out before each scan.

Unlike the manual EBSD system where the operator identifies the zone axes from Kikuchi line intersections, the diffraction pattern in the **OIM** system is indexed automatically. There are two automatic pattern indexing routines used by the **OIM**, namely the Hough and Burns algorithms[111]. The former uses the Hough transform to identify prominent bands in the EBSD pattern which enables crystal orientation determination[94]. The Hough transform is a means by which lines in real space are transformed into points of high or low intensity in Hough space. The location of these points is directly related to the inclination of the line in real space and its distance from the origin of the image. The Hough parameters ρ and θ are defined as follows:

$$\rho = x \sin\theta + y \sin\theta$$

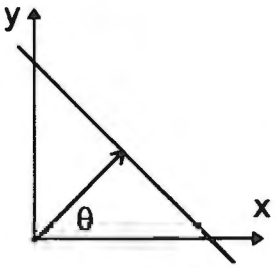

Once the points are located in Hough space by passing a mask through the Hough image, the position of the corresponding line in real space is calculated. In addition, the quality and sharpness of the real image or diffraction pattern determine the intensity of the points in Hough space, thereby quantifying the state of strain of the sample. Alternatively, the user may select the Burns algorithm which analyses the contrast gradients along groups of pixels and joins together equivalent gradients above a set limit to identify lines which are the edges of Kikuchi bands. Both methods provide the same result and have been reliably used to index diffraction patterns. Once the diffraction pattern has been captured, the **OIM** system will index the pattern according to the current input parameters and will provide the best solution available.

From the raw data file of orientations created during a scan, a number of post-processing analyses can be performed using the **OIM** software. The most powerful is the construction of a grain morphology map that can be manipulated to show particular features of interest. Grain and sub-grain boundaries are constructed by specifying misorientation limits, for example 5° between neighbouring sub-grains and 15° between neighbouring grains. The

thickness of the line drawn on the image represents the maximum angle of misorientation. Shading of the grains (colour or grey levels) can be dependent upon grain size, crystal orientation, plastic deformation or simply to emphasise grain morphology (figure 3.19). These facilities would allow, for example, the location of dislocation cells and regions of high strain, as well as the spatial distributions of specific texture components.

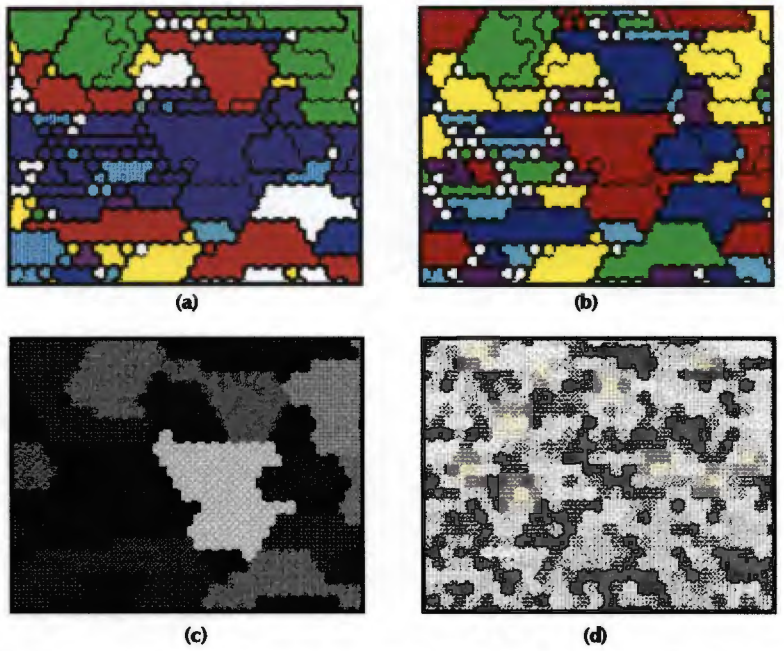

Figure 3.19: An Orientation Image Micrograph shaded according to four material properties. (a) Orientation Map: A constant colour represents a specific orientation within a 15° mismatch. (b) Morphology Map: A constant colour fills each grain, where the grain boundaries correspond to a 15° mismatch (colours not related to orientation). (c) Grain Size Map: Grains are shaded according to size, where the largest grain is the brightest. (d) Strain Level Map: The various grey levels correspond to varying amounts of internal deformation, related to the quality of the EBSD pattern.

Grain boundaries can also be highlighted using various colours or line thickness according to a misorientation angle or a user defined parameter e.g. twin or special coincidence site lattice (CSL) boundaries. Single grain orientations can be plotted in Euler or Rodriques space as pole figures, inverse pole figures or ODFs, both discreetly and with use of contours. Furthermore, a misorientation distribution function (MDF) can be calculated and plotted in Rodriques or Euler space and thereby providing information on grain boundary relationships within the sample. The **OIM** post processing techniques used in the current investigation are outlined in section 3.4.4.6.

3.4.4.4 Sample Preparation for Microtexture Measurements

Stainless steel samples were polished according to the procedures for SEM analysis summarised in section 3.3.1. The aluminium samples for EBSD measurements were mechanically polished using 0.25 μm diamond paste and given an electropolish in a 30% nitric acid / 70% methanol electrolyte at -10°C and 15 V for approximately 30 seconds. This ensured complete removal of the mechanically deformed layer allowing high quality EBSD patterns. In the microscope chamber, samples were held in a clamp at a fixed angle of 70.5° to the horizontal.

3.4.4.5 Samples Analysed using OIM System

To obtain a measure of the texture distribution with the sample material, the microtexture of the stainless steel and aluminium samples was analysed across the transverse and rolling plane sections. The orientation measurements were acquired on predetermined grids or texture 'windows' across the rolling plane section and from centre to surface of the transverse section. This arrangement provides an overall view of preferred orientation distribution and allows a comparison of the texture components from window to window. Optimum diffraction patterns were obtained at an accelerating voltage of 20 kV and a set working distance of 15 mm. More than 400 000 orientation measurements were recorded in the current investigation using the **OIM** system, covering over 30 mm^2 of sample surface. The sample orientation and format of the microtexture measurements are detailed in the section below. Table 3.4 indicates the assigned sample numbers.

Table 3.4: Sample numbers for microtexture measurements.

Sample: Aluminium		Sample: Stainless Steel	
ALU2 Transverse Section	1	C430 Transverse Section	5
ALU2 Rolling Plane	2	C430 Rolling Plane	6
ALU1 Transverse Section	3	D3 Transverse Section	7
ALU1 Rolling Plane	4	D1 Transverse Section	8

Aluminium Alloys

Both samples ALU1 and ALU2 were analysed across the transverse and rolling plane sections (samples 1-4, Table 3.4). Schematics of the area scans performed on the **OIM** system are indicated below. The step size indicated beneath the diagrams refers to the distance between each orientation measurement point and is dependent on the grain size. The aim was to record between two and three measurements within each grain to ensure accurate orientation results and good grain morphology mapping.

Sample 1: Sample ALU2 Transverse Section

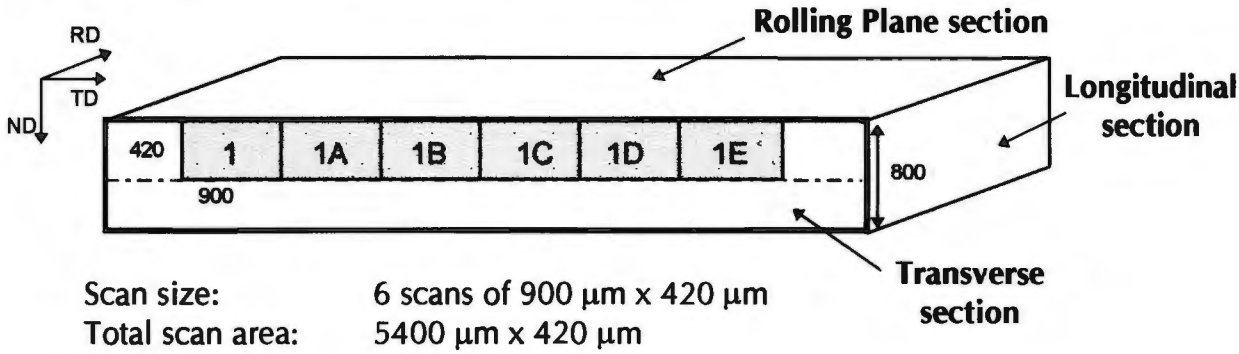

Scan size:	6 scans of 900 µm x 420 µm
Total scan area:	5400 µm x 420 µm
Step Size:	10 µm

Sample 2: Sample ALU2 Rolling Plane Section (Mid-plane)

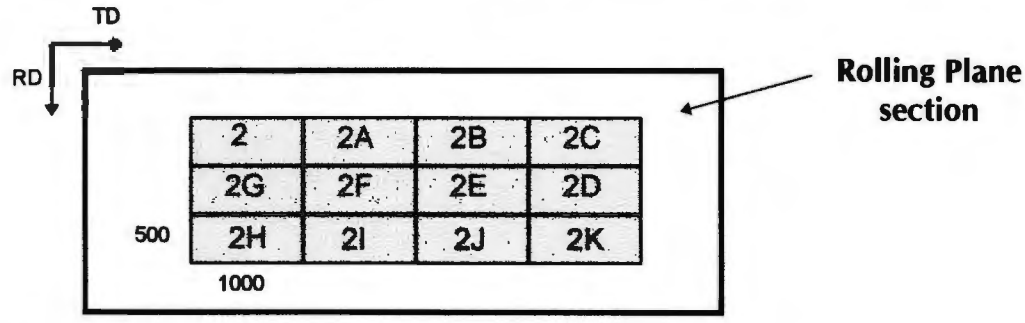

Scan size:	12 scans of 1000 µm x 500 µm
Total scan area:	4000 µm in the TD x 1500 µm in the RD
Step Size:	20 µm

Sample 3: Sample ALU1 Transverse Section

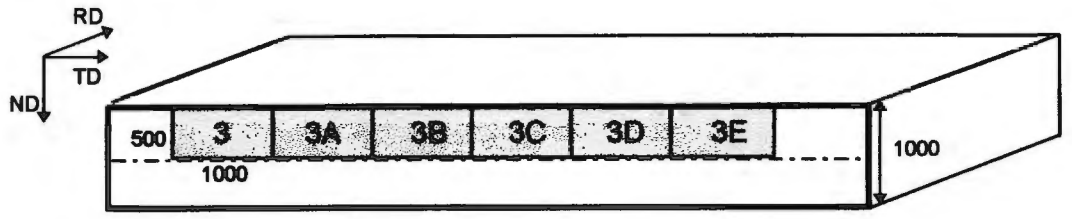

Scan size: 6 scans of 1000 μm x 500 μm
Total scan area: 6000 μm x 500 μm
Step Size: 10 μm

Sample 4: Sample ALU1 Rolling Plane Section (Mid-plane)

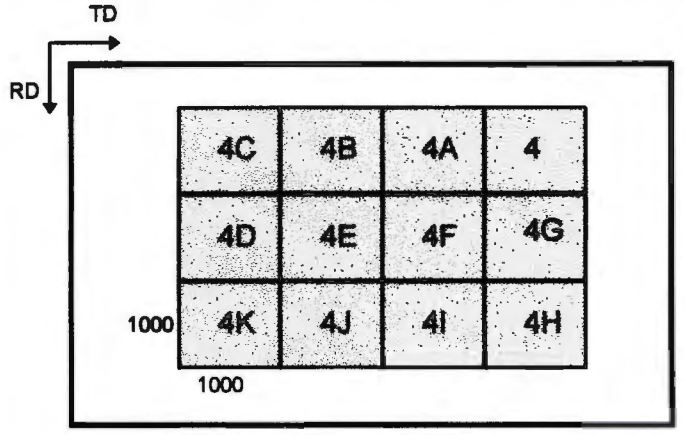

Scan size: 12 scans of 1000 μm x 1000 μm
Total scan area: 4000 μm in the TD x 3000 μm in the RD
Step Size: 20 μm

Ferritic Stainless Steel

Sample C430 was also examined across both the transverse and rolling plane sections. A total area of 5000 μm (TD) x 300 μm (ND) was scanned on the transverse plane, divided into five texture windows of 1000 μm x 300 μm each. For the rolling plane an area of 400 μm (TD) x 5000 μm (RD) was measured in five regions of 1000 μm x 400 μm. A small step size of 5 μm was used for the commercial steel due to the fine grain size. The microtexture of the laboratory rolled stainless steel was measured after the final stage of the TMP, namely the cold rolled-anneal stage. Only the heats with the highest (920°C, D1) and lowest (654°C, D3) hot roll finish temperatures were examined. Measurements

were recorded across the transverse planes from centre to surface over a total area of 800 μm x 6000 μm. This area was divided into six windows each measuring 800 μm x 1000 μm and the step size used was 10 μm. The layout of the **OIM** scans are illustrated schematically below.

Sample 5: Sample C430 Transverse Section

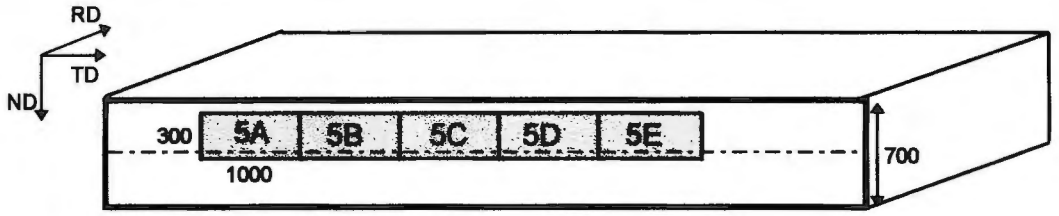

Scan size:	5 scans of 1000 μm x 300 μm
Total scan area:	5000 μm x 300 μm
Step Size:	5 μm

Due to the limited through-thickness dimension of the sample, the microtexture scans were shifted slightly such that a quarter of each scan was below the centre line as indicated in the diagram.

Sample 6: Sample C430 Rolling Plane Section

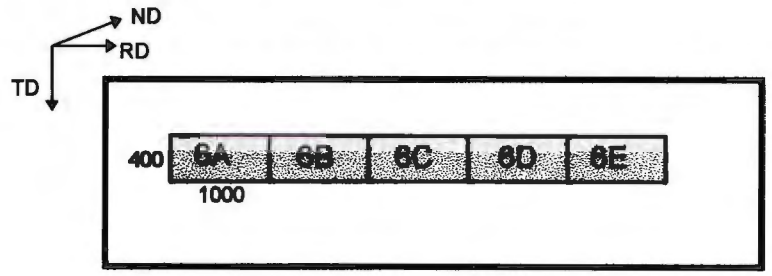

Scan size:	5 scans of 1000 μm x 400 μm
Total scan area:	5000 μm x 400 μm
Step Size:	5 μm

Sample 7: Sample D3 Transverse Section, cold rolled-anneal condition

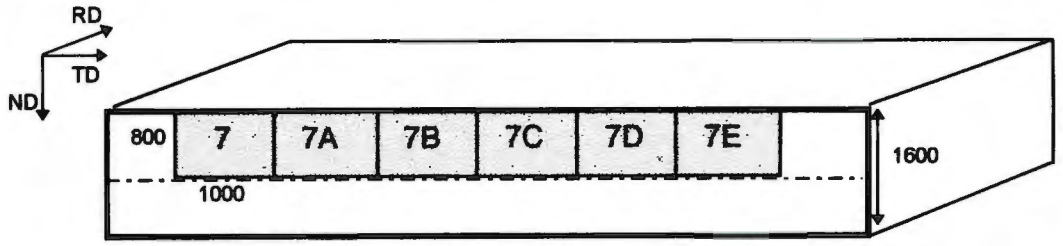

Scan size:	6 scans of 1000 µm x 800 µm
Total scan area:	6000 µm x 800 µm
Step Size:	10 µm

Sample 8: Sample D1 Transverse Section, cold rolled annealed condition

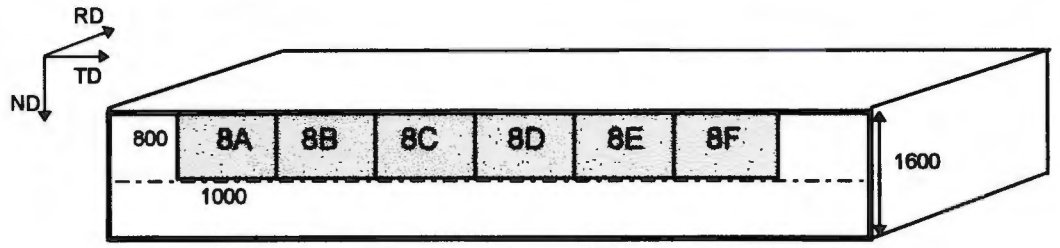

Scan size:	6 scans of 1000 µm x 800 µm
Total scan area:	6000 µm x 800 µm
Step Size:	10 µm

3.4.4.6 Microtexture Data Representation

Methods for the display of microtexture data can be much more involved than those used for conventional bulk data, due to the nature of the single grain orientation information. Microtexture data representations concentrate either on maintaining the spatial information of each data point or on the misorientation or grain boundary relationships between the grains. A number of new techniques to extract additional information from EBSD microtexture data are currently being developed.

Microtexture information acquired on the manual EBSD system was superimposed on the microstructure using colour mapping of orientations in

Rodriques-Frank space. The theory behind the technique and the procedures used for the colour display are presented in the sections below. Representation involving colour was also used for the display of automatically acquired microtexture data. Orientation maps were constructed using colour referencing in Euler space from the stainless steel and aluminium orientation data. A program was written in Visual Basic specifically for this assignment. Discrete orientation plots of the microtexture data were produced using the plotting routines available in the software package PopLA[3(114)], which facilitated the identification of the principal texture components present in each sample.

3.4.4.7 Microtexture Representation for the Current Project

As mentioned previously, the aim of the manual microtexture survey was to gain an understanding of the distribution of the preferred orientations within the sample material, with particular emphasis on the identification of texture clustering. Similarly, texture data acquired automatically using the **OIM** was also analysed to determine the spatial distribution of texture components. In addition, the data was able to be captured in such a way as to allow a subsequent spatially related plasticity analysis. In summary, the identification of texture clustering and principal preferred orientations was performed using:

(i) Discrete ODFs plotted in polar representation (laboratory heats, commercial stainless steel and aluminium).

(ii) Texture maps using colour coding in RF space (laboratory heats).

(iii) Texture maps constructed using colour coding in Euler space (laboratory heats, commercial stainless steel and aluminium).

A description of each of these procedures is given below:

(i) Principal preferred orientations were identified from the **OIM** microtexture data using discrete orientation representation plotted in polar coordinates via the software program PopLA. The data was reduced by applying cubic-orthorhombic symmetry and could thus be plotted within reduced Euler space

---

[3] PopLA: Preferred orientation package - Los Alamos, U.F. Kocks, J.S. Kallend, H-R. Wenk, A.D. Rollett and S.I. Wright., Los Alamos National Laboratory.

($0 \leq \varphi_1, \phi, \varphi_2 \leq 90°$). Representation is in Bunge notation, i.e. using $\varphi_1, \phi, \varphi_2$, and the sections were plotted at 10° intervals keeping φ_2 constant, with the first plot centred on zero. (A projection of the sections in the ND is equivalent to the conventional (001) pole figure). The RD of the sheet is plotted at the top of the quadrant and the TD to the right. The data file used for the plots had been pre-processed using the **OIM** system such that the orientations stored in the file correspond to individual recalculated grains, and not to the original measured data points. The variation in point size on the plots therefore relates to a variation in grain size in the simulated microstructure. (All data points below a volume fraction of 0.1 have been discarded). Analysis of these plots facilitated the identification of the principal preferred orientations for each sample, which was useful information when constructing the texture maps.

(ii) Representation of the manually acquired EBSD data from the UCT system was manipulated for the construction of texture maps using Rodriques-Frank Space. The theory on which this technique is based, as well as the procedures used for the texture maps, are detailed in the section below.

As explained in section 3.4.2, the orientation of an individual crystal is expressed in the form of a 3x3 matrix that describes its orientation in direction cosines with respect to a sample reference system, e.g. rolling, normal and transverse directions (figure 3.15). The components of the orientation matrix are

$$g = \begin{pmatrix} \cos\alpha_1 & \cos\alpha_2 & \cos\alpha_3 \\ \cos\beta_1 & \cos\beta_2 & \cos\beta_3 \\ \cos\gamma_1 & \cos\gamma_2 & \cos\gamma_3 \end{pmatrix}$$

This, however, is an over determination as nine values are used to quantify an orientation that possesses only three degrees of freedom i.e. only three independent variables are required. The orientation is more concisely described using the angle/axis of rotation where the axis, (l_1, l_2, l_3), is a vector common to both the crystal and sample axes, and the angle, θ, is the rotation about the vector which will result in the crystal and sample axes being coincident. These values are calculated from the orientation matrix using the following equations:

$$\cos\theta = (\cos\alpha_1 + \cos\beta_2 + \cos\gamma_3 - 1)/2$$

$$l_1 = \cos\beta_3 - \cos\gamma_2$$

$$l_2 = \cos\gamma_1 - \cos\alpha_3$$

$$l_3 = \cos\alpha_2 - \cos\beta_1$$

When $\theta = 180°$, l_1, l_2, l_3 are given by

$$(l_1\ l_2\ l_3) = (\cos\alpha_1 + 1)^{1/2}(\cos\beta_2 + 1)^{1/2}(\cos\gamma_3 + 1)^{1/2}$$

This form of notation is particularly appropriate when dealing with misorientations as it provides direct physical information regarding the boundary, i.e. if a low or high angle type boundary exists between the grains. The opposite is true for the more commonly used Miller index notation, $\{hkl\} < uvw >$, which is physically descriptive of the orientation in terms of a rolling plane and direction but provides no information on lattice misorientations. In the present case, however, the angle/axis pair is simply a step towards calculating the Rodriques vector (*R*-vector) which has advantages for generating a texture map as will be explained in subsequent sections.

Considering that an orientation requires only three independent variables for its complete definition, it is logical to combine together the four numbers used by the angle/axis pair thereby reducing the number of variables to three. The Rodriques vector is then given by the following equations:

$$R_1 = l_1 \tan(\theta/2)$$

$$R_2 = l_2 \tan(\theta/2)$$

$$R_3 = l_3 \tan(\theta/2)$$

where (l_1, l_2, l_3) is a unit vector. Therefore, all orientations within RF space will exist in a three-dimensional space whose axes are the *R*-vectors of the reference system.

Due to symmetry, each orientation in a cubic system has 24 possible rearrangements of the orientation matrix described above, and therefore 24 symmetrically equivalent angle/axis pairs or *R*-vector solutions will be generated. (This is not considering an inversion centre which would provide 48 different rearrangements). To produce these solutions the orientation matrix can be premultiplied by each of the symmetry matrices given in figure 3.20. The

question now arises as to which R-vector should be chosen to represent the rotation.

$$\begin{bmatrix}100\\010\\001\end{bmatrix}\ \begin{bmatrix}\bar{1}00\\0\bar{1}0\\00\bar{1}\end{bmatrix}\ \begin{bmatrix}00\bar{1}\\010\\100\end{bmatrix}\ \begin{bmatrix}\bar{1}00\\010\\00\bar{1}\end{bmatrix}\ \begin{bmatrix}001\\010\\\bar{1}00\end{bmatrix}\ \begin{bmatrix}100\\00\bar{1}\\010\end{bmatrix}$$

$$\begin{bmatrix}100\\0\bar{1}0\\00\bar{1}\end{bmatrix}\ \begin{bmatrix}100\\001\\0\bar{1}0\end{bmatrix}\ \begin{bmatrix}0\bar{1}0\\100\\001\end{bmatrix}\ \begin{bmatrix}\bar{1}00\\0\bar{1}0\\001\end{bmatrix}\ \begin{bmatrix}0\bar{1}0\\\bar{1}00\\001\end{bmatrix}\ \begin{bmatrix}001\\100\\010\end{bmatrix}$$

$$\begin{bmatrix}010\\001\\100\end{bmatrix}\ \begin{bmatrix}00\bar{1}\\\bar{1}00\\010\end{bmatrix}\ \begin{bmatrix}0\bar{1}0\\001\\\bar{1}00\end{bmatrix}\ \begin{bmatrix}010\\00\bar{1}\\\bar{1}00\end{bmatrix}\ \begin{bmatrix}00\bar{1}\\100\\0\bar{1}0\end{bmatrix}\ \begin{bmatrix}001\\\bar{1}00\\0\bar{1}0\end{bmatrix}$$

$$\begin{bmatrix}0\bar{1}0\\00\bar{1}\\100\end{bmatrix}\ \begin{bmatrix}010\\100\\00\bar{1}\end{bmatrix}\ \begin{bmatrix}\bar{1}00\\001\\010\end{bmatrix}\ \begin{bmatrix}001\\0\bar{1}0\\100\end{bmatrix}\ \begin{bmatrix}0\bar{1}0\\\bar{1}00\\00\bar{1}\end{bmatrix}\ \begin{bmatrix}\bar{1}00\\00\bar{1}\\0\bar{1}0\end{bmatrix}$$

Figure 3.20: Matrices representing 24 symmetry operations for a cubic system.

The R-vector is defined in such a way that the direction of the vector is governed by the rotation axis, and the length of the vector depends on the rotation angle. Therefore, the solution having the smallest angle will reside closest to the origin in RF space and this is the solution normally chosen for representation. As a consequence, all possible lowest angle solutions will be below 62.8° and will lie in a region surrounding the origin known as the fundamental zone. For cubic symmetry this zone takes the form of a cube with truncated corners (figure 3.21a), where the values for R_1, R_2 and R_3 respectively will be less than or equal to 0.414.

This is the basic shape of RF space used to represent all cubic orientations or misorientations when sample symmetry is not taken into account. However, if the sample reference axes are not fixed, as in the case of a rolled sheet which has orthorhombic symmetry, a further four symmetry elements need to be considered. The four symmetrically equivalent ways of expressing the sample reference axes are:

$$\begin{bmatrix}100\\010\\001\end{bmatrix} \quad \begin{bmatrix}100\\0\bar{1}0\\00\bar{1}\end{bmatrix} \quad \begin{bmatrix}\bar{1}00\\0\bar{1}0\\001\end{bmatrix} \quad \begin{bmatrix}\bar{1}00\\010\\00\bar{1}\end{bmatrix}$$

Thus if the 24 equivalent matrices of cubic symmetry are expressed with respect to these four orthorhombic sample symmetries, 24 x 4 = 96 matrices will arise. This results in four symmetrically equivalent "smallest" vectors plotting within the fundamental zone. Once again this is an over representation as only one of the set of four need be plotted which divides the fundamental zone into four quadrants. Therefore, only one quarter of the zone is required to plot an orientation arising from a cubic crystal in a rolled sheet possessing orthorhombic symmetry (figure 3.21b). In order to colour code a quadrant, the end points of the R_1, $+R_2$, $-R_2$ and R_3 axes are assigned the colours red, green, black and blue respectively. For the purposes of generating a colour matrix, the colour scheme was computer coded using a 256 bit colour range. This means that $-R_{2(max)}$ was assigned the values 0,0,0 for red, green and blue respectively (i.e. black), and $+R_{2(max)}$ was assigned 0,255,0 (i.e. green). The origin (R_1,R_2,R_3 = 0,0,0) was assigned the colours 0,128,0, while $+R_{1(max)}$ and $+R_{3(max)}$ were assigned 255,0,0 (i.e. red) and 0,0,255 (i.e. blue) respectively.

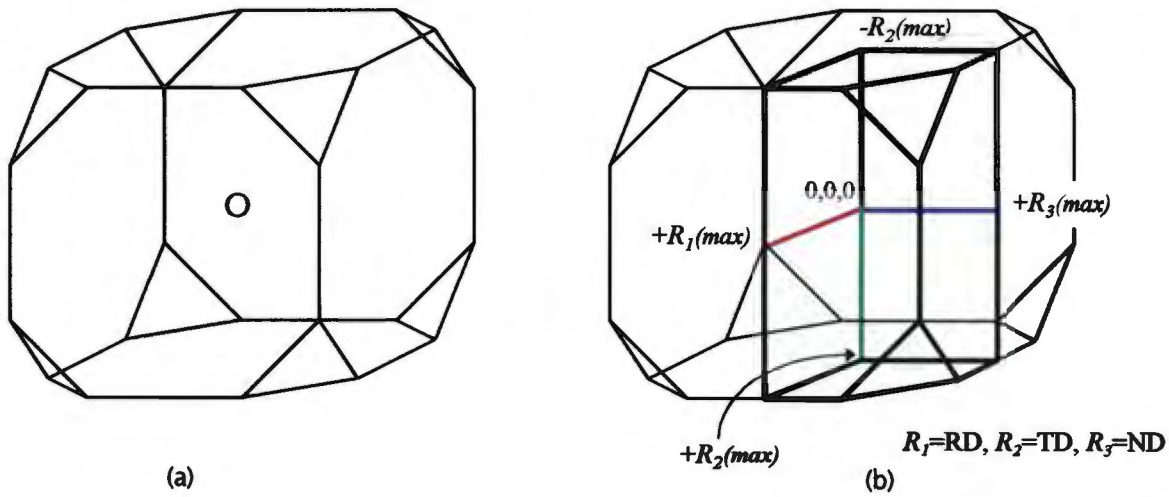

Figure 3.21: Orientation spaces in the Rodrigues representation for cubic lattices: a) sample without symmetry b) sample with orthorhombic symmetry.

A computer program has been written which converts individual grain orientation data to *R*-vectors and assigns a colour to each grain according to this reference quadrant. The program reads in a stored image of the skeletised grain structure obtained from the original ECC image, and fills the appropriate colour within each grain boundary. Thus a texture map is produced which conveys complete orientation information. Grains of similar colour imply that they have similar orientation. An image employing this method was constructed for each laboratory rolled stainless steel sample using the grain orientation data measured on the manual system. An interpretation of the orientations images is provided in the section below. Orientation measurements for the non-coloured regions were not possible due the quality of the backscattered pattern during microtexture measurement. These results are included within the Experimental Approach chapter as they did not contribute to the final conclusions for the laboratory rolled stainless steel samples but rather provided direction for the microtexture investigation.

Interpretation of Texture Maps constructed using RF Space

Sample B2 Centre region (Partially recrystallised, figure 3.22)

Unfortunately only a very limited number of recrystallised grains were analysed, but the indications are that the α-fibre components are well represented (refer to colour reference chart, figure 3.28). However, it is not possible to determine whether or not any particular α-fibre component dominates.

Sample D2 Centre region

The texture map in figure 3.23 exhibits adjacent regions with distinct differences in grain size. In addition, the general RF colour distribution is different in the two regions which demonstrates different textures associated with the respective coarse and fine grained populations. No discernible clustering of like orientations is evident in the coarse region, yet there is a distinct less than random clustering of similar orientations in the fine grained region.

Sample B3 Surface region

The map in figure 3.24 exhibits a more or less random distribution of orientations.

Sample B3 Centre region

With reference to the image in figure 3.25, the grains in the top left-hand area have a generally different orientation compared to the grains in the remaining part of the image. The average RF colour signifies a near-Goss orientation. The bulk of the grain structure possesses a wider range in orientation distribution, although there is a dominance of certain colours that indicates some degree of clustering.

Sample D3 Surface and Centre region

The texture distribution in the surface and centre regions is similar, and can generally be described as random (figures 3.26 and 3.27). In excess of 1400 grains were measured in the centre region of D3 which represents by far the largest sampling area. **Nevertheless, it is clear that larger sampling areas are needed in order to allow a more significant interpretation of microtexture distribution.**

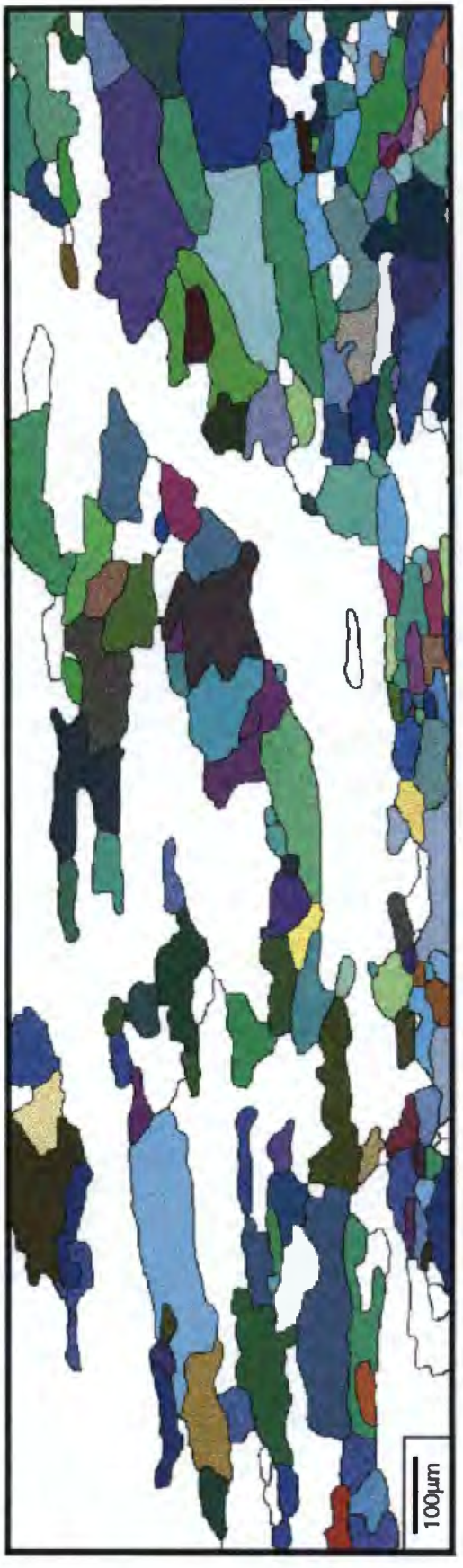

Figure 3.22: Texture map of sample B2 mid-plane.

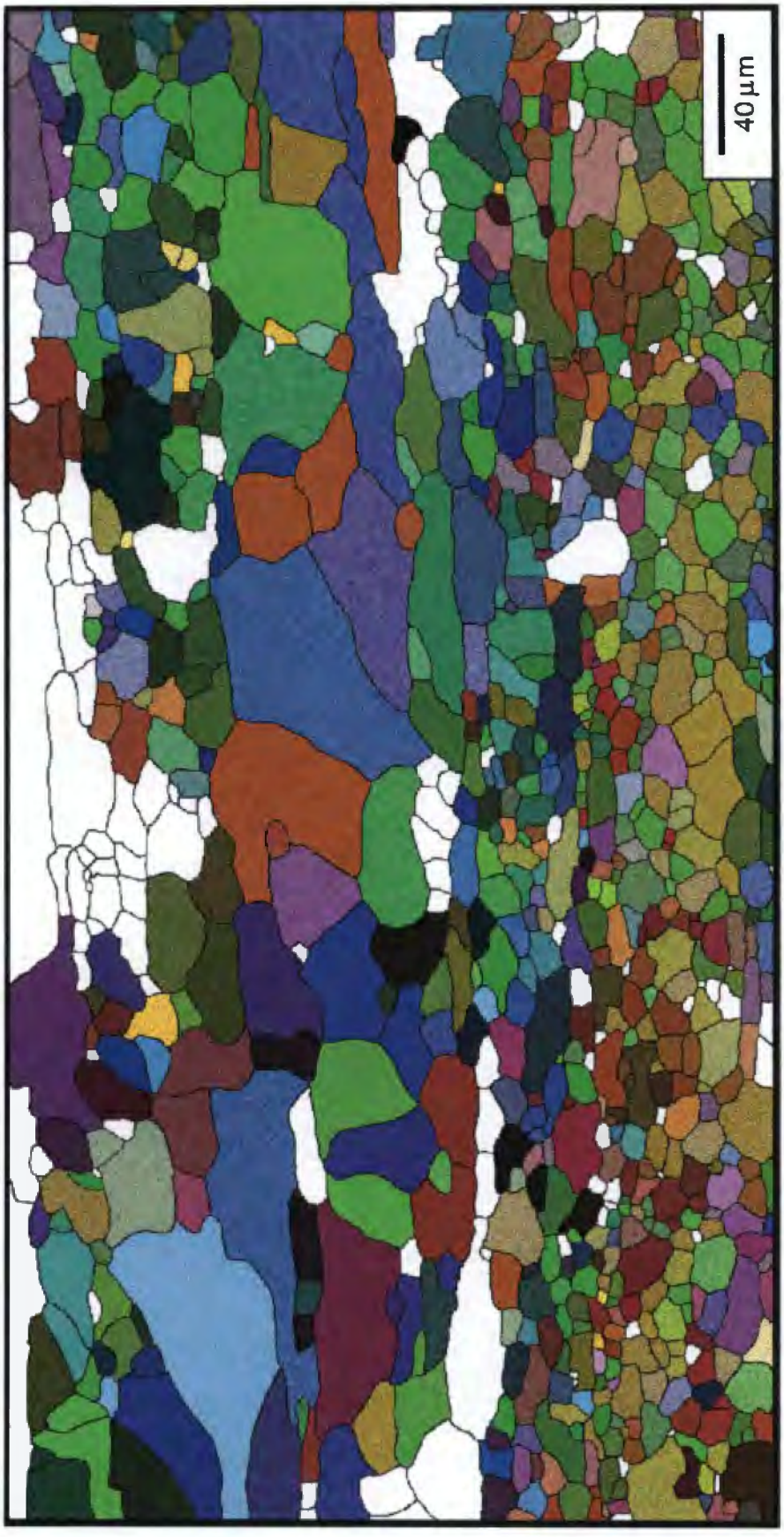

Figure 3.23: Texture map of sample D2 mid-plane.

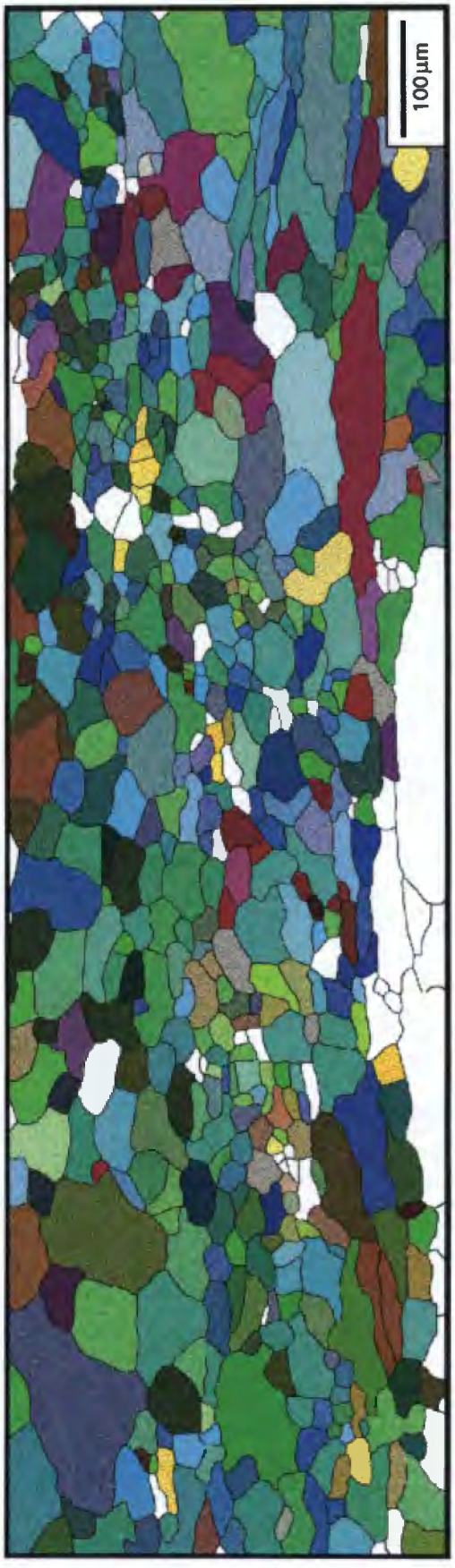

Figure 3.24: Texture map of sample B3 near surface.

Figure 3.25: Texture map of sample B3 mid-plane.

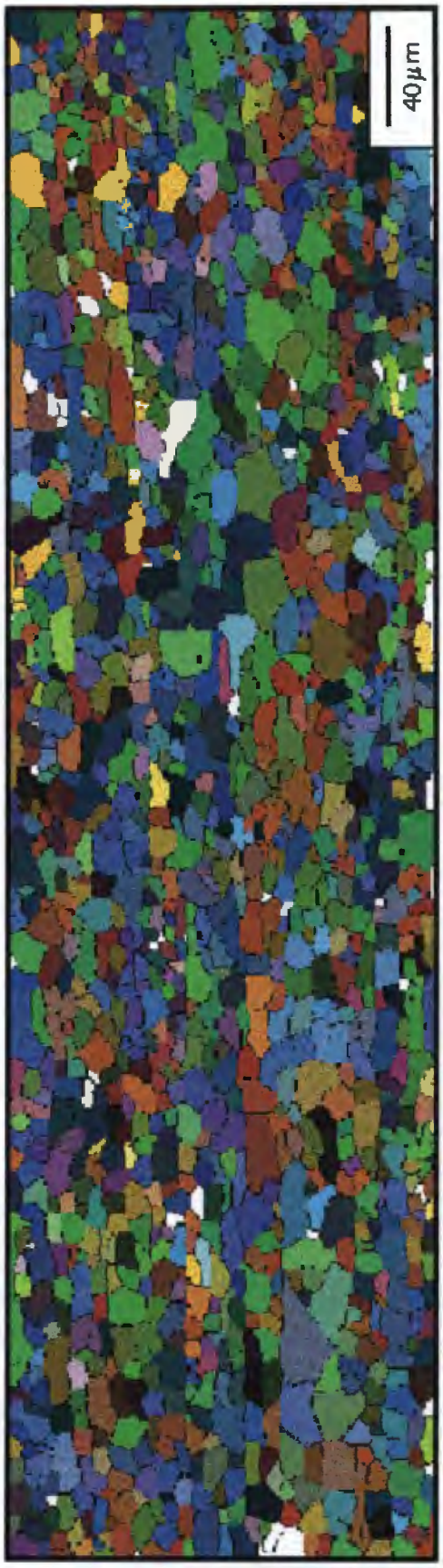

Figure 3.26: Texture map of sample D3 mid-plane.

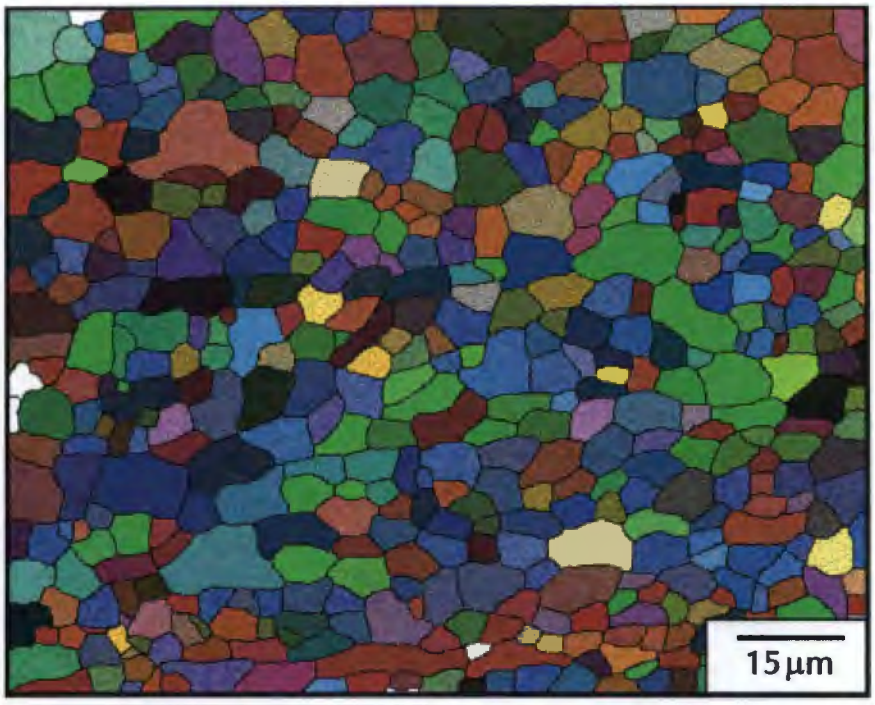

Figure 3.26: Texture map of sample D3 near surface.

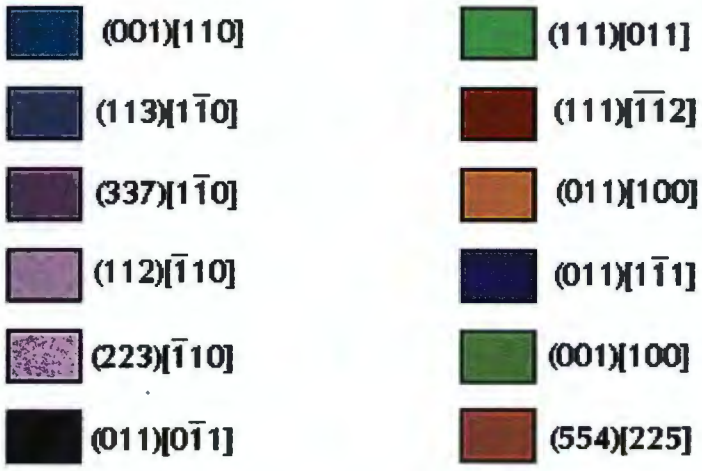

Figure 3.28: Rodriques-Frank space colour chart.

(iii) Texture maps using the automatically acquired stainless steel and aluminium microtexture data were constructed using colour coding in Euler space via a software program written in Visual Basic. The main advantage of using colour coding in Euler space as opposed to RF space is the ability to assign a single colour to a group of orientation data points possessing a low misorientation relative to a particular ideal orientation. In other words, all grains which posses orientations near a certain ideal orientation will be identically coloured and classified as the same texture, which facilitates the identification of texture clustering. Also, it does not have the disadvantage of RF space of certain orientations which possess low misorientations being coloured differently if they lie near the extremes of the fundamental zone. Similar to the **OIM** system, colour mapping of preferred orientations is facilitated by specifying certain reference orientations or ideal orientations in Euler space and assigning to each a specific colour. A variance about this ideal orientation is created by specifying a spherical radius, where the radius is equal to the maximum variance, for example 15° to 20° around the ideal orientation. In this way, each ideal orientation and its specified variance forms a coloured sphere in Euler space (centre of sphere = ideal orientation, figure 3.29). If a measured orientation falls within one of the coloured spheres it will be assigned that particular ideal orientation and coloured accordingly on the texture map. During the operation of the program, the user initially specifies the relevant ideal orientations using the three Euler angles φ_1 ϕ φ_2, their colours and their variance. (This information can be stored as a file that can be retrieved at a later stage for further texture mapping). The measured microtexture data is also in the form of three Euler angles, reduced either by cubic crystal symmetry only, or by both cubic crystal and orthorhombic sample symmetries.

In the case of cubic crystal symmetry only, the volume of Euler space required for complete texture representation is $\varphi_1 = 360°, \phi = 90°, \varphi_2 = 90°$, as explained in section 3.4.2. In this case, where orthorhombic symmetry is not applied, it is possible to distinguish between separate variants of a single ideal orientation. The distribution of these variants can be identified using the software by assigning a different colour to the ideal spheres of each variant (figure 3.29).

For example, to map the distribution of the $(111)[1\bar{2}1]$ orientation the following three Euler angle sets must be specified (30°,55°,45°), (150°,55°,45°) and (270°,55°,45°), and for its variant $(111)[1\bar{1}2]$, (90°,55°,45°), (210°,55°,45°) and (330°,55°,45°) must be coloured (figure 3.29).

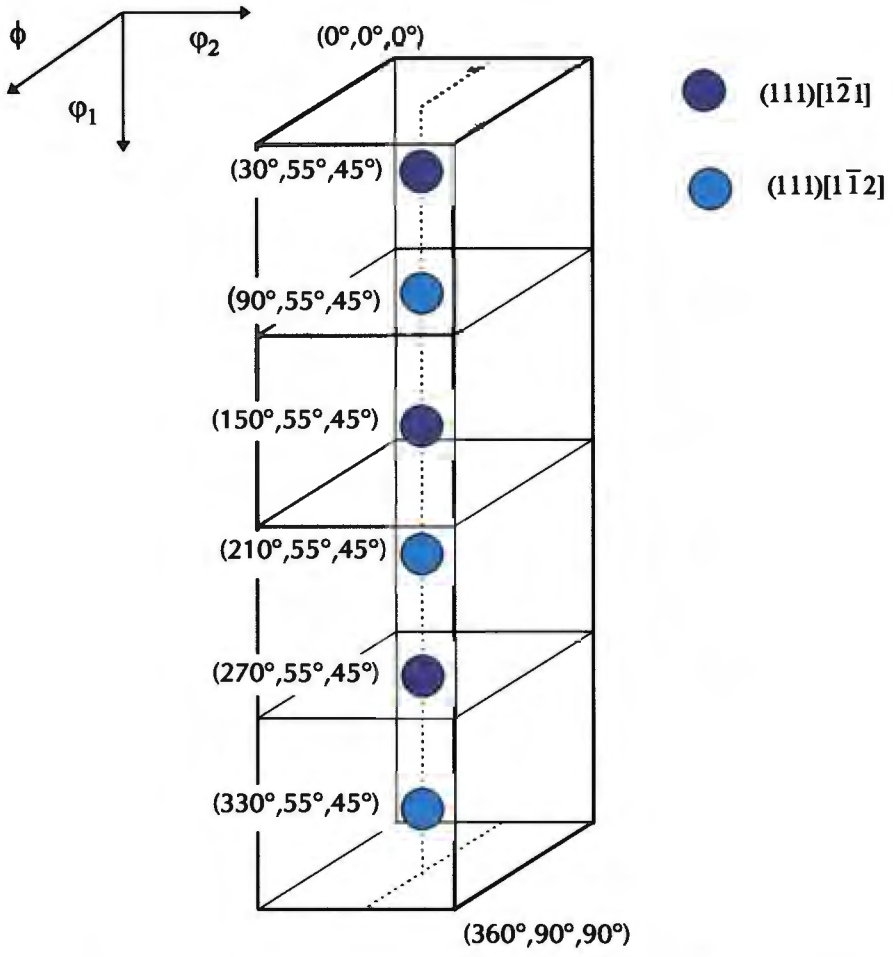

Figure 3.29: Euler space for cubic symmetry indicating the position of the two texture variants $(111)[1\bar{2}1]$ and $(111)[1\bar{1}2]$.

For complete cubic-orthorhombic symmetry on the other hand, the reduced Euler space of 90°,90°,90° is sufficient to fully represent the texture distribution within a material, and so only those orientations falling within this space need be specified (figure 3.30). In this format the texture variants are indistinguishable and thus the identification of their distribution using this form of texture mapping is not possible.

During operation, the program reads each orientation point in the data file and determines whether the orientation falls within the volume of Euler space

around any one of the specified ideals. If so, a small hexagon of colour is placed in the appropriate position in a TIF file, while if it fails to correspond to any sphere, the hexagon remains white.

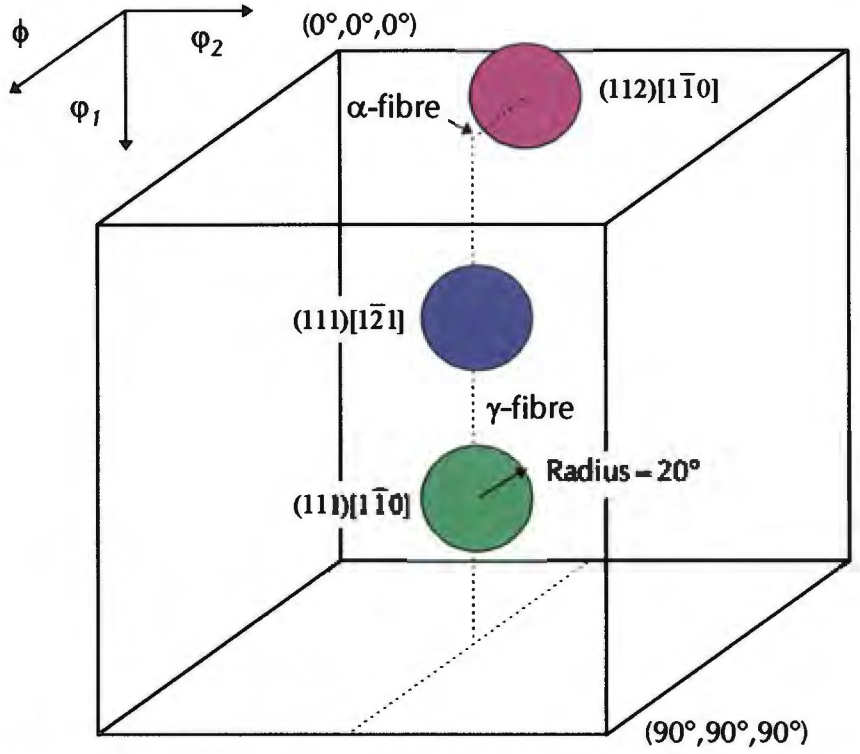

Figure 3.30: Euler cube indicating three ideal orientations within a coloured sphere

Thus a map of the preferred texture components present within the material can be constructed where the colour position is superimposed on the original microtexture measuring grid. To provide a more accurate result, fading of the ideal colour sphere away from the centre point has been incorporated in the program. An orientation therefore falling at the edge of the sphere will appear lighter in colour than an orientation near the centre of the ideal sphere. The time taken to construct a texture map containing 3000 points is approximately 20 seconds.

The two common textures, namely cube $\{100\}<001>$ and α-fibre component $\{100\}<011>$, which are affected by the degeneration of Euler space at $\phi = 0°$, are handled differently. This is best illustrated by considering the plotting of the cube texture for reduced cubic-orthorhombic symmetry as an example. The ideal cube plots at 0°,0°,0° and $\phi = 0°$ and $\varphi_1+\varphi_2 = 90°$. In the latter case, the

level of specified variance about the ideal is dealt with as follows. A certain maximum value, say 10°, is assigned to ϕ such that all ϕ values less than ϕ_{max} are captured. The sum of the $\varphi_1+\varphi_2$ values is then considered, and if the condition $70° < \varphi_1+\varphi_2 < 110°$ is met, where the variation about the ideal $\varphi_1+\varphi_2 = 90°$ is now 20°, then the measured orientation is allocated the cube texture. When only cubic crystal symmetry is considered, then the ideal values for $\varphi_1+\varphi_2$ include 180°, 270° and 360° as well. For the α-fibre texture, the ϕ limit remains the same, but the ideal value for $\varphi_1+\varphi_2$ is 45° for cubic-orthorhombic symmetry, and the values 135°, 225° and 315° are included when only cubic crystal symmetry is considered.

A texture map using this program was constructed for all the microtexture data acquired on the **OIM** system, i.e. the rolling plane and transverse sections of the commercial steel and aluminium samples and the transverse plane of the laboratory rolled stainless steel samples. Again a number of ideal orientations were selected based on the major texture components present in the material. Collages combining the various texture windows could also be constructed to form one large microtexture map of each measured section. Superimposed on these collages of the laboratory heats, the areas of large and small grains were manually delineated in an attempt to identify a correlation between texture components and grain size.

3.5 Plasticity Analysis

It has been suggested that the origin of the ridging phenomenon in ferritic stainless steel is related to the anisotropic plastic flow of inhomogeneous texture components present within the sheet. The original proposals for the mechanism of ridging all involved the theory of crystal plastic anisotropy and each made an attempt at predicting the yield behaviour of the constituent texture components under a tensile stress[32,34,38]. The flow characteristics for single crystals of different orientations were investigated, using Schmid's law for slip in BCC materials. In addition, the variation in strain ratio, *r*, caused by the anisotropic texture distribution within the material was examined, with the aim of determining whether or not plastic flow behaviour could account for ridging.

A similar situation is applicable to the current project where the objective of the plastic analysis is to characterise the flow behaviour of the sample material in an attempt to correlate the predicted plastic behaviour with the ridging profile. The microtexture measurements were acquired over adjacent texture windows across both the rolling plane and transverse sections of the sample material. This mode of data capture allows a comparison of the flow behaviour characteristics of the material on a scale equivalent to the windows size. As part of the plastic analysis, a two dimensional yield surface was calculated for each texture window. Any variations in predicted deformation behaviour for the sample material will be evident from the differences in yield surface morphology. To provide a more quantitative description of the plastic properties, the Lankford strain ratios (r-value) and Taylor factors (M) were also calculated. The r-value provides an indication of the anisotropy of the yield behaviour, while the Taylor factor provides an idea of the flow stress. The ultimate aim is to utilise this yield information in a finite element modelling experiment which attempts to simulate the deformation behaviour of the material.

All plasticity calculations were performed using the Los Alamos polycrystal plasticity simulation code (LApp). The following section describes the methods used in LApp for the calculations, including the procedures followed to determine the Lankford strain ratios, Taylor factors and yield surfaces for each data set. Furthermore, the rearrangement of the texture windows to allow a comparison on a smaller scale is detailed. For completeness definitions of the Lankford strain ratio and the Taylor factor have been provided, as well as a brief summary of the Taylor[96] and Bishop and Hill[98,99] plasticity theories which are used in the current investigation.

LApp is a Taylor based plasticity simulation code that requires as input a data file of discrete orientations. It is Taylor based as a sufficient number of deformation modes must be identified to complete the single crystal yield surface. The LApp software is able to account for the development of work hardening during deformation and, if necessary, the relaxed constraints modification of the Taylor theory[96] can be incorporated for flat or non-equiaxed

grains. It is an interactive code that can be applied to data from a number of materials to calculate the development of strength and texture properties during deformation. It is also able to calculate the yield surface of a polycrystal and the strain ratios and Taylor factors for uniaxial deformation, which are the three functions used in the current plastic analysis. The input data file should contain a list of single grain measurements in the form of three Euler angles (in Kocks notation) and their relative weights. As output LApp provides the details of deformation for each individual grain as well as those for the material as a whole. Information regarding grain orientation, grain shape, stress and strain vectors, slip systems and volume fractions for each grain are stored in a data file.

For the calculations, a file containing information concerning the material properties is needed, including parameters describing the strain rate sensitivity and the number of available deformation modes. In addition, LApp requires a reference file containing details of slip for a single crystal of the appropriate crystal system. The type of slip experienced by the sample is selected by the user, for example for FCC crystals $\{111\}<110>$ slip can be chosen, or for BCC crystals restricted glide along $\{110\}<111>$. These are the two selections made for the present plastic analysis. Also, the type of deformation analysis desired, either Bishop and Hill or Sachs, is specified by the user. During the calculation of a yield surface, LApp uses the orientation data file, plus the two reference files mentioned above, to compute the coordinates of the yield surface.

For each **OIM** data file or texture window, a two-dimensional yield surface was calculated and plotted at a section where stress in the normal direction (z direction) is zero. A Bishop and Hill[98,99] type analysis was used in the simulation, incorporating the relaxed constraints criteria when possible. The values on the X and Y axes correspond to the yield stress divided by the shear stress or σ_x/τ and σ_y/τ respectively, and thus the values at the intercepts of the plot provide a measure of the Taylor factor for uniaxial deformation in that direction. The plots also provide a means to characterise and compare the predicted yield behaviour from window to window across a section of material.

LApp was also used in conjunction with the **OIM** microtexture data to calculate the Lankford strain ratios for uniaxial tensile deformation at angle increments of 45°. Again a Bishop and Hill type deformation analysis was used with a relaxed constraints criteria. For all calculations, cubic orthorhombic symmetry was applied to the microtexture data during the calculations.

To facilitate the comparison of plasticity behaviour on a smaller scale, the texture windows for the stainless steel sample material were subdivided in four equal sections through the thickness of the sheet (figure 3.31). The yield surfaces and Lankford strain ratios were then recalculated for the reduced data files and comparisons were made within each texture window, as well as across the section.

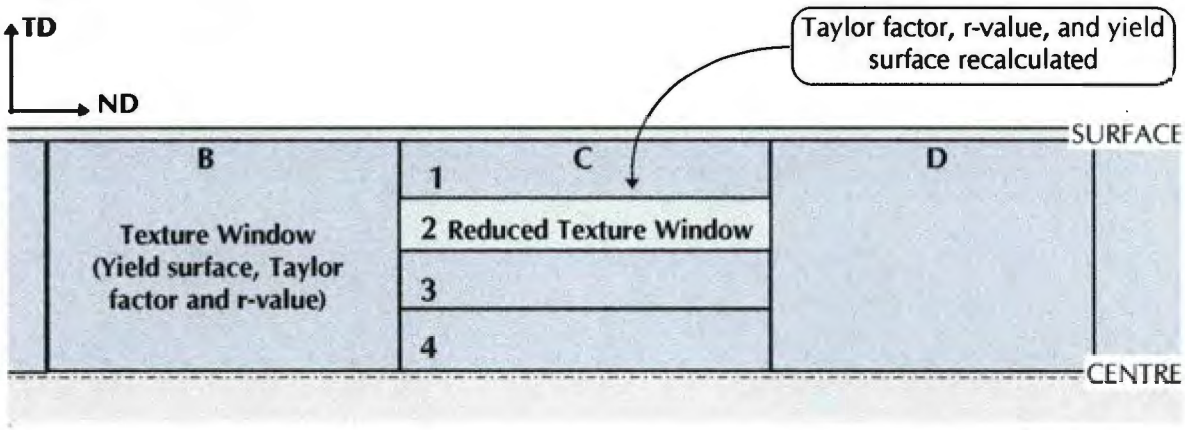

Figure 3.31: Subdivided texture windows into four equal quadrants.

The following section includes a description of the Taylor analysis[96,97] of deformation in polycrystals, outlining the calculation of the Taylor factor, and a summary of the Bishop and Hill analysis[98,99] which is used to calculate the yield surfaces. Brief mention is made of the modified Taylor relaxed constraints model[101-103] which was also utilised in the operation of LApp. In addition, an explanation of the fundamentals of an upper-bound yield surface are given, including a definition of the Lankford strain ratio.

3.5.1 Taylor and Bishop and Hill Analyses

During straining most crystals experience ***slip*** as the primary deformation mode, which is a lattice mechanism operating within the crystalline lattice. Slip

directions are almost always the crystallographic directions with the shortest repeat distance, while the slip planes correspond to the closest packed planes. The slip systems for BCC and FCC crystals are given in Table 3.5.

Table 3.5: Common slip systems.

Structure	Slip Direction	Slip Planes
FCC	<110>	{111}
BCC	<111>	{110},{112},{123}, pencil glide

The yield criterion for slip in a single crystal is termed ***Schmid's Law***. Under uniaxial tension along direction x, the resolved shear stress, τ, can be found from the equation for stress transformation, as follows:

$$\tau_{nd} = l_{nx}\, l_{dx}\, \sigma_{xx}$$

where l_{nx} = direction cosine between tensile axis and the slip plane normal

l_{dx} = direction cosine between tensile axis and slip direction

σ_{xx} = external applied stress

The deformation mechanisms operative in single crystals are the same as those in polycrystals, and therefore in theory it is possible to relate quantitatively the plastic deformation properties of a polycrystal to those of a single crystal. **Sachs**[102] calculated the Schmid factor for a single crystal and then, by assuming that the overall strength of a polycrystal is the average of the strengths of the individual crystals, it was possible to estimate the yield strength of a randomly orientated FCC polycrystal (m = 2.238). For this it was also necessary to assume that only one slip system was active during deformation within each grain.

Taylor[96] recognised the weakness in the assumption of a single active slip system and proposed an alternative method. Taylor[96] assumed that firstly, all grains undergo the same shape change as the entire polycrystal, and secondly that under uniaxial tension parallel to the x direction, deformation is axially symmetric in a randomly orientated polycrystal. Thus $d\varepsilon_y = d\varepsilon_z = -\frac{1}{2}d\varepsilon_x$,

$d\gamma_{yz} = d\gamma_{zx} = d\gamma_{xy} = 0$ and the work per volume, dw, that is internally expended by slip on all active slip systems within a grain is:

$$dw = \sum_i \tau \, d\gamma_i = \tau \sum_i d\gamma_i .$$

The critical resolved shear stress, τ, is assumed to be equal for all slip systems and $d\gamma_i$ is the incremental shear stress on the individual slip systems. For uniaxial tension the incremental work supplied by the external stress is $\sigma_x d\varepsilon_x$ and can be equated to the internal work per volume. Therefore, if $\sum_i d\gamma_i = d\gamma$, the work per volume is:

$$dw = \tau \, d\gamma = \sigma_x d\varepsilon_x$$

or

$$\frac{\sigma_x}{\tau} = \frac{d\gamma}{d\varepsilon_x} = M$$

where M is the ***Taylor factor***. By calculating the value of M for all orientations and averaging to find $\overline{M}$, the flow behaviour of a random polycrystal can be estimated as:

$$\sigma_x = \overline{M}\tau \quad \text{and} \quad d\varepsilon_x = \frac{d\gamma}{\overline{M}}.$$

Taylor[96] derived the following method to calculate M for a single crystal. Firstly, the external strains $d\varepsilon_x$, $d\varepsilon_y$,....., $d\gamma_{xy}$ are expressed relative to the 1, 2, 3 cubic axes of the crystal as $d\varepsilon_1$, $d\varepsilon_2$,....., $d\gamma_{23}$. These strains ($d\varepsilon_1$, $d\varepsilon_2$,....., $d\gamma_{23}$) are then related to the crystallographic shear strains, $d\gamma_i$ on all possible slip systems. Taylor[96] assumed that the critical shear stress is the same for all active slip systems and that they work harden at the same rate. No volume change occurs during tensile deformation and therefore $d\varepsilon_1 + d\varepsilon_2 + d\varepsilon_3 = 0$, with the result that there are only five independent relationships among the six shear strain terms. This means that to satisfy a general shape change at least five of the shear terms must be finite or rather five slip systems must be active. The equations, however, are still not solvable as there are twelve unknowns in five independent equations. To resolve this problem Taylor[96] assumed that slip would occur in such a way as to minimise the energy, $\sum(\tau_i d\gamma_i)$, expended in slip. This is equivalent to slip occurring on as few

systems as geometrically possible (i.e. 5) while the rest remain inactive (i.e. 7). In this way it is possible to solve the shear strain equations and calculate $d\gamma / d\varepsilon_x$. This was repeated for all possible combinations of five active and seven inactive systems until the lowest and correct value of $M = d\gamma / d\varepsilon_x$ was found. Although there are 792 ways of selecting five things from a group of twelve, the condition of independence imposed by Taylor[96] reduces this number to 96.

These calculations were performed for a number of orientations within the basic stereographic triangle (figure 3.32). It was found that for some orientations the same value of M was calculated for several combinations of slip systems.

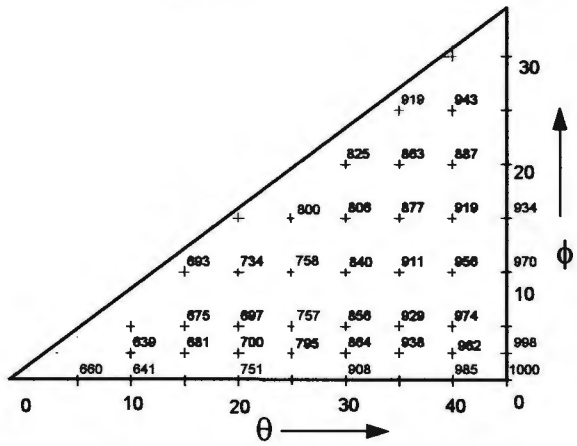

Figure 3.32: Orientation dependence of M for axisymmetric flow[105].

The method used by Taylor[96] concentrates on discovering the slip systems which can produce a specific shape change, while minimising energy expenditure. No concern is given to whether there actually exists a stress state which could physically activate the particular slip systems. **Bishop and Hill**[98,99] considered this fact when investigating plastic flow behaviour of FCC crystals and developed an alternative approach. It has a similar basis to the theory by Taylor[96] but a less complex method is used for the calculations.

Firstly, all the possible stress states that could simultaneously activate five or more slip systems, were identified. Then an appropriate stress state for a particular shape change was selected, and finally the work per unit volume, $\frac{dw}{d\varepsilon_x}$, expended by that stress state during slip was calculated:

$$\frac{dw}{d\varepsilon_x} = \sigma_1 \frac{d\varepsilon_1}{d\varepsilon_x} + \sigma_2 \frac{d\varepsilon_2}{d\varepsilon_x} + \ldots.$$

As with the analysis by Taylor[96], the value of M is calculated for various orientations and then averaged over all the orientations to find $\overline{M}$, which again is used to relate random polycrystal to single crystal behaviour. A single stress (σ_x) is assumed, and therefore the plastic strength is given by $dw/d\varepsilon_x$. Then the shear stress on each system is equated to the stresses on the cubic axes, $\sigma_1, \sigma_2 \ldots \sigma_{23}$. For example,

$$\sigma_{a1} = l_{a1}l_{I1}\sigma_{11} + l_{a2}l_{I2}\sigma_{22} + \ldots . (l_{a1}l_{I2} + l_{a2}l_{I1})\sigma_{12}$$

$$= (1/\sqrt{6})(\sigma_{22} - \sigma_{33} - \sigma_{31} + \sigma_{12})$$

Yielding will occur when $\sigma_{aI} = \pm\tau$, the critical stress for slip, so the yield criterion is given by:

$$(\sigma_{22} - \sigma_{33} - \sigma_{31} + \sigma_{12}) / (\sqrt{6}\tau) = \pm 1.$$

The yield criterion for all systems were then calculated and are listed below:

$$aI: A - G + H = \pm 1 \quad aII: B + F - H = \pm 1 \quad aIII: C - F + G = \pm 1$$

$$bI: A + G + H = \pm 1 \quad bII: B - F - H = \pm 1 \quad bIII: C + F - G = \pm 1$$

$$cI: A + G - H = \pm 1 \quad cII: B + F + H = \pm 1 \quad cIII: C - F - G = \pm 1$$

$$dI: A - G - H = \pm 1 \quad dII: B - F + H = \pm 1 \quad dIII: C + F + G = \pm 1$$

where

$$A = \frac{\sigma_{22} - \sigma_{33}}{\sqrt{6}\tau} \qquad F = \frac{\sigma_{23}}{\sqrt{6}\tau}$$

$$B = \frac{\sigma_{33} - \sigma_{11}}{\sqrt{6}\tau} \qquad G = \frac{\sigma_{31}}{\sqrt{6}\tau}$$

$$C = \frac{\sigma_{11} - \sigma_{22}}{\sqrt{6}\tau} \qquad H = \frac{\sigma_{12}}{\sqrt{6}\tau}$$

Bishop and Hill[98,99] identified 28 stress states which reach the critical value of shear stress on five slip systems without it being exceeded on any other system. All the stress states either activate six or eight slip systems simultaneously, which explains why Taylor[96] found several combinations of five systems producing the same minimum value of M. Bishop and Hill[98,99] used the principle of ***maximum virtual work*** to select which stress states would provide a particular shape change. It states that the appropriate stress state for a given shape change is the

one for which the calculated plastic work per volume, dw, is the largest, i.e. where $dw = \sigma_x d\varepsilon_x + \sigma_y d\varepsilon_y + ... + \sigma_{xy} d\gamma_{xy}$ is a maximum. The work provided by the external stresses is:

$$dw = (\sigma_1 - \sigma_3)d\varepsilon_1 + (\sigma_2 - \sigma_3)d\varepsilon_2 + \sigma_{23} d\gamma_{23} + \sigma_{31} d\gamma_{31} + \sigma_{12} d\gamma_{12}$$

where the constant volume relationship is applied, i.e. $d\varepsilon_1 + d\varepsilon_2 + d\varepsilon_3 = 0$.

From this equation M may be expressed as:

$$M = \left(\frac{1}{\tau}\right)\frac{dw}{d\varepsilon_z} = \sqrt{6}\left(-B\frac{d\varepsilon_1}{d\varepsilon_z} + A\frac{d\varepsilon_2}{d\varepsilon_z} + F\frac{d\gamma_{23}}{d\varepsilon_z} + G\frac{d\gamma_{31}}{d\varepsilon_z} + H\frac{d\gamma_{12}}{d\varepsilon_z}\right)$$

The appropriate values of M are found by substituting into this equation the values of A, B,...,H for all the 28 possible stress states and selecting the absolute largest value of M. The results are indicated in the stereographic triangle in figure 3.33.

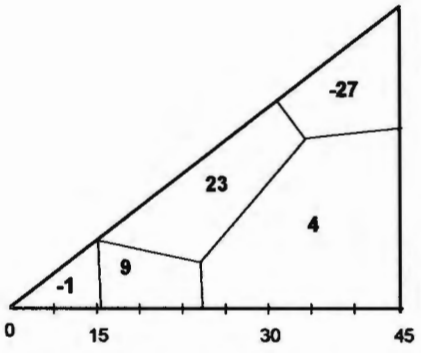

Figure 3.33: Basic orientation triangle indicating the Bishop and Hill Stress States[98,99].

Both Taylor[96] and Bishop and Hill[98,99] assumed the criterion, first suggested by von Mises, that a minimum of five slip systems must be active within a single grain for yielding to occur. Since then it has been suggested that this limitation is too extreme and that fewer systems may be operative while still maintaining strain compatibility. This forms the basis of the modified Taylor model which was first introduced by Leffers[103] and later developed by Honneff and Mecking in 1978[101]. It was proposed partly in an attempt to explain the discrepancies between stress-strain curves in tension, compression and torsion at high strains. The model suggests that once yielding has advanced such that the grains are no longer equiaxed, a partial relaxation of the Taylor criterion of equal strain throughout the material occurs. The shear strain for yielding, in a particular volume of material within the centre of each grain, is relaxed.

3.5.2 Yield Surfaces

The Bishop and Hill model[98,99] may be used to calculate upper-bound yield surfaces or loci as it assumes geometrically self consistent deformation, by assuming that all grains undergo the same shape change. In other words there is strain compatibility throughout the material. A yield surface is based on the ***yield criterion***, which is a mathematical function of the tensor stress components responsible for plastic deformation within a crystal[100,105]. In the most general form it is defined as:

$$f(\sigma_{ij}) = f(\sigma_x, \sigma_y, \sigma_z, \tau_{yz}, \tau_{xz}, \tau_{xy}) = C$$

where C is a critical value below which yielding will not occur. In the situation where the principal stress axes correspond to the x, y and z axes (i.e. $\tau_{yz} = \tau_{xz} = \tau_{xy} = 0$), the yield criterion can be written as:

$$f((\sigma_y - \sigma_z), (\sigma_z - \sigma_x), (\sigma_x - \sigma_y)) = C,$$

This expression can be graphically represented as a yield surface in principal stress space as a cylinder, indicated in figure 3.34(a).

With no sample symmetry the general yield criterion has six stress components and therefore would require six-dimensional stress space for complete representation. The dimensions and extent of a yield locus are significantly simplified by considering symmetry[104]. For example, as mentioned previously, when the principal stress axes coincide with the sample symmetry ($\tau_{yz} = \tau_{xz} = \tau_{xy} = 0$), a three dimensional cylinder is sufficient for representation. Often two slices or sub-spaces of the three dimensional cylinder are shown, namely the plane of zero hydrostatic stress, also called the π-plane (figure 3.34c); and the $\sigma_z = 0$ plane (figure 3.34b). As mentioned previously, the latter representation was used for the yield surfaces of the current plastic analysis. The π-plane represents the projection of the normal stresses on the deviatoric plane such that the vectors for the diagonal components of the stress tensor form a set of coplanar axes 120° to each other.

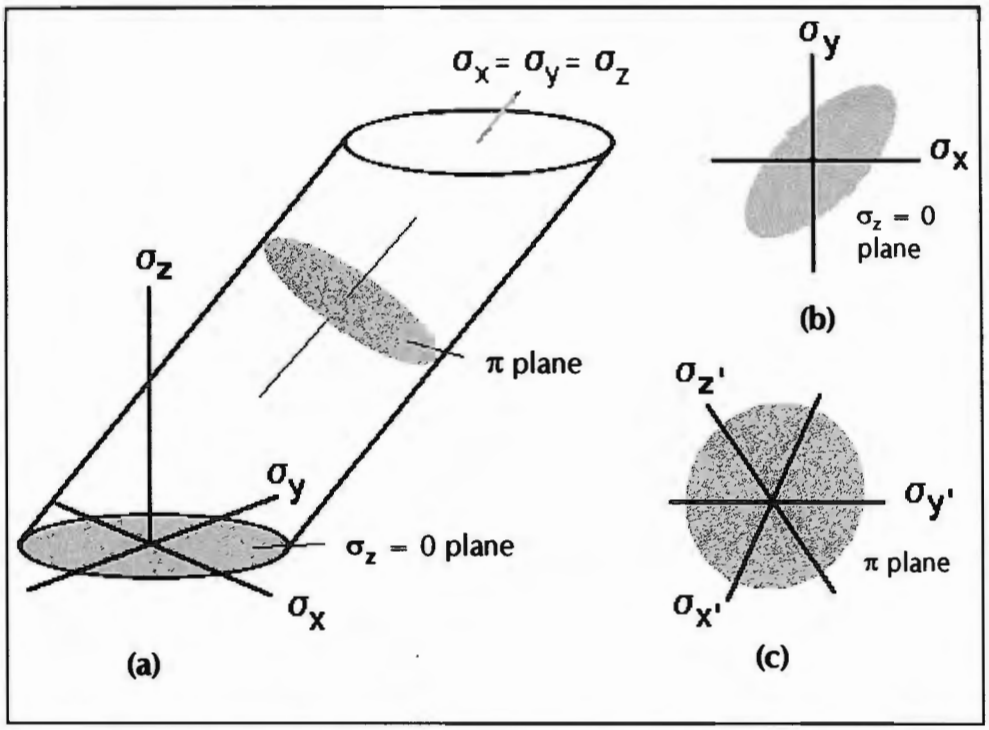

Figure 3.34 (a) A three dimensional yield locus. (b) two dimensional $\sigma_z = 0$ plane (c) two dimensional π plane[105].

A material property that can influence the yield criterion is the isotropy or crystallographic texture of a material. To be isotropic a polycrystalline material must have a random texture and this will result in isotropic yielding during deformation. Thus, if a material does possess a preferred orientation, anisotropic effects during yielding will distort the shape of the yield surface. During a tensile test of a specimen with a non-random texture, often different strains levels are observed in the width and thickness directions of the specimen. A measure of the anisotropy is the Lankford strain ratio, *r*, which is the ratio of the strain experienced in the width direction, $d\varepsilon_w$, and the strain in the thickness direction, $d\varepsilon_t$[105]:

$$r = \frac{d\varepsilon_w}{d\varepsilon_t}$$

If $r = 1$, isotropic yielding is expected during deformation. Therefore, the further the deviation from this value the greater the anisotropy experienced by the specimen during yielding. Assuming that the yield criterion, $f(\sigma_{ij})$, is proportional to the plastic potential, the ***principal of normality*** (or flow rule) relates the Lankford strain ratio to the yield criterion, and can be expressed as

$$d\varepsilon_{ij} = d\lambda \left(\frac{\partial f(\sigma_{ij})}{\partial \sigma_{ij}} \right)$$

where $f(\sigma_{ij})$ is the yield function and $\partial\lambda$ is a scalar value. Graphically this means that the ratio of the strains can be portrayed as a vector normal to the yield locus at the particular stress state. Thus the ratio of the strains ε_x and ε_y is equivalent to the ratio of the components of the vector parallel to the σ_x and σ_y axes. In two dimensions this is expressed as:

$$\frac{d\varepsilon_x}{d\varepsilon_y} = -\frac{\partial \sigma_y}{\partial \sigma_x},$$

where $\partial\sigma_y / \partial\sigma_x$ is the slope of the yield locus. This has the result that a yield surface cannot be outwardly concave at any point, only convex or have straight edges. The stresses along the edges will all produce the same shape change, while the stress state at a corner will be able to yield many shape changes (figure 3.35).

Despite the fact that the Taylor[96] and Bishop and Hill[98,99] analyses were initially devised for random polycrystals, they can also be used to explain the properties of anisotropic materials. The procedure for calculating a yield locus for a single crystal under biaxial straining, (σ_x, σ_y) is as follows:

Step 1: Assume several external shape changes, $d\varepsilon_x, d\varepsilon_y, d\varepsilon_z$.

Step 2: Transform these strains onto the crystallographic axes. (i.e. calculate $d\varepsilon_1, d\varepsilon_2, d\varepsilon_3, d\gamma_{23}, d\gamma_{31}, d\gamma_{12}$. in terms of external strain).

Step 3: Use the Bishop and Hill[98,99] analysis to find the appropriate stress states A, B,...,H which will support these shape changes. In other words identify the stress states for which work expended, *dw*, is a maximum.

Step 4: Transform these stresses back onto external co-ordinate system.

Following this, the corresponding stress values for the appropriate stress states can be plotted on a graph of σ_y *vs* σ_x or, as the case of the LApp output, σ_y/τ *vs* σ_x/τ.

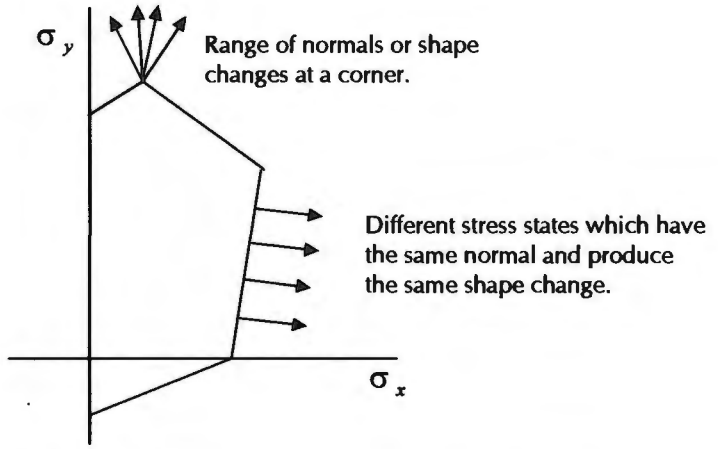

Figure 3.35: Shape changes at corners and straight edges[105].

If a polycrystal contains more than one preferred orientation, the yield surface is found by averaging the yield behaviour of the individual components. Whereas the yield locus for a single crystal (figure 3.36) will always be bounded by straight sides, the number of corners and straight edges in a locus for a polycrystal increases with the number of orientations considered. The yield locus of a polycrystal will be approximated by a smooth curve only when a very large number of orientations are present.

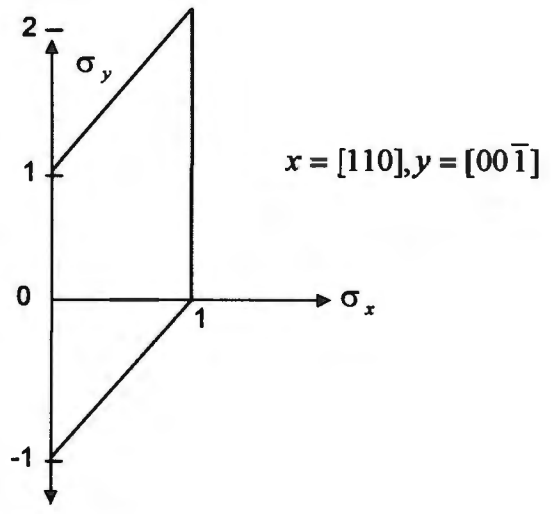

Figure 3.36: Yield locus for a single crystal[105].

3.6 Finite Element Modelling

Modelling procedures utilising the microtexture data from the stainless steel samples were performed using routines in ABAQUS software. The spatially related yield information was used to simulate the plastic behaviour of the stainless steel under uniaxial tension. The aim was to use the predicted plastic yield behaviour on a small scale (texture windows) to simulate the macroscopic flow behaviour of the material by employing a finite element modelling approach. The calculated r-values and Taylor factors, of the laboratory rolled steel and the commercial steel across the transverse section, were incorporated into a finite element mesh in such a way as to maintain the texture window arrangement. The mesh was deformed to 10% strain by applying a uniform prescribed displacement to one end of the specimen while keeping the opposite end fixed. Strain hardening was incorporated using a simple power law relationship with a strain hardening exponent of 0.2. The boundary conditions on each end of the mesh were varied to prevent distortions and rotation of the specimen during straining. The table below outlines the various FEM experiments performed using the stainless steel yield data.

Table 3.6: FEM Experiments performed using stainless steel yield data.

Exp.	Yield Data	Direction of strain	Microstructural component (mm)	Total specimen size (mm)	Arrangement of components
1	C430	RD	0.13 x 1 x 20	0.8 x 10 x 20	Layered and Mirrored
2	C430	RD	0.13 x 1 x 20	0.8 x 10 x 20	Layered and Random
3	C430	RD	0.13 x 1 x 5	0.8 x 10 x 20	Layered and Random
4	C430	RD	0.13 x 1 x 5	0.8 x 10 x 10	Layered and Random
5	C430	TD	0.13 x 1 x 5	0.8 x 25 x 15	Layered and Random
6	Homog.	RD	0.13 x 12 x 20	0.8 x 10 x 20	Layered
7	D1	RD	0.20 x 1 x 5	0.8 x 12 x30	Random
8	D3	RD	0.20 x 1 x 5	0.8 x 12 x30	Random

An elastic-plastic analysis was performed on the mesh using a Hill-type anisotropic constitutive model implemented in the ABAQUS software. The anisotropic stress ratios which are needed for the model were calculated from

the Lankford strain ratios for each texture window. See Appendix C for an explanation of the method used to calculate the stress ratios.

3.6.1 Experiments on the Commercial Stainless Steel

To maintain the through-thickness properties of the material, the yield information was inserted into the model in layers, corresponding to the upper three layers of reduced sections of the microtexture data. The fourth layer was below the centre line of the sheet and therefore was not included in the FEM experiments. For sample C430, fifteen microstructural components were devised where each component was assigned data specific to a reduced window.

As an initial experiment (Exp.1), the microstructural components (0.13 mm x 1 mm x 20 mm) (ND x TD x RD) were extended continuously in the RD across the entire specimen (0.8 mm x 10 mm x 20 mm). The yield information from the transverse section of the microtexture samples was thus extrapolated in the rolling direction. In view of the expected symmetry of the material, the layers of microstructural components were mirrored across a central plane, as indicated in figure 3.37. Each component consisted of 100 elements which provided a total of 6000 elements for the complete mesh. (The total number of elements was kept constant for all the experiments). Boundary conditions were implemented such that on each end of the mesh three nodal point constraints were applied, preventing movement in the three principal directions. One point on the left and right sides of the mesh and the third in the centre (repeated at each end). See figure 3.37. A strain of 10% was applied in the RD and the development of surface roughness and specimen thinning were monitored.

The result of this simulation indicated that some rotation of the specimen occurred about the RD and that through-thickness thinning (ND) appeared at areas of low strain ratio. For this reason the experiment was repeated (Exp.2) without the mirror symmetry and instead the components of yield data were distributed randomly throughout each layer. After 10% strain, a degree of transverse bending of the specimen was visible producing a concave and convex effect.

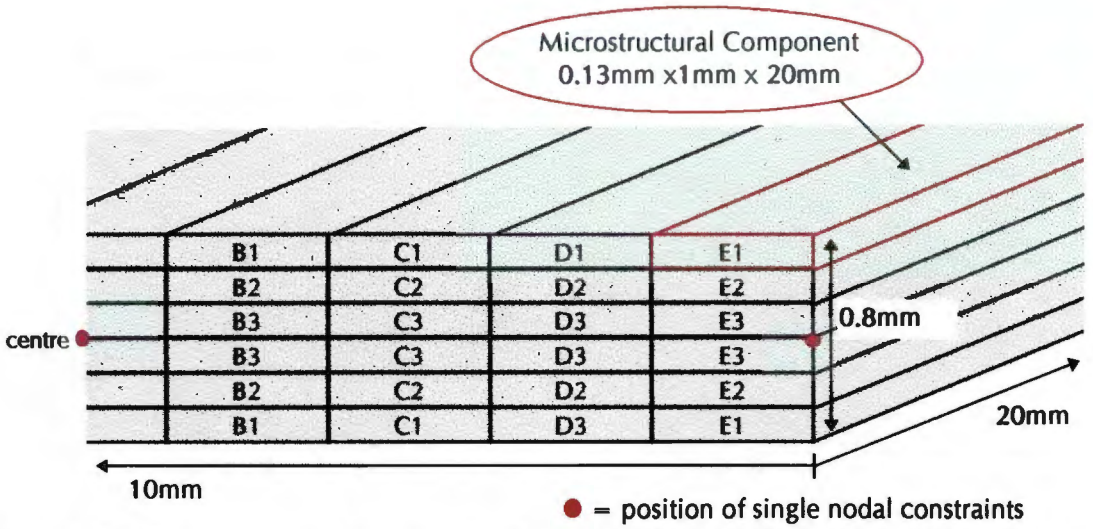

Figure 3.37: Mirrored layered arrangement of microstructural components for the commercial steel simulations. (Division of elements not shown).

Following this, a number of experiments were implemented in which the boundary conditions were varied in order to establish the effect of end constraints on deformation behaviour. Eventually after more than six variations it was concluded that the displacement of the specimen is the least affected when a full boundary constraint is applied. In other words, when the entire node set on each end of the mesh is constrained in the three principal directions, and therefore this condition was used for the remaining experiments.

An analysis of the texture maps for the rolling plane section of the commercial steel indicated the presence of extended bands of preferred orientation running for a few millimetres in the RD. Therefore, to allow for a more accurate approximation of the actual microstructure, the components of the FEM experiment were shortened to 5 mm in the RD (Exp.3, figure 3.38). The specimen now consisted of the 15 microstructural components, of new dimension 0.13 mm x 1 mm x 5 mm, distributed randomly within each layer. The total specimen size remained 0.8 mm x 10 mm x 20 mm with the components repeated (not mirrored) across a central plane.

To further investigate the influence of the boundary conditions on the deformation behaviour, the specimen length was reduced to 10 mm (Exp.4) and subjected to 10 % strain in the RD. In addition, a simulation using the commercial steel yield data was performed by rearranging the microstructural

components such that elongation could be applied in the transverse direction (Exp.5). The size of the microstructural components remained the same, while the overall mesh dimensions were altered to 0.8 mm x 25 mm x 15 mm. The information was again maintained within each layer and the texture components were arranged randomly.

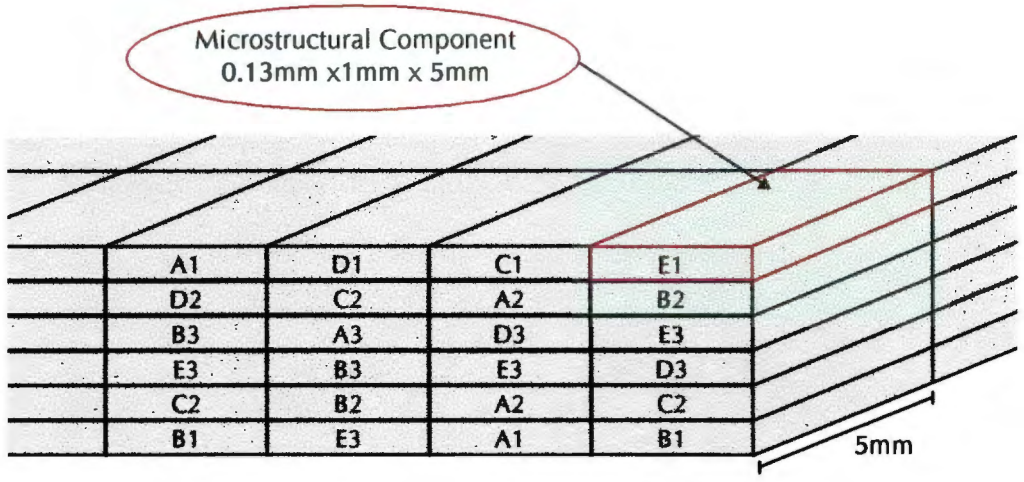

Figure 3.38: Random layered arrangement of microstructural components for the commercial steel simulations.

For comparative purposes, a simulation was performed on a specimen possessing homogeneous properties (Exp. 6). An average value of the yield properties within each layer was calculated and subsequently assigned to the elements within that layer (figure 3.39).

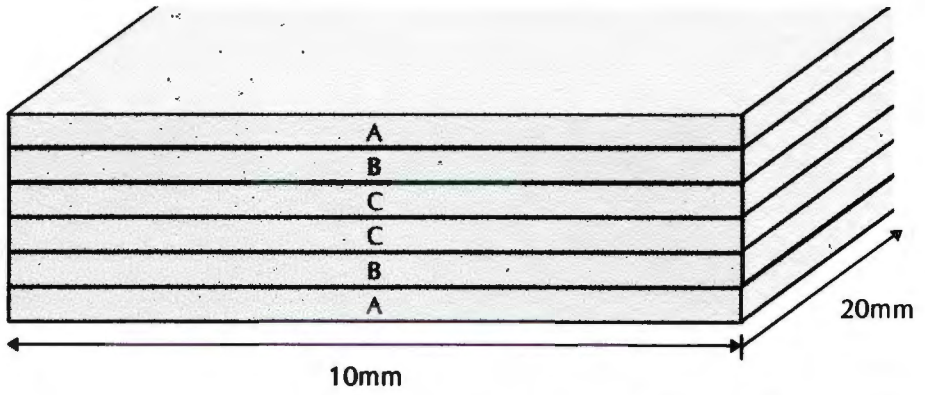

Figure 3.39: Homogeneous distribution of yield properties within each layer of the specimen.

3.6.2 Experiments on the Laboratory Rolled Stainless Steel

For the two laboratory rolled samples, namely D1 and D3, a total of 24 microstructural components were devised, measuring 0.2 mm x 1.0 mm x 5.0 mm, where each component corresponded to a reduced texture window of the transverse microtexture data. These components were arranged randomly in a mesh measuring 0.8 mm x 12 mm x 30 mm, ensuring a constant volume of each component (figure 3.40). No repetition across the centre line was imposed and a total displacement of 10% was applied to both specimens in the RD.

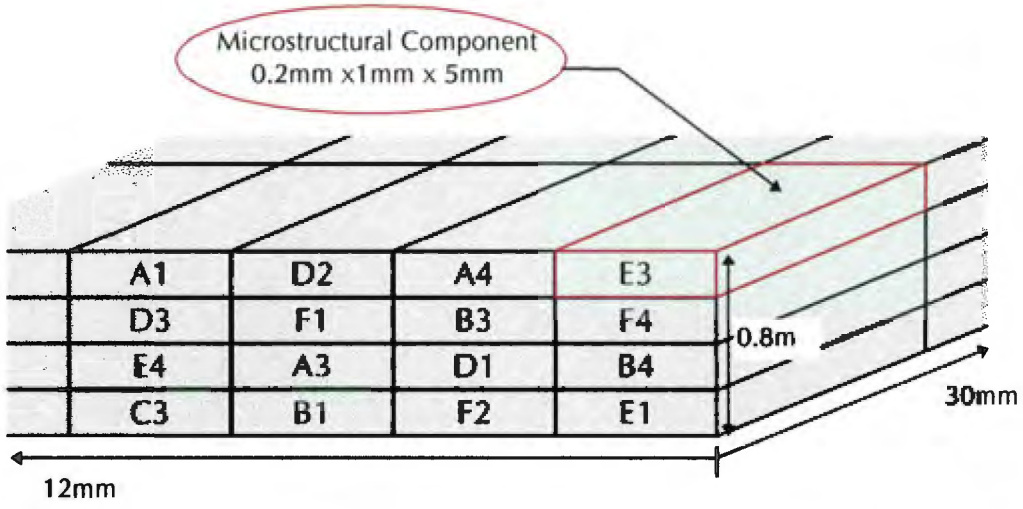

Figure 3.40: Random arrangement of microstructural components in samples D1 and D3.

After straining, the surface topography of all the specimens was assessed by plotting on a contour diagram the displacement in the ND (U3). Changes in specimen thickness across the transverse plane were evaluated by constructing transverse surface profiles at set intervals along the specimen length. Comparisons could thus be made as to variations in the specimen thickness and strain distribution for each experiment. The stress distribution within the specimens after straining was also analysed. A contour plot of the stress distribution in the transverse direction for each layer of the specimens was constructed. This allowed a visual assessment of the distribution of transverse stress within each layer of the specimens.

CHAPTER 4

RESULTS OF THE COMMERCIAL STAINLESS STEEL

4.1 MICROSTRUCTURE

Electron channelling contrast images of the commercial steel (C430) samples acquired using the SEM are shown in figures 4.1 to 4.3. The images illustrate the microstructure across the longitudinal, transverse and rolling plane sections of the material in the cold rolled-annealed condition. The grain structure is approximately equiaxed across all three sections with only limited elongation of the grains in the RD. A distinct increase in grain size, however, is visible extending from the surface towards the centre of the sample. The microstructure through the thickness of the sample can be divided into two regions of fine and coarse grains. The finer grained region extends for about 200 μm from the surface towards the centre and possesses an average grain size of 8.0 μm, while the coarse grains extend for the remaining 150 μm to the centre line. The average grain size in the coarse region is 13 μm and the grains are more elongated in the RD compared to the finer surface regions.

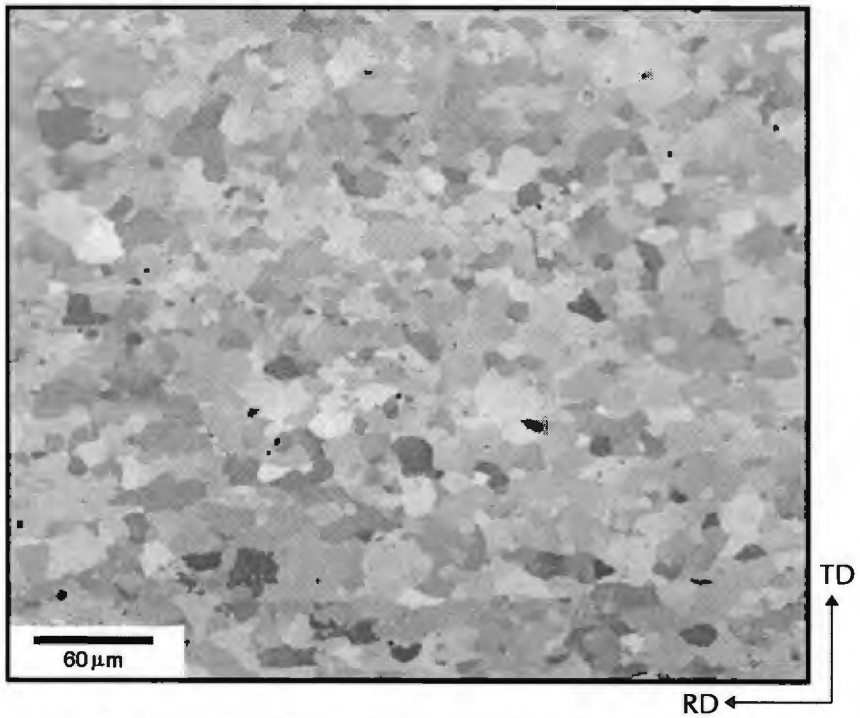

Figure 4.1: Rolling plane section of the commercial stainless steel using ECC.

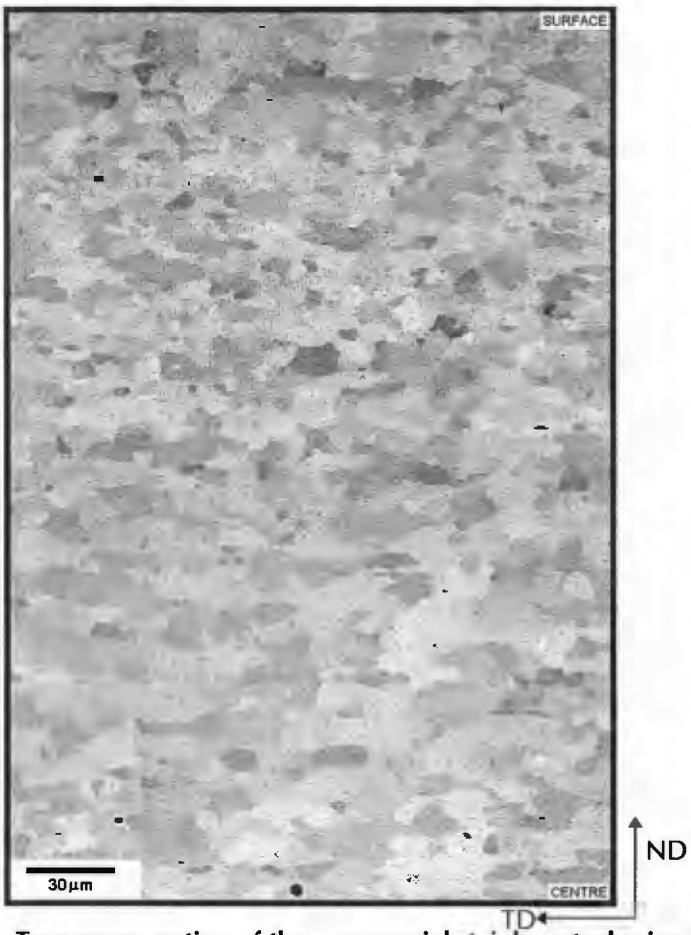

Figure 4.2: Transverse section of the commercial stainless steel using ECC.

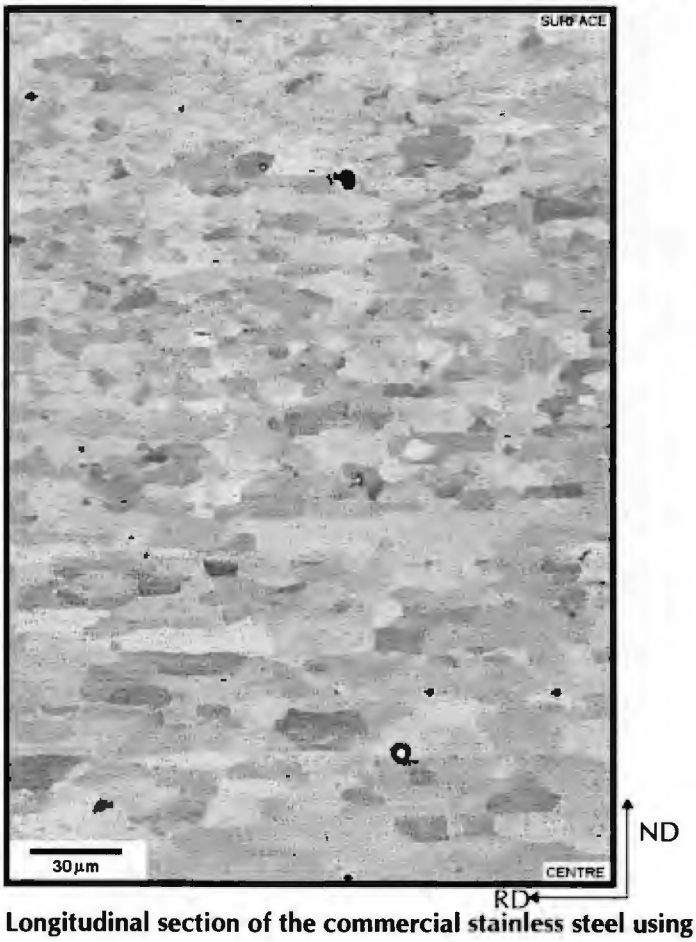

Figure 4.3: Longitudinal section of the commercial stainless steel using ECC.

4.2 Ridging Analysis

A visual examination of the commercial steel tensile specimen after 20% elongation in the RD indicates the presence of severe surface roughening. The roughness can be characterised as continuous ridges in the RD which extend across the entire length of the specimen. Figures 4.4 and 4.6 illustrate the three-dimensional contour and two-dimensional topography maps respectively of the upper and lower surfaces of the specimen. The ridges persist across the length of the measured area and are visible on both the upper and lower surfaces. From these images a ridging wavelength of between 1.5 mm and 2.0 mm can be identified. The surface profile measurements, along the lines indicated on the 2D plot, are shown in figure 4.5(a). The image clearly illustrates the corrugated nature of the tensile specimen. The lower traces have been reversed about the horizontal line to provide a correct view of the through-thickness profile. The undulations of the upper surface match those of the lower surface and no major variations in specimen thickness have occurred across the measured profile. Besides the corrugations, the surface of the sample appears fairly smooth with limited roughening on a scale of the grain size.

The tensile specimens with varying gauge lengths elongated in the RD provide an interesting result. A visual assessment suggests that both the ridging height and the frequency of the ridges decreases with a decreasing gauge length. The specimens possessing gauge lengths of 10 mm and 15 mm show only slight corrugations while the specimens with gauge lengths of 45 mm and 55 mm indicate severe corrugations extending in the RD. This can be confirmed by examination of the surface maps of the tensile specimen with a gauge length of 25 mm, illustrated in figures 4.7 and 4.9. By comparison of these images with the same plots for the specimen possessing a gauge length of 55 mm (figures 4.4 and 4.6), it is possible to verify that the continuity of the corrugations, as well as their frequency, has decreased with decreasing gauge length. Also, the surface profile measured on the 25 mm gauge length specimen confirms the decrease in height and regularity of the corrugations (figure 4.9).

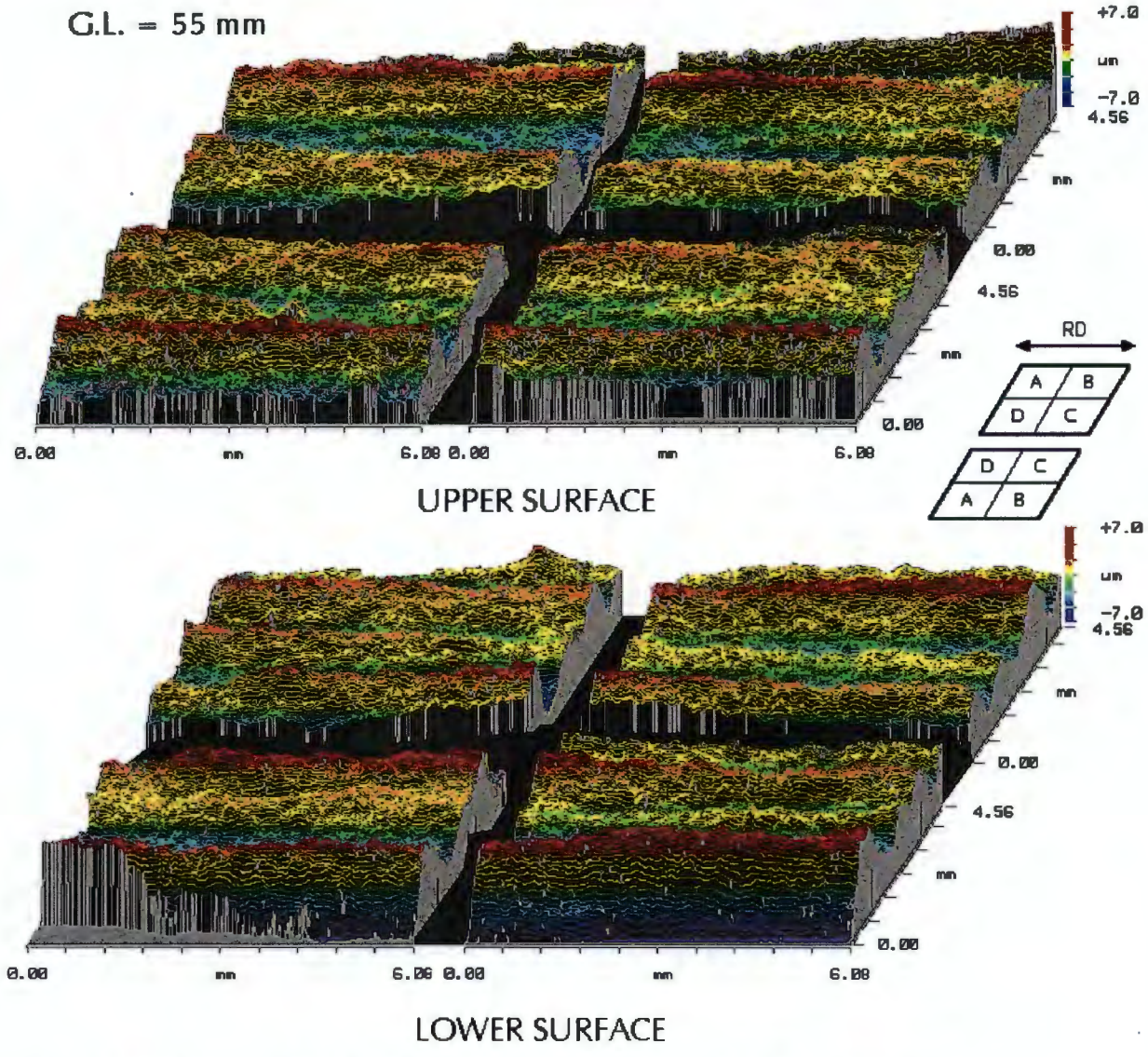

Figure 4.4: 3D topography map for the upper and lower surface for tensile specimen elongated in the RD (GL = 55mm).

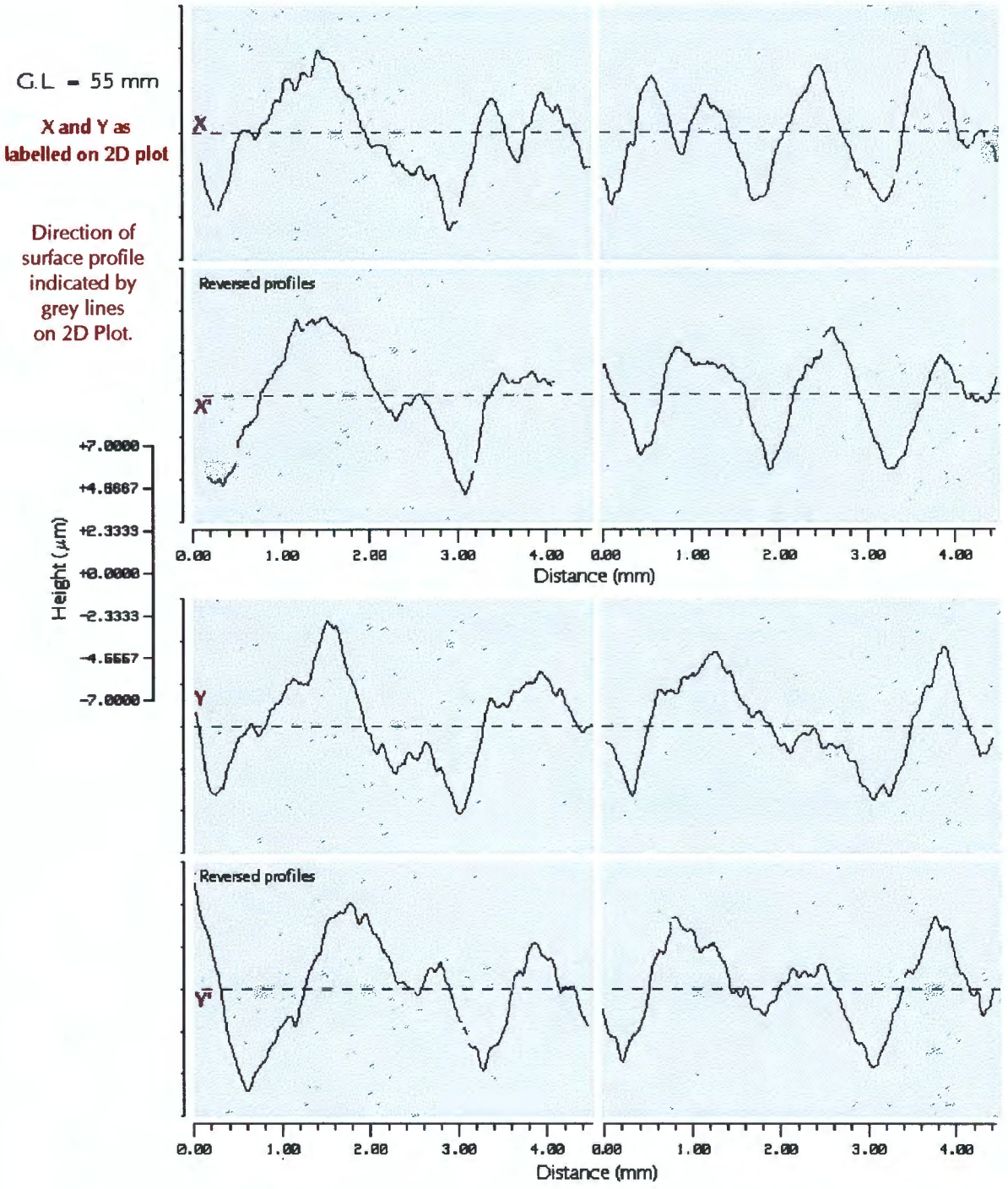

Figure 4.5: Surface profiles for tensile specimen elongated in the RD (GL = 55mm).

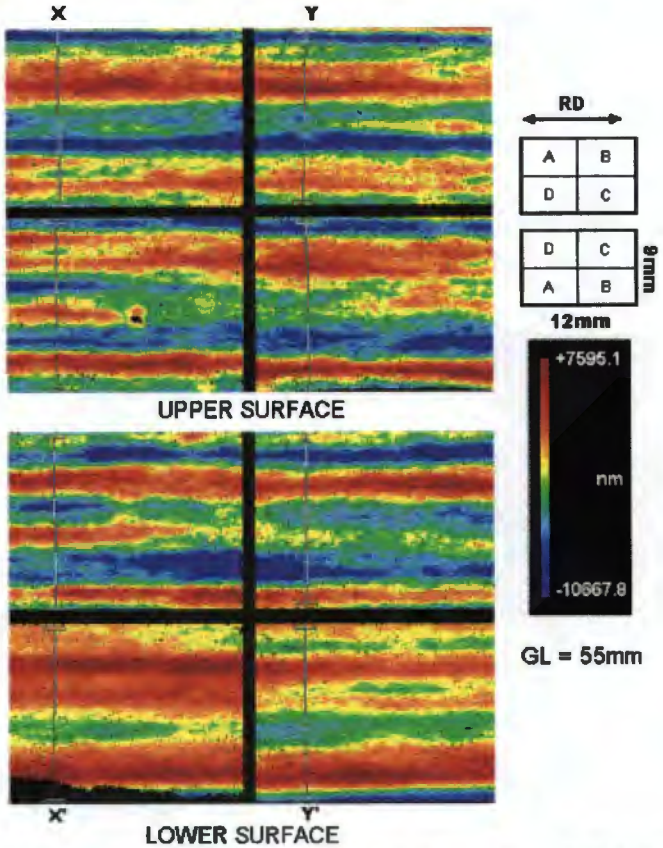

Figure 4.6: 2D Contour plot for the upper and lower surface for the tensile specimen elongated in the RD (GL = 55mm).

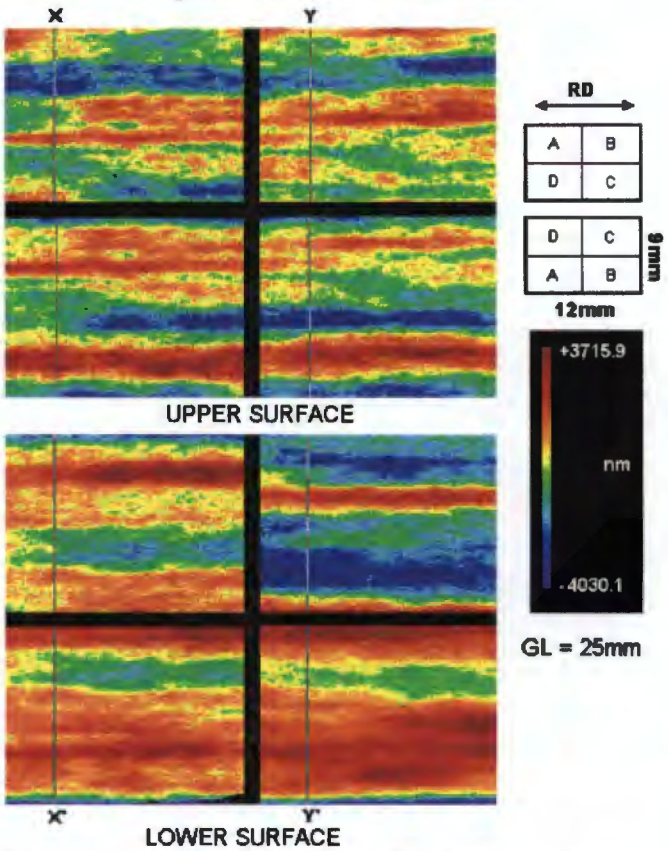

Figure 4.7: 2D Contour plot for the upper and lower surface for the tensile specimen elongated in the RD (GL = 25mm).

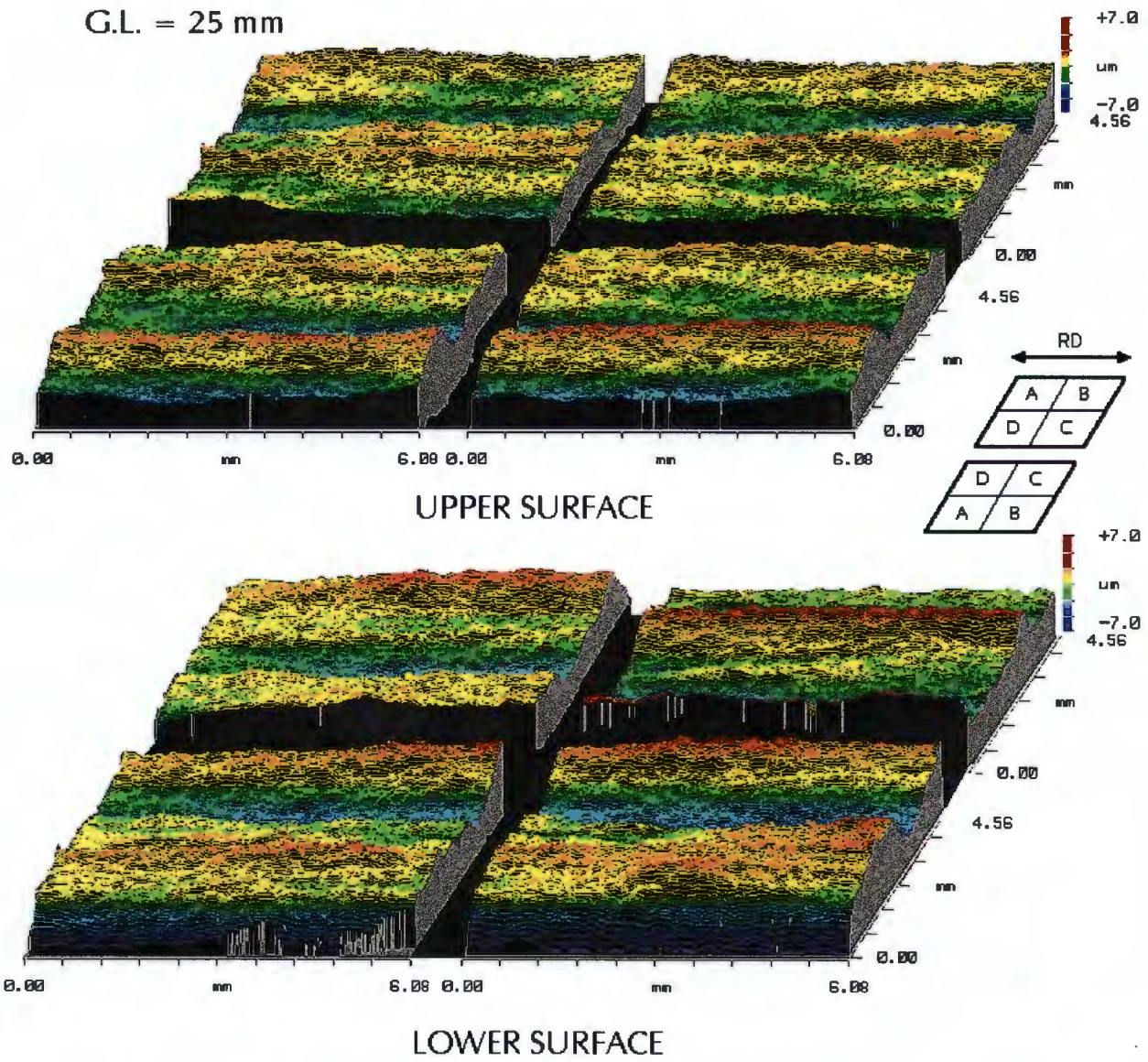

Figure 4.8: 3D topography map for the upper and lower surface for tensile specimen elongated in the RD (GL = 25mm).

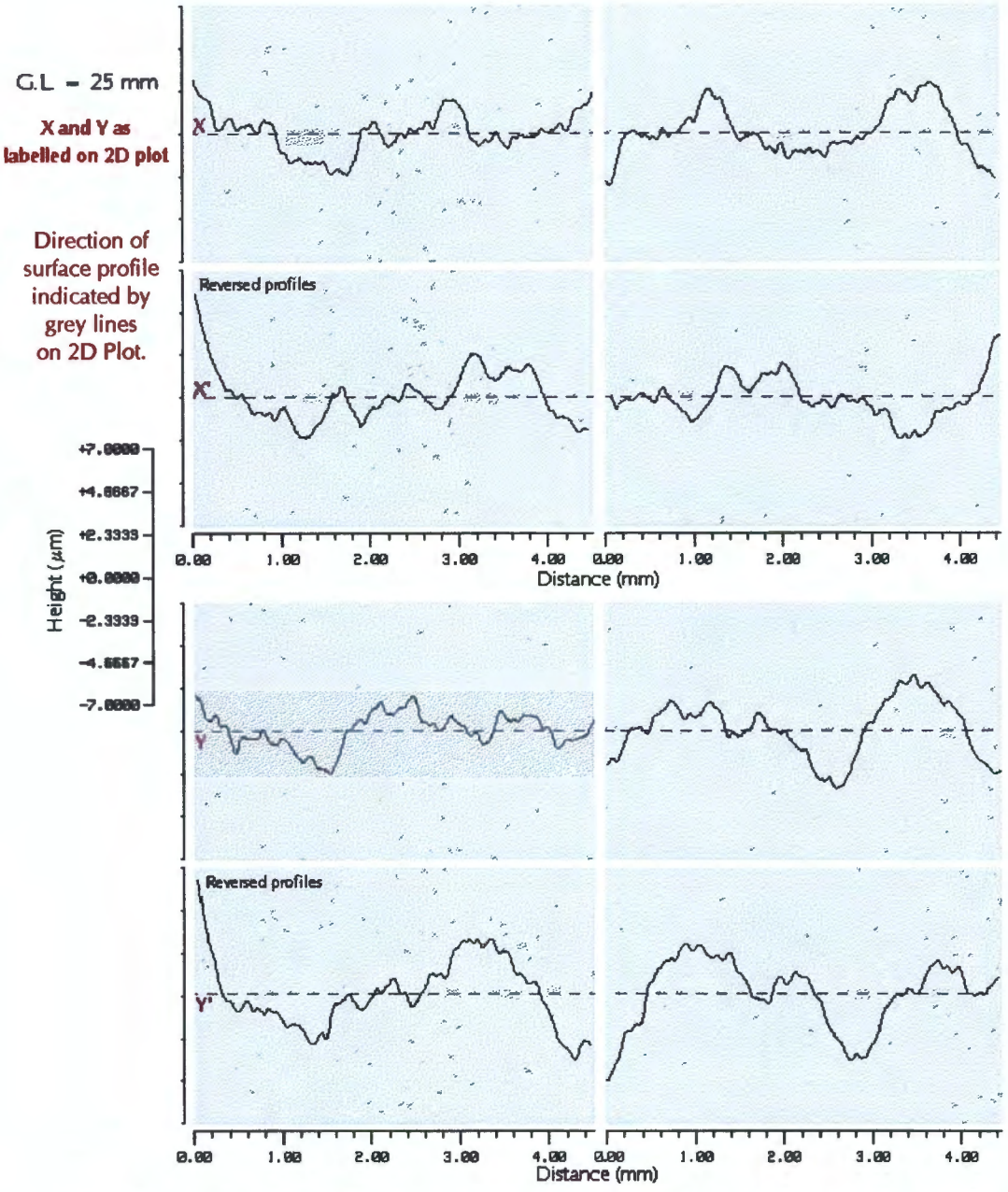

Figure 4.9: Surface profiles for tensile specimen elongated in the RD (GL = 25mm).

The tensile specimen elongated in the TD demonstrates a marked difference in surface topography compared to the RD-tensile axis specimens. From the contour plot (figure 4.10) and topography maps (figure 4.11) of the upper and lower surfaces of this sample, it is clear that no major surface roughening has occurred. Despite a slight streaking evident in the RD and a very fine surface roughening on a scale of the grain size, the surface is homogeneous and free of corrugations. The fine grain scale roughening effect is evident from the surface

plots, as well as from the line profiles for the upper and lower surfaces which are shown in figure 4.12, along with a surface profile of the same length from the sample elongated in the RD. The difference in surface topography for the two tensile directions is clearly evident.

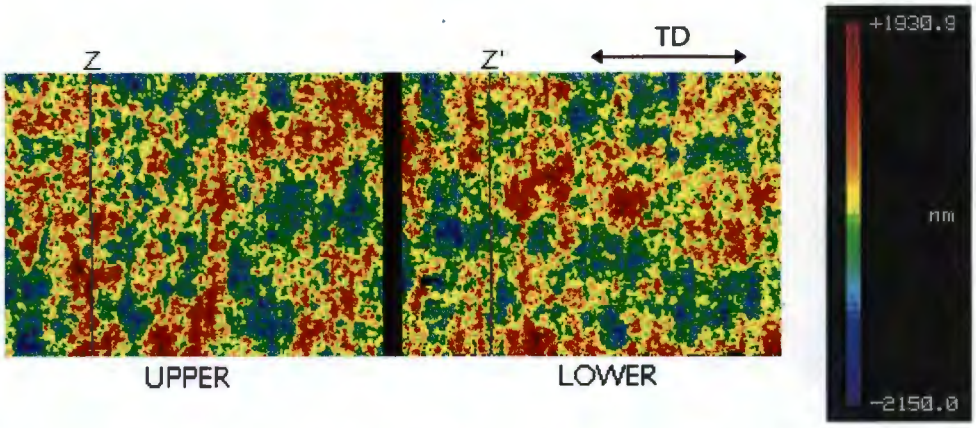

Figure 4.10: 2D Contour plot for the upper and lower surface for the tensile specimen elongated in the TD (GL = 55mm).

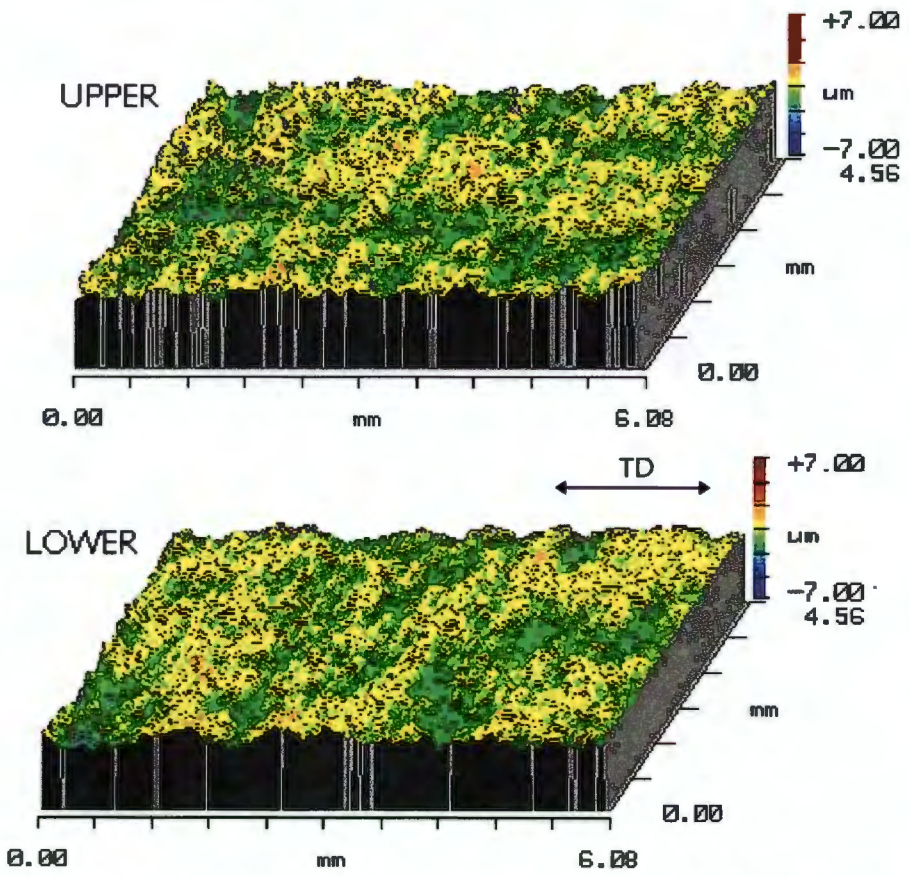

Figure 4.11: 3D Topography map for the upper and lower surface for the tensile specimen elongated in the TD (GL = 55mm).

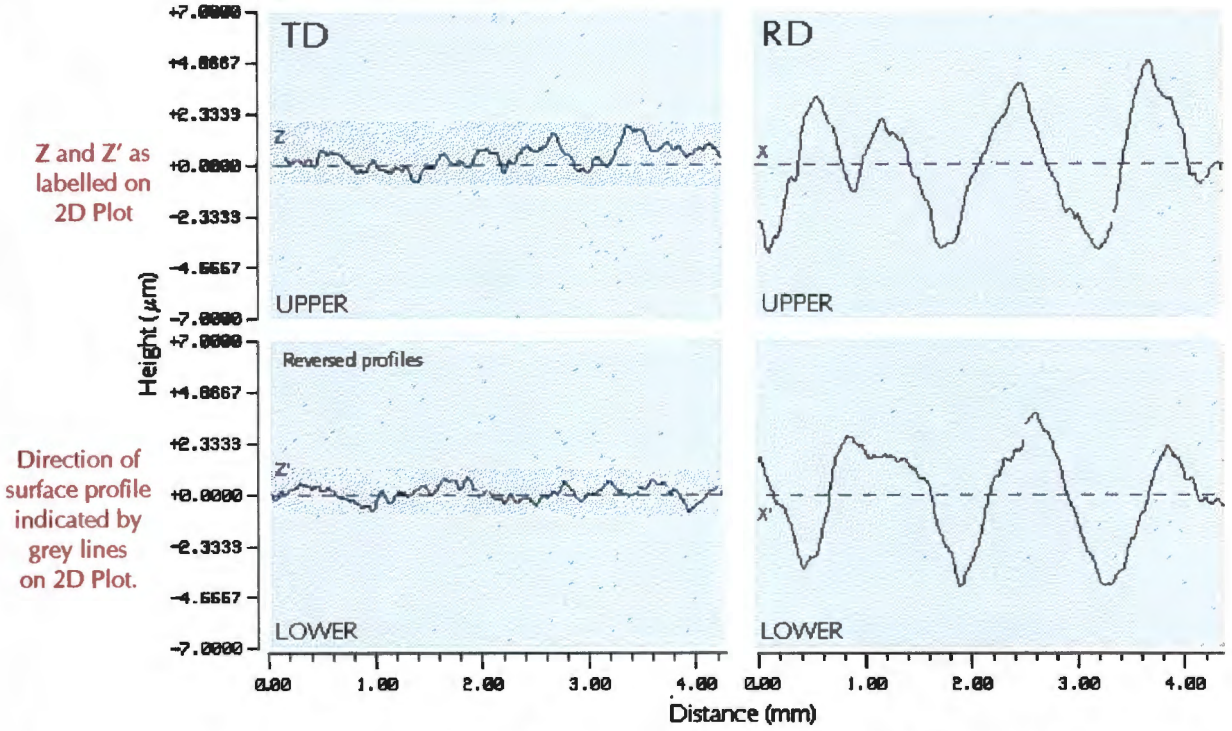

Figure 4.12: Surface profiles for tensile specimen elongated in the TD and RD (GL = 55mm).

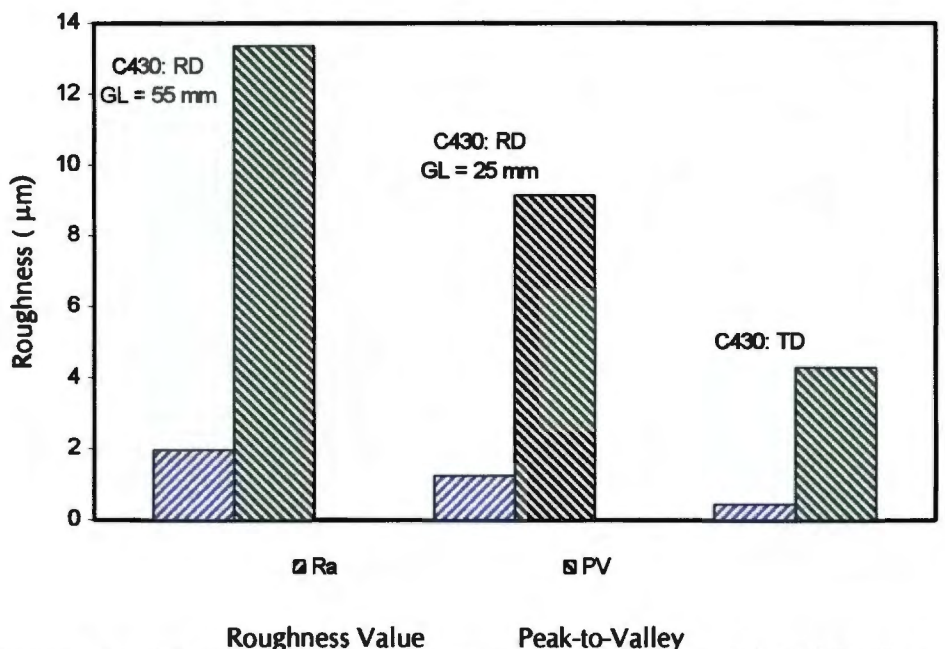

Figure 4.13: Surface roughness measurements of the commercial steel tensile samples elongated in the TD and RD.

The graph of average roughness and peak-to-valley measurements shown above indicates a decrease in roughness with a reduction in gauge length, as well as a further decrease in the measured values for specimens elongated in the TD. An

Ra value of 1.95 μm and PV value of 13.55 μm is evident for the specimen deformed in the RD. The measurements decreased significantly to 1.22 μm and 9.12 μm respectively for the specimen with a reduced gauge length of 25 mm, and again to 0.43 μm and 4.26 μm for the specimen elongated in the TD. These results are in agreement with the visual assessment of the tensile specimens.

Severe corrugations are also visible for the sample which had been reduced to half its thickness by machining and elongated in the RD. The specimen is shown together with the unreduced specimens elongated in the rolling and transverse directions in figure 4.14. The frequency of the corrugations on the reduced specimen is higher than those on the unreduced specimen.

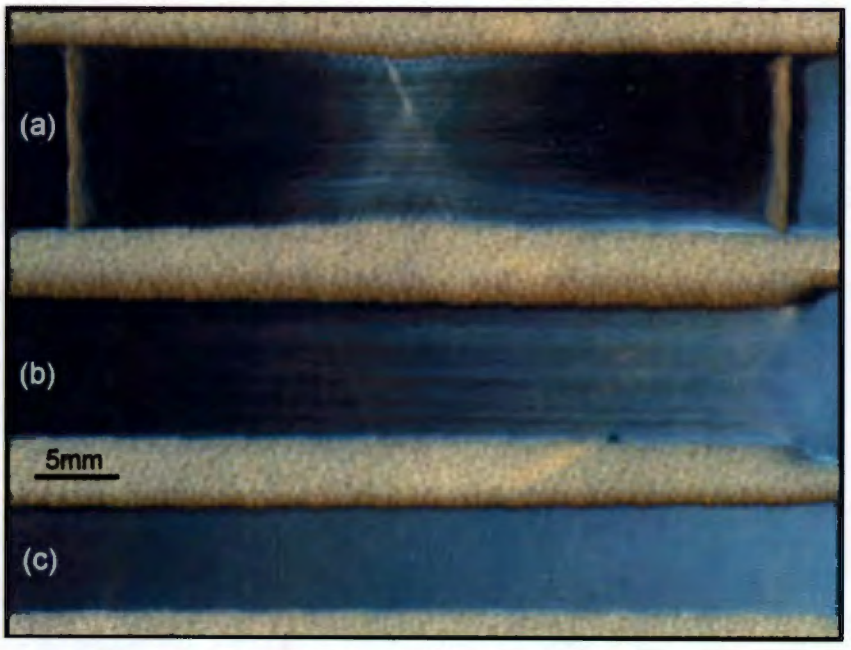

Figure 4.14: Tensile specimens of commercial stainless steel: (a) Thickness reduced to half from both sides, tensile axis // RD (b) Unreduced thickness, tensile axis // RD (c) Unreduced thickness, tensile axis // TD.

Table 4.1 indicates the average roughness and peak-to-valley values for those tensile tests which were subjected to surface characterisation, as well as a summary of the ridging behaviour of all the commercial steel tensile samples.

Table 4.1: Results of tensile tests performed on the commercial stainless steel.

Test Direction	Ra (μm)	PV (μm)	Corrugations	Frequency of Corrugations
RD: GL 55 mm	1.95	13.35	Severe	High
RD: GL 45 mm	—	—	Severe	High
RD: GL 35 mm	—	—	Moderate	Medium
RD: GL 25 mm	1.22	9.12	Moderate	Medium
RD: GL 15 mm	—	—	Shallow	Low
RD: GL 10 mm	—	—	Shallow	Low
TD: GL 55 mm	0.43	4.26	None	(Streaking in RD and fine roughness)
RD: GL 40 mm (Reduced)	—	—	Severe	Very high, increased relative to unreduced sample with GL=45mm

GL = Gauge Length

4.3 MICROTEXTURE

Transverse Section

Examination of the discrete orientation plots, derived from the microtexture data for the transverse and rolling plane sections, allowed the identification of the principal preferred orientations. As mentioned in the experimental methods, the variation in point size on the polar plots corresponds to a variation in grain size in the material. In each window across the transverse section, the γ-fibre texture can be identified as the main component of sample C430 with clustering around both components, namely {111}<112> and {111}<110>. Little variation, however, exists in principal texture components from window to window across the section. A large number of randomly orientated grains are also present within each window which ensures that the overall texture remains moderate. The lack of variation in texture distribution on a scale of the texture windows is demonstrated by the similarity in the polar plots from two texture windows of sample C430 presented in figures 4.15 and 4.16 (using Bunge notation). A plot of common ideal BCC orientations has been included as a reference (figure 4.17).

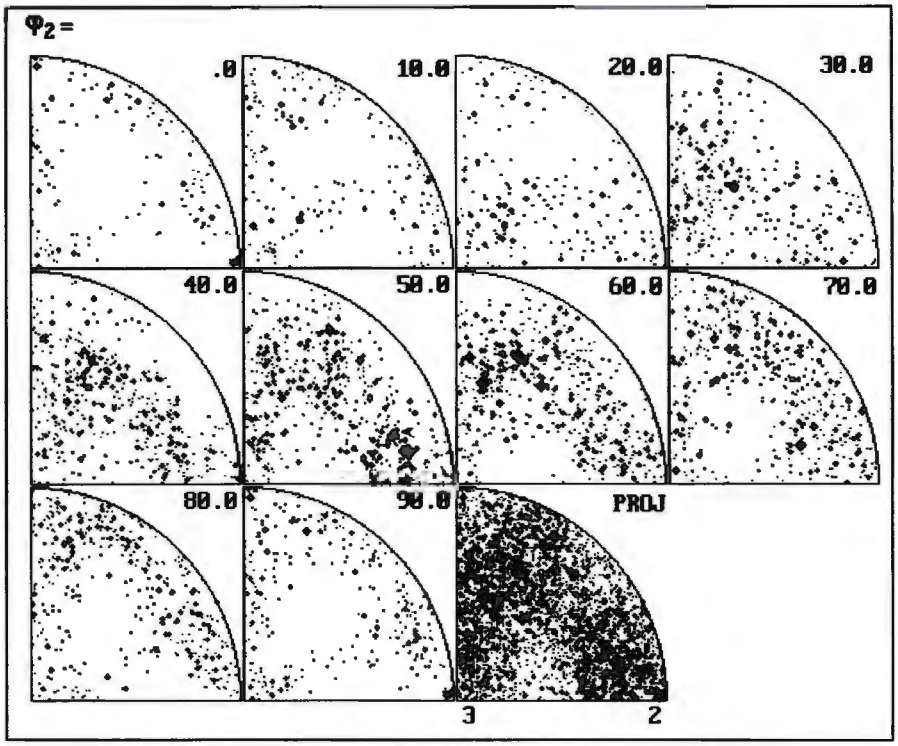

Figure 4.15: Polar plot of orientations for a single texture window of the commercial steel transverse section.

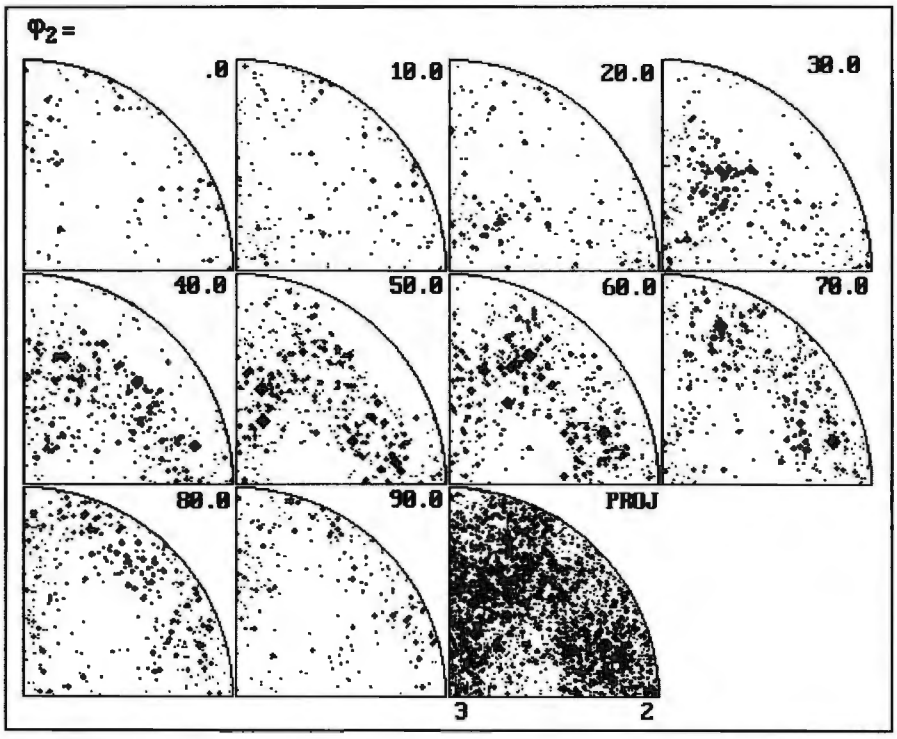

Figure 4.16: Polar plot of orientations for a different texture window of the commercial steel transverse section.

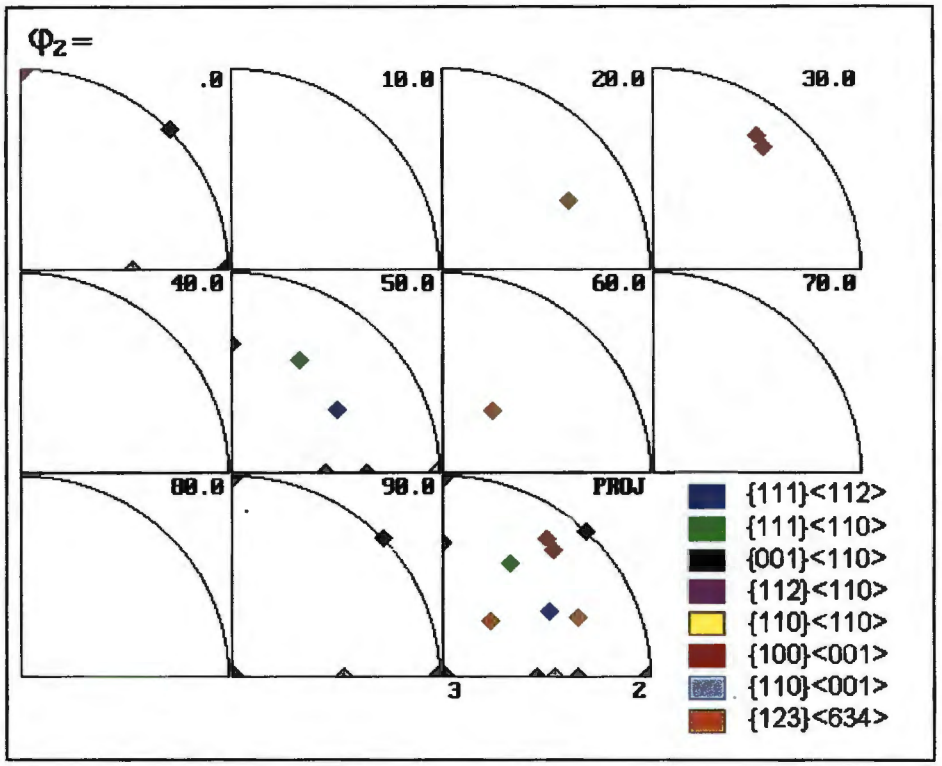

Figure 4.17: Polar plot of common ideal BCC textures.

Division of each of the texture windows into four equal sections through-the-thickness allowed a more accurate specification of the principal texture components. A variation in preferred orientation and grain size is visible extending from the centre to the near surface region of the sheet. A strong $\{111\}<110>$ texture is evident at the centre of each texture window which incorporates most of the large grains within each window. Figures 4.18 and 4.19 illustrate the texture components representative of the near surface and central regions respectively. Identification of the texture components near the surface is hindered by the overall weaker texture and the reduction in grain size; nevertheless, it is possible to identify orientations spread mainly along the γ-fibre, with traces of the cube texture.

The orientation image or texture map for the transverse section of the commercial steel, which was constructed using colour mapping in Euler space, is presented in figure 4.21. The image represents a collage of the texture maps for the five texture windows across the section and provides a total measured area of 300 μm (ND) x 5000 μm (TD). A key for the identification of the textures is given in figure 4.20.

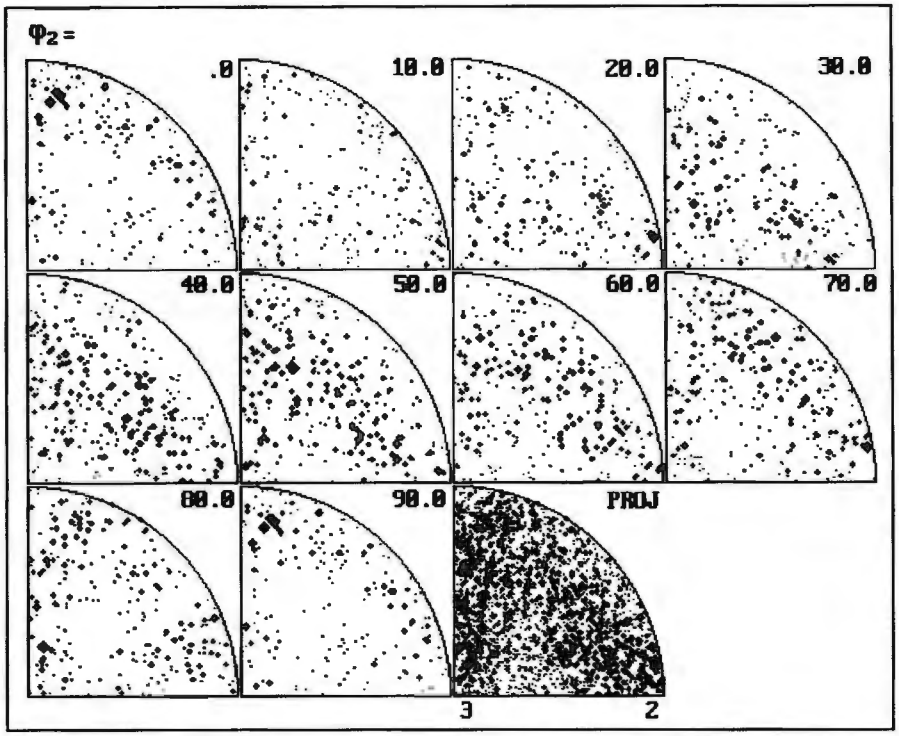

Figure 4.18: Polar plot of orientations representative of the near surface region of the commercial steel transverse section.

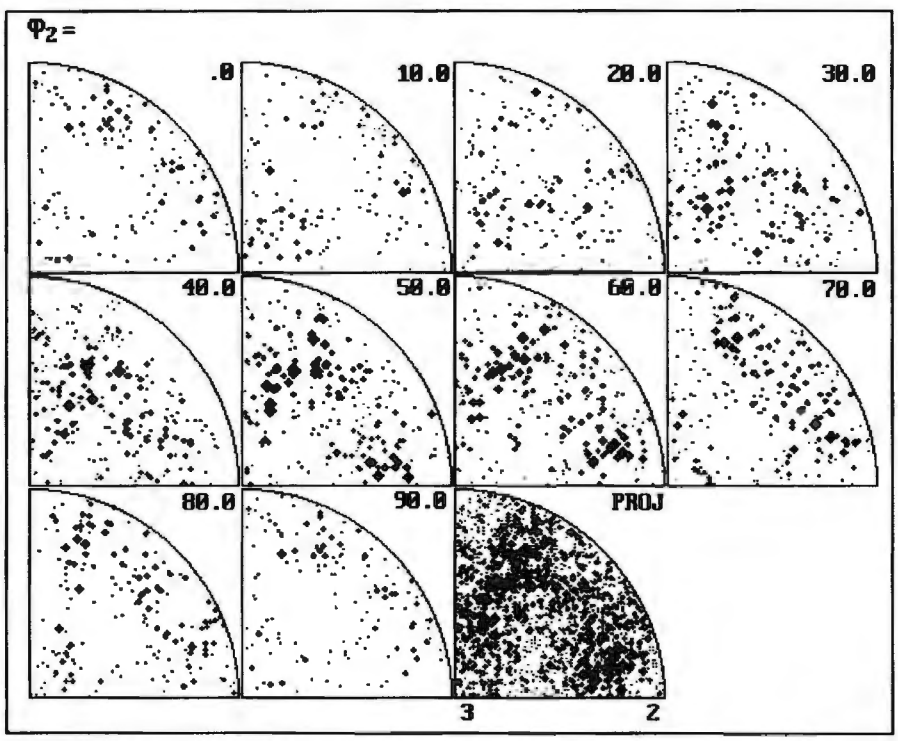

Figure 4.19: Polar plot of orientations representative of the central region of the commercial steel transverse section.

A comparison of the orientations present in each window of the texture map shows little variation in principal texture components from window to window (figure 4.21). However, the variation in grain size and texture from surface to centre, noted in the microstructural examination and the polar plots, is clearly visible. Also evident is the concentration of large grains possessing a {111}<110> orientation distributed near the centre of the sheet. Large grains of the {100}<110> and {123}<634> textures are also found near the central region of each texture window, as well as smaller grains of the {111}<112> texture. The fine grains near the surface possess mostly {111}<112>, {111}<110> and {100}<001> orientations, while the cube texture, which is largely absent in the centre, increases significantly towards the surface regions. Minor components across both regions include {110}<110> and {123}<634> textures. The limited number of fine grains possessing a {112}<110> orientation are evenly distributed within each texture window and across the section.

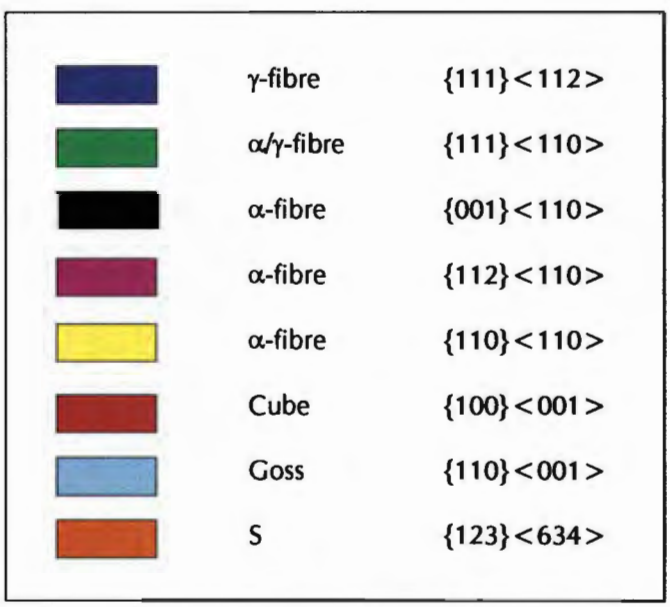

Figure 4.20: Colour chart indicating common BCC textures.

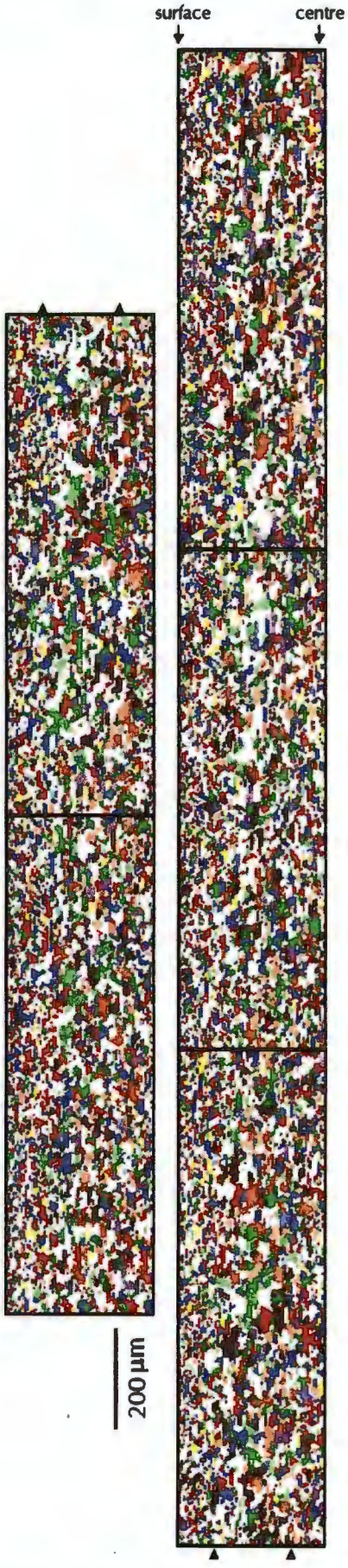

Figure 4.21: Texture map of the commercial steel transverse section.

Rolling Plane Section

Notable textures identified via the polar plots for the rolling plane section include components of both the α and γ fibres, as well as a significant percentage of cube orientations. The microtexture measurements for the rolling plane were acquired near the surface of the sheet and therefore the large percentage of cube texture corresponds with the analysis of this texture in the transverse section. Similar to the transverse section, no differences in preferred orientation could be detected when comparing the plots for the individual windows. Two polar plots from the rolling plane section of the commercial steel are shown in figures 4.22 and 4.23.

After reduction of the original window size into four regions measuring 100 μm (TD) x 1000 μm (RD), clear differences in preferred orientation could be detected. Figure 4.24 illustrates a polar plot for a reduced section possessing a large percentage of cube texture, while the plot shown in figure 4.25 is of a region with a concentration of {111}<112> and {110}<110> orientations. Therefore, it can be concluded that texture clustering occurs across the rolling plane section on a scale of the reduced texture windows.

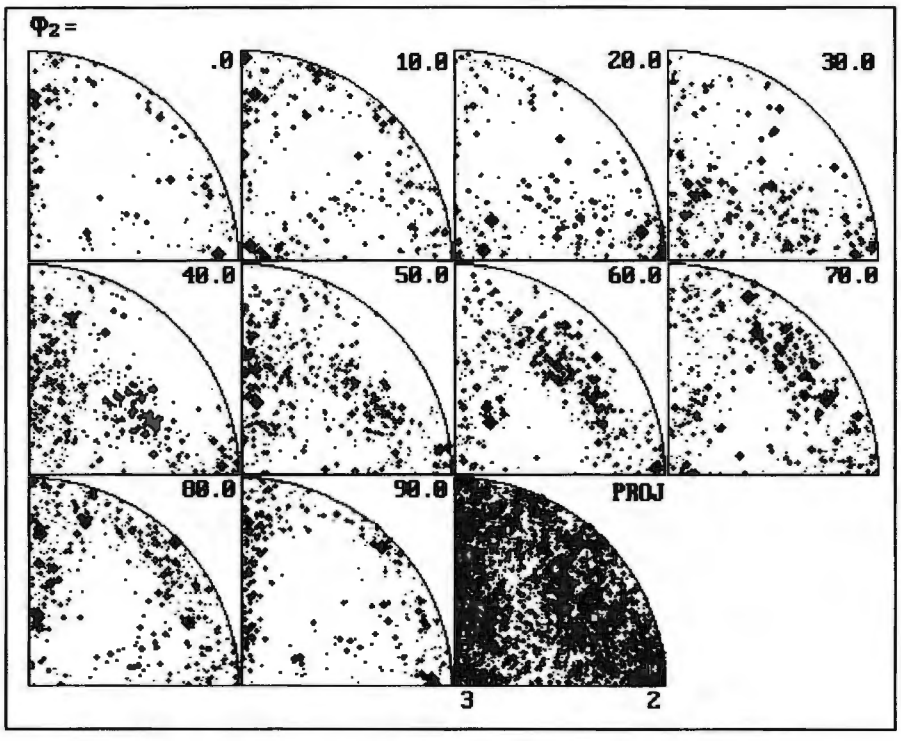

Figure 4.22: Polar plot of orientations for a single texture window of the rolling plane section.

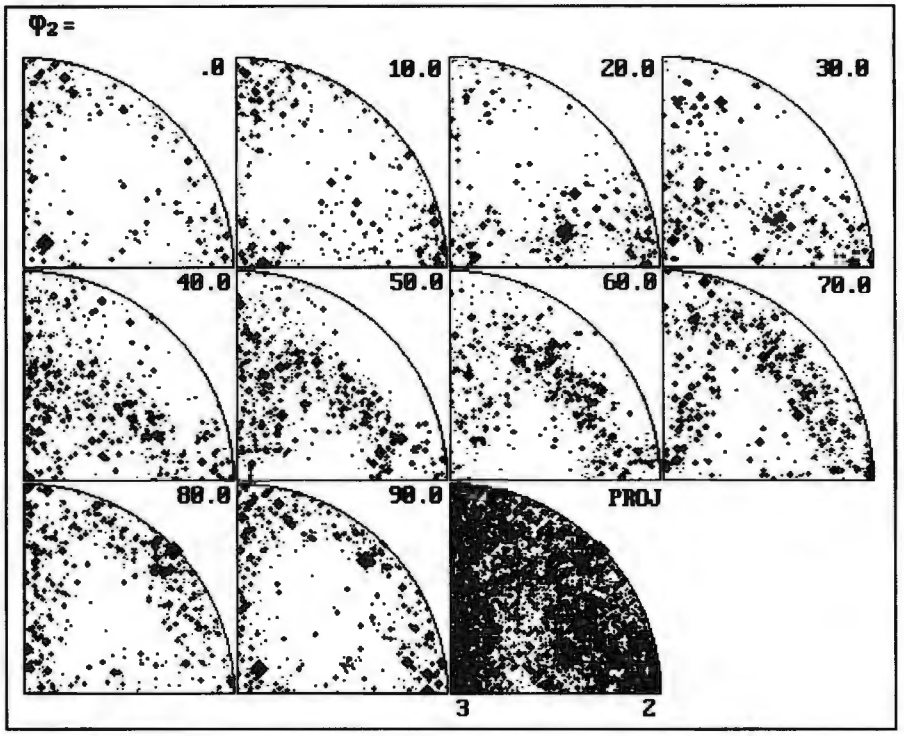

Figure 4.23: Polar plot of orientations for a single texture window of the rolling plane section.

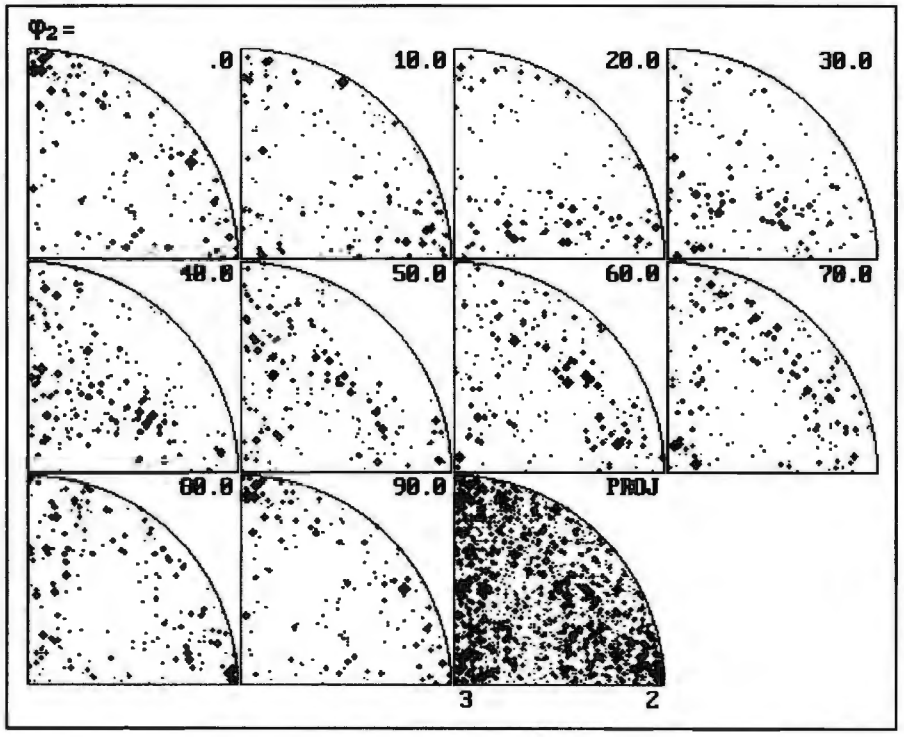

Figure 4.24: Polar plot of discrete orientations from a reduced section of the rolling plane possessing a large percentage of cube orientations.

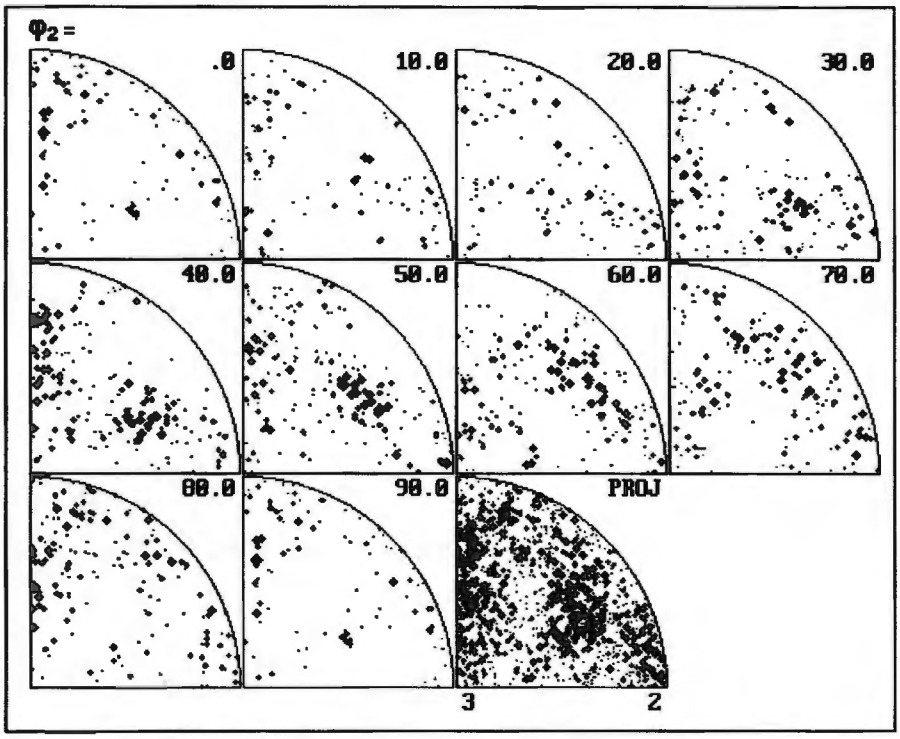

Figure 4.25: Polar plot of discrete orientations from a reduced section of the rolling plane possessing a large percentage of {111}<112> and {110}<110> orientations.

The textures identified in the polar plots can be confirmed via examination of the texture map constructed for the rolling plane section (figure 4.26). Major components present are {111}<112> and the cube texture, with lesser amounts of {111}<110>, {110}<110> and {100}<110>. It is also possible to conclude that the regions or clusters of preferred orientation, identified via the polar plots, are not confined to within a single reduced window but extend across more than one window for a few millimetres in length. For example, colonies of cube texture approximately 150 μm wide in the TD, are seen to extend for distances up to 2 mm in the RD. Although less obvious, other textures namely {100}<110>, also have a tendency to persist in bands elongated in the RD.

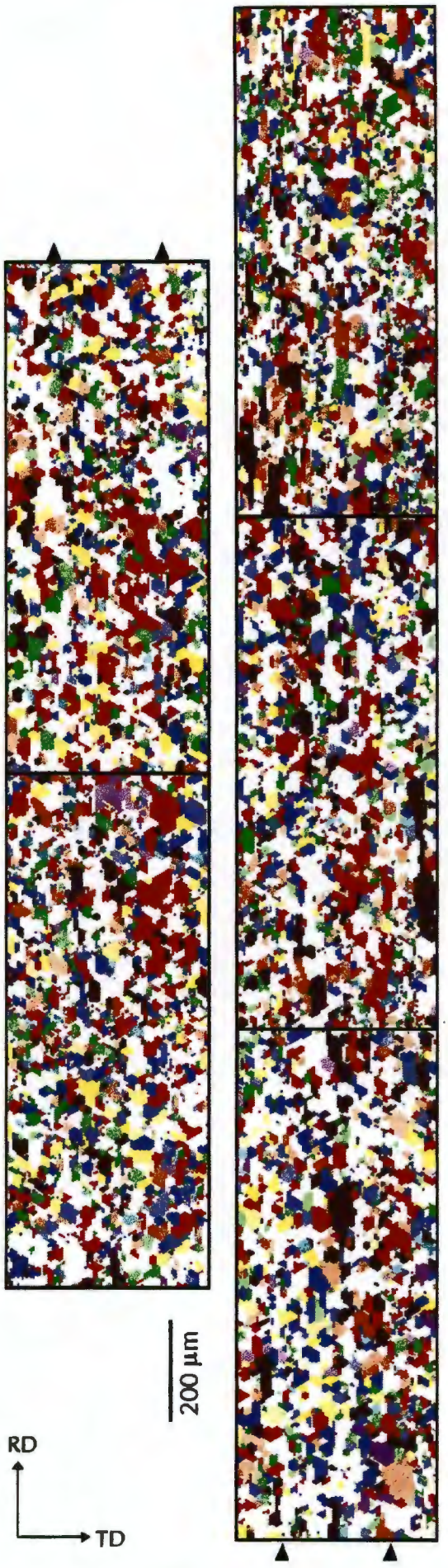

Figure 4.28: Texture map of the commercial steel rolling plane section.

4.4 Plasticity Results

The yield surfaces calculated for each texture window across the transverse plane of the commercial steel are almost identical. The lack of variation in yield surface morphology suggests a similar lack of variation in plastic behaviour across the transverse plane on a scale of the window size. Figure 4.27 indicates the yield surfaces from three texture windows of the transverse section. After reduction of the individual windows into four equal sections, however, the recalculated yield surfaces indicate some deviation in predicted yield behaviour. Figure 4.28, which depicts four yield surfaces corresponding to the reduced sections of a single texture window, demonstrates this trend. These results are in agreement with the microtexture analysis of this sample.

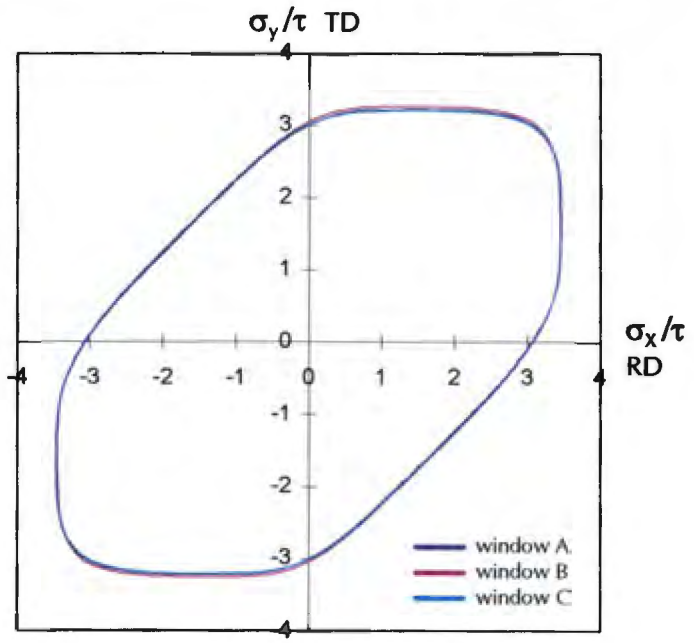

Figure 4.27: Yield surfaces from three textures windows of the transverse section.

A similar trend is evident for the Lankford strain ratios calculated for commercial steel across the transverse section. Figure 4.29 illustrates the strain ratios for elongation in the RD and TD for the original texture windows, while figure 4.30 illustrates the same values for each reduced window. A constant value of r_{TD} = 1.00 is evident, which implies isotropic deformation behaviour during uniaxial deformation in the TD. In contrast, for deformation in the RD the strain ratios

deviate significantly from 1.00 indicating anisotropic yield behaviour. Comparison of the r_{RD} values from window to window though predicts little variation across the section as a whole.

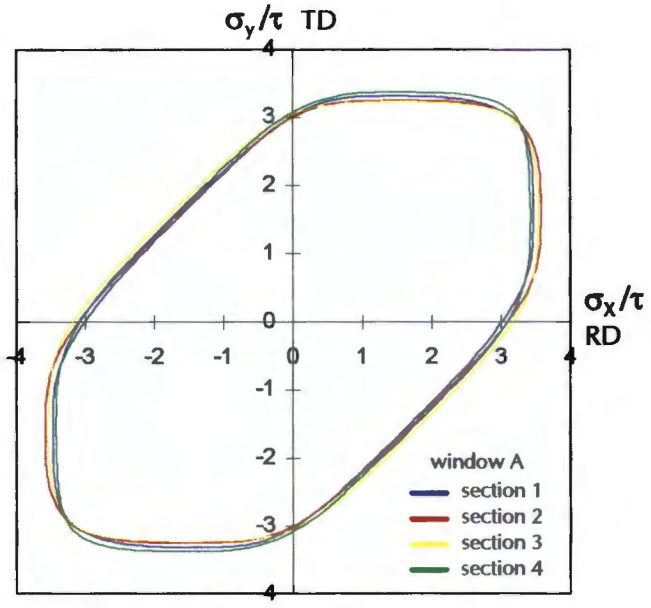

Figure 4.28: Yield surfaces for the four sections of a single texture window.

After reduction, the difference in strain ratio across the section increases significantly. The values for r_{RD} range from 2.52 to 1.31, while a slight variation in r_{TD} is also visible.

r_{RD} = 1.82 r_{TD} = 1.00	r_{RD} = 1.62 r_{TD} = 1.00	r_{RD} = 1.90 r_{TD} = 1.00	r_{RD} = 1.86 r_{TD} = 1.00	r_{RD} = 1.78 r_{TD} = 1.00	NEAR SURFACE CENTRE

Figure 4.29: Strain ratios for elongation in the RD and TD for the original texture windows.

r_{RD} = 2.01 r_{TD} = 1.09	r_{RD} = 1.88 r_{TD} = 1.08	r_{RD} = 2.24 r_{TD} = 1.24	r_{RD} = 2.06 r_{TD} = 1.35	r_{RD} = 2.42 r_{TD} = 1.24	NEAR SURFACE
r_{RD} = 2.34 r_{TD} = 1.02	r_{RD} = 2.52 r_{TD} = 1.53	r_{RD} = 1.50 r_{TD} = 0.65	r_{RD} = 2.40 r_{TD} = 1.00	r_{RD} = 2.12 r_{TD} = 1.00	
r_{RD} = 1.60 r_{TD} = 0.91	r_{RD} = 1.58 r_{TD} = 1.00	r_{RD} = 1.45 r_{TD} = 0.76	r_{RD} = 1.84 r_{TD} = 0.72	r_{RD} = 1.83 r_{TD} = 1.00	
r_{RD} = 1.57 r_{TD} = 1.00	r_{RD} = 1.62 r_{TD} = 1.00	r_{RD} = 1.31 r_{TD} = 0.72	r_{RD} = 1.39 r_{TD} = 1.12	r_{RD} = 1.61 r_{TD} = 1.17	CENTRE

Figure 4.30: Strain ratios for the reduced texture windows.

4.5 Finite Element Modelling

The results of the FEM experiments performed using the calculated yield information from the microtexture data are presented below. Table 4.2 summarises the input as well as the results of the FEM experiments conducted using the microtexture data from sample C430. Note that all experiments were performed with full fixed constraints on all nodes at each end of the mesh.

Table 4.2: Results of FEM experiments performed using commercial stainless steel yield data.

Exp	Tensile Direction	Microstructural component (mm)	Arrangement of components	Result
1	RD	0.13 x 1 x 20	Mirrored	Thinning in the ND at low r-values
2	RD	0.13 x 1 x 20	Random	Convex / concave bending
3	RD	0.13 x 1 x 5	Random	Longitudinal corrugations in the RD
4	RD	0.13 x 1 x 5	Random	Decreased bending, 10mm sample
5	TD	0.13 x 1 x 5	Random	No corrugations, surface roughening
6	RD	0.13 x 12 x 20	Layered	Homogeneous thinning

Experiment 1 models the deformation behaviour of a mirrored structure where the microstructural components extend in the RD throughout the entire specimen. After deformation, surface profiles taken at intervals along the specimen length indicated the development of through-thickness thinning at areas of low strain ratio. Figure 4.31(b) represents two surface profiles measured in the TD together with the corresponding cross section of strain ratios. The reduction in specimen thickness is clearly visible at areas of low r-value. Figure 4.31(a) is a contour plot of the displacement in the normal direction and clearly shows the extension of the thinned bands in the RD.

The effect of randomising the microstructural components in experiment 2 is to produce a convex/concave bending of the specimen as opposed to the previous thinning effect (not shown).

For experiment 3, the microstructural components were shortened to 5 mm while the specimen length remained at 20 mm. The contour plot of displacement in the ND, recorded after 10% strain in the RD, indicates the development of longitudinal corrugations extending in the direction of the

applied stress. Figure 4.32(a) shows the contour plot for experiment 3, while figure 4.32(b) indicates two transverse surface profiles measured at separate intervals along the specimen length. The corrugated nature of the through-thickness profile of the sheet is clearly visible from the surface profiles. In an attempt to provide an explanation for the results of the FEM experiments, a plot of stress in the transverse direction, S_{22}, was constructed for each layer of the specimen. Figure 4.33(a) illustrates a cross section of S_{22} values at 15 mm along the specimen length. The distribution of transverse stress for the microstructural components varies from negative values indicating a compressive stress, to positive values indicating a tensile stress. After a thorough examination it was concluded that a similar distribution of transverse stress was found throughout the specimen. On closer inspection of the individual elements, it is evident that the microstructural components possessing a low r-value are in compression, while those with a relatively higher r-value are in tension (figure 4.33b).

In the case of experiment 4 the specimen length was decreased to 10 mm in order to investigate the influence of boundary constraints on the deformation behaviour. After 10% applied strain, the result showed no corrugation effect through-the-thickness but rather a simple thinning of the specimen in the ND (figure 4.34b). Therefore, it seems feasible to assume that the constraint imposed on the material by the specimen ends is sufficient to significantly alter the deformation behaviour of the specimen and influence the mechanism which is responsible for the development of the corrugations..

The result of the specimen elongated in the transverse direction (Experiment 5) is presented in figure 4.35. The surface topography of the specimen after 10% strain showed no indication of longitudinal corrugations in either the transverse or rolling directions (figure 4.35a). A general fine surface roughening has occurred, as demonstrated by the surface profiles in figure 4.35(b). Indicated in the figure are profiles recorded in both the transverse and rolling directions.

Finally as a comparison, the results of the specimen possessing homogeneous layered properties are displayed in figure 4.36. The surface of the specimen remained smooth during tensile deformation with no indication of corrugations

or general roughness. Figure 4.36(a) indicates the smooth surface topography after 10% strain. The distribution of transverse stress, shown in figure 4.36(b), also remains homogeneous throughout each layer of microstructural components.

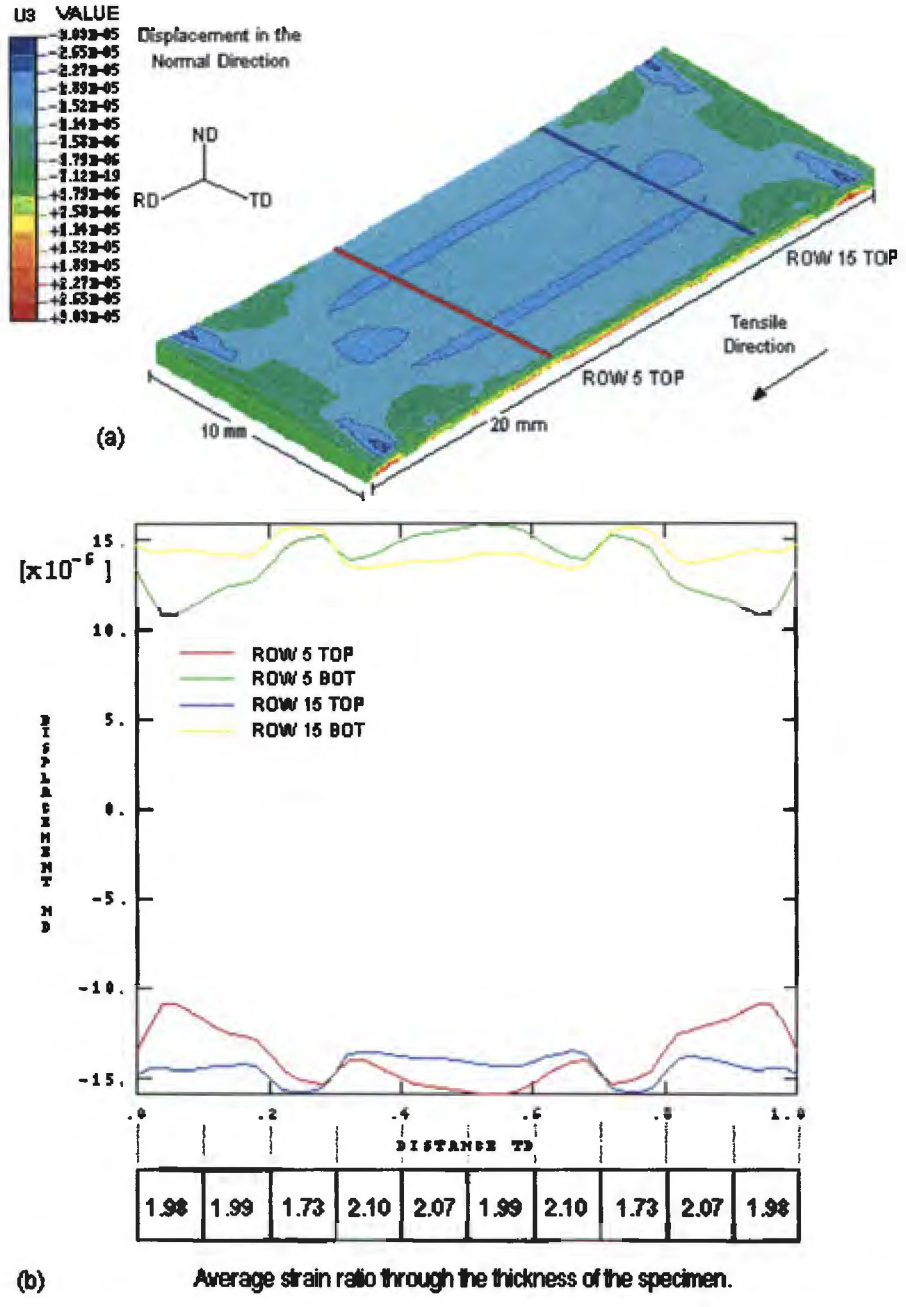

Figure 4.31: (a) Contour plot of displacement in the ND and (b) Surface profiles in the TD across the upper and lower surfaces of experiment 1.

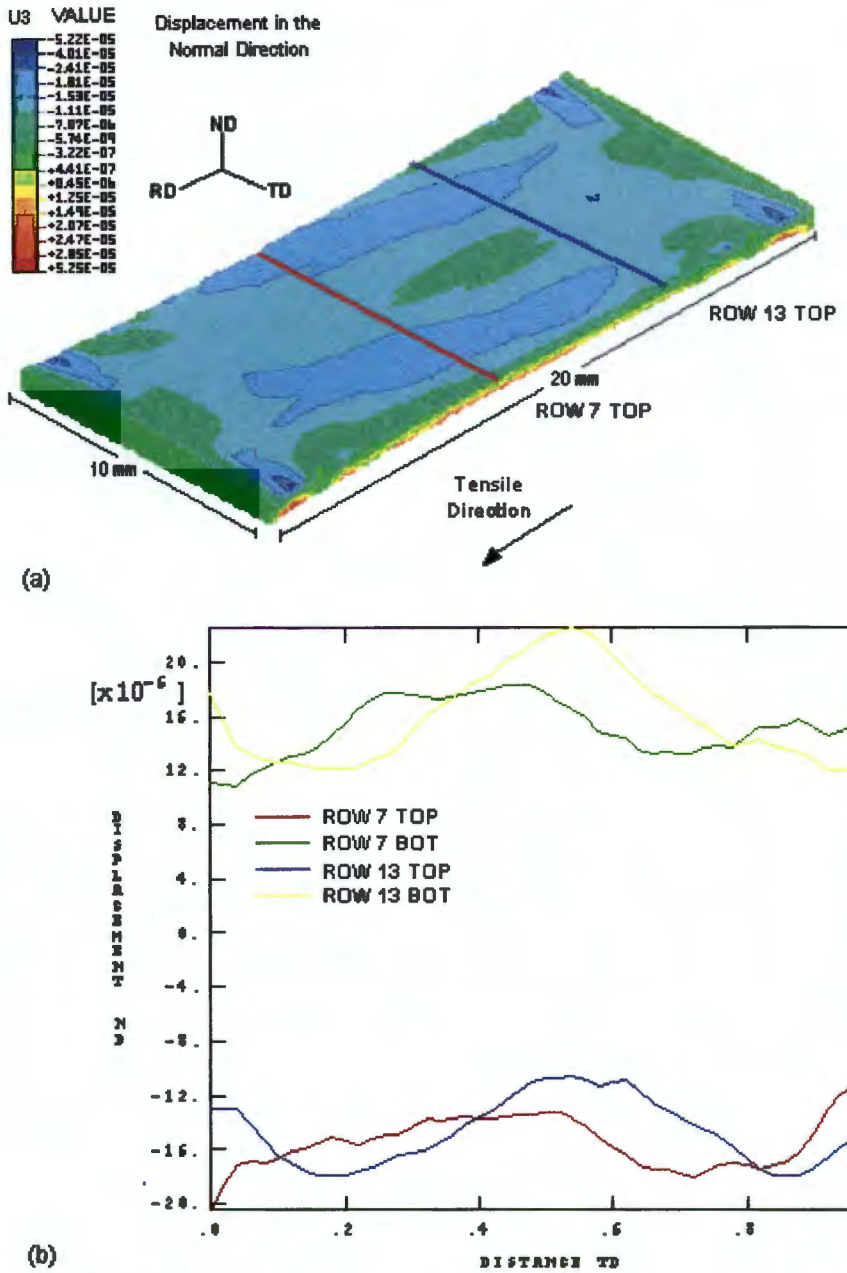

Figure 4.32: (a) Contour plot of displacement in the ND indicating longitudinal corrugations and (b) Surface profiles in the TD across the upper and lower surfaces of experiment 3.

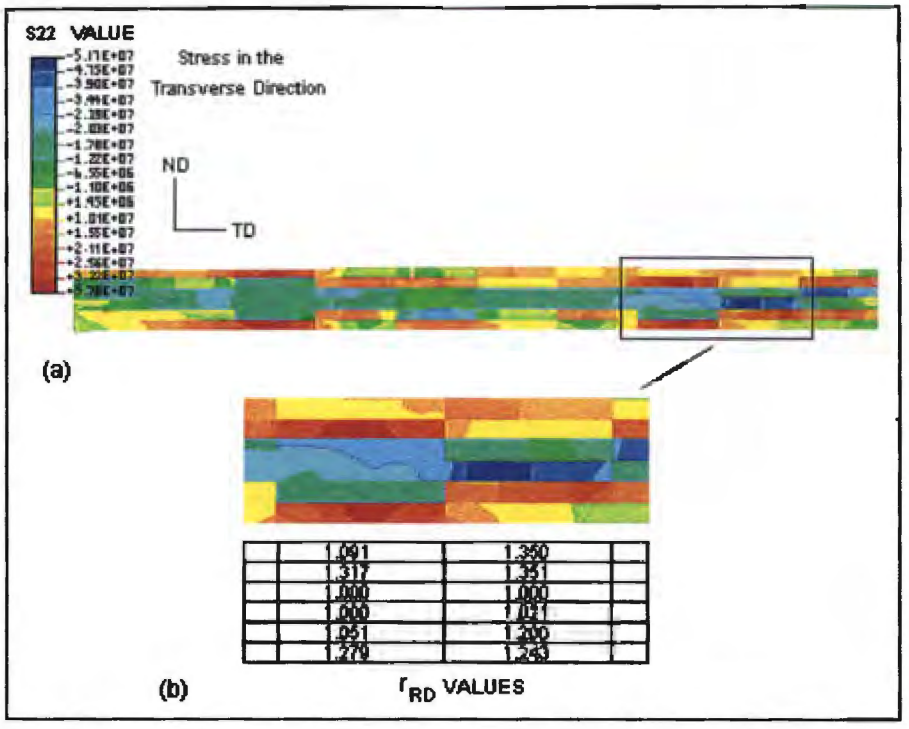

Figure 4.33: (a) A cross section of transverse stress, S_{22}, at 15 mm along the specimen length. (b) r-values for each microstructural component of the magnified region of specimen 3.

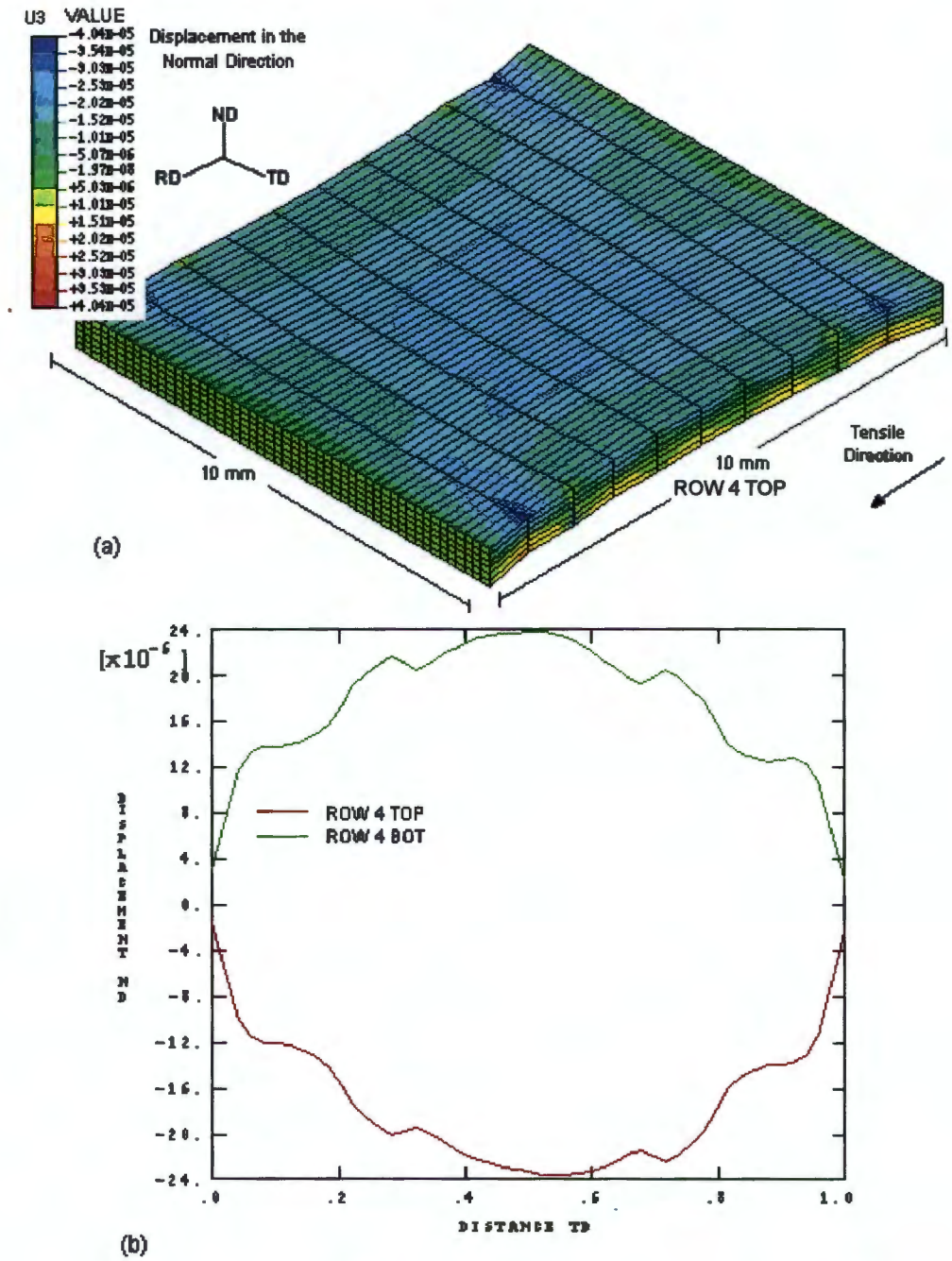

Figure 4.34: (a) Contour plot of displacement in the ND indicating a through-thickness thinning (b) Surface profiles in the TD across the upper and lower surfaces of experiment 4.

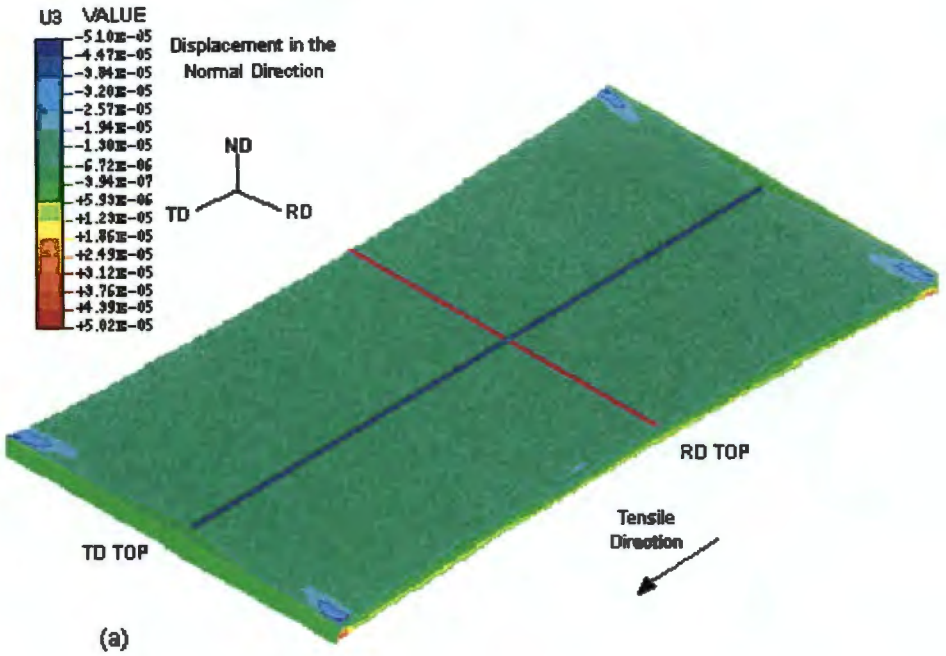

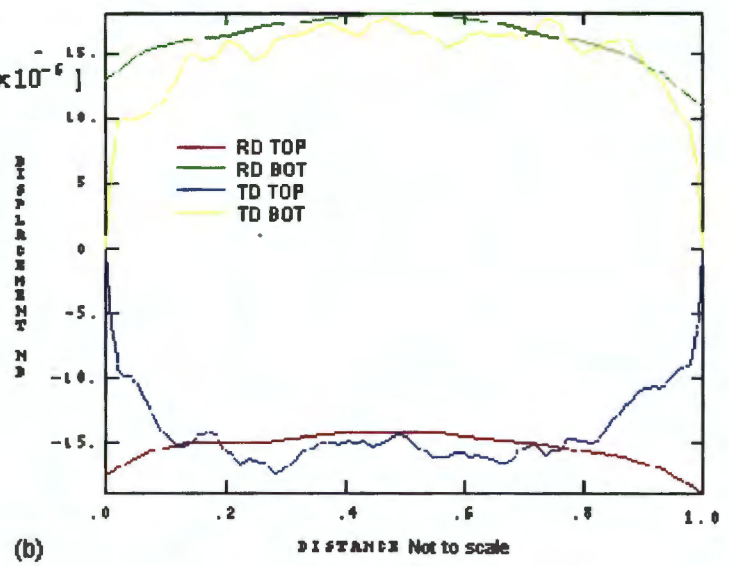

Figure 4.35: (a) Contour plot of displacement in the ND and (b) Surface profiles measured in the TD and RD across the upper and lower surfaces of experiment 5.

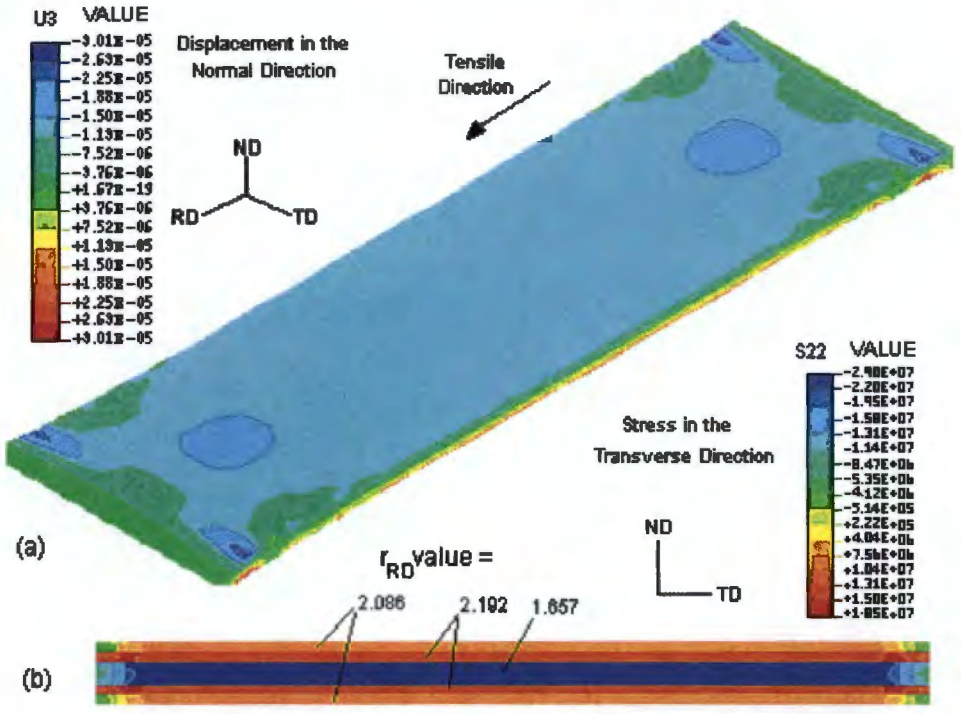

Figure 4.36: (a) Contour plot of displacement in the ND of experiment 6. (b) A cross section of transverse stress, S_{22}, at 15 mm along the specimen length.

4.6 Discussion of the Commercial Stainless Steel Results

Ridging in ferritic stainless steel has previously been attributed to a number of microstructural features related to grain morphology and texture distribution. The different explanations suggested to date for the cause of ridging, as well as the proposals for the mechanism of ridging, are outlined in chapter 2. The results of the present study on ridging in a commercial ferritic stainless steel provide new evidence, which in some areas challenges the conclusions of previous investigations. An analysis of the current results is detailed in the following section, including a suggestion for a new mechanism of ridging based on the microstructural features of the commercial stainless steel and the finite element modelling experiments. A discussion of the contradictions and similarities to existing ridging models is also presented.

The majority of ridging mechanisms suggested to date depend on a variation in plastic flow behaviour across the transverse section of the material, owing to a through-thickness clustering of texture components on a scale similar to that of the ridging profile (figure 4.37a)[32,34,38]. In the case of sample C430, examination of the texture distribution across the transverse section reveals no large groups of similar orientations extending through-the-thickness of the sample (figure 4.37b). This immediately constitutes a major discrepancy relative to former investigations. Figure 4.37 illustrates schematically the difference in local texture distribution between the former theories and the present results. The lack of texture clustering across the transverse section of sample C430 suggests a similar lack of variation in average through-thickness plastic flow properties on a scale of the ridging profile, which calls into question the ridging mechanisms of Chao[32], Takechi *et al*[38] and Wright[34]. Without a variation in plastic flow properties on a scale of the texture windows, it is not feasible that ridging is the result of anisotropic yielding due to through-thickness bands of similar orientations.

Microtexture measurements across the transverse section of the commercial steel did, however, show a variation in principal texture components from the surface to the centre of the sheet, which could contribute to inhomogeneous

deformation between the surface and centre layers and thus add to the corrugated effect. In particular, the cube texture increases significantly from the centre to the surface, while the $\{111\}<110>$ component is concentrated in the centre of the sheet.

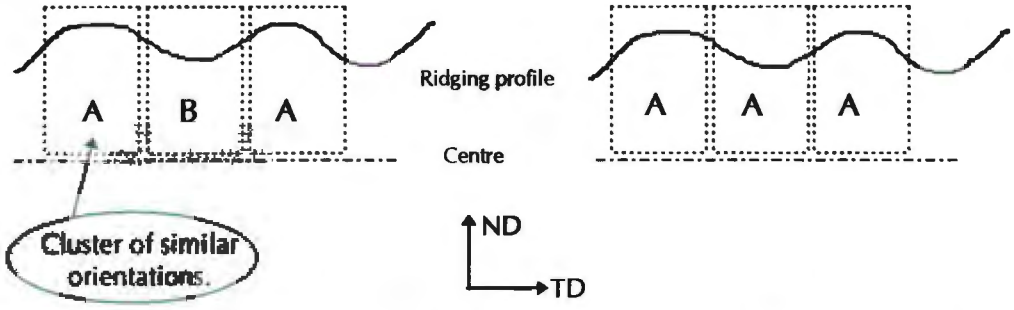

Figure 4.37 (a) Previous Mechanisms: Plastic flow properties vary on a scale of the ridging profile.

Figure 4.37 (b) Current Project: No variation in plastic flow properties on a scale of the ridging profile.

Texture maps constructed for the rolling plane section of the commercial steel demonstrate a continuity of texture components in the RD. Narrow bands of texture, particularly $\{100\}<001>$ and $\{100\}<011>$ orientations, having a width of approximately 100 μm are elongated for a few millimetres in the RD. An inhomogeneous distribution of texture components therefore does exist across the rolling plane of the commercial stainless steel. However, the average width of the texture bands is 100 μm which is significantly smaller than that of the ridging profile which possesses a wavelength of about 1500 μm.

An examination of the microstructure across the rolling plane of the sheet also reveals no *grain size* banding. This is in contrast to the results of Sheppard and Richards[28] in which ridging is attributed to inhomogeneous deformation due to elongated bands of differing grain size. *The results of the microstructural characterisation and texture analysis of sample C430 suggest that, although texture clustering and grain size banding could contribute to ridging, the origin of the defect must be dependent on additional factors.*

The tensile tests of sample C430 indicate the development of severe corrugations during uniaxial deformation in the RD, yet during deformation in the TD no corrugations are visible at all. This supports the findings of Wright[46] in the debate with Chao[44] on the directional characteristics of ridging. Despite

a very slight streaking in the RD on the sample elongated in the TD, the surface remains smooth during elongation. The streaking itself can be attributed to a spatial variation in surface grain rotations due to the elongated bands of texture identified via the microtexture examination. During elongation in the RD the corrugations mask any evidence of this fine roughening effect. The absence of corrugations during deformation in the TD is supported by the strain ratio calculations from the plasticity analysis. The constant value of 1.00 for applied strain in the TD predicts equal thinning in the width and transverse directions, while the average strain ratio of 1.8 for deformation in the RD, suggests anisotropic deformation in these two directions.

Interesting results are provided by the tensile tests in which the gauge length is varied. The reduction in gauge length has an obvious effect on the corrugation behaviour of the specimens, in as much as the frequency and severity of the corrugations decrease with gauge length. The dependence of deformation behaviour on sample geometry suggests that the corrugated effect is more likely to be caused by a summation (macroscopic) of deformation events, as opposed to a plastic flow variation on a scale of the texture clustering. The increased constraint caused by a reduction in gauge length limits the material flow and prevents the contraction of the sample in the transverse direction. If the corrugations are the direct result of bands of preferred orientation, then the change in gauge length should have little or no effect on the surface roughening behaviour.

Furthermore, the tensile tests show that a reduction in specimen thickness results in a decrease in the frequency of the corrugations. Two important conclusions can be drawn from these results. Firstly, ridging is not a "surface phenomenon", and secondly, the operative deformation mechanism is influenced by specimen thickness. The latter result clearly supports a macroscopic deformation type mechanism for ridging. If the thickness of a sheet is reduced, the stiffness of the sheet will be decreased and the section which will wrinkle or bend during deformation will be reduced accordingly.

The lack of texture clustering on a scale of the window size results in little variation in the predicted plastic behaviour across the transverse section of the commercial steel. However, after discretisation of the texture windows into reduced sections (75 μm ND x 1000 μm TD), a change in average plastic properties from section to section is exposed. A similar trend is obtained from the microtexture data acquired across the rolling plane of the sample. This demonstrates that the level of texture clustering within sample C430 is sufficient to cause differences in predicted plastic flow behaviour on a scale greater than the grain size, but not on a scale of the original texture windows. Subsequent finite element modelling experiments utilising the microtexture data demonstrate that the variation in plastic flow properties on a scale of the reduced windows is sufficient to produce a variation in transverse strain across the specimen. This results in inhomogeneous deformation and the formation of corrugations during uniaxial tensile deformation.

Using an arrangement of microstructural components mirrored across the specimen mid-plane for the FEM simulation produces a ribbed effect or through-thickness thinning of the specimen at areas of low strain ratio. This is expected as a material possessing a low r-value, $(r = d\varepsilon_w / d\varepsilon_t)$, will offer a low resistance to through-thickness thinning and will therefore contract more easily in the ND during deformation. By randomising the arrangement of microstructural components within each layer and shortening them to 5 mm, a corrugated specimen profile is produced rather than elongated areas of thinning. The corrugations extend in the direction of applied stress for almost the entire length of the specimen with a peak-to-valley measurement of approximately 10 μm. If we examine the transverse stress distribution of the specimens whilst still under load (figure 4.33), it is evident that the regions of high strain ratio are in tension, while those regions with a lower strain ratio are in compression. The regions possessing a high r-value have a greater tendency to contract in the TD during deformation in the RD, but are prevented from doing so by the surrounding material which possesses a lower r-value. This results in the high r-value regions experiencing a tensile stress in the transverse direction, while the lower r-values regions are placed under compression.

4.6.1 Mechanism of Ridging:

Finite element modelling has indicated that when a material possesses a mirrored or symmetric arrangement of yield properties about the specimen mid-plane (figure 4.38), a ribbed effect will develop during uniaxial deformation. The regions containing a low average strain ratio will be able to contract more easily in the ND than the surrounding regions which possess a relatively higher average strain ratio. Alternate regions of high and low r-value will lead to a ribbed through-thickness profile as illustrated schematically in figure 4.38. As mentioned previously, the regions of low average r-value will experience a transverse compressive stress (σ_{22}) due to a greater resistance to contraction in the transverse direction relative to the adjacent material.

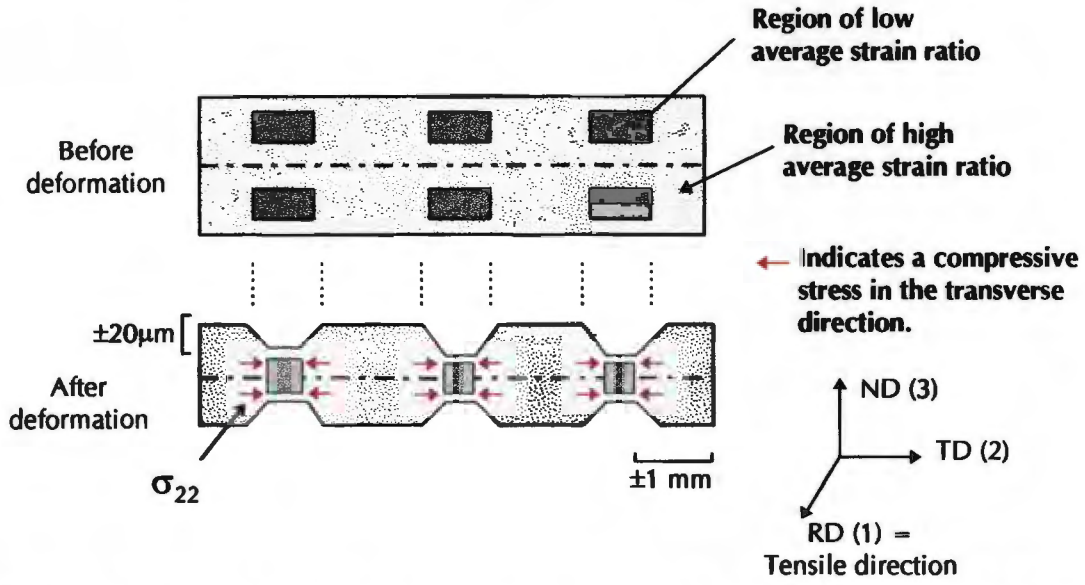

Figure 4.38: Mirrored arrangement of yield properties about the mid-plane to produce a ribbed through-thickness profile.

The arrangement of through-thickness yield properties and compressive stresses shown above is comparable to the situation suggested in Wrights[34] buckling mechanism. The model assumes elongated clusters of (111)[11$\bar{2}$] texture which are distributed within a matrix of (001)[110] orientations (Figure 2.7). During deformation, the longitudinal bands of texture resist transverse strain, which in turn initiates the development of compressive stresses in these regions. This leads to the localised plastic buckling of the texture bands and the formation of

the corrugated profile. To be effective, the model requires that the bands of preferred orientation extend through almost the entire thickness of the sheet.

The results of the FEM experiments of the current project suggest that a symmetrical distribution of yield properties of this nature (about the mid-plane of the material) will produce a ribbed effect as opposed to a corrugated through-thickness profile. In addition, the microtexture results across the transverse section of sample C430 indicate no clustering of preferred orientations through-the-thickness of the sheet on a scale of the ridging profile. This also casts doubt on the buckling mechanism suggested by Wright[34], as well as the mechanisms of Chao[32]and Takechi *et al*[38]. Thus, although one might be tempted to favour the buckling mechanism proposed by Wright[34] as a result of the extensive development of internal transverse compressive stresses during RD elongation, as shown by several FEM simulations in this thesis, the explanation below gives rise to another proposal.

Finite element modelling has indicated that if the microstructural components are arranged such that the variation in yield properties across the transverse section is *asymmetric* about the midplane (figure 4.39), the specimen will form corrugations during deformation. It is proposed that the r-value fluctuation across the transverse section of the specimen causes a spatial variation in the rate of width change of the microstructural components which results in an inhomogeneous distribution of transverse strain.

Consider a section of the specimen where a variation in r-value exists through-the-thickness of the sheet (figure 4.39a). During tensile deformation, differences in average strain ratio will lead to a variation in the transverse strain experienced by the upper and lower regions of the sheet. The lower material which possesses a higher average strain ratio will contract more easily in the transverse direction, compared to the upper region which has a lower average strain ratio. This will generate a localised bending of the sheet in the transverse plane as indicated in figure 4.39(b) below.

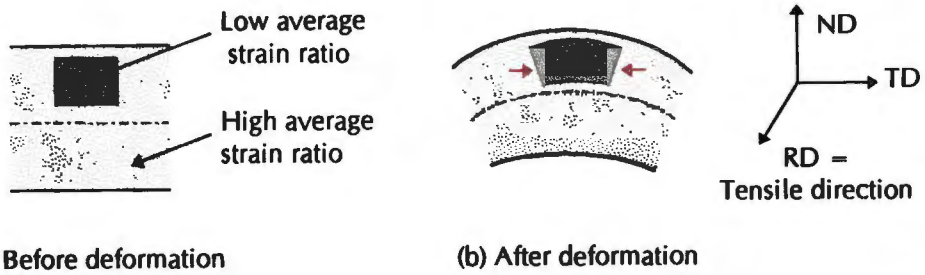

Figure 4.39: Section of a specimen indicating a variation in strain ratio through-the-thickness.

It follows therefore that if the r-value varies asymmetrically across the entire transverse section of the sheet, alternate localised bending events will produce a corrugated through-thickness profile as indicated in figure 4.40. Again the regions with low strain ratio will experience a compressive transverse stress while the adjacent material will be placed under tension. The internal stress distribution will naturally influence the inhomogeneous deformation behaviour of the sheet and may contribute to the formation of the corrugations.

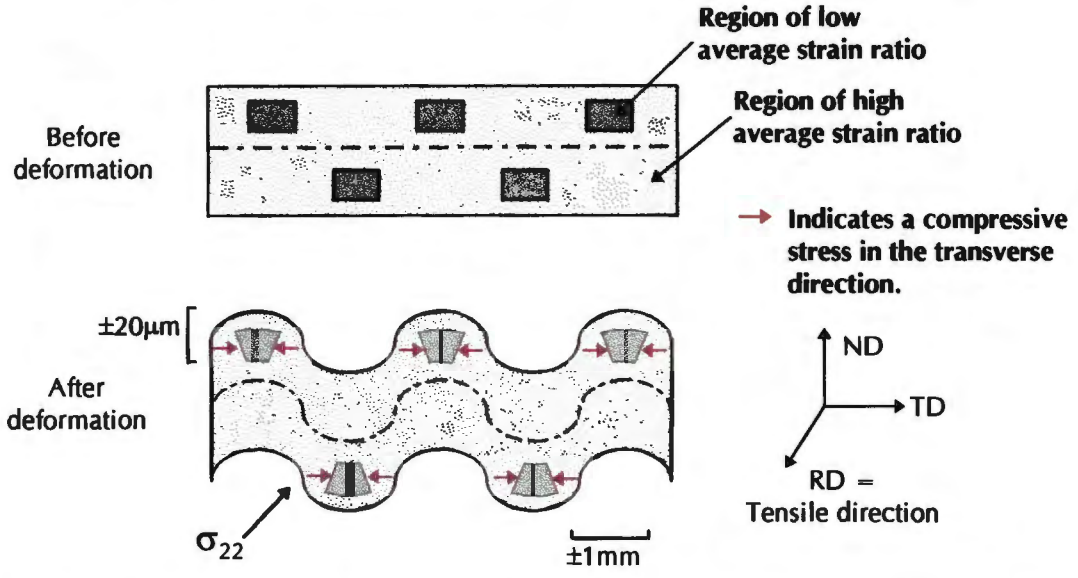

Figure 4.40: The development of a corrugated profile due to an asymmetric arrangement of r-values about the mid-plane of the sheet. The height of the corrugations have been exaggerated in the ND.

It is suggested that corrugations will form during uniaxial tensile deformation whenever there exists an asymmetric arrangement of yield properties resulting, for example, from an inhomogeneous distribution of texture components about the mid-plane of the material. It is not required that a single texture component is clustered in large regions through-the-thickness of the sheet, but rather that on a macroscopic scale an overall asymmetric arrangement of texture components

exists about the mid-plane of the sheet. Adopting the alternating bending approach obviates the necessity to have a direct correspondence between surface topography and microstructural features such as texture or grain size banding, which has been the downfall of many previous investigations[32,36,38].

The elongated texture bands and resultant extension of yield properties contributes to the extension of the corrugations in the RD. In the case of elongation in the TD, the conditions necessary for bending will not arise due to the geometry of the elongated texture bands. The texture clusters extend for a few millimetres in the RD and therefore, during tensile deformation in the TD, the development of differential strain perpendicular to the applied stress will not favour localised bending events which are able to produce longitudinal corrugations.

For the same reason, no corrugations are exhibited by the FEM specimen when the tensile axis is parallel to the TD. Although a variation in strain may appear during elongation in the TD, the arrangement and geometry of the microstructural components will not support bending of the specimen to produce corrugations parallel to the RD. The microstructural components extend for 5 mm in the RD and 1 mm in the TD which means that elongation applied in the TD does not provide the correct geometry for localised bending.

The continuity of the corrugations across the entire length of the tensile specimens elongated in the RD, including their extension beyond the reduced gauge, supports a localised bending mechanism for ridging. Although extended texture clusters do exist within sample C430, as seen from the microtexture examination of the rolling plane section, it is not feasible that they extend across the entire specimen length for more than 55 mm. Also the width of the clusters, which is approximately 100 μm, is an order of magnitude smaller than the wavelength of the ridging profile.

When considering the FEM specimen where the properties are homogeneous throughout each layer, there is no competition for shrinkage in the width direction, and if the assumption is made that the material contracts with no constraint, then the strain distribution in the width direction is uniform

throughout the layers. There is consequently no driving force to cause bending and the specimen remains level during uniaxial tensile deformation.

Summary:

Based on the results of the finite element modelling and microtexture analysis it is suggested that the ridging phenomenon is the result of an asymmetric distribution of texture components about the mid-plane of a material. This arrangement of preferred orientation leads to a variation in plastic flow properties across the material which initiates the development of differential transverse strains during tensile deformation. The variation in transverse strain in turn results in a series of localised bending events which on a macroscopic level produces corrugations.

4.6.2 Comparison with Previous Ridging Models

The microtexture examination of sample C430 highlights the inhomogeneous distribution of texture components through the thickness of the sheet. Salsgiver *et al*[39], in an examination on the ridging behaviour of 3%-silicon steel, suggested that the texture gradient through-the-thickness of the alloy causes inhomogeneous deformation between the centre and near surface layers which results in the ridging phenomenon[39]. Yet ridging has been reported in steels possessing little variation in texture from the centre to the surface of the sheet,[107] while many steels which possess texture gradients do not exhibit ridging. This implies that a further explanation for the ridging mechanism is required.

An examination of the texture distribution across the transverse section of sample C430 indicates no variation in preferred orientation on a scale of the window size, or rather no through-thickness clustering of texture components is visible on a scale corresponding to the ridging profile. This result immediately casts doubt on the ridging mechanism suggested by Chao[32], Takechi *et al*[38] and Wright[34], which all rely on bands of similar texture which extend through the sheet thickness. In the model by Chao[32], bands of $\{111\}<110>$ texture lie adjacent to bands of $\{110\}<110>$ or $\{100\}<110>$ texture, while for Wrights buckling mechanism[34] elongated clusters of $(111)[11\bar{2}]$ texture are distributed in

a (001)[110] matrix. In both cases, the bands must persist through the majority of the sheet thickness for the mechanism to operate.

In the model by Takechi *et al*[38], bands of partial α-fibre <110>//RD orientation are suggested to cause alternate shear stresses in the material resulting in the corrugated profile. Examination of the texture distribution within the commercial steel, however, does not reveal bands of <110>//RD texture extending in the RD on a scale similar to the ridging morphology. Also, Harase *et al*[37] attributed ridging to the bending moment set up by an uneven distribution of the {100}<011> texture about the centre line of the sheet. Again this texture is not evident in the commercial steel in the arrangement suggested in the proposed model, which casts doubt on the generality of the mechanisms. The model by Harase *et al*[37] nevertheless seems more feasible, as it does not depend on a concentrated through-thickness clustering of texture components. An asymmetric distribution of certain textures about the mid-plane is a more plausible explanation for the origin of ridging considering the lack of through-thickness texture clustering across the transverse section of the commercial stainless steel C430.

Bethke *et al*[36] proposed a ridging mechanism based on the distribution of ε_{23} shear stresses during deformation. Examination of the texture components in sample C430 indicates an approximate 25% volume of shearing textures, i.e. {111}<110> and {112}<110> orientations. These are the ideal textures which experience ε_{23} shear during deformation. The remainder and therefore the majority of textures present in the sample will contribute minor amounts of ε_{23} shear only if they are rotated off their ideal orientations. Furthermore, the stochastic model suggested by Bethke *et al*[36] depends on the alignment of similar textures in the RD to produce the continuity of the corrugations in that direction. As detailed in the literature review, Bethke *et al*[36] identified a high MCI value, indicating a strong orientation difference correlation, for between 50 and 100 measuring points in the RD, which is equivalent to between 0.5 mm to 1.0 mm. The ridges on the commercial steel of the present investigation however extend for more than 50 mm in the RD and, therefore, it is suggested

that the transverse bending explanation for ridging is better able to account for the extension of the corrugations in the RD of the sheet.

In 1997, the first investigation on the ridging phenomenon in ferritic stainless steel incorporating microtexture data covering a total area of more than 5 mm^2 was published[107]. Brochu *et al*[107] presented large scale texture maps across the transverse and rolling plane sections of two steels which exhibited severe and mild ridging during deformation. The texture maps across the transverse section of both samples, covering an average of 1.6 mm^2 on each sample, demonstrated little clustering of the dominant orientations, namely $<111>$//ND and $<211>$//ND. A similar situation was evident across the rolling plane of the sample which exhibited mild ridging. However, across the rolling plane of the severely ridged sample, a distinct banding of the texture components was visible. Bands of $<111>$//ND and $<211>$//ND texture with a width of about 100 μm were evident extending in the RD across the entire texture map for 1.05 mm. Also, bands with a $<110>$//ND orientation were elongated in the RD.

Brochu *et al*[107] then used this information to formulate a new mathematical model which attempts to explain the ridging behaviour of ferritic stainless steel. As a first stage of the model, slip in a single crystal is analysed in a similar manner to previous models[32,34,38]. Following this, a new parameter is introduced, namely E_x^{ND}, which is the total deformation in the ND and is defined as the sum of the plastic deformations of each unit through the thickness of the sheet. If each unit is identical, E_x^{ND} can be expressed as:

$$E_x^{ND} = (1/n)\sum_{y=1}^{n}(\varepsilon_{xy}^{ND}/\varepsilon_{xy}^{RD}),$$

where n is the number of units through the thickness, y is the axis normal to the sheet and x is the transverse axis. Therefore, using this equation the deformation profile across the transverse section of the sheet can be calculated. To avoid the problem of the hills and valleys on the upper surface mirroring those on the lower surface and producing a ribbed profile, a second parameter was introduced, Y_x^c, which is defined as the centre of deformation. Assuming that deformation is asymmetrical about the mid-plane and to maintain

continuity, it was suggested that deformation of the units is accompanied by a translation of the material in the ND. Thus, by supposing that the centre of deformation is the most deformed unit, the necessary corrugated ridging profile could be produced.

The model was applied to the microtexture data from the two samples and the deformation profiles compared to measured surface profiles of tensile tests performed on the materials. The general form of the profile was similar in both cases, but a better agreement of frequency and amplitude was found for the sample which exhibited severe ridging. The calculated profile for the mildly ridged sample showed notable deviation from the measured profile.

Although the mathematical model proposed by Brochu *et al*[107] represents well the general tendency of the ridging profile, the accuracy of the model is called into question by the significant variation between the experimental and theoretical results for the mildly ridged sample. Also, no specific explanation is provided for the extension of the ridges in the RD for both the mildly or severely ridged samples. Nevertheless, the model is an improvement on previous theories in as much as it takes into account both the large and small frequency ridges, and is not dependent on a variation in through-thickness average properties on a scale of the ridging profile.

Comparison of the microtexture results from the investigation by Brochu et *al*[107] with the texture maps of the commercial steel of the present project indicates a significant similarity in texture clustering. Although the principal texture components differ slightly, in both investigations bands of similar orientations (width ≈ 100 μm) extend for a few millimetres in the RD. Also, an important similarity is the lack of large scale texture clustering across the transverse section of both the ridged samples. The fact that the severely ridged sample from the study by Brochu *et al*[107] and sample C430 show a good correlation with regards to texture distribution across both the transverse and rolling plane sections, confirms the microtexture results of the present texture investigation.

CHAPTER 5

RESULTS OF THE LABORATORY ROLLED STEEL

5.1 Microstructure

The development of the microstructure for the laboratory rolled stainless steel through the thermomechanical process is summarised in the section below. The three heats which possess hot roll finish temperatures of 920°C (Heat 1), 785°C (Heat 2) and 654°C (Heat 3), are presented.

Hot Rolled (stage A) and Hot Rolled-Annealed (stage B)

The mottled effect of the ferrite matrix obtained from electron channelling contrast (ECC) indicates a highly deformed microstructure for sample A3, which has a hot roll finish temperature of 654°C. Darker streaks are also visible within the deformed matrix indicating the presence of martensite stringers (figure 5.1). Increasing the hot roll finish temperature to 920°C has a significant effect on the microstructure evident from the micrograph of sample A1 shown in figure 5.2. The streaky appearance of martensite is once again apparent but the matrix is considerably less deformed. The mottled effect is still present but the ferrite structure has recovered to a far greater extent and the channelling contrast is consistent with a recovered subgrain structure.

During annealing, the martensitic regions of sample B1 undergo recovery but the ferrite matrix is unable to recrystallise, which produces instead the mottled effect consistent with a subgrain structure during ECC examination (figure 5.3). On closer inspection, the areas within the original martensite stringers have undergone tempering to an extent where polygonised subgrains have formed from the prior martensite laths. An example of this polygonisation is reproduced in figures 5.4(a) and 5.4(b), where 5.4(b) is a high magnification view of the outlined region in figure 5.4(a). The subgrain ferrite matrix is also distinguishable from the martensitic regions. Electron channelling in the case of sample B3 produced clear grain contrast indicative of a fully recrystallised

microstructure (figure 5.5). Also of importance to note are the bands of coarse and fine grains which persist through-the-thickness of the sample.

The sample with the intermediary hot roll finish temperature of 785°C produced an intermediate microstructure. The hot roll condition (A2) (figure 5.6) demonstrates a less recovered structure than A1, while the hot rolled-annealed condition (B2) (figure 5.7) exhibits a partially recrystallised microstructure.

Cold Rolled (stage C) and Cold Rolled-Annealed (stage D)

Specimens cropped after the cold rolled and cold rolled-annealed stage were also examined using electron-channelling contrast. In view of the 72% reduction, the three samples all produce highly stained microstructures after cold rolling. The effect of subsequent annealing on the microstructure is evident in figures 5.8, 5.9 and 5.10. Clear grain contrast indicating a fully recrystallised microstructure is apparent in each case. A distinct decrease in overall grain size is also visible with a decrease in hot roll finish temperature. For sample D1, the grain size is distinctly bimodal with approximately equal amounts of fine (10 - 20 μm) and coarse (30 - 100 μm) grained regions (figure 5.8). Sample D3, on the other hand, is dominated by fine grains (10 - 20 μm) with approximately 30% coarse-grained regions. The grain size distribution of sample D2, with a hot roll finish temperature of 785°C, can again be characterised as intermediate. For all three samples the elongation of the recrystallised grains in the RD is limited. An additional feature to note is the banded distribution of the fine and coarse grains through-the-thickness of the samples. Particularly apparent in D1 and D2, the bands have a width of between 20 μm and 100 μm in the ND and in most cases extend across the entire images area of 1000 μm in the RD. The rolling plane section of D1 shown in figure 5.11 indicates this grain size banding clearly. The bands for D3 have persisted from the hot rolled-annealed stage of the thermomechanical process. The microstructural examination shows therefore, that the laboratory rolled samples in the cold rolled-annealed condition possess elongated 'plate-like' clusters of similar grain size extending in the RD.

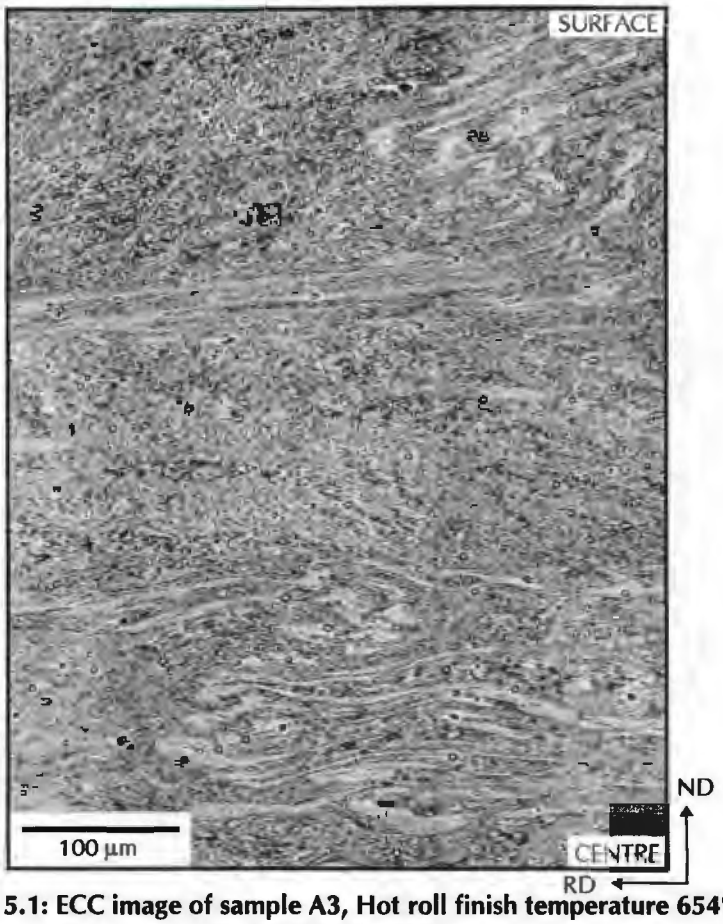

Figure 5.1: ECC image of sample A3, Hot roll finish temperature 654°C. Hot Rolled Condition

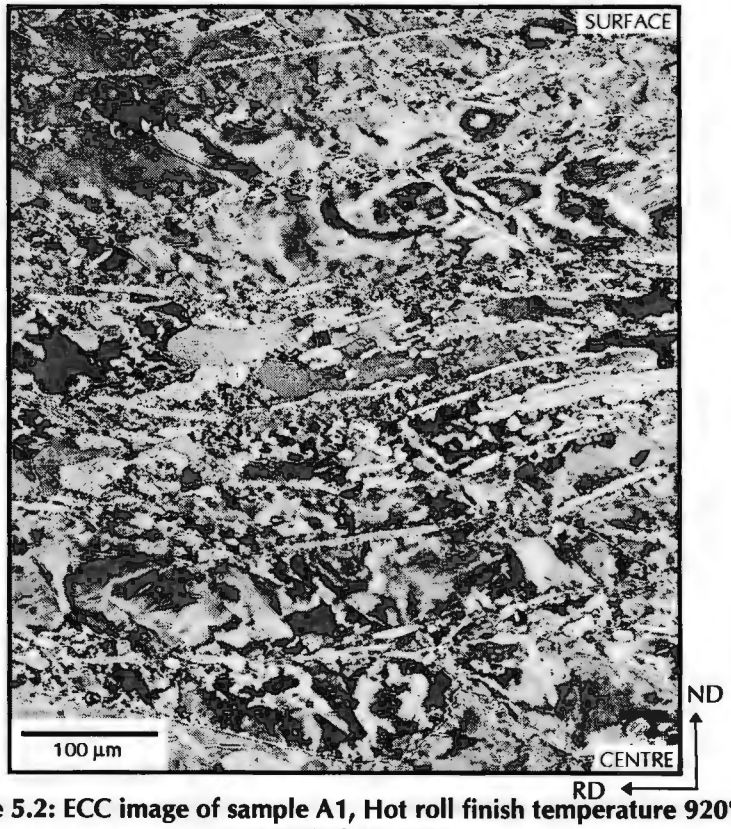

Figure 5.2: ECC image of sample A1, Hot roll finish temperature 920°C. Hot Rolled Condition

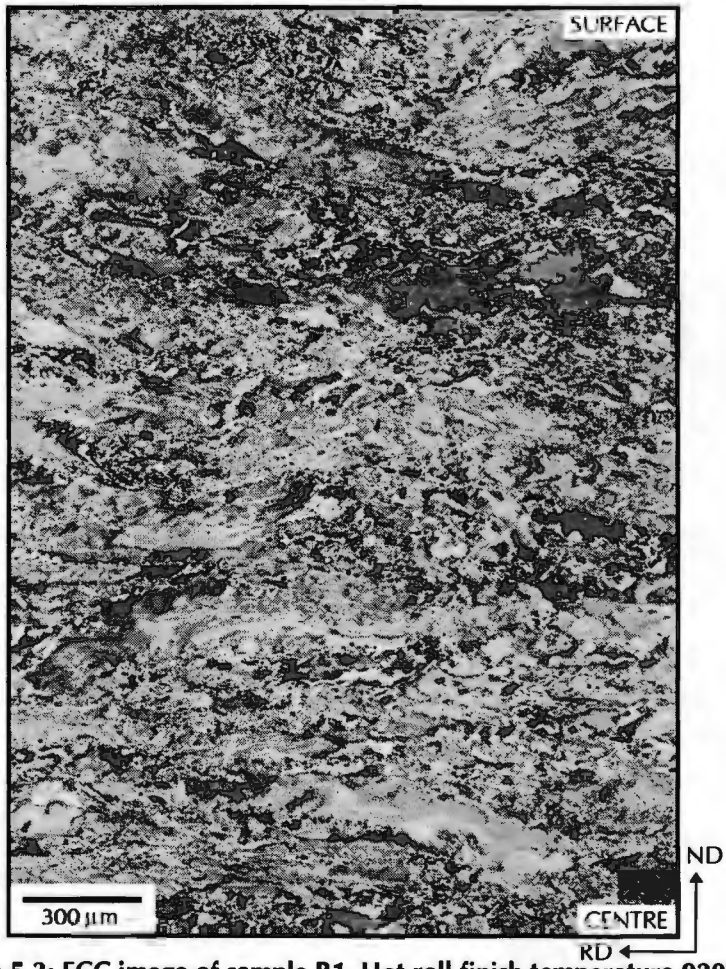

Figure 5.3: ECC image of sample B1, Hot roll finish temperature 920°C. Hot Rolled - Annealed Condition

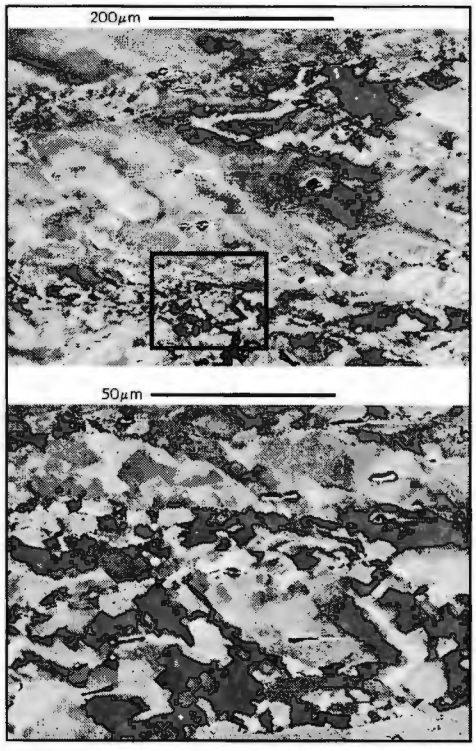

Figure 5.4: ECC image of sample B1 at higher magnification (a) above and (b) below. Hot Rolled - Annealed Condition

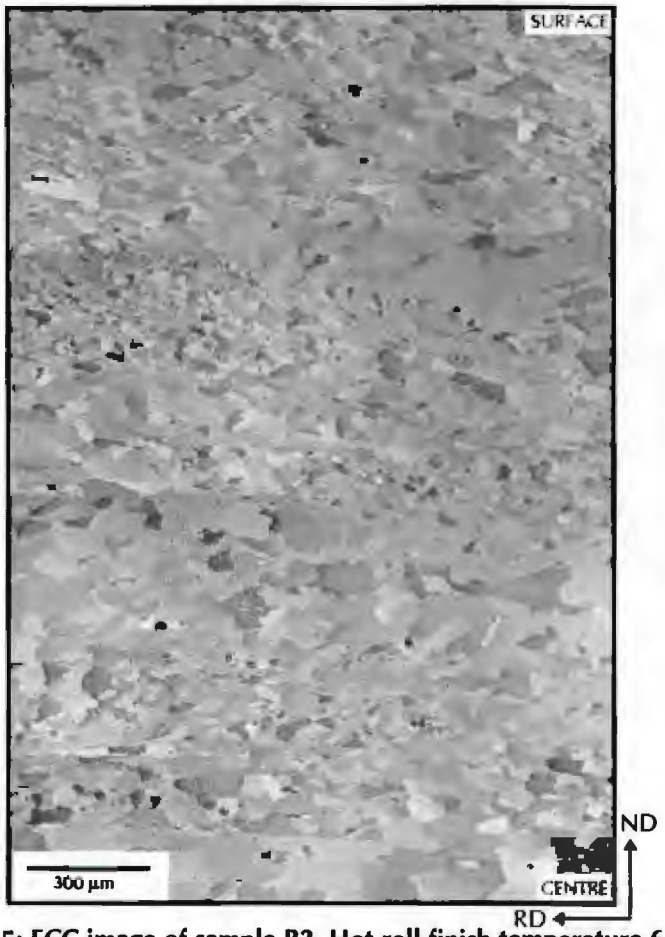

Figure 5.5: ECC image of sample B3, Hot roll finish temperature 654°C. Hot Rolled - Annealed Condition

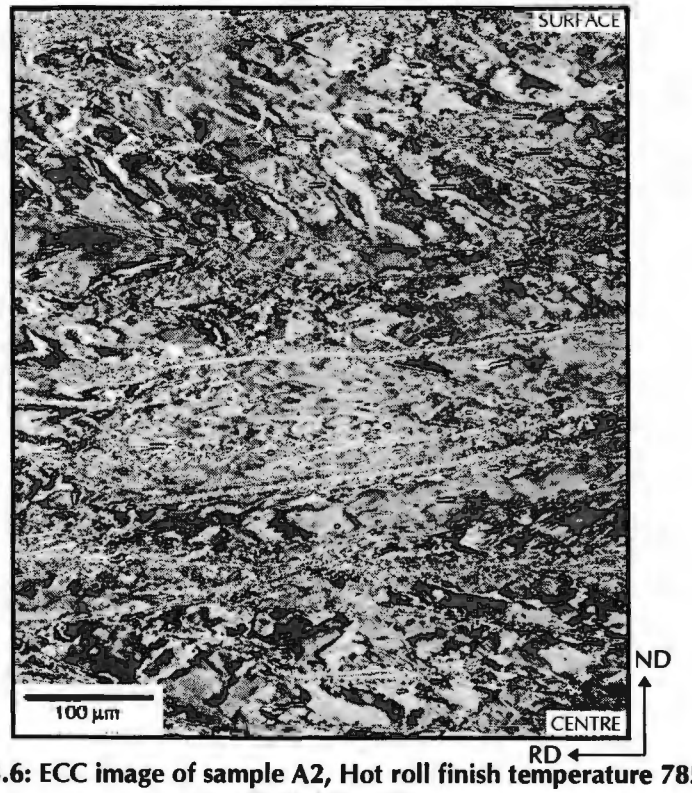

Figure 5.6: ECC image of sample A2, Hot roll finish temperature 785°C. Hot Rolled Condition

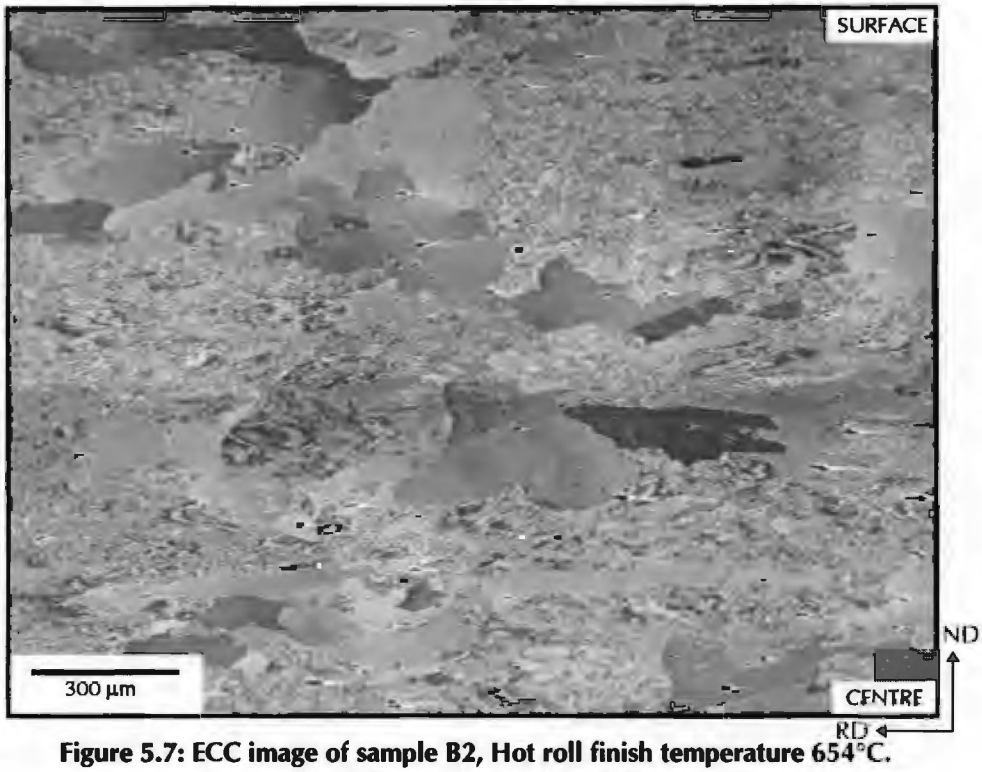

Figure 5.7: ECC image of sample B2, Hot roll finish temperature 654°C. Hot Rolled - Annealed Condition

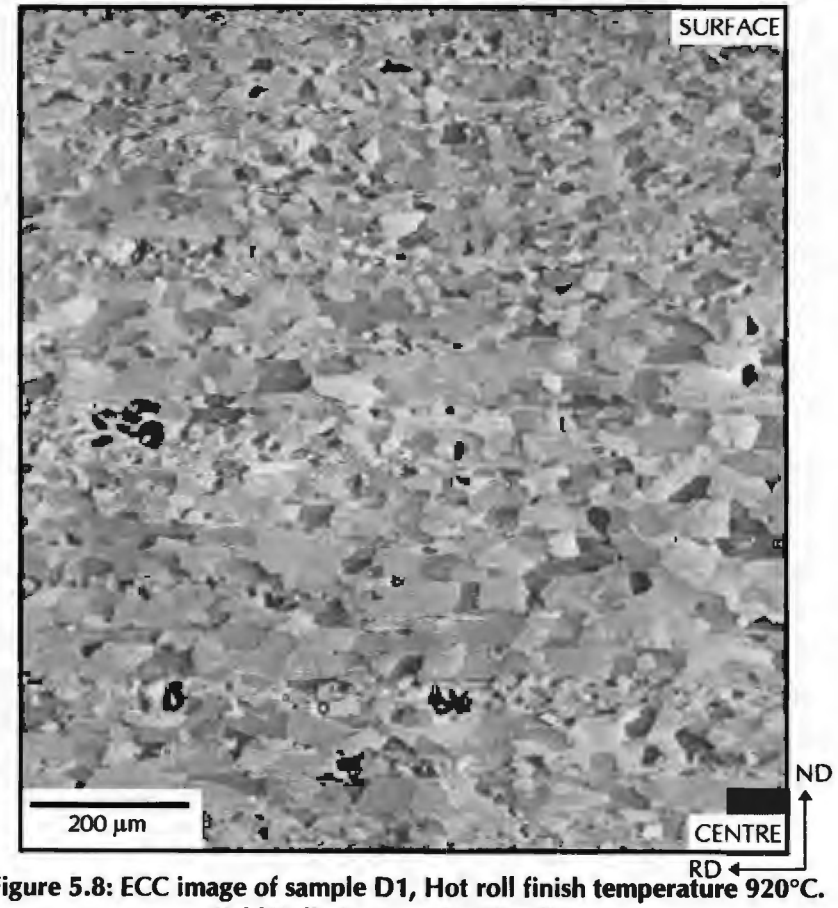

Figure 5.8: ECC image of sample D1, Hot roll finish temperature 920°C. Cold Rolled - Annealed Condition

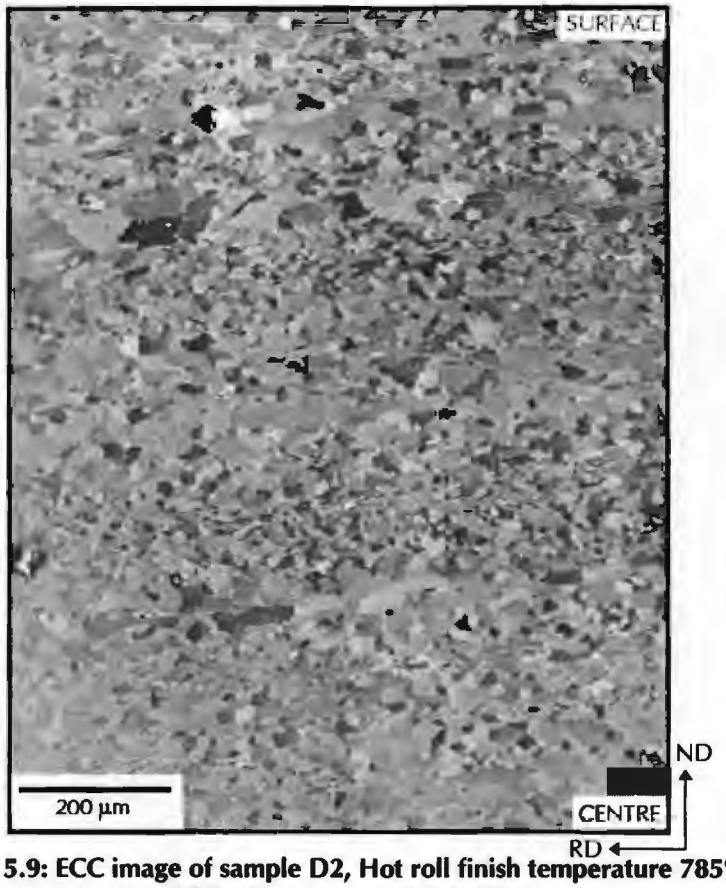

Figure 5.9: ECC image of sample D2, Hot roll finish temperature 785°C. Cold Rolled - Annealed Condition

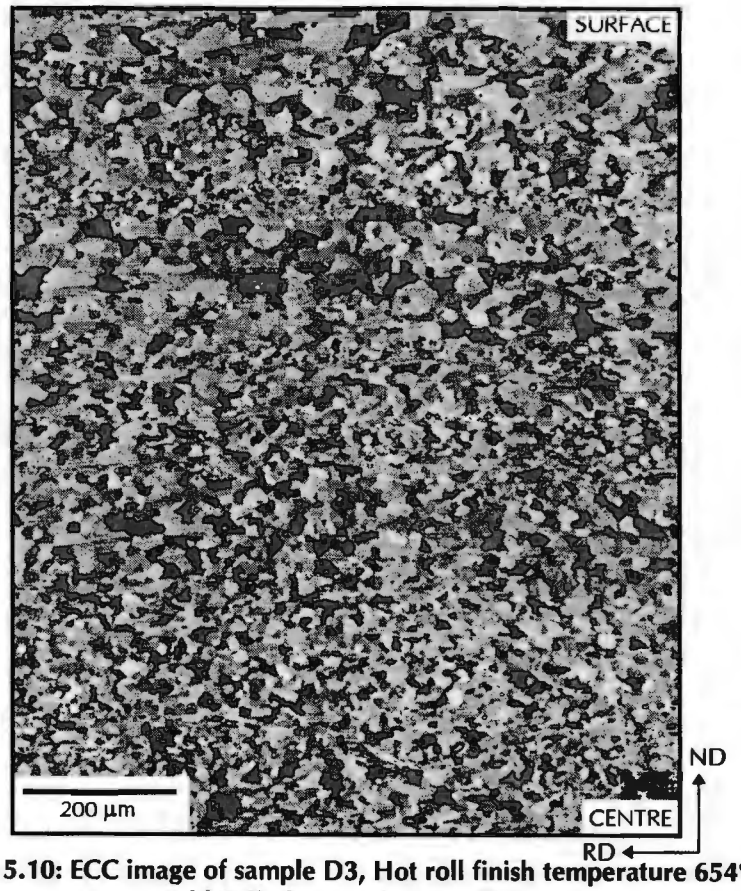

Figure 5.10: ECC image of sample D3, Hot roll finish temperature 654°C. Cold Rolled -Annealed Condition

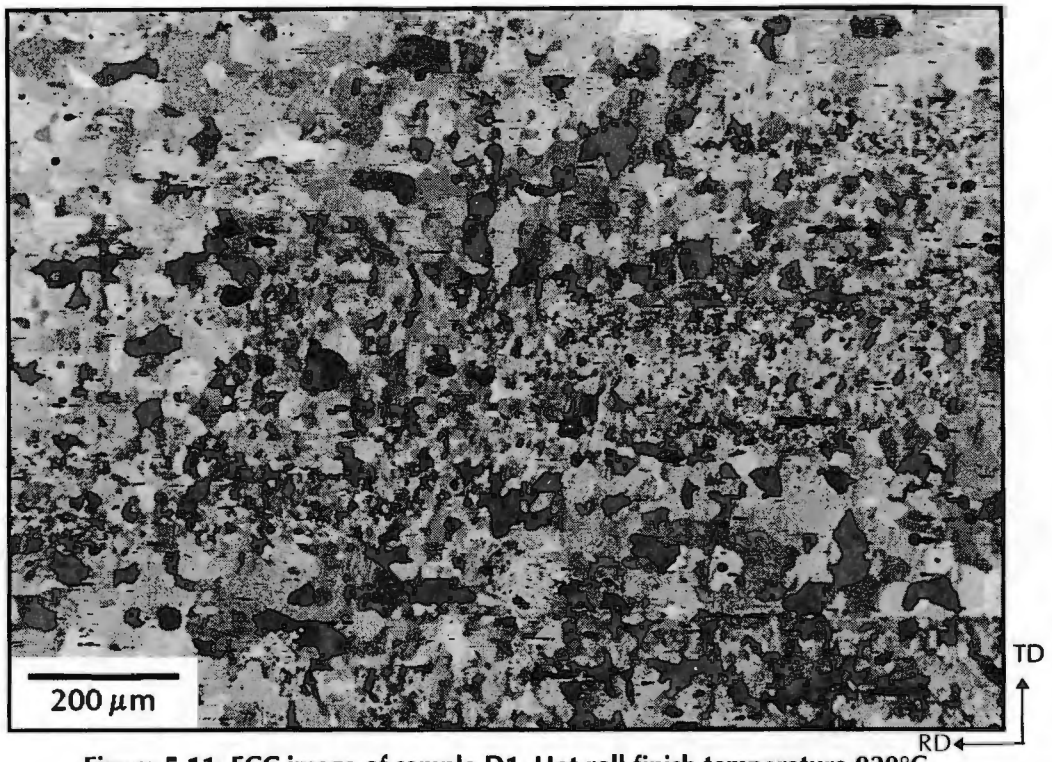

Figure 5.11: ECC image of sample D1, Hot roll finish temperature 920°C. Cold Rolled - Annealed (Rolling plane section).

5.2 Bulk Texture

Hot Rolled (stage A)

The near surface regions of the three specimens A1, A2 and A3 all show the presence of Goss texture. This texture is the most well defined in specimen A3 and an example of the φ_1 constant ODF for this specimen is presented in figure 5.12. Although the α-fibre is present to a limited extent in specimen A1, and to a much lesser extent in specimen A3, there is a relatively strong presence of the $\{001\}<110>$ texture in specimen A2. The rotated cube texture is also most well formed in specimen A2. The φ_1 constant ODF for specimen A2 is shown in figure 5.13.

The texture in the centre of the specimens differs quite significantly across the range of hot roll finish temperatures. By far the most convincing texture is the development of a γ-fibre texture in the centre of specimen A3. The φ_1 constant ODF is presented in figure 5.14 and demonstrates a dominant $\{111\}<110>$ texture. The mid-plane of specimen A2 is dominated by the presence of the α-fibre texture with the $\{001\}<110>$ component being the most well defined

(figure 5.15). Goss orientations are absent in the centre of both sample A2 and A3. The textures in the centre of sample A1 are not well defined but there are indications that both near Goss and near α-fibre textures are present. The φ_1 constant ODF in figure 5.16 demonstrates these textures more clearly.

Hot Rolled-Annealed (stage B)

The Goss texture remains evident in the near surface region of all three samples. Figure 5.17 indicates the φ_1 constant ODF for sample B1. In all cases Goss is the dominant texture although it is less defined in sample B2. Variants of the cube texture are also present to some extent. The central regions of alloys B1 and B2 demonstrate dominant α-fibre textures. The α-fibre texture is most convincing in sample B1 and the components include $\{001\}<110>$, $\{110\}<110>$ and near $\{112\}<110>$. The φ_1 constant ODF is presented for the sample in figure 5.18. Some indications of a ζ-fibre (<011>//ND) exists in sample B2 and the strong components are near $\{011\}<411>$ and $\{011\}<111>$. The φ_2 constant ODF displays this texture in figure 5.19. The Goss texture is dominant in the mid-plane region of sample B3 although indications are that it is near-Goss rather than ideal. There are also signs of residual γ-fibre texture as shown by the φ_2 constant ODF in figure 5.20.

Cold Rolled (stage C)

The textures in the cold rolled condition produce by far the most well defined ODF diagrams. The expected α-fibre texture dominates in all three samples in both the near surface and mid-plane regions. Although there is a definite variation in texture produced during hot rolling and annealing across the sample range, there is little difference in intensities after cold rolling. However, in all cases the texture intensity in the mid-plane region is stronger than the corresponding near surface texture. The ODF diagrams are well defined for the cold rolled condition and the α-fibre components $\{001\}<110>$ and $\{112\}<110>$ are both identifiable. An example of the φ_1 constant ODF for the mid-plane section of sample C2 is presented in figure 5.21.

Cold Rolled-Annealed (stage D)

Near Surface

Careful examination of the φ_2 constant ODF (figure 5.22) for sample D1 indicates the presence of a number of textures which include γ-fibre, ζ-fibre and cube. The ζ-fibre is the strongest texture incorporating both a strong Goss component and a $(011)[2\bar{1}1]$ component, although the Goss is rotated slightly from the ideal. The γ-fibre is comparatively weaker with equal intensities of the $\{111\}<112>$ and $\{111\}<110>$ variants. In the case of sample D2, the φ_1 constant ODF section exhibits both strong γ-fibre and Goss texture in equal proportion (figure 5.23). A minor component for this sample is the cube texture. For sample D3, a similar situation occurs where both Goss and γ-fibre textures are strongest. Examination of the φ_1 constant ODF (figures 5.24) also indicates minor components of cube and the α-fibre.

Mid-Plane

As opposed to the γ-fibre of the near surface region, the mid-plane regions of sample D1 are dominated by a partial α-fibre and Goss texture. Secondary components comprise of weak cube and γ-fibre textures (figure 5.25). The mid-plane region of D2, however, has similar textures to the surface regions in that the γ-fibre and Goss texture are dominant and are similar in intensity. Examination of the φ_1 constant ODF for sample D3 shows a very strong $\{111\}<112>$ component of the γ-fibre, and to a lesser extent the $\{111\}<110>$ component, and weaker Goss textures (figure 5.26). The cube or α-fibre components visible in D1 are absent in this sample.

In order to provide confirmation on the principal textures, the α-fibre and γ-fibre diagrams have been included in Appendix A. The overall textures are generally weak, but the trends identified in the ODF diagrams are well supported in the fibre diagrams.

Summary

Table 5.1 summarises the main textures which occur after each process stage. In each case all the texture components are listed, where the major components are presented in bold typeface.

Table 5.1: Summary of the main texture components of the laboratory rolled heats.

	HOT ROLLING		ANNEALING		COLD ROLLING		FINAL ANNEALING	
	SURFACE	*CENTRE*	*SURFACE*	*CENTRE*	*SURFACE*	*CENTRE*	*SURFACE*	*CENTRE*
SAMPLE 1 FINISH TEMP 920°C	**Goss**	**Near Goss** Near α-fibre	**Goss**	**α-fibre**	**α-fibre**	**α-fibre**	**γ-fibre** **ζ-fibre** Cube	**Partial α-fibre** **Goss** γ-fibre Cube
SAMPLE 2 FINISH TEMP 785°C	**Goss** α-fibre	**α-fibre**	**Goss** (weaker than B1 and B3)	**α-fibre**	**α-fibre**	**α-fibre**	**γ-fibre** **Goss** Cube	**γ-fibre** **Goss**
SAMPLE 3 FINISH TEMP 654°C	**Goss**	**γ-fibre**	**Goss**	**Near-Goss** γ-fibre	**α-fibre**	**α-fibre**	**γ-fibre** **Goss** Cube α-fibre	**γ-fibre** Goss

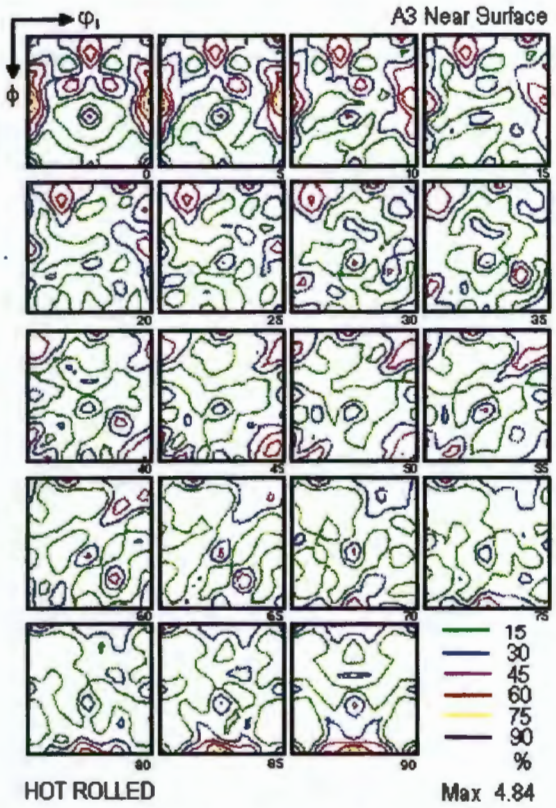

Figure 5.12: A3, φ_1 constant, near surface.

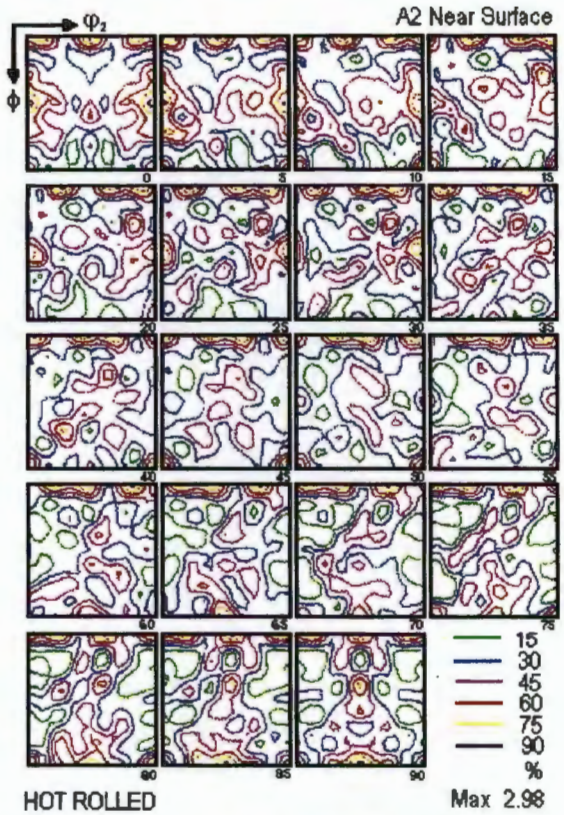

Figure 5.13: A2, φ_1 constant, near surface.

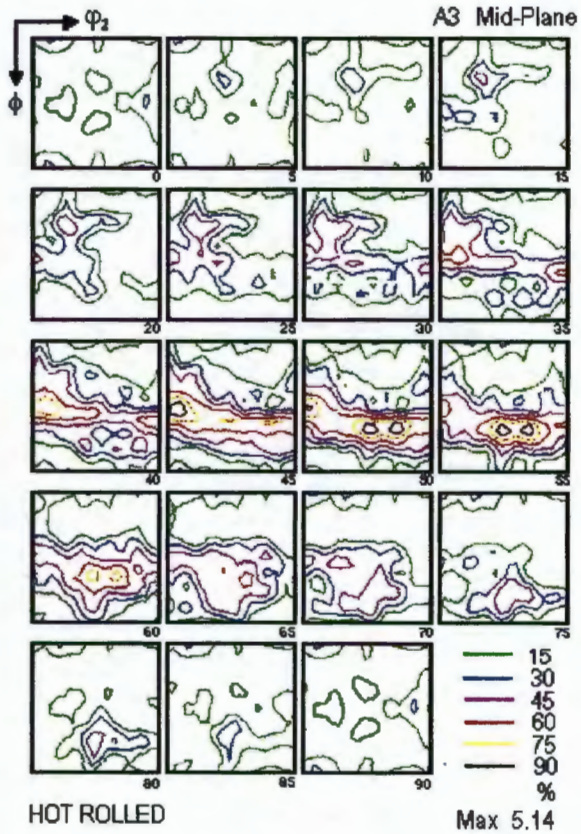

Figure 5.14: A3, φ_1 constant, mid-plane.

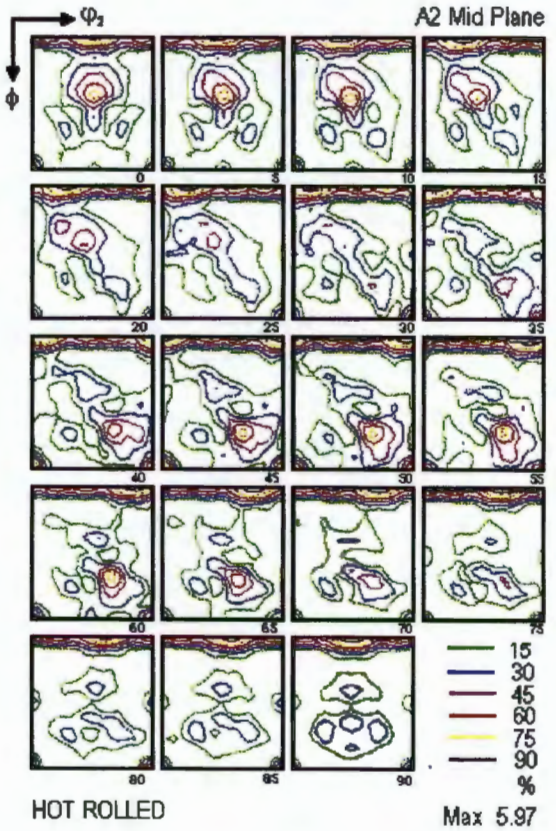

Figure 5.15: A2, φ_1 constant, mid-plane.

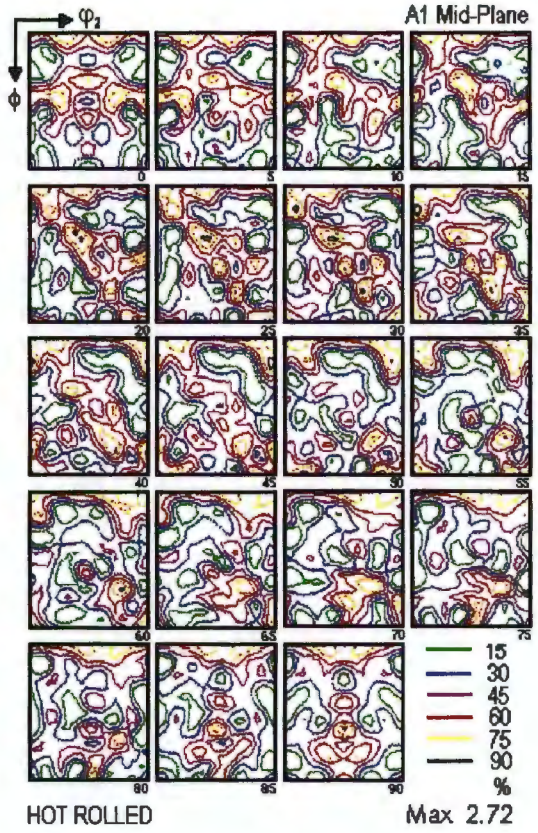

Figure 5.16: A1, φ_1 constant, mid-plane.

Figure 5.17: B1, φ_1 constant, near surface.

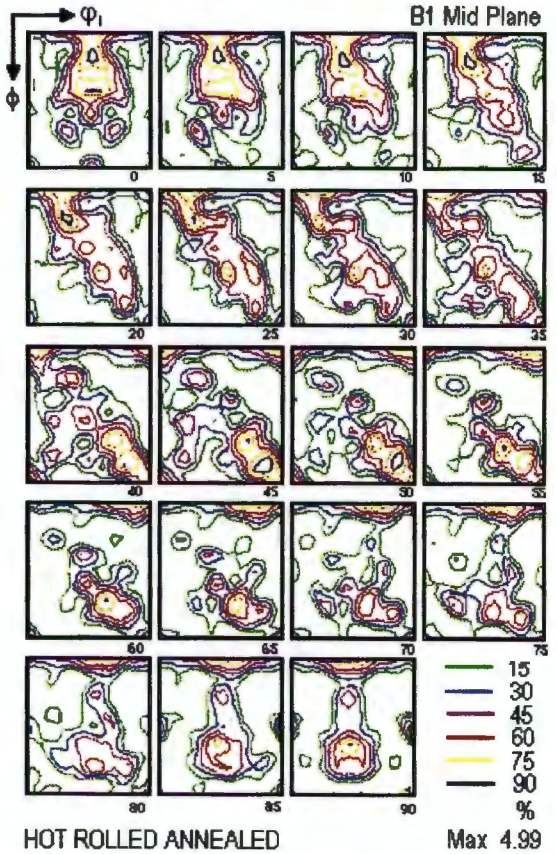

Figure 5.18: B1, φ_1 constant, mid-plane.

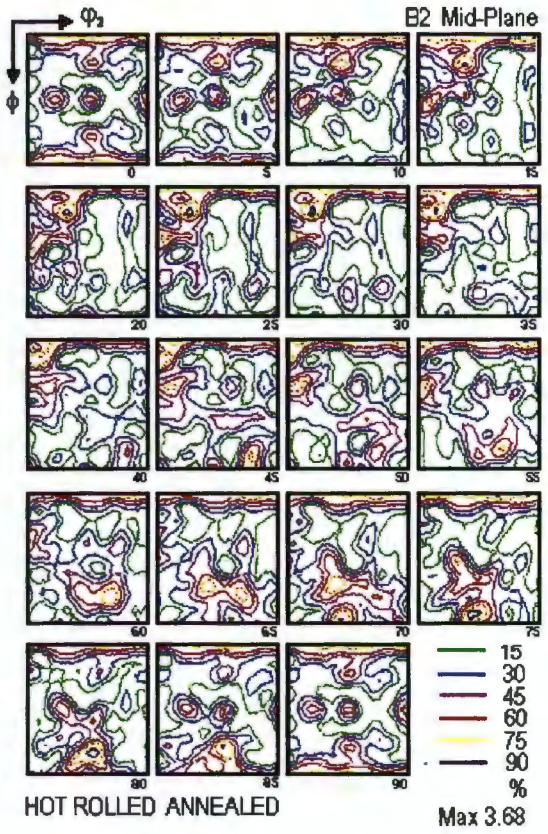

Figure 5.19: B2, φ_2 constant, mid-plane.

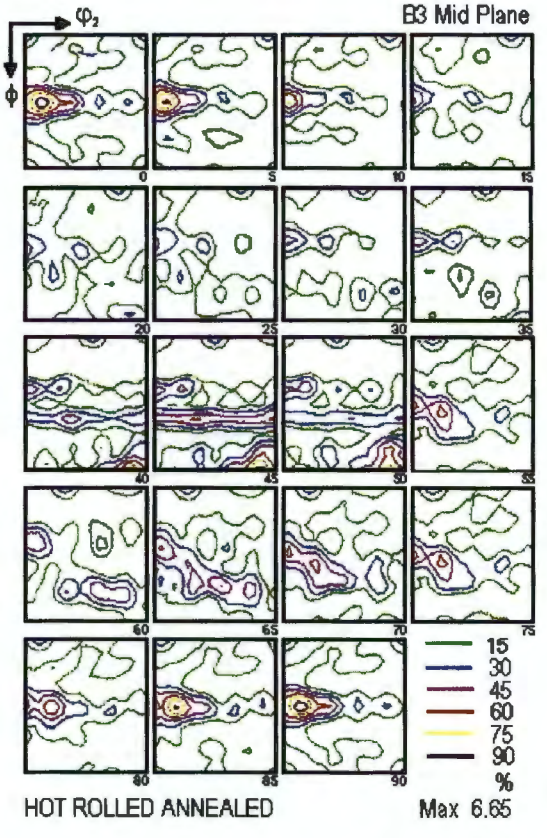

Figure 5.20: B3, φ_2 constant, mid-plane.

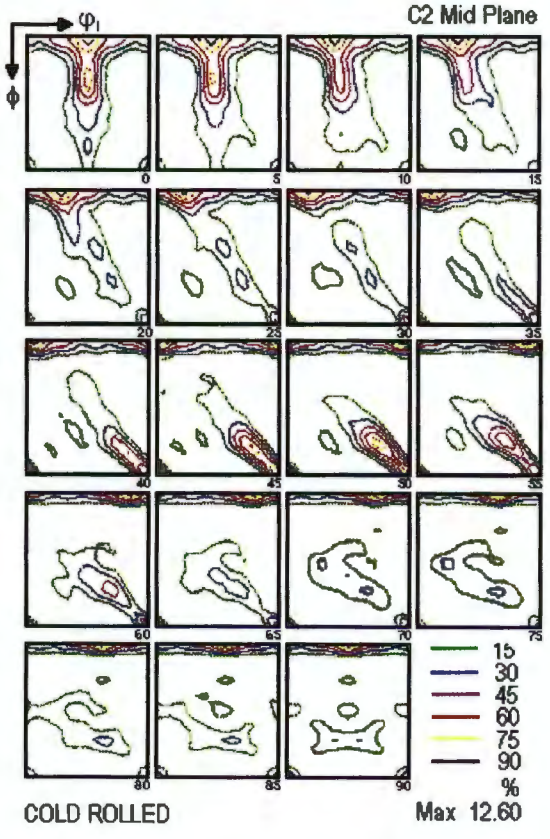

Figure 5.21: C2, φ_1 constant, mid-plane.

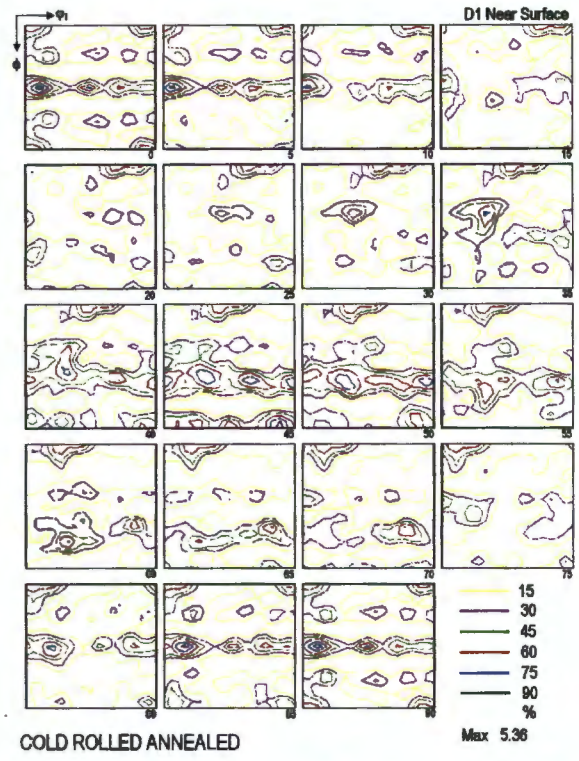

Figure 5.22: D1, φ_2 constant, near surface.

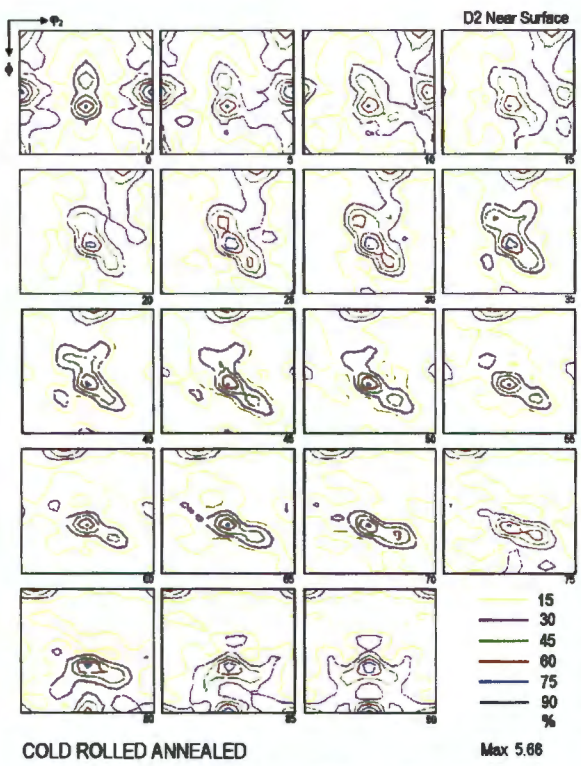

Figure 5.23: D2, φ_1 constant, near surface.

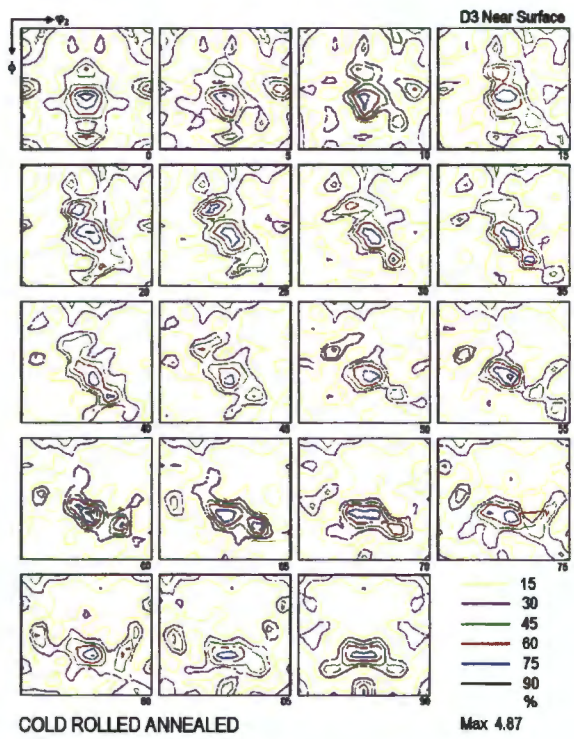

Figure 5.24: D3, φ_1 constant, near surface.

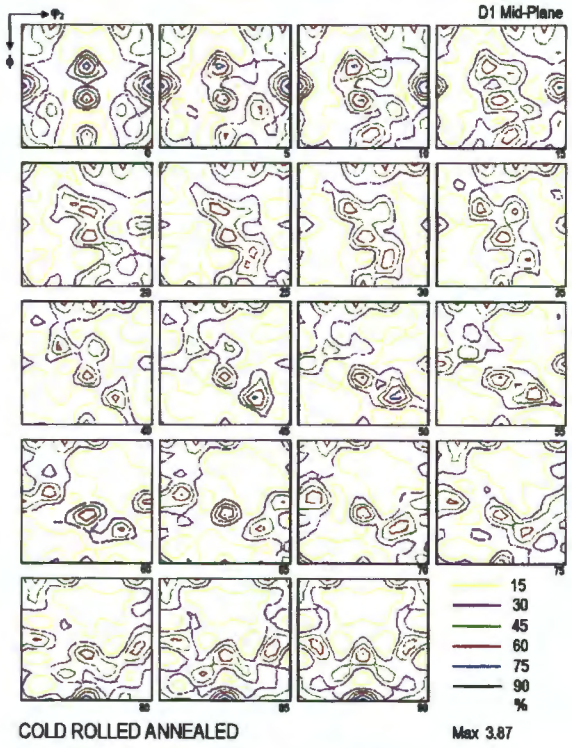

Figure 5.25: D1, φ_1 constant, mid-plane.

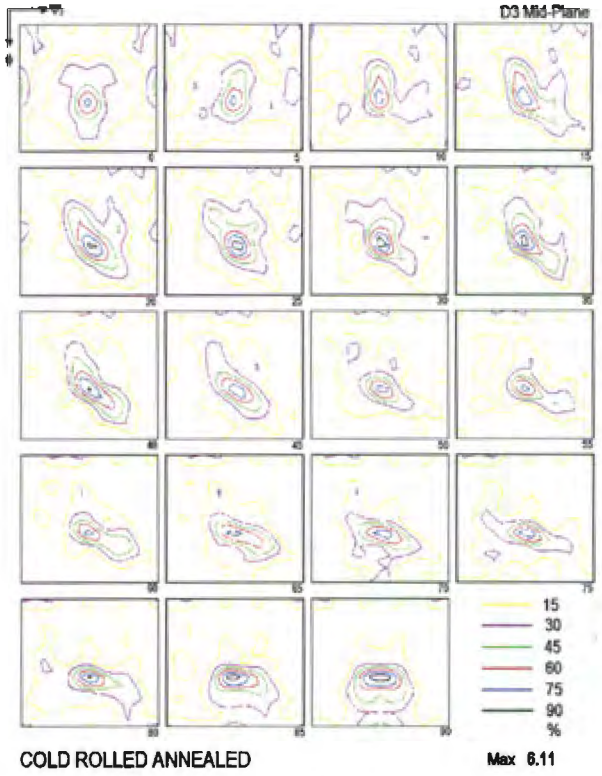

Figure 5.26: D3, φ_1 constant, mid-plane.

5.3 Ridging Analysis

The 3D topographical sections and the 2D contour maps for specimens D1, D2 and D3 elongated in the RD are presented in figures 5.27 to 5.30. Two principal features can be used to describe the form of the ridged surfaces, namely an overall corrugated or wavy effect, and a roughness effect superimposed on the corrugations. The corrugated nature of the surface is most clearly seen in specimen D3 where both the upper and lower surface maps are presented (figure 5.27). It is clear that the wavy profile of the lower surface follows that of the upper profile. (The lower surface has been inverted as a consequence of the measuring technique). The ridges produced by the corrugations are also fairly continuous in the RD. Notwithstanding the presence of the corrugations, the surface of specimen D3 is relatively smooth. In contrast, the corrugations in specimen D1 are less regular, and the overall surface produces a much rougher effect (figure 5.28). However, the amplitude of the corrugations is similar to specimen D3. Comparison of the two dimensional contour maps of specimen D1 and D3 highlights the differences in the overall roughness (figures 5.28 and 5.29).

The surface roughness of specimen D2 appears intermediate between that of D1 and D3 as shown in figure 5.30. A summary of the surface roughening effects for the tensile tests performed on the laboratory rolled heats is given in Table 5.2.

Table 5.2: Results of tensile tests performed on the laboratory rolled heats.

Tensile axis (from RD)	Ra (μm)	PV (μm)	Corrugations	Roughness Effect
D1: 0°	3.38	23.25	Severe	High
45°	2.91	22.53	None	High
90°	1.82	14.59	None	High
D2: 0°	2.88	22.75	Severe	Medium
D3: 0°	2.71	18.90	Severe	Low
45°	1.38	11.21	None	Low
90°	1.15	8.41	None	Low

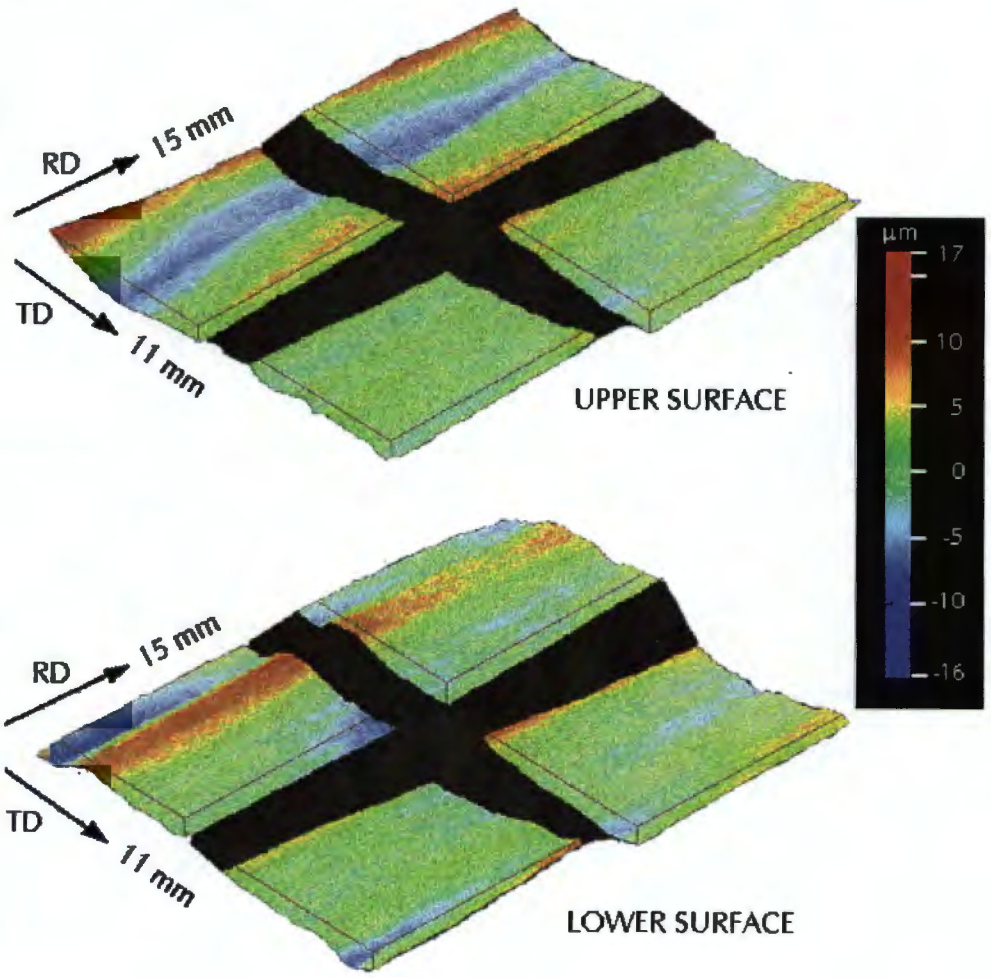

Figure 5.27: Specimen D3 upper and lower surfaces, elongated in the RD.

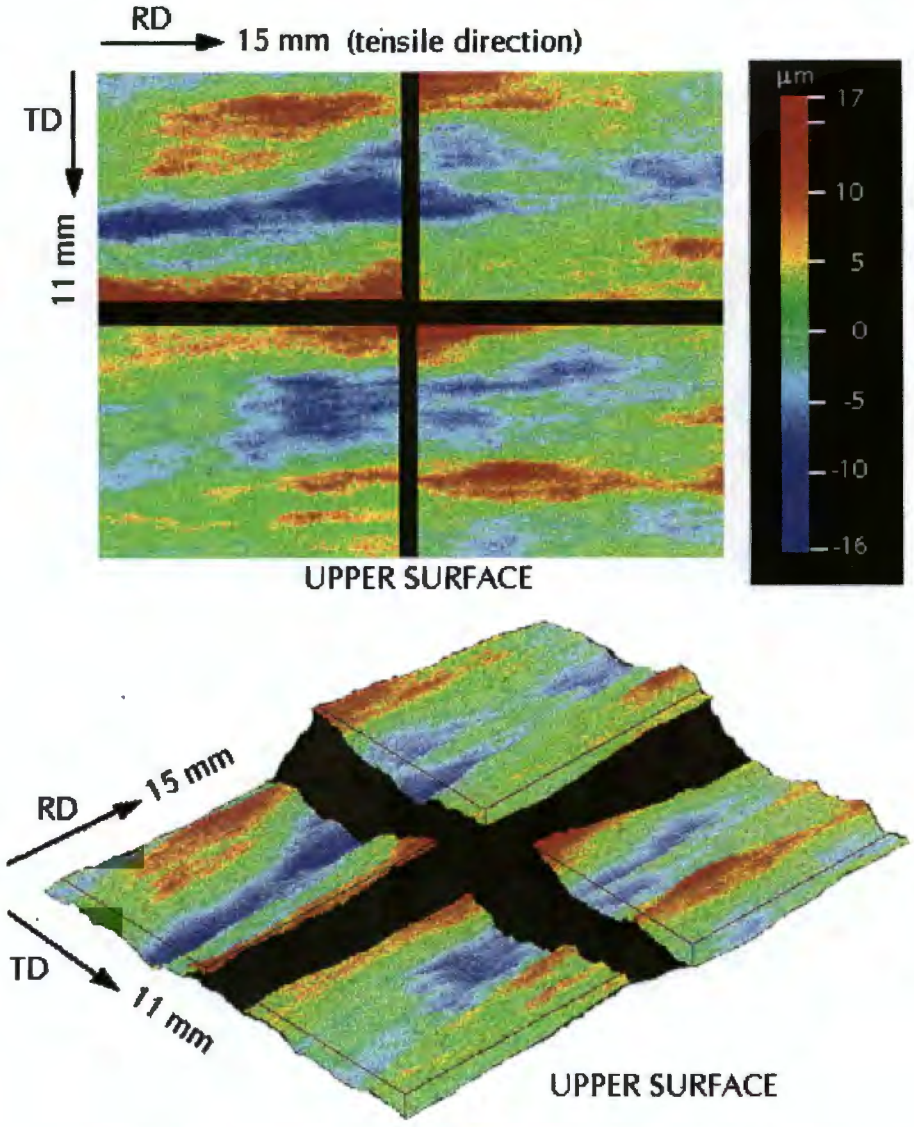

Figure 5.28: Specimen D1 upper surface, elongated in the RD.

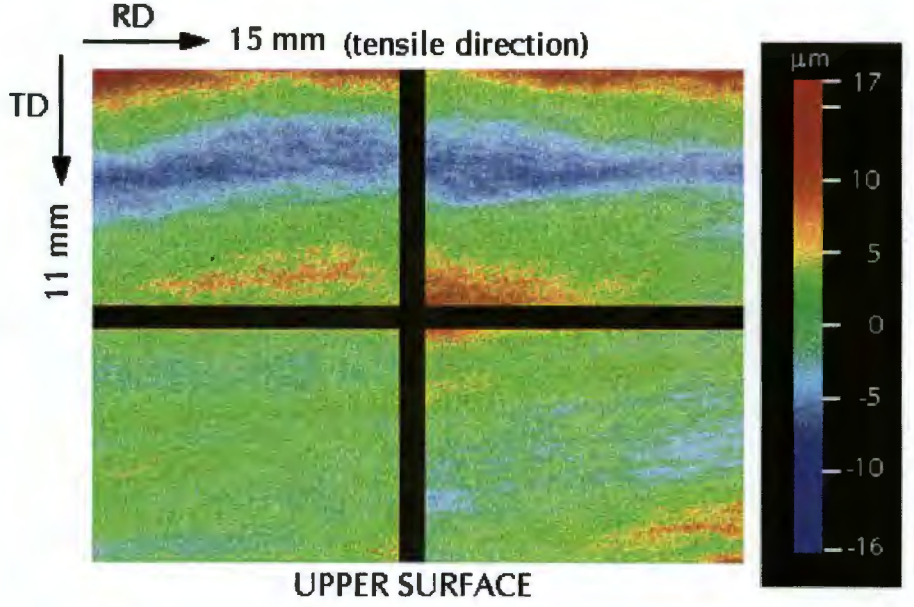

Figure 5.29: Specimen D3 upper surface, elongated in the RD.

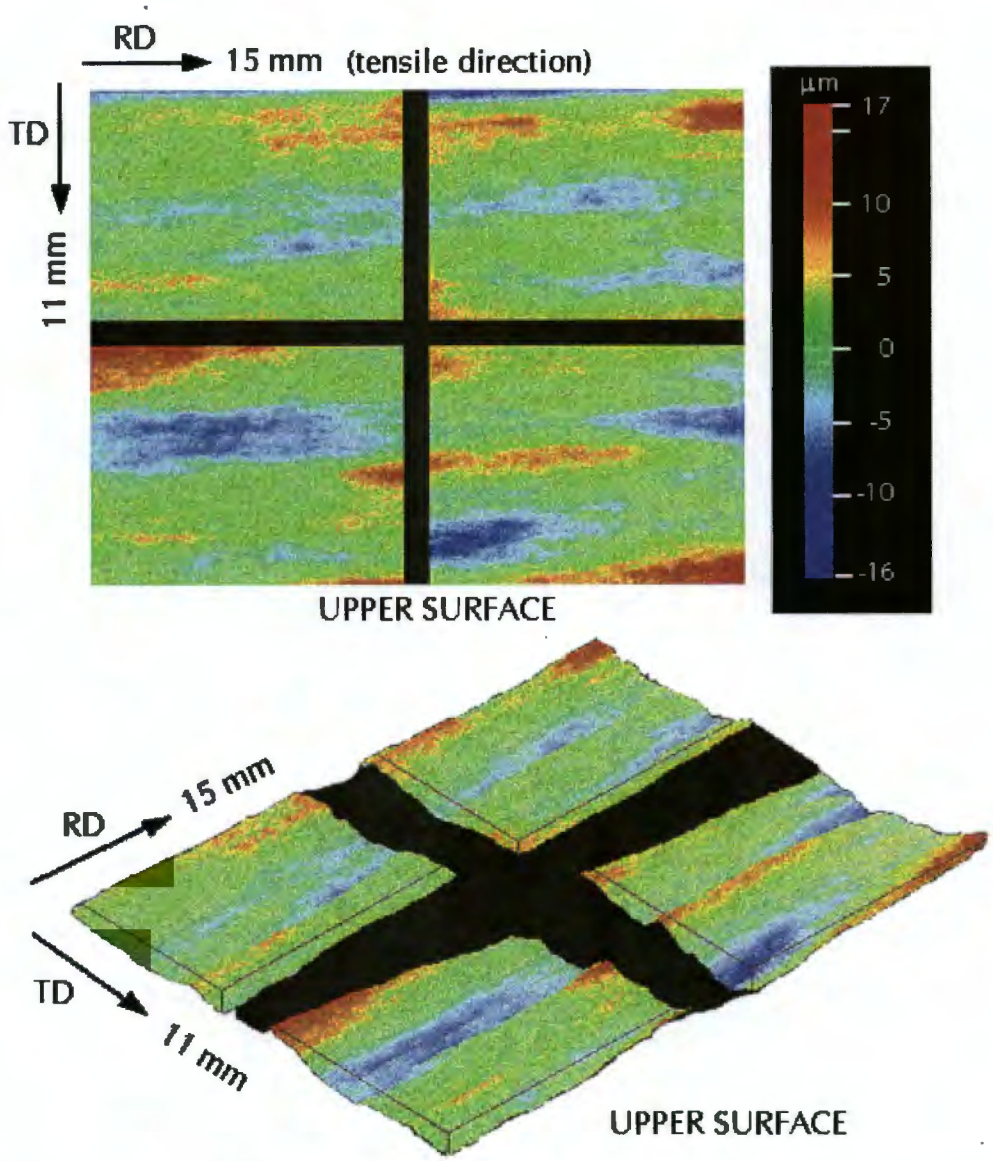

Figure 5.30: Specimen D2 upper surface, elongated in the RD.

For tensile specimens of heats D1 and D3 elongated at 45° and 90° degrees to the RD, the situation is modified. Of the two features used to describe the topography of the specimens elongated in the RD, namely a surface roughness and a corrugation effect, it is the roughening effect which remains almost unchanged, while the corrugation behaviour is altered. Comparison of the topography for specimens D1 and D3 elongated in the RD against those elongated in the TD, shows little variation in surface roughness between the respective orientations. Compare the 3D topography sections in figures 5.27 and 5.28 against figures 5.31 and 5.32. Specimen D1, which exhibited the most severe roughness when elongated in the RD, again indicates a greater

surface roughening effect relative to specimen D3, (compare figures 5.33 and 5.34). The surface of specimen D3 is relatively smooth with extended bands of fine roughness in the RD (figure 5.34). The only notable difference in roughening behaviour, when the tensile axis is rotated by 90° so that it is aligned parallel to the TD, is that the bands of roughness, particularly on specimen D3, are broader in the transverse direction.

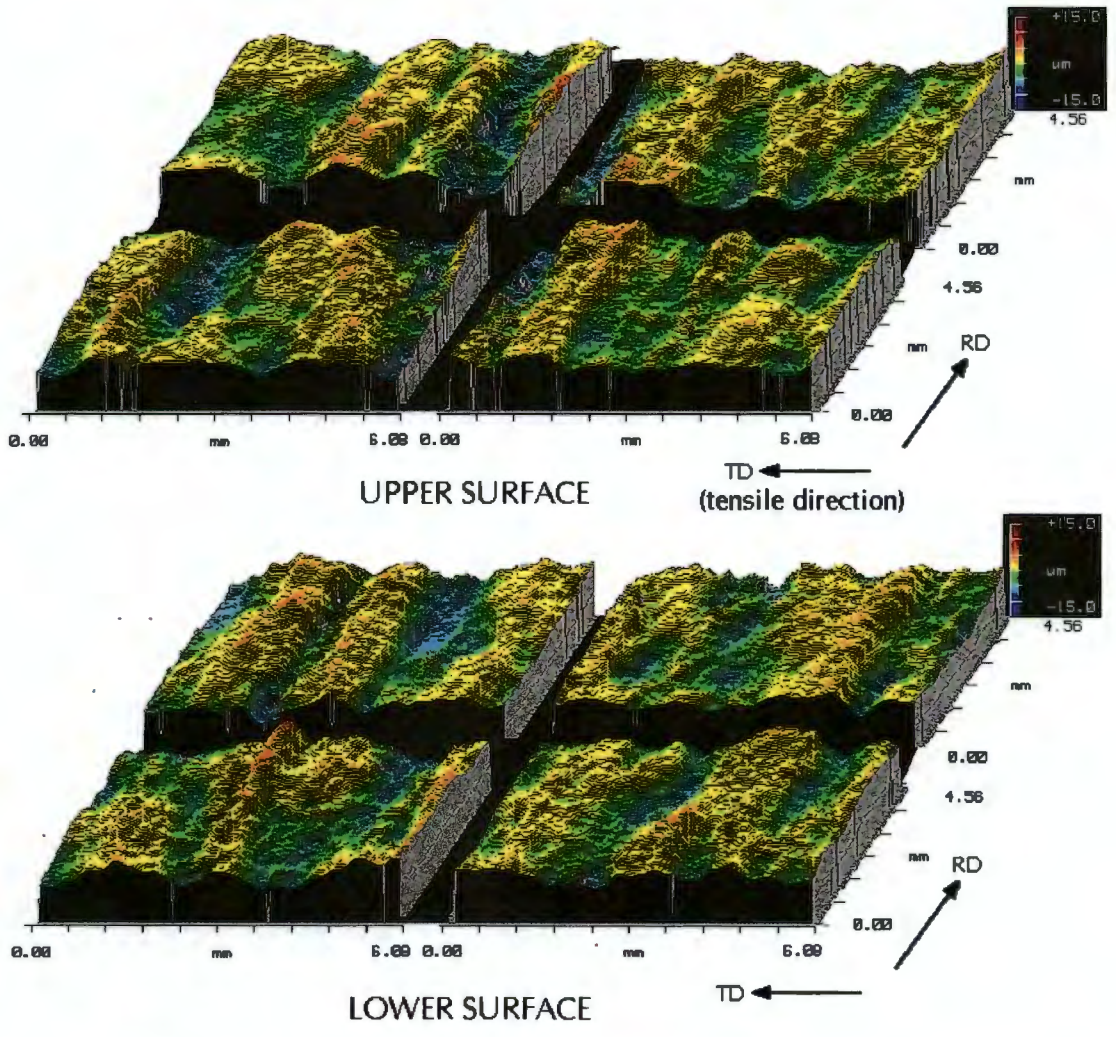

Figure 5.31: Specimen D1 upper and lower surfaces, elongated in the TD.

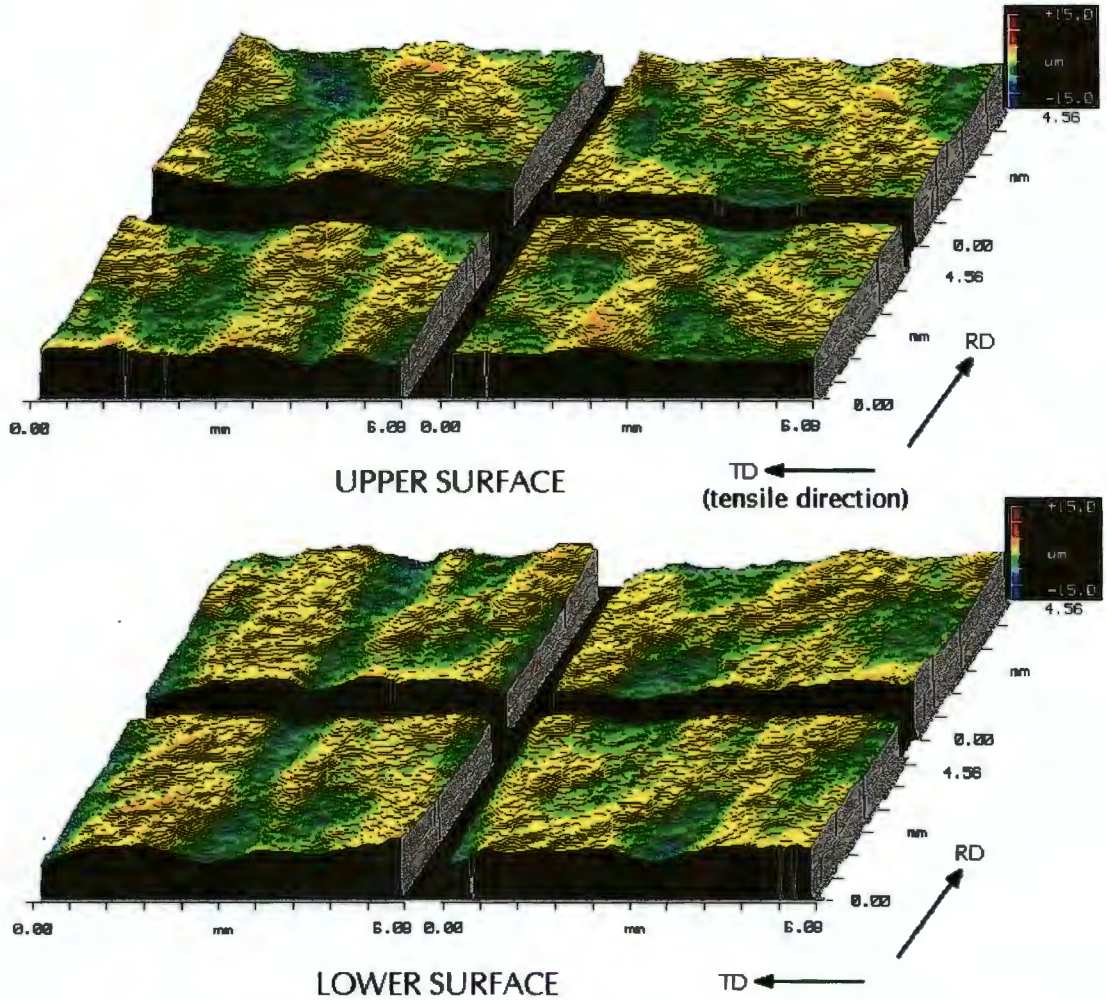

Figure 5.32: Specimen D3 upper and lower surfaces, elongated in the TD.

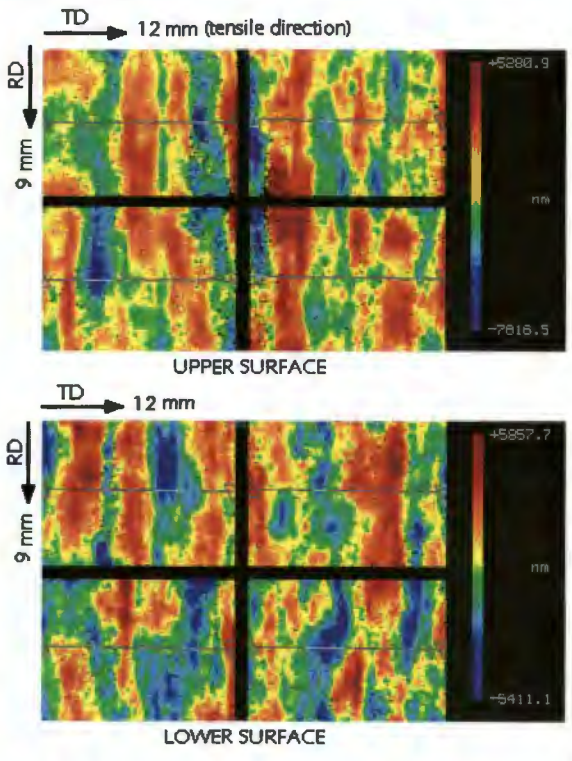

Figure 5.33: D1 elongated in the TD.

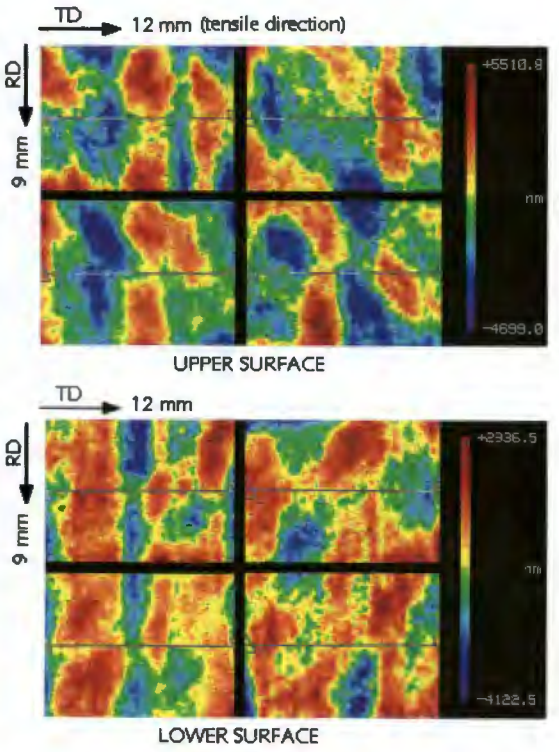

Figure 5.34: D3 elongated in the TD.

The overall corrugated effect visible on the specimens elongated in the RD is, however, not apparent for the specimens elongated in the TD. Results of three parallel surface profiles (both upper and lower surfaces) for specimen D3 elongated in the RD and TD are presented in figures 5.35 and 5.36 respectively. The lower surface profiles have been reversed to allow a correct through-thickness profile. The surface profiles in figure 5.35 for elongation in the RD demonstrate a severely distorted surface topography. The grain scale surface roughness is evident superimposed upon the low frequency undulations (full scale of displacement = 24 μm). In general, the peaks and valleys of the upper and lower surfaces correspond, which indicates that the sheet has corrugated, however, the finer roughness masks this corrugated effect. In contrast, the three profiles for the specimens elongated in the TD in figure 5.36 indicate a shallow and consistent surface roughness occurring across the entire measured length of 25 mm (full scale of displacement = 10 μm). Little similarity between the upper and lower surfaces is visible which marks the absence of a corrugated effect.

A similar situation is evident for the specimens deformed at 45° to the RD. The surface topography for D1 and D3 deformed at 45° are shown in figures 5.37 and 5.38. Elongated areas of surface roughness, resembling those on the specimens elongated in the RD and TD, are also found on both these specimens. Again D1 appears rougher than D3 and neither specimens indicate a corrugated effect.

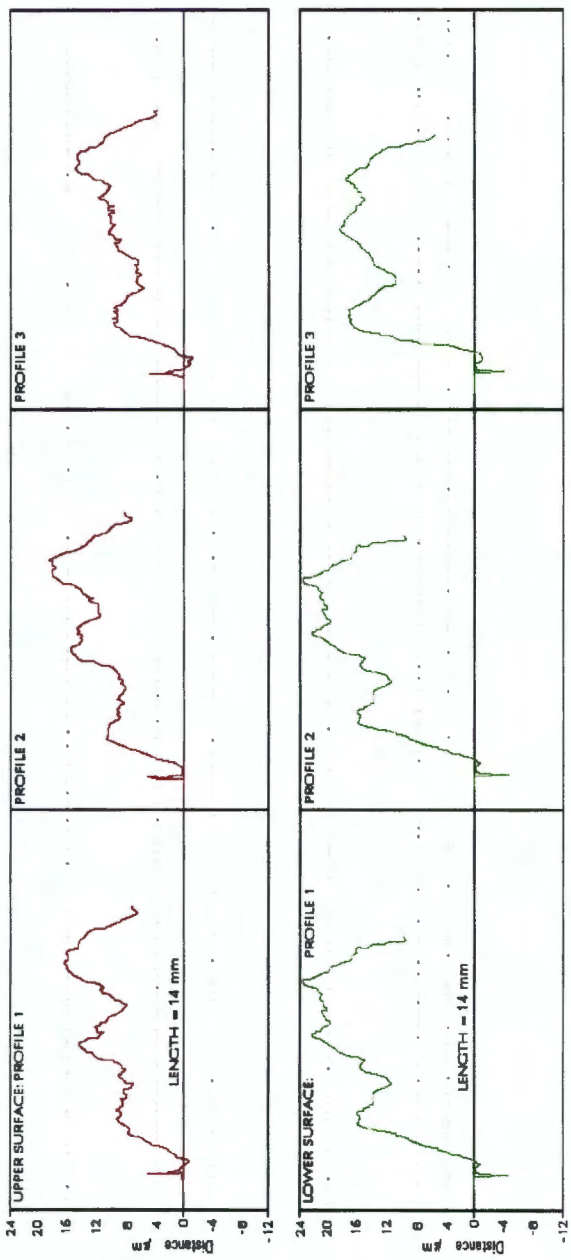

Figure 5.35: Profiles for D3 elongated in the RD.

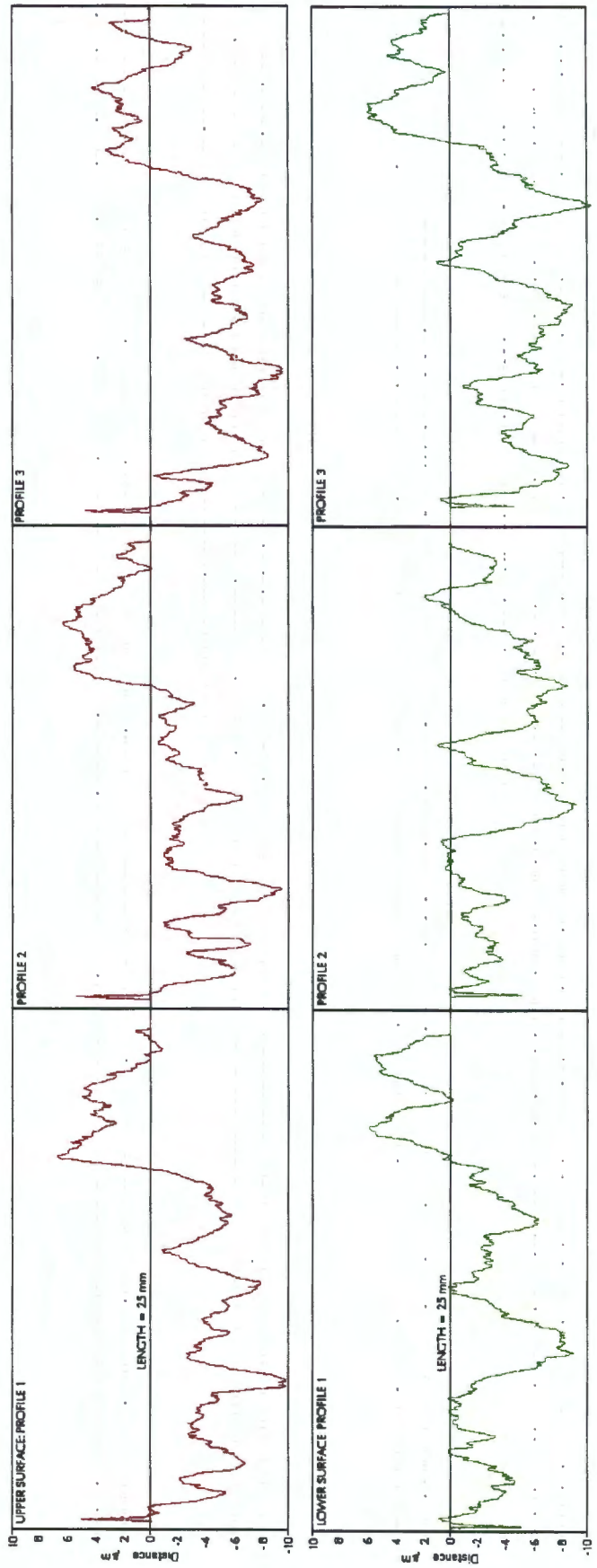

Figure 5.36: Profiles for D3 elongated in the TD.

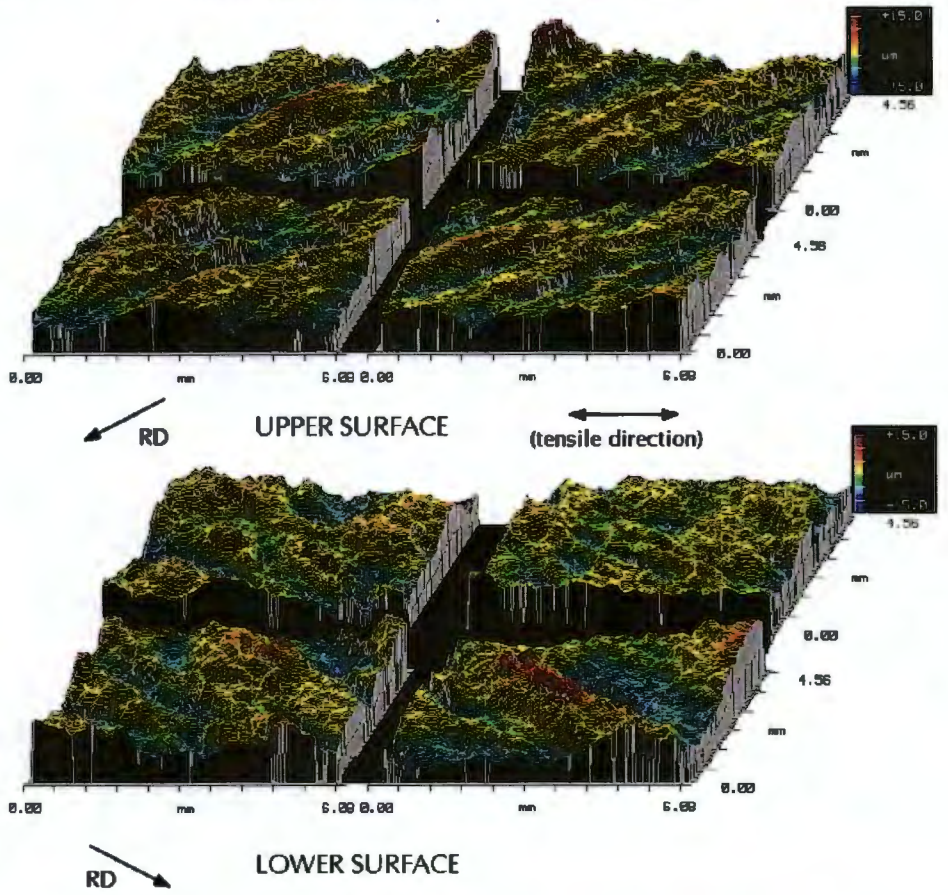

Figure 5.37: Specimen D1 upper and lower surfaces, elongated at 45° to RD.

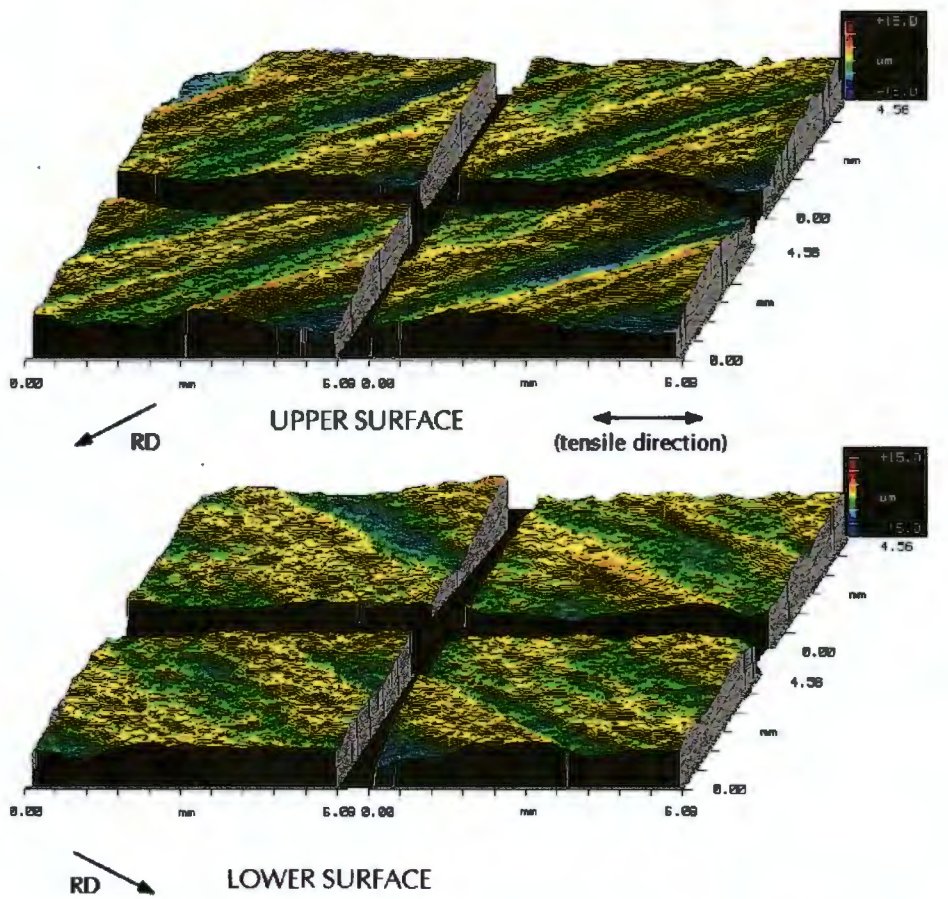

Figure 5.38: Specimen D3 upper and lower surfaces, elongated at 45° to RD.

The average surface roughness values for the tensile specimens D1 and D3 and the commercial steel are indicated in figure 5.39. A decrease in roughness value is evident for all the specimens as the tensile direction rotates away from the RD. In each case the roughness value after deformation in the TD is approximately half of the roughness value in the RD. Also, the roughness values for D1 and D3 are greater than those of the commercial steel when elongated in a similar direction.

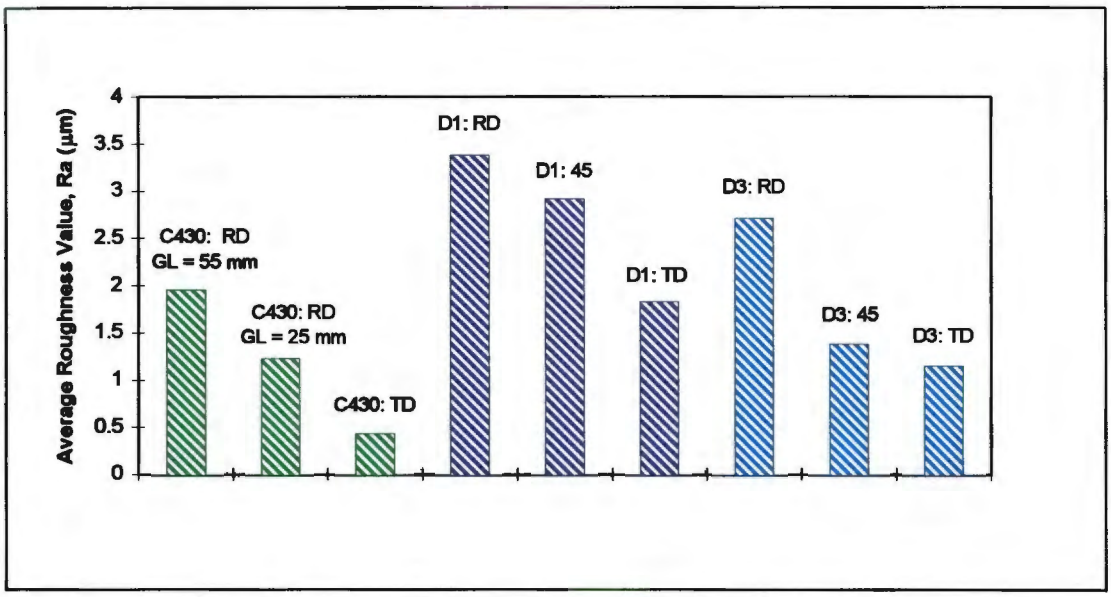

Figure 5.39: Graph of surface roughness measurements for tensile specimens. Labels indicate the alignment of the tensile axis.

5.4 MICROTEXTURE

The orientation and distribution of the principal texture components have been characterised via discrete polar plots and texture maps constructed from the microtexture data. The results of this investigation for samples D1 and D3 (cold rolled - annealed condition) are presented below. Refer to figures 4.19 and 4.23 for a polar plot and colour chart of ideal BCC textures.

D3 Transverse Section (Hot Roll Finish Temperature 654°C)

Two major components, namely $\{111\}<112>$ and $\{100\}<001>$, can be identified via the discrete orientation plots for sample D3. Comparison of the plots for each window across the section shows little variation in preferred orientation on a scale of the window size. However, as in the case of the

commercial steel transverse section, a greater deviation in preferred orientation is found when the windows are divided into four equal sections. Figure 5.40 indicates a polar plot for sample D3 which is representative of the texture components present in a single window, while figure 5.41 illustrates the projections of the polar plots recalculated for the reduced sections of the same window. The variation in preferred orientation between the sections is evident. A concentration of $\{112\}<110>$ and $\{001\}<110>$ orientations are found in section 3 while a larger percentage of $\{111\}<112>$ orientations are located in section 4 near the centre of the sheet.

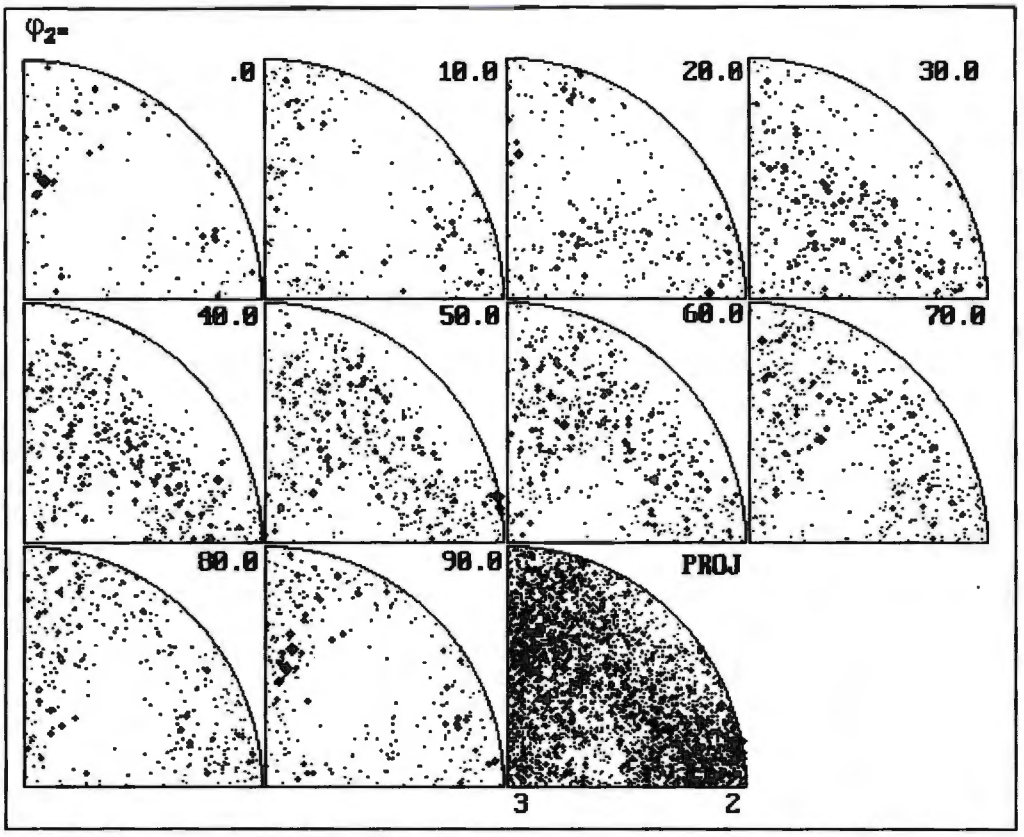

Figure 5.40: Polar plot representative of the texture components present in sample D3.

The constituent texture components could be more easily identified from the texture map constructed for this sample from the OIM microtexture data. Figure 5.42 illustrates the texture map using the same ideal orientations and colour assignments as used for the commercial steel texture maps. The two main texture components identified from the polar plots, namely $\{111\}<112>$ and $\{100\}<001>$, are visible throughout the section.

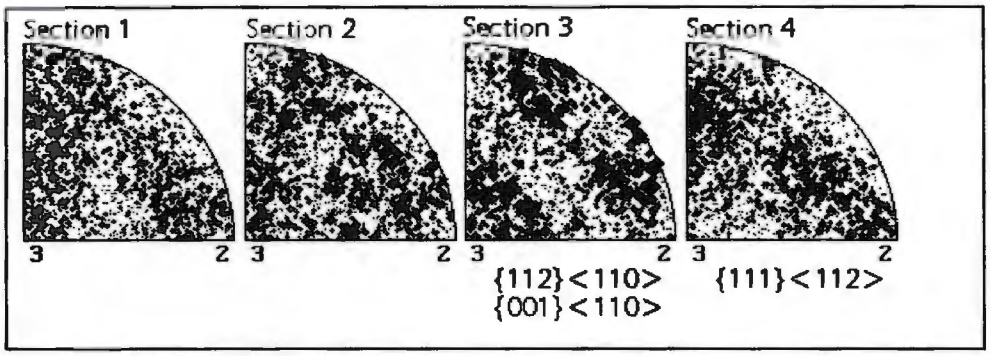

Figure 5.41: Polar plots for the four reduced sections of the above texture window.

They are however, not evenly spread across the texture windows but rather have a tendency to occur in bands extending in the TD. For example, there is a 200 μm thick band of mainly $\{111\}<112>$ texture which extends for approximately 3 mm in the TD near the centre line region. The minor component $\{111\}<110>$, on the other hand, is made up of small to medium grains which are distributed homogeneously across the section, while the $\{100\}<110>$ component occurs more often near the surface where it is fine grained. The $\{110\}<110>$ texture is also a minor component and is generally evenly spread across the section. In addition, the grain size variation visible in the microstructural investigation is evident in the texture map. Fine grains constitute the majority of the section (5-15 μm) with narrow patches of coarse grains (20-50 μm) running in the TD.

D1 Transverse Section (Hot Roll Finish Temperature 920°C)

For sample D1 the bimodal grain size, identified via the microstructural examination, is evident in the texture map (figure 5.43). Elongated bands of large grains extend in the TD and dominate the mid-section of the sample. Major texture components include $\{110\}<110>$ and $\{100\}<001>$ orientations. The $\{110\}<110>$ texture, which is a minor component in sample D3, is distributed unevenly over a large percentage of the section, while a greater percentage of cube grains are aggregated in the finer grained areas. In addition, the three minor components $\{112\}<110>$, $\{100\}<110>$ and $\{123\}<634>$ occur more often as large grains.

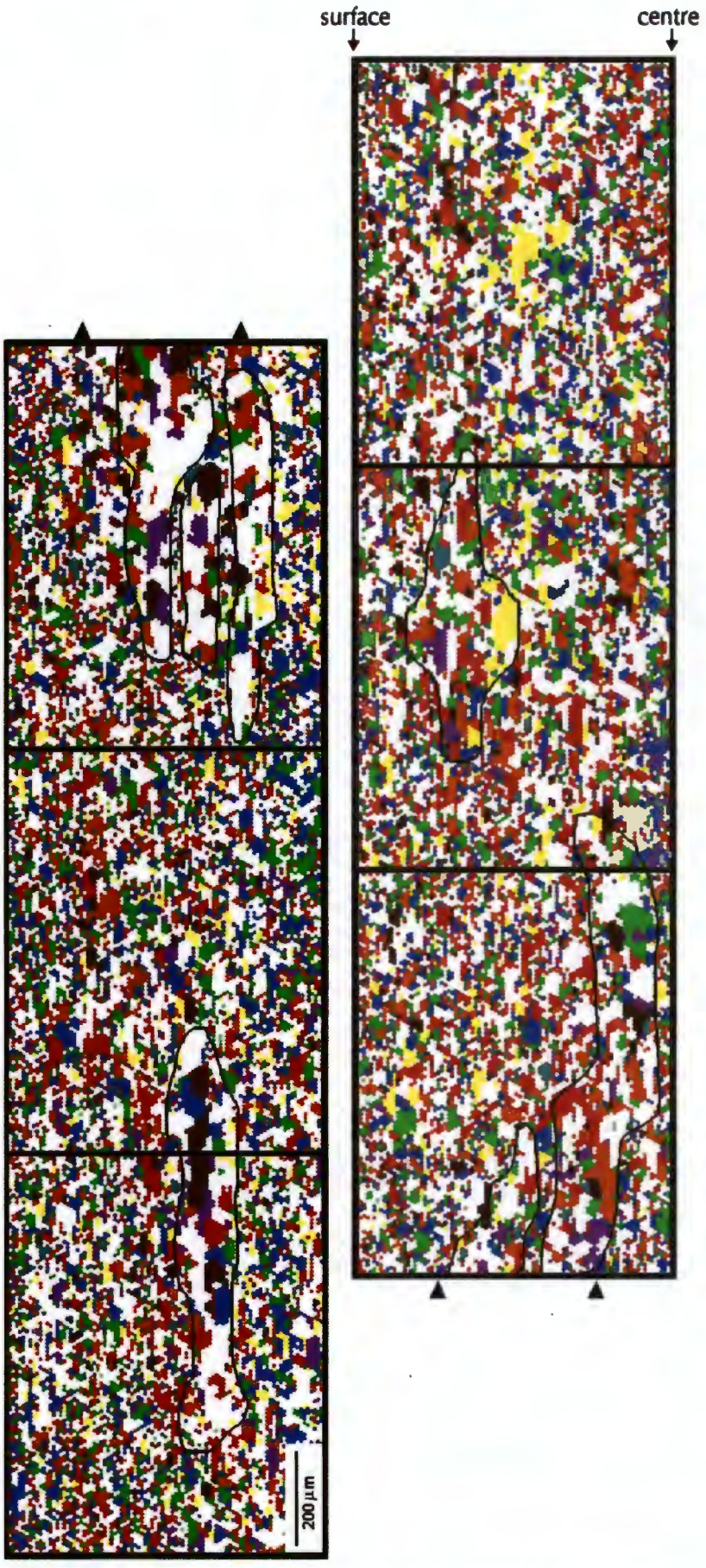

Figure 5.42: Texture map of sample D3 constructed in Euler space.

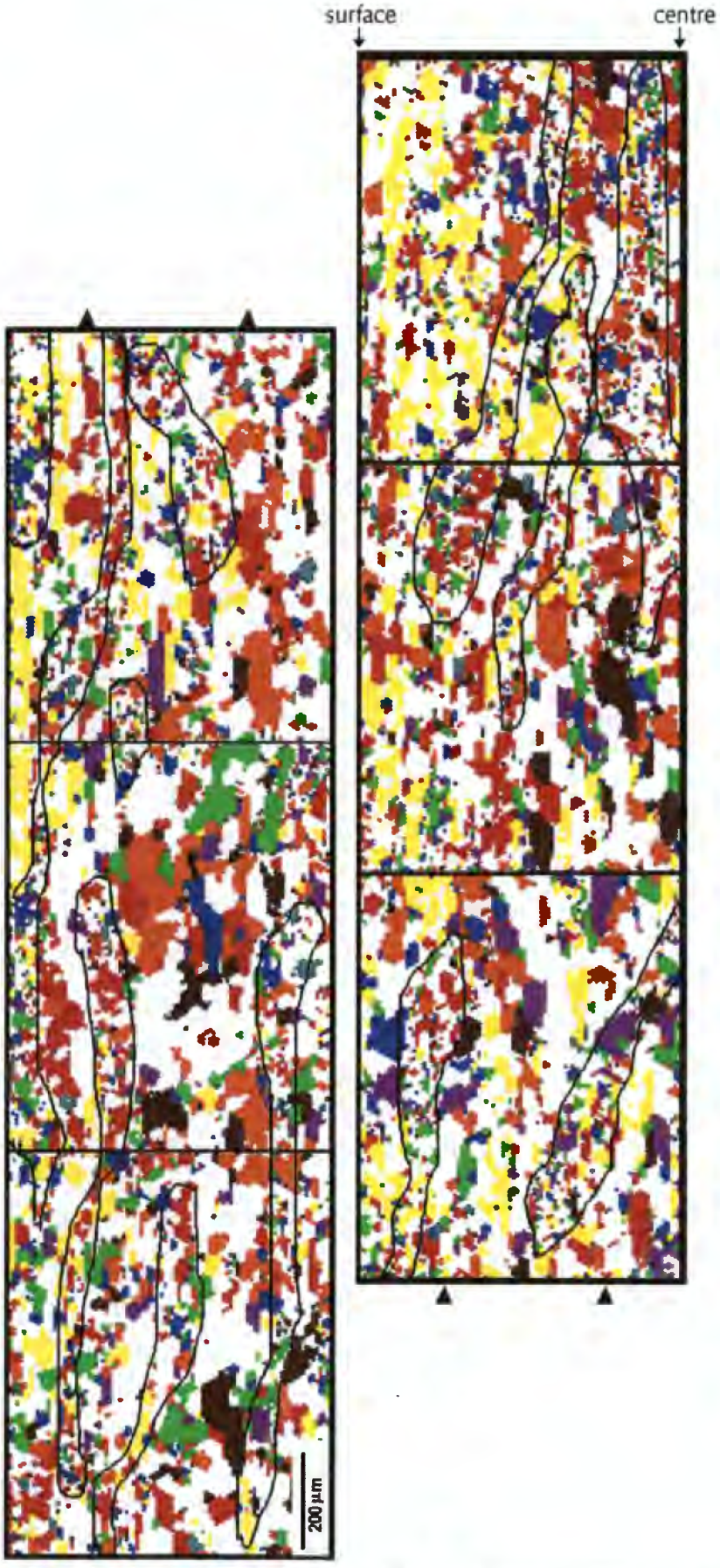

Figure5.43: Texture map of sample D1 constructed in Euler space.

The inhomogeneous distribution of the texture components from window to window could be confirmed from the polar plots for this sample. Figures 5.44 and 5.45 clearly demonstrate the variation in texture components for two texture windows of sample D1. The texture window in figure 5.44 shows a preponderance for {110} <110> texture while the window in figure 5.45 shows a more random texture including {110} <110>, {112} <110> and {111} <110> orientations. After reduction the sections of each texture window indicate distinct variations in texture as indicated by the four projections of a single window in figure 5.46.

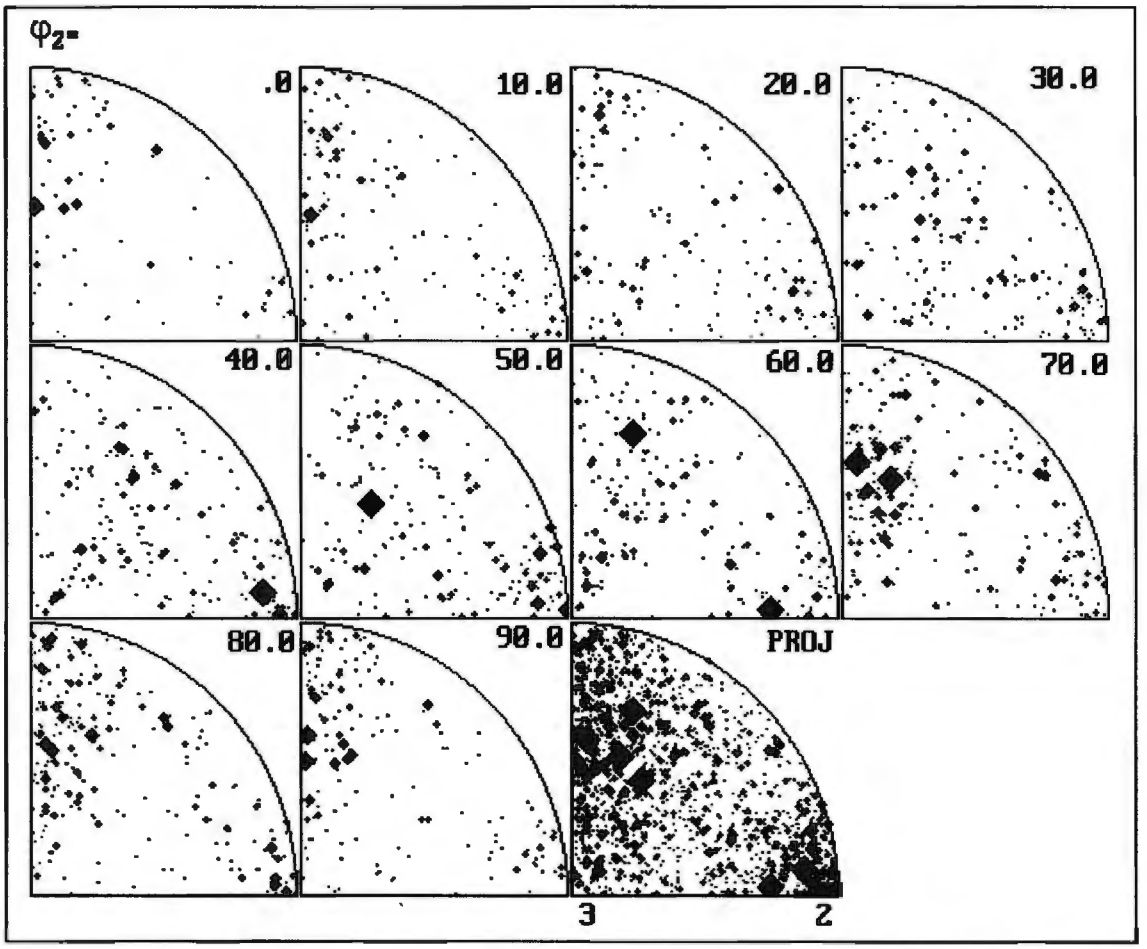

Figure 5.44: Polar plot for a single texture window of sample D1 indicating a concentration of {110} <110> texture.

A visual examination of the areas of fine and coarse grains, which have been delineated on the texture maps of both D3 and D1, and their respective orientations provides some evidence of a correlation between texture and grain size. This is particularly true for the {111} <112> orientation in sample D3 and

the {110}<110> orientations of sample D1 which appear mainly in the coarse grained regions.

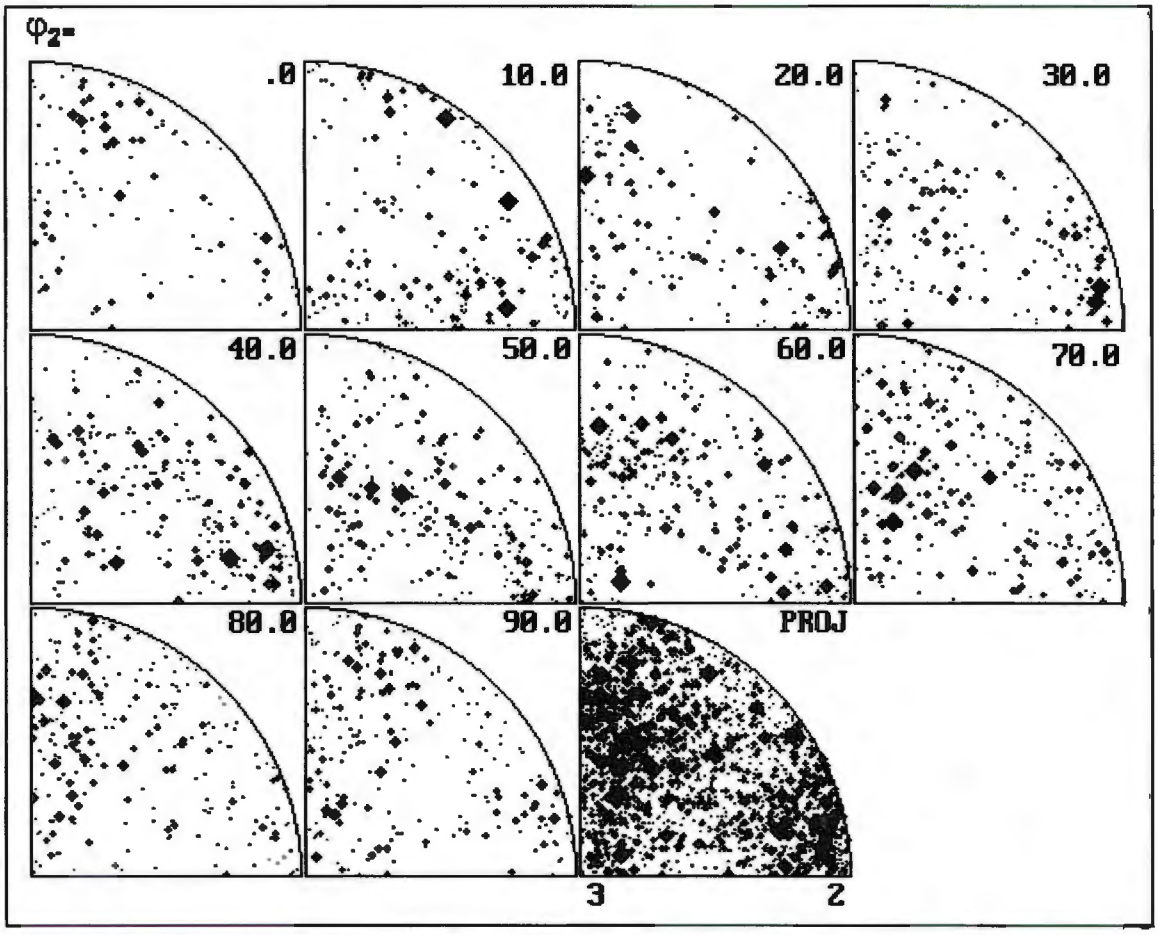

Figure 5.45: Polar plot for a single texture window of sample D1 indicating a more random texture.

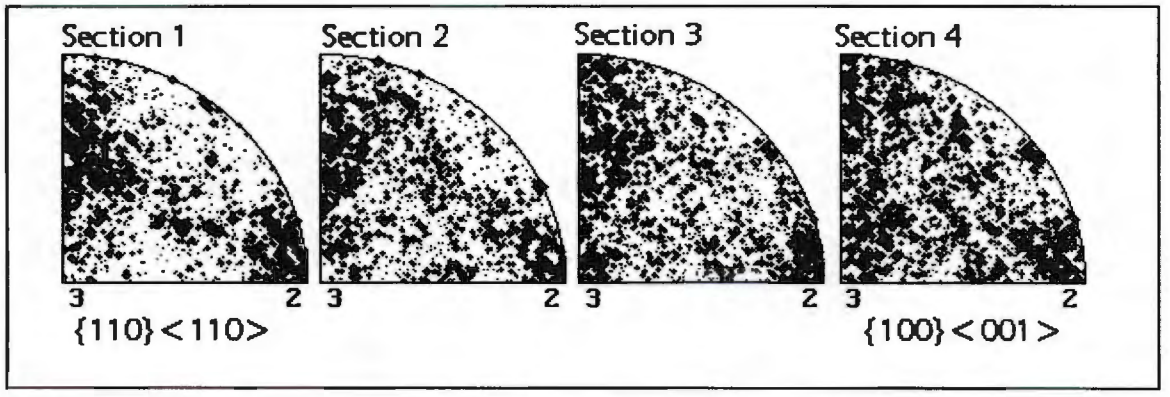

Figure 5.46: Projections from four sections of a single texture window of sample D1.

5.5 Plasticity Analysis

It follows from the microtexture examination, that the spatial variation of the principal texture components across the transverse section suggests a corresponding variation in plastic flow behaviour. In order to quantify this assumption, the yield surfaces and strain ratios were determined (from the microtexture) for the original texture windows and reduced sections of D1 and D3.

The trends demonstrated by the yield surfaces for these two samples resemble those of the discrete orientation diagrams. Comparison of the yield surfaces on a scale of the window size for D3 reveals no anisotropy or variation in predicted deformation behaviour. The slopes and intercept values for the yield loci are almost identical for each window. On the other hand, yield surfaces recalculated for the reduced sections in each window of this sample demonstrate a greater variation in predicted yield behaviour. Yield surfaces from the four reduced sections of a single texture window are shown in figure 5.47. For sample D1, the differences in yield surface shape from window to window are more pronounced compared to the situation for D3, with small changes in slope and intercept value. Figure 5.48 indicates on one set of axes the yield surfaces from three texture windows from sample D1. Figure 5.49 represents the yield surfaces for the reduced sections of a single texture window of sample D1. A large difference in overall yield surface shape is again evident, which suggests a large variation in predicted flow behaviour through the thickness of the sample as well as across the transverse section.

In a similar approach to the commercial steel investigation, the strain ratios and Taylor factors were calculated from the microtexture data for the reduced sections of each sample. Figures 5.50 and 5.51 show the calculated strain ratios for elongation in the RD for D3 and D1 respectively. A greater variation in r_{RD}-value for uniaxial deformation in the RD is visible across the transverse section for D1 compared to D3, which is in agreement with the assessment of the texture results.

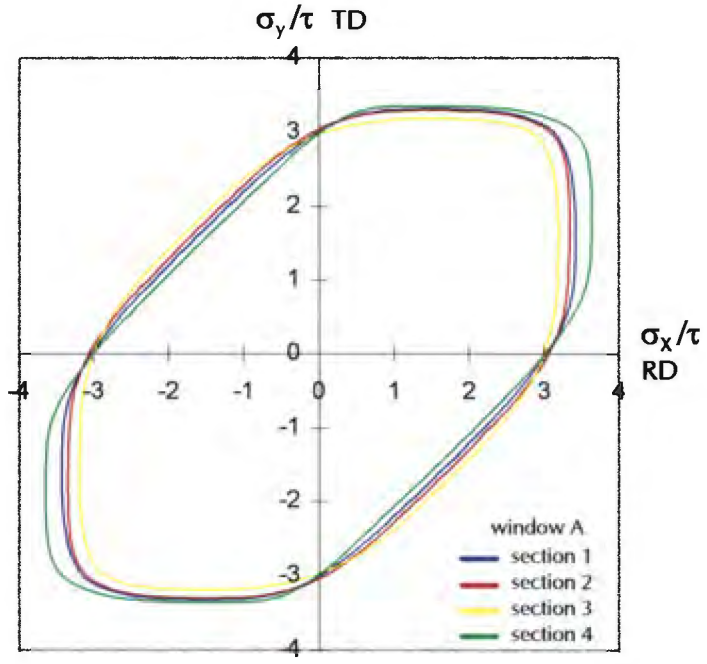

Figure 5.47: Yield surfaces for the reduced sections of a texture window from the transverse section of D3.

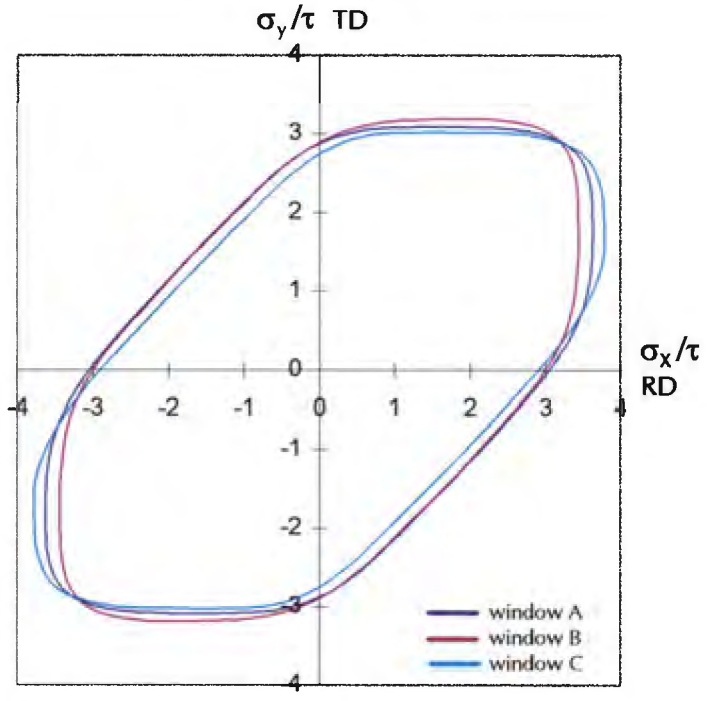

Figure 5.48: Yield surfaces for three texture windows from the transverse section of D1.

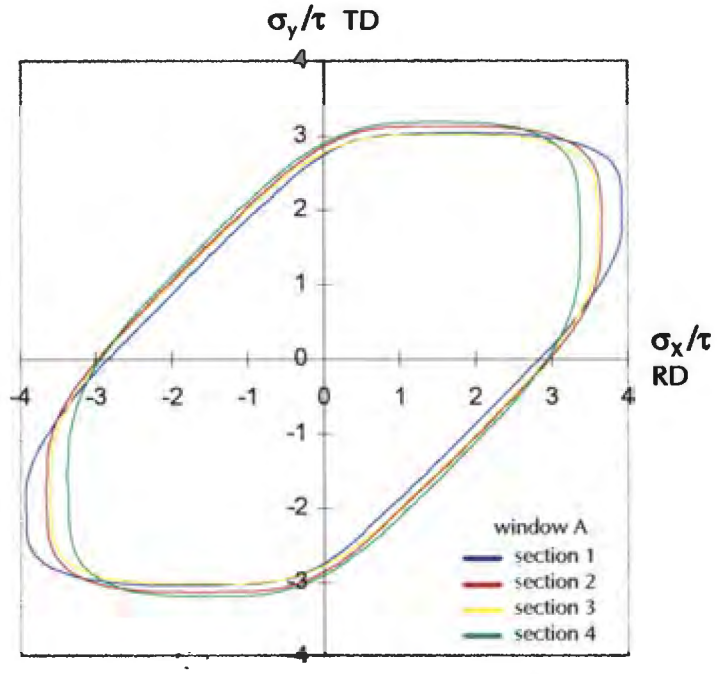

Figure 5.49: Yield surfaces for the reduced sections of a texture window from the transverse section from sample D1.

SURFACE

1.0 mm

r_{RD} = 2.14	r_{RD} = 1.99	r_{RD} = 1.81	r_{RD} = 2.82	r_{RD} = 2.01	r_{RD} = 1.23
r_{RD} = 2.01	r_{RD} = 1.65	r_{RD} = 1.00	r_{RD} = 1.80	r_{RD} = 2.04	r_{RD} = 2.02
r_{RD} = 1.00	r_{RD} = 2.04	r_{RD} = 0.61	r_{RD} = 1.28	r_{RD} = 3.58	r_{RD} = 6.22
r_{RD} = 3.79	r_{RD} = 3.62	r_{RD} = 3.36	r_{RD} = 1.75	r_{RD} = 1.84	r_{RD} = 2.84

200μm

CENTRE

Figure 5.50: Strain ratios for each reduced windows across the transverse section of D3.

SURFACE

r_{RD} = 6.41	r_{RD} = 1.67	r_{RD} = 6.87	r_{RD} = 4.82	r_{RD} = 5.72	r_{RD} = 9.32
r_{RD} = 4.03	r_{RD} = 0.81	r_{RD} = 3.22	r_{RD} = 3.81	r_{RD} = 1.75	r_{RD} = 4.86
r_{RD} = 1.14	r_{RD} = 1.64	r_{RD} = 2.24	r_{RD} = 2.14	r_{RD} = 1.53	r_{RD} = 3.70
r_{RD} = 1.64	r_{RD} = 1.00	r_{RD} = 0.83	r_{RD} = 3.49	r_{RD} = 0.81	r_{RD} = 1.78

CENTRE

Figure 5.51: Strain ratios for each reduced window across the transverse section of D1.

5.6 Finite Element Modelling

Simulation of deformation behaviour of the laboratory rolled samples produced similar results to the finite element experiments performed using yield information from the commercial steel The results of the two simulations performed using yield data calculated from the microtexture results from samples D1 and D3 are summarised in the table below. In both cases the simulations have been designed with tensile axis parallel to the RD.

Table 5.3: Results of FEM experiments performed using commercial stainless steel yield data.

Exp.	Yield Data	Tensile Direction	Arrangement of components	Result
7	D1	RD	Random	Longitudinal corrugations in the RD.
8	D3	RD	Random	Longitudinal corrugations in the RD.

A contour map of displacement in the ND for experiment 7, which simulates the behaviour of sample D1, is given in figure 5.52. In addition, surface profiles at two intervals along the specimen length are presented below the contour map. As in the case of the commercial steel simulations, longitudinal corrugations are visible extending in the RD of the specimen. A similar result is found for experiment 8 which utilises plastic flow data from sample D3. Approximately 2.5 corrugations (including a peak and a valley) appear across the 12 mm specimen (figure 5.53). In a similar manner to sample C430, an examination of transverse stress distribution shows the presence of tensile and compressive stresses spread throughout the specimens. A cross section of transverse stress for samples D3 and D1 is shown in figure 5.54. The amount of stress experienced by the microstructural components in experiment 8 is lower than in experiment 7, which can be attributed to a general decrease in the range of r_{RD}-values for sample D3.

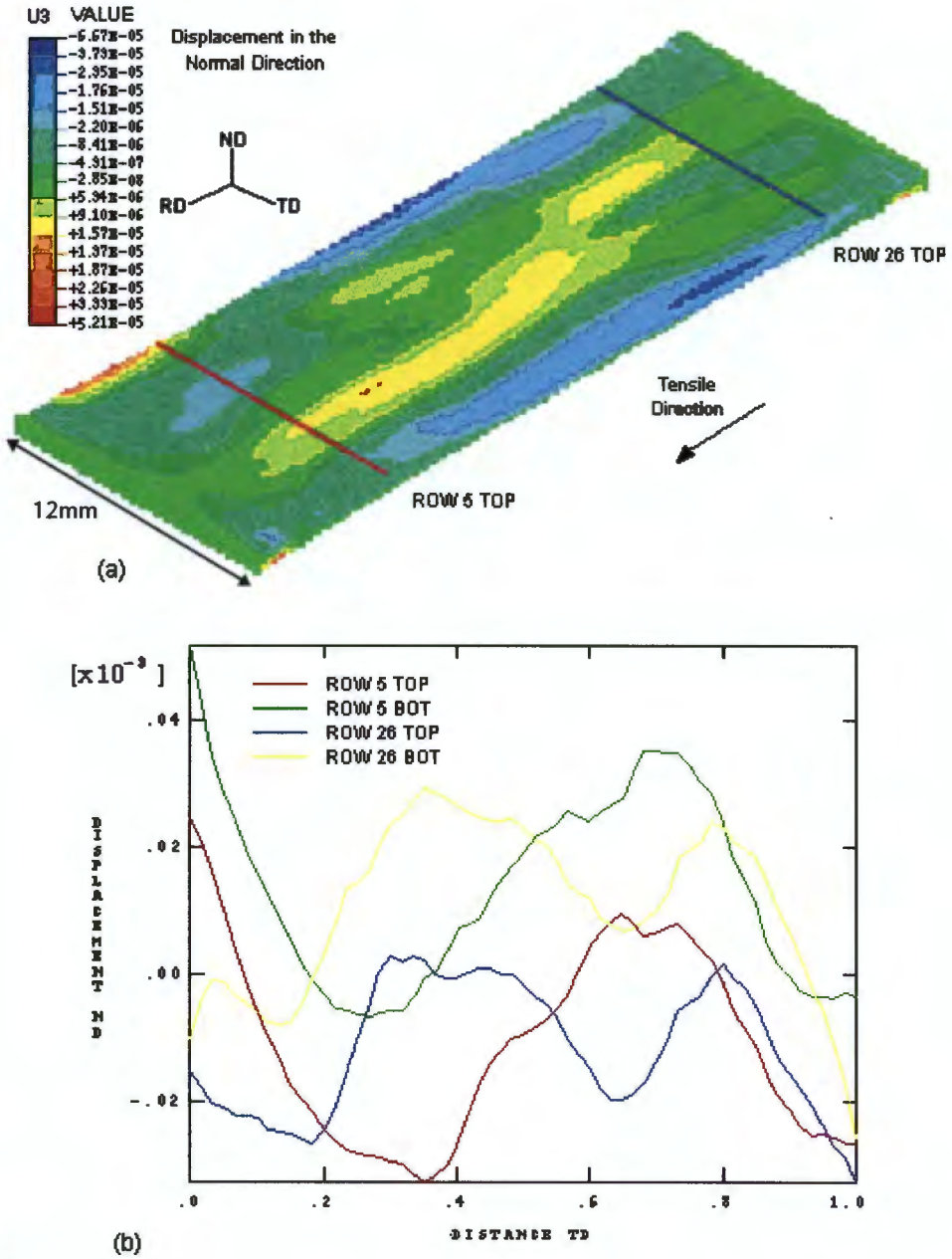

Figure 5.52 (a): Contour plot of displacement in the normal direction for experiment 7, sample D1. (b) Surface profiles in the TD across the upper and lower surfaces of experiment 7.

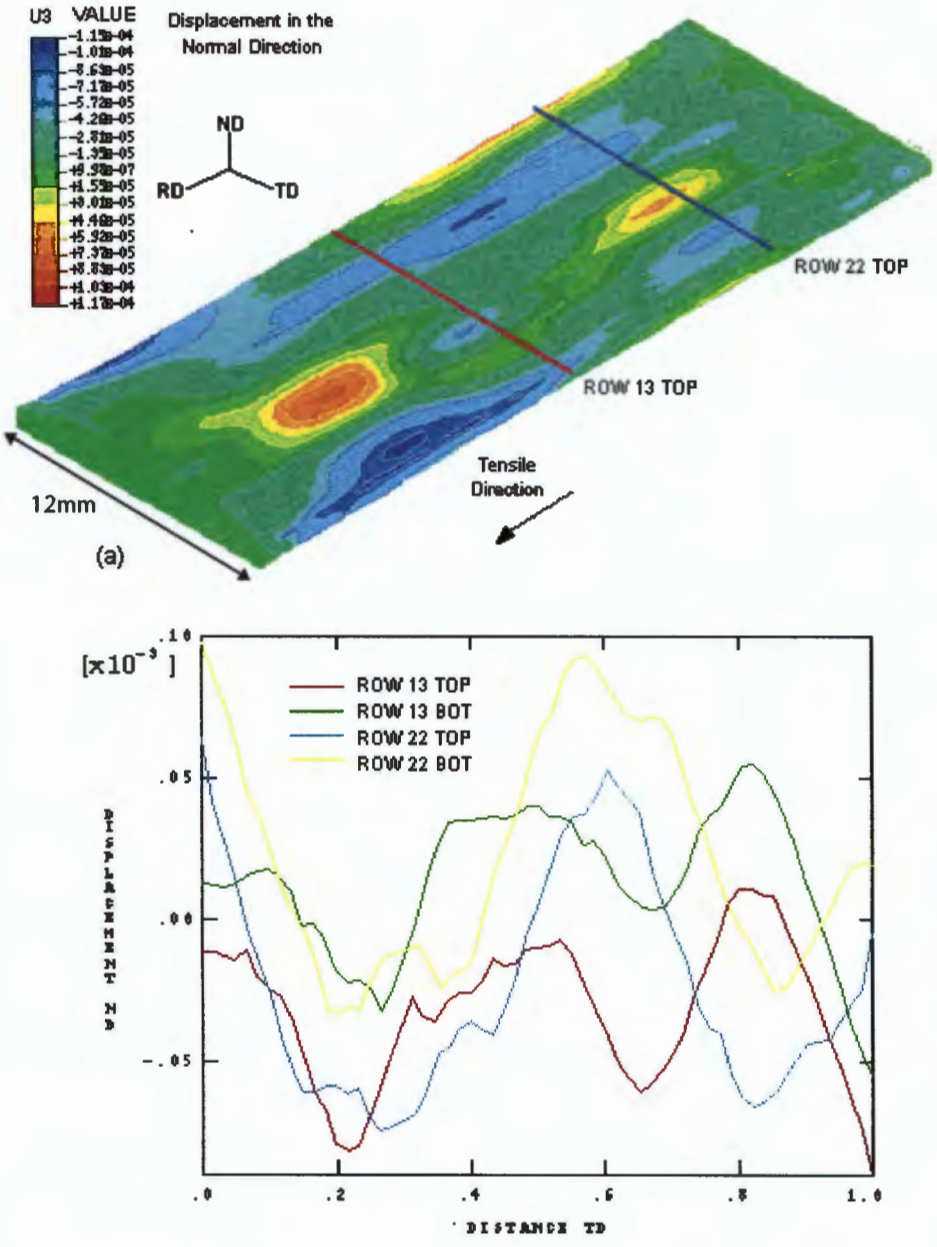

Figure 5.53 (a): Contour plot of displacement in the normal direction for experiment 8, sample D3. (b) Surface profiles in the TD across the upper and lower surfaces of experiment 8.

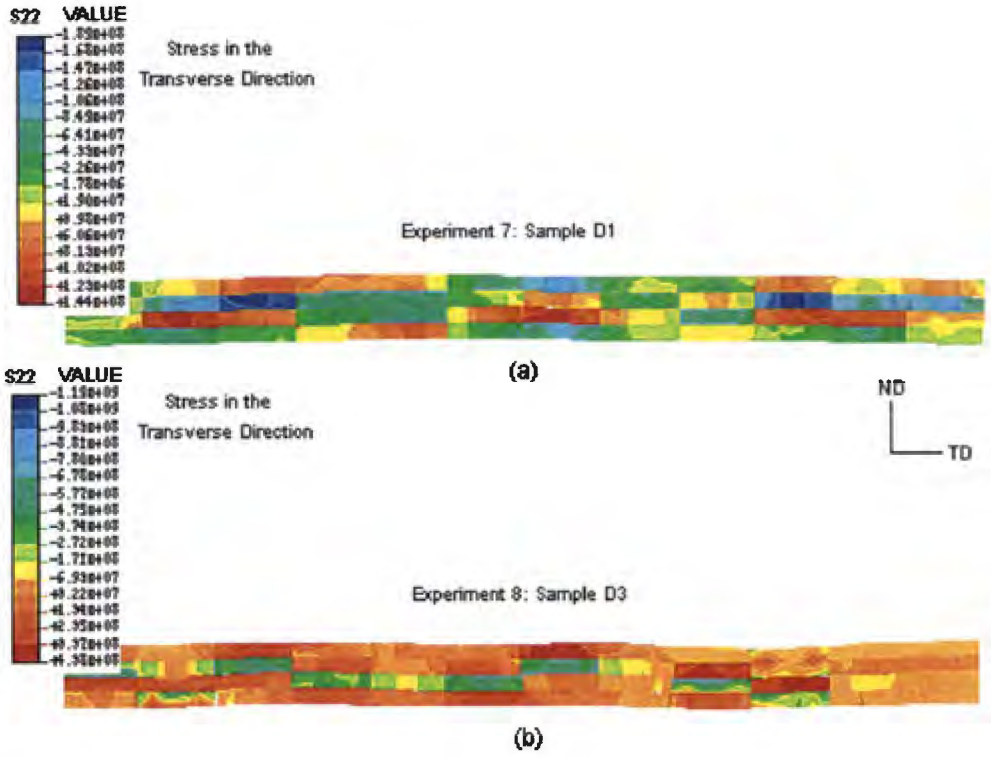

Figure 5.54: A cross section of transverse stress, S_{22}, at 15 mm along each specimen length.

5.7 Discussion of Laboratory Rolled Stainless Steel Results

Distinct variations have occurred in the evolution of the microstructure and bulk texture in the three alloy heats. These differences can be traced back to the hot rolling schedules, and in particular to the response to recovery and recrystallisation following the hot roll-annealing stage. After hot rolling, there is no immediate evidence in any of the samples of recrystallisation; however, the extent of recovery in the deformed grain structure increases with increasing hot roll finish temperature. Martensite stringers are visible in all the samples which indicates a transformation to austenite during hot rolling. During the post-hot roll annealing stage, the samples respond quite differently and three distinct microstructures are produced. Sample B1 remains unrecrystallised (but recovers to a greater extent), sample B2 produces a partially recrystallised microstructure, and sample B3 becomes fully recrystallised. Thus the starting structures before cold rolling differ considerably. The final post-cold roll annealing process gives rise to fully recrystallised microstructures in all cases, but there is a decrease in final grain size in the order of sample D1 to D3. It is clear that the hot roll finish temperature has played a significant roll in the grain structure evolution, and therefore one can expect that variations in texture are also likely to occur.

An important similarity in the final cold roll-annealed microstructures is the presence of grain size banding through the thickness of the sheet product. Apart from the variation in the average grain size between the different alloy heats, the relative degree of grain size banding is similar for all three heats. The origin of the grain size banding is most likely related to the presence of the martensite stringers in the hot rolled microstructure which is thought to influence the microstructural evolution in two principal ways. Firstly, since two phases exist at hot rolling temperatures, namely ferrite and austenite, texture evolution and the response to stored deformation energy is expected to be different for the two phases. In the second instance, the response of the martensitic regions to heat treatment during the post-hot roll annealing process will be different to the ferritic matrix. This is particularly noticeable for sample B1 where it is clear that the ferritic matrix has not recrystallised, but polygonisation has occurred in the

martensitic regions during tempering to produce a very fine localised ferrite structure.

Consideration should be given as to the possible influence that grain size banding might have on ridging behaviour[115]. The Petch equation describes the relationship between grain size and yield strength as : $\sigma_y = \sigma_i + k\, d^{-\frac{1}{2}}$ where σ_i is a lattice friction stress and k is a constant. The parameter k depends on two main factors, namely the stress required to operate a source dislocation, and secondly, on the Taylor factor. So yielding is dependent on grain orientation as well as grain size. Since previous investigators have emphasised yielding effects based on orientation alone, it seems pertinent at this stage to include the influence of grain size effects on yielding as well. In view of the presence of grain size banding (or grain size clustering), the variation in yield behaviour associated with the different grain size domains could produce crystal plasticity inhomogeneity on a scale which contributes towards the development of surface ridging. The ridging mechanism proposed by Wright[34] involves the development of compressive stresses in the transverse direction as a result of the resistance of cube-on-face domains to deform in the transverse direction during tensile straining parallel to the rolling direction. The compressive stresses are reported to cause localised buckling which produces the corrugated surface profile. This model is not without shortcomings and has been seriously challenged by Chao[44], particularly with regard to whether deformation of the cube-on-face component produces a compressive or tensile stress in the transverse direction. Despite these arguments, the suggestion that variation in yield behaviour can give rise to ridging raises sufficient interest in the inhomogeneous yielding behaviour associated with grain size banding. The fact that grain size banding is present in all three alloy heats, and the fact that ridging behaviour is not dissimilar across the sample set, may well indicate that there is a connection between these two factors. The role that grain size banding might play in the development of general surface roughness is discussed later.

The variation in bulk texture of the samples in the final cold roll-annealed condition can also be related to the differences in microstructural development after the hot roll-annealing stage. After hot rolling the near surface regions of all

three samples indicate Goss textures due to deformation by shear. The centre textures which form under plane strain conditions vary with hot roll finish temperature from α-fibre for sample A1 to a moderate γ-fibre texture for sample A3. The α-fibre is the expected texture in sample A1 as the high hot roll finish temperature prevents any recrystallisation while promoting dynamic recovery.

After annealing, the near-surface textures are retained and again all three samples exhibit Goss textures. The low hot roll finish temperature of 654°C for sample B3 results in increased internal strain during rolling which provides the driving force for recrystallisation on subsequent annealing. The outcome is a Goss texture at the surface of the sheet and a near-Goss texture with a minor γ-fibre component at the centre. Sample B1, on the other hand, experiences only recovery during annealing which results in the "rolling texture" or α-fibre being retained in the centre of the sheet.

For the final cold roll-annealed samples, evidence of the γ-fibre recrystallisation texture can be found at the surface and centre of all the samples. This texture forms mainly at the expense of the $\{112\}<110>$ cold rolling texture component which is strong in all three samples before final annealing[63]. Also, the γ-fibre texture is able to develop from the Goss texture, which during rolling rotates simultaneously towards both the $\{111\}<112>$ and $\{001\}<110>$ orientations[63]. The stronger final textures of sample D3 in the centre compared to sample D1 are due to more intense initial textures in the hot band. Sample D3 indicates a γ-fibre texture at the centre and a γ-fibre plus Goss texture at the surface, which is a consequence of the fully recrystallised structure after the hot roll-anneal stage. Sample D1 has a number of weaker textures at the centre which is caused by the recovery process during previous annealing. The texture variation through the thickness of the samples suggests that under tensile elongation the surface and centre layers will not deform homogeneously, which could be a contributing factor to the surface roughening behaviour of this material during uniaxial tensile deformation.

An examination of the microtexture across the transverse sections of samples D1 and D3 also reveals an inhomogeneous spread of textures. Clusters of like

orientations are found in both samples extending as bands in the TD, for example the $\{111\}<112>$ texture in sample D3. Other textures are concentrated in large groups, for example the $\{110\}<110>$ texture in sample D1. Furthermore, certain preferred orientations are segregated according to grain size. For example, the clusters of $\{110\}<110>$ texture in sample D1 are more prominent in the coarse grained regions, while the secondary textures of sample D1 also appear more frequently as large grains. These microstructural aspects suggest a level of texture colonisation which could make a significant contribution to inhomogeneous plastic behaviour, but at the same time it is important to note that there is no direct physical correspondence between the form of the corrugated surface and the occurrence of texture colonisation.

Analysis of the discrete orientation plots for the individual texture windows, as well as the reduced sections within each window, allows confirmation of the various texture components and highlights their inhomogeneous distribution. For sample D1, a variation in preferred orientation on a scale of the original window size is clearly visible from the polar plots, but for sample D3, the uneven spread of textures is only visible from the polar plots when the windows are divided into four smaller regions covering 200 μm X 1000 μm. These results suggest that the level of texture clustering increases with grain size of the sample, which in turn is related to the influence of hot roll finish temperature on microstructural evolution.

A quantitative analysis of the predicted plastic behaviour of samples D1 and D3 shows a considerable variance in yield behaviour across the transverse section. The yield surface morphologies for the reduced texture windows indicate a variation in predicted flow behaviour across both samples. In much the same trend as the microtexture results, the differences for sample D1 are more severe. This variation in yield properties is directly related to the inhomogeneous texture distribution described above. In addition, the calculated strain ratios for both samples on a scale of the reduced windows suggest anisotropic yielding of the specimen when subject to uniaxial tensile deformation in the RD. Consideration should now be given as to how these microstructural

inhomogeneities can affect the macro-plastic behaviour of the material when subjected to uniaxial tensile conditions.

The results of the uniaxial tensile tests provide valuable information regarding the surface roughening behaviour of the laboratory rolled samples. It is suggested that two simultaneous roughening effects are occurring during elongation parallel to the RD to produce the surface morphology visible on the tensile samples. Firstly, a banded roughness appears on the surface of the samples, and secondly a corrugated bending occurs superimposed on the roughness. Although the microtexture of the rolling plane section was not examined, it is reasonable to assume that the laboratory rolled samples will possess a segregated distribution of texture components extending as bands in the rolling direction. This is inferred, firstly, due to the inhomogeneous distribution of texture across the transverse section, and secondly, due to the texture clustering identified in the commercial stainless steel. Texture maps of the commercial stainless steel reveal texture clustering in the form of narrow 'plate-like' bands of similar orientations extending in the rolling direction. It is suggested that the elongated areas of roughness which appear during tensile deformation are the result of a spatial variation in deformation of the surface grains due to the texture clustering, and can thus be likened to the streaking effect on the commercial steel sample elongated in the transverse direction.

In addition, the microstructural examination has indicated that grain size clustering occurs within the laboratory rolled samples in similar elongated bands, as schematically illustrated in figure 5.55. The size, orientation and frequency of the bands closely resembles that of the roughness effect appearing on the tensile specimens. Therefore, in a similar manner to the texture clustering, the variation in surface deformation as a result of grain size may also contribute to the elongated areas of roughness appearing during tensile deformation.

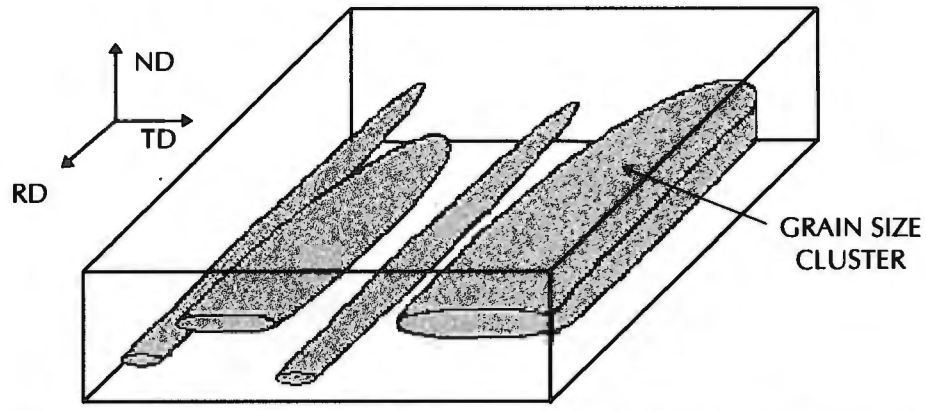

Figure 5.55: Schematic illustrating grain size banding in laboratory rolled heats.

In support of this theory are the results from the tensile tests of the laboratory rolled heats with the tensile axis parallel to the TD. The elongated roughening effect appears to be identical regardless of the orientation of tensile axis. This would be expected if the roughness was due to grain size and texture banding, as the variation in deformation would persist despite a change in the orientation of the tensile axis. Furthermore, sample D1 has an overall larger grain size and a greater variation in grain size between the fine and coarse grained regions. As expected, this results in a greater degree of roughness during elongation in both directions, which provides additional evidence that the roughness effect is related to grain structure.

The large scale corrugations, on the other hand, of the laboratory samples elongated in the RD form due to an asymmetric distribution of yield properties about the centre plane of the material, by the same alternating bending mechanism suggested for the commercial steel. The fact that the corrugations do not appear when elongation is applied in the TD also sustains this suggestion, as explained in the discussion on the commercial stainless steel.

In a similar manner to the commercial stainless steel, the results of the finite element analysis experiments indicate that the differences in calculated yield properties across the transverse section of samples D1 and D3, coupled to the geometrical properties of the microstructure and texture, are sufficient to cause localised bending. Longitudinal corrugations develop on the surface of the specimens during deformation in the RD. Once again these corrugations are attributed to bending due to the asymmetric distribution of transverse strain

within the specimen. The larger range of transverse stress values found within sample D1 (figure 5.54) can be explained by the fact that the variation in r-value within sample D1 is higher than in D3.

5.8 Correlation of the Laboratory Rolled and Commercial Steel Results

It is proposed that the same deformation mechanism is operative in both the commercial stainless steel and the laboratory rolled heats to produce the corrugated effect during elongation in the RD. A spatial variation in yield properties is evident in both sample C430 and heats D1 and D3, which results in a variation in rate of width change within each specimen and leads to a series of localised bending events during deformation. The elongated areas of roughness, however, are only visible in the laboratory samples and can be attributed to grain size banding and texture clustering in the RD. The same roughness effect is absent on the surface of the commercial steel after elongation, due to the very fine grain size and the lack of grain size banding.

The FEM approach of course excludes the role of differential yielding arising from discrete grain size domains. Although it has been hinted that grain size could contribute towards the ridging mechanism, it is felt that the crystal plasticity anisotropy arising from texture aspects is a much stronger contribution to ridging. This is supported by the fact that grain size clustering is generally absent in the C430 material, yet significant ridging still occurs.

CHAPTER 6

RESULTS OF THE ALUMINIUM ALLOYS

6.1 MICROSTRUCTURE

Samples ALU1 and ALU2 both reveal a fully recrystallised grain structure with fine randomly distributed intermetallic phases. An analysis of the grain size in the transverse and normal directions for the alloys is provided in Table 6.1.

Table 6.1: Grain size analysis for samples ALU1 and ALU2.

Orientation	Sample ALU2 Height (μm)	Length (μm)	Sample ALU1 Height (μm)	Length (μm)
Transverse	22	39	30	83
Longitudinal	23	39	31	100

Tensile and hardness properties of the alloys were provided by the suppliers and are indicated in the table below.

Table 6.2: Tensile and hardness properties of samples ALU1 and ALU2.

Alloy	UTS (MPa)	YS (MPa)	% Elongation	Hardness VHN
ALU1	76	30	28	23
ALU2	93	39	40	23

Anodised samples examined under polarised light reveal undeformed recrystallised microstructures. A view of the rolling plane and longitudinal sections of sample ALU1 are exhibited in figures 6.1 and 6.3. A matrix of cube orientations (red) could be identified interspersed with smaller non-cube grains (yellow and blue), incorporated into clusters or bands extending in the RD. For example in figure 6.3, a band of non-cube grains with a width of 300 μm in the ND is visible extending across the micrograph for about 2 mm in the RD. The images provide clear evidence of an inhomogeneous distribution of the texture components in sample ALU1. Sample ALU2, in contrast, indicates a more homogeneous distribution of cube and non-cube textures as shown by figures 6.2 and 6.4 of the rolling plane and longitudinal plane respectively.

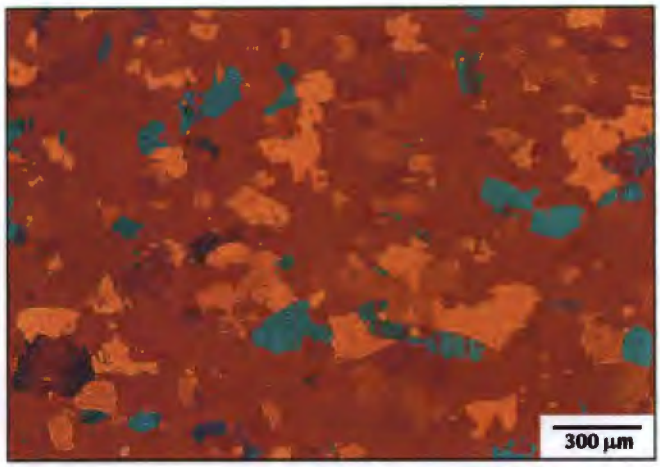

Figure 6.1: Sample ALU1 rolling plane section showing clusters non-cube grains (yellow and blue) within a cube matrix (red).

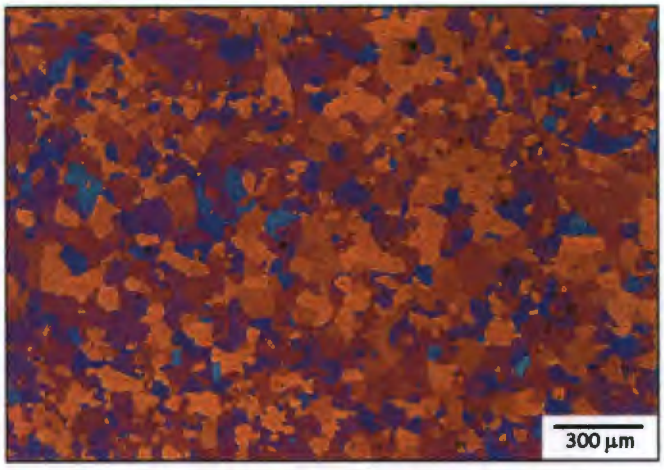

Figure 6.2: Sample ALU2 rolling plane section indicating homogeneous grain structure.

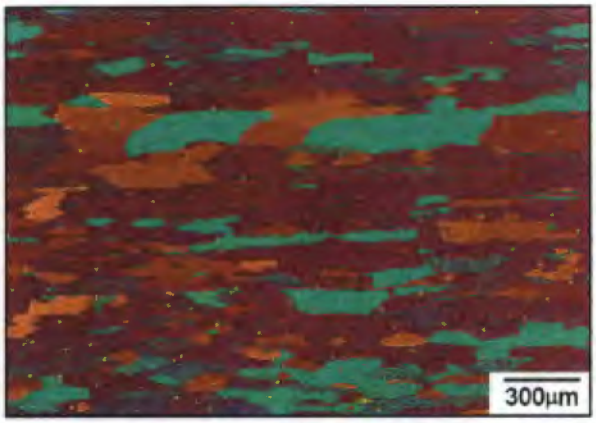

Figure 6.3: Sample ALU1 longitudinal section showing bands non-cube grains (yellow and blue) within a cube matrix (purple).

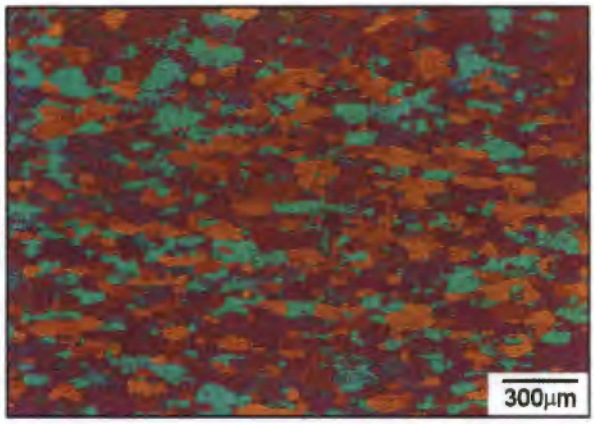

Figure 6.4: Sample ALU2 longitudinal section.

A notable difference in sample ALU2 is the significant reduction in the amount of cube texture and corresponding increase in smaller non-cube grains compared to sample ALU1.

6.2 Bulk Texture

(i) Sample ALU1

Despite slight traces of R texture $\{124\}<211>$, the cube texture is very strong in both the near-surface and mid-plane regions (figures 6.5 and 6.6).

(ii) Sample ALU2

In contrast to the predominance of cube texture in ALU1, this alloy exhibits a much sharper presence of R texture as well as a strong cube component. When comparing the near-surface to the mid-plane regions, the R texture component is stronger in the mid-plane. The respective ODFs are presented in figures 6.7 and 6.8. In addition, evidence of Goss $\{110\}<001>$ can also be identified in the mid-plane.

Although the thermomechanical process history is not known for the ALU2 alloy, it is assumed that cold rolling was carried out to produce the final gauge, followed by some form of annealing. Thus textures similar to the β-fibre, which comprises of the copper component $\{112\}<111>$ through the S-component $\{123\}<634>$ to the brass component $\{110\}<112>$, are evident.

Analysis of Bulk Texture:

During recrystallisation (annealing after cold rolling) the cube texture is expected to evolve. However, the formation of the cube orientations is dependent on several factors including annealing temperature, heating rate, time at temperature and the influence of particles on recrystallisation. For example, small amounts of Fe are known to affect the influence of annealing temperature on the development of cube texture. At high annealing temperatures (e.g. 520°C) the Fe-containing dispersoids have little effect on boundary migration because precipitation occurs before recrystallisation is complete. Thus a stronger cube texture is able to develop. Similarly at low temperatures,

precipitation will occur after recrystallisation is complete and the precipitates once again do not drastically affect the cube development.

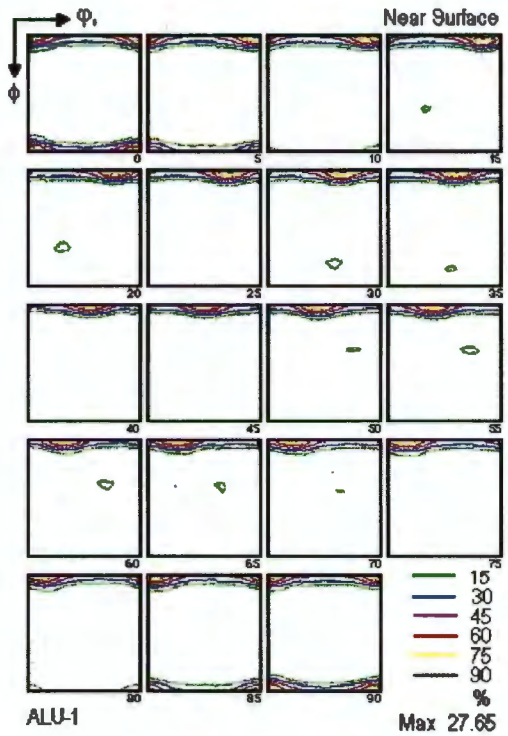

Figure 6.5: ALU1, φ_2 constant near surface.

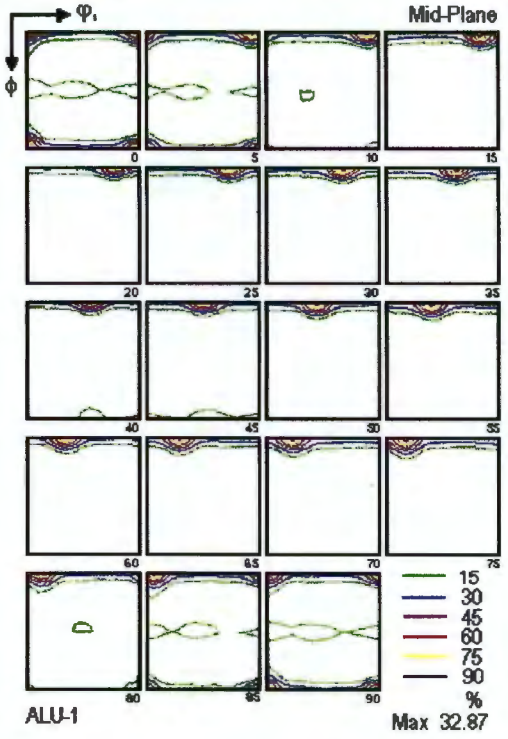

Figure 6.6: ALU1, φ_2 constant mid-plane.

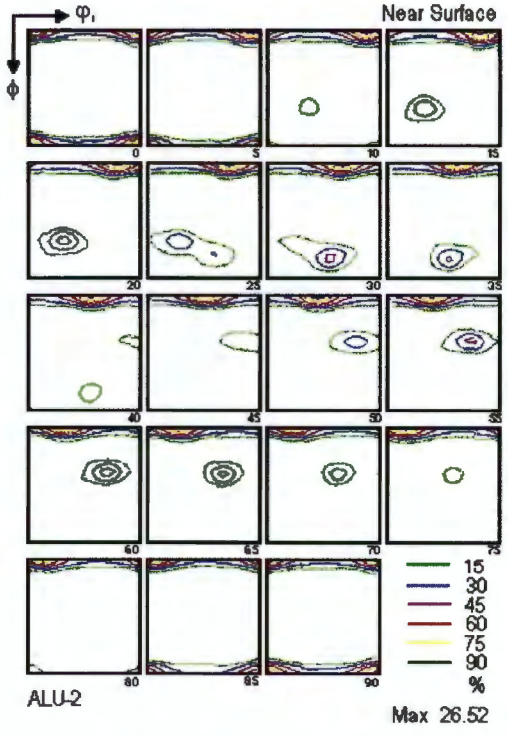

Figure 6.7: ALU2, φ_2 constant near surface.

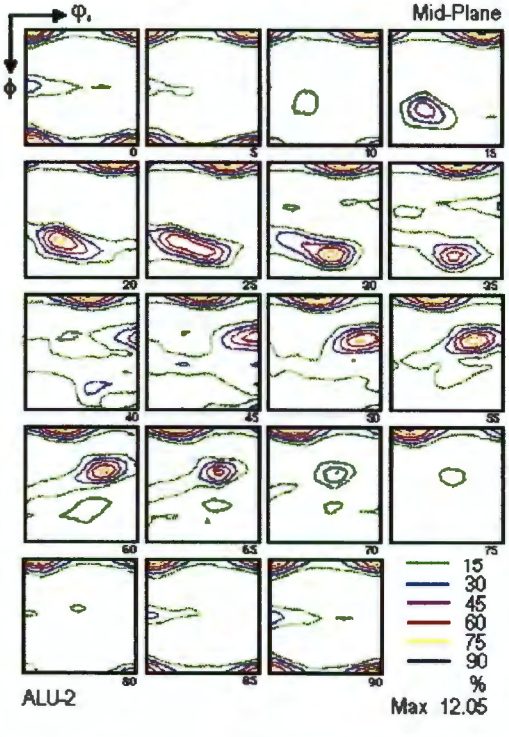

Figure 6.8: ALU2, φ_2 constant mid-plane.

However, at intermediate temperatures the precipitation of an Fe-rich phase hinders grain boundary migration due to the synergy between precipitation and grain boundary migration. The consequent solute drag and/or precipitation leads to slower growth of the dominant cube grains and allows the rolling component to develop, thereby reducing the strength of the cube component. This could be the situation which has arisen in the ALU2 alloy to produce the stronger R texture.

6.3 Ridging Analysis

The tensile deformation behaviour of the two alloys was investigated using tensile tests in both the RD and TD. In the situation where the tensile axis is parallel to the TD, alloy ALU1 after 20% elongation indicates severe surface roughening in the form of elongated ridges or grooves perpendicular to the direction of strain on both the upper and lower surfaces. Also, the specimen exhibits a grain scale surface roughening superimposed on the longitudinal grooves. Figure 6.9 indicates the 2D contour plot for a corresponding region on the upper and lower surfaces of the specimen. Comparison of these images suggests that a through-thickness thinning of the specimen has occurred during deformation as the valleys and peaks on the upper surface correspond directly to those on the lower surface. This characteristic is also visible from the 3D plot and surface profiles presented in figure 6.10. The lower surface traces have been inverted about the centre line to allow a correct view of the transverse section. The average roughness value of the specimen is 3.00 μm and the peak-to-valley measurement 25.43 μm. During straining the grooves, which have a wavelength of about 1.5 mm, appear in the RD after approximately 2% strain and increase in severity until 15% elongation.

After prior removal of the surface layers on each side of the tensile specimen of alloy ALU1, the deformation behaviour remains relatively constant. The deformed surface appears unchanged relative to the unreduced specimen with extended bands of roughness as well as large scale undulations elongated in the RD. Figure 6.11 indicates the 3D plot and surface profiles of the reduced

specimen. The specimen has also undergone a general bending during deformation which hinders the identification of the ridges. It is suggested that this bending is the result of the narrow specimen width (5 mm) which was necessary due to limited sample material and is therefore unrelated to the groove formation.

In contrast, the surface features of tensile specimens of alloy ALU1 elongated in the RD indicate a different plastic flow behaviour. The parallel grooves previously visible extending in the RD are not apparent. The overall topography of the surface is flat and no indication of through-thickness thinning is evident. The grain scale surface roughening, however, has occurred on the specimen to a similar extent as during elongation in the TD. Figure 6.12 indicates tensile specimens of alloy ALU1 elongated in the TD and RD.

Sample ALU2 exhibits a further variation in plastic flow behaviour. No evidence of anisotropic yielding is visible for specimens elongated in both the transverse or rolling directions. The surface remains relatively smooth and flat during deformation in both directions (figure 6.13). A fine surface roughening is visible on the specimens, but to a lesser extent than on specimens ALU1.

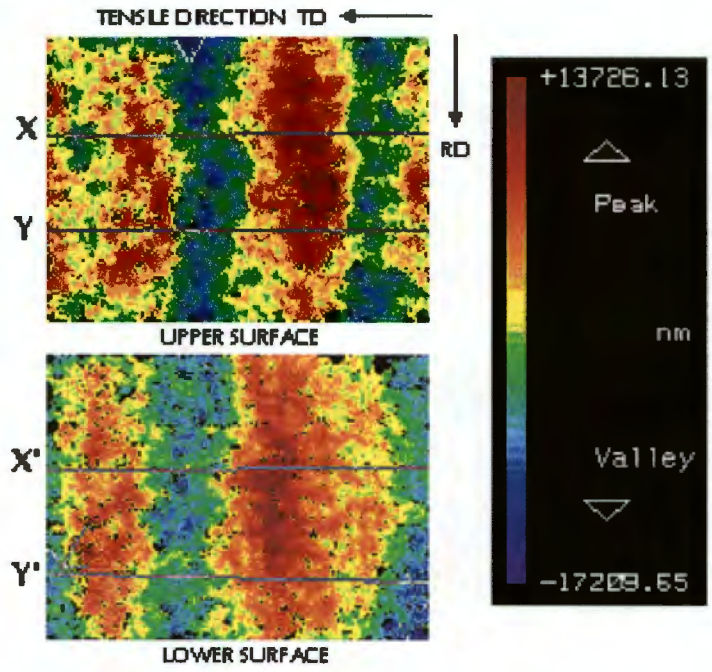

Figure 6.9: Sample ALU1 2D contour plot indicating the position of the surface profiles.

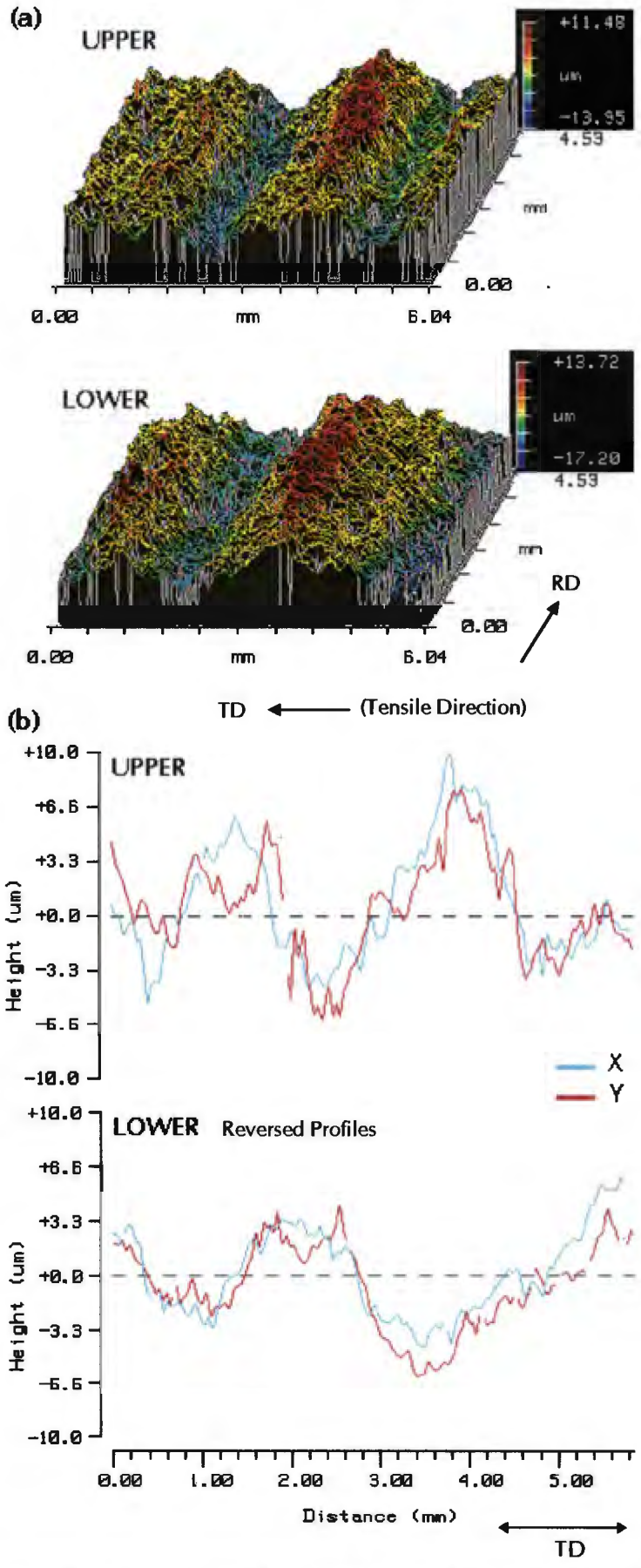

Figure 6.10: Sample ALU1 (a) 3D plot and (b) profiles on upper and lower surfaces.

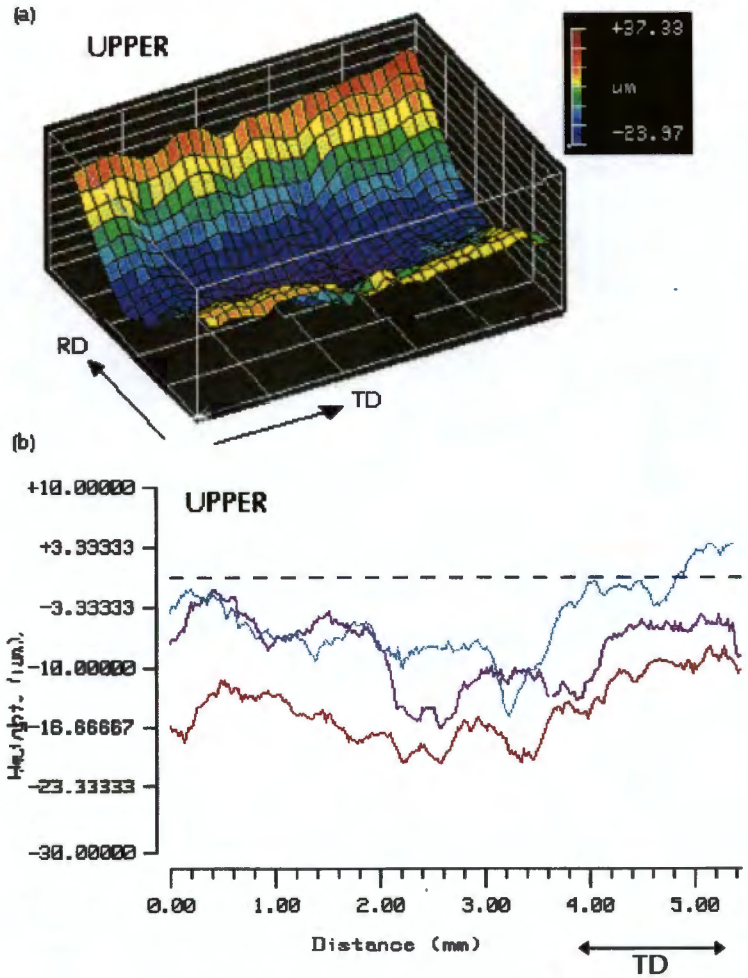

Figure 6.11: Sample ALU1 reduced to half thickness from both sides. (a) 3D plot and (b) surface profiles of upper surface.

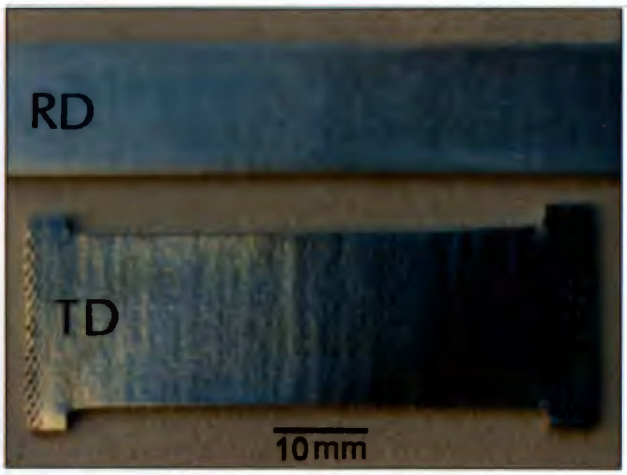

Figure 6.12: ALU1 elongated in the TD and RD.

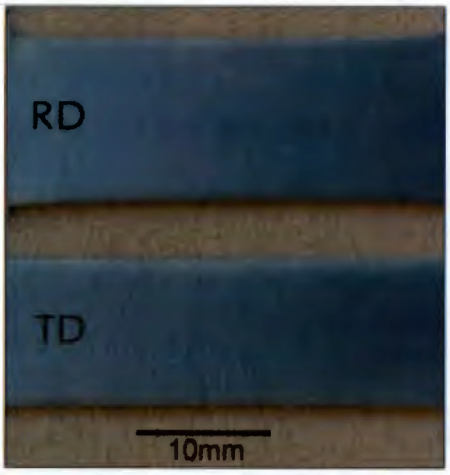

Figure 6.13: ALU2 elongated in TD and RD.

6.4 MICROTEXTURE

The discrete orientation plots in polar coordinates and texture maps constructed for the aluminium samples are presented in the following section. A colour

chart and a polar plot of common ideal FCC orientations are included as a reference (figures 6.14 and 6.24). The white areas of the texture maps correspond to orientations which did not fall within a specified ideal sphere. The fact that the bulk texture results indicate fairly strong textures for both samples, while the large white areas of the texture maps suggest many non-ideal textures, can be attributed to the fact that the bulk texture measurements are recorded over a large area of the specimen (10 mm x 14 mm) while the microtexture measurements indicate the texture over a very limited area.

ALU2 Transverse Section: The preferred orientations of this sample, namely cube, brass $\{011\}<211>$ and R $\{124\}<211>$, are randomly distributed throughout the scan area. Similar proportions of each component are present, and no clustering of any one texture component is visible. The texture map for the transverse section of ALU2 constructed using colour coding in Euler space is shown in figure 6.15. The texture distribution and type is generally considered to be replicated in each texture window. An example of the polar plot for this sample using Bunge notation is given in figure 6.16.

ALU2 Rolling Plane (Mid-plane): The proportion and spatial arrangement of the texture components present within the rolling plane section are similar to those found in the transverse section (See texture map in figure 6.18). A preponderance for the R, brass and cube textures can be identified from the polar plot (figure 6.17). The reduced percentage of cube orientations found in the mid-plane section is consistent with results of bulk texture analyses previously performed on the material. There is also no evidence of texture clustering in the rolling plane section of this sample.

Goss	$\{110\}<001>$
Cube	$\{100\}<001>$
Copper	$\{225\}<554>$, β-fibre
R	$\{124\}<211>$, β-fibre
Brass	$\{011\}<211>$, β-fibre
Rot. Cube ND	$\{001\}<310>$
Rot. Cube RD	$\{013\}<100>$
α-fibre	$\{100\}<011>$

Figure 6.14: Colour chart indicating common FCC textures.

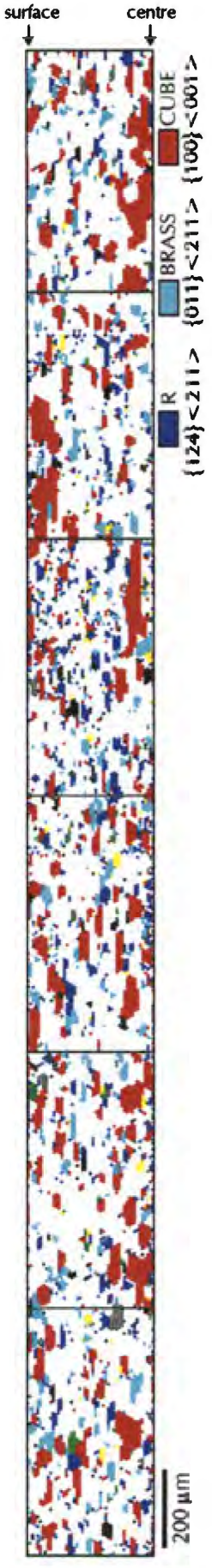

Figure 6.15: Texture map of transverse section of ALU2.

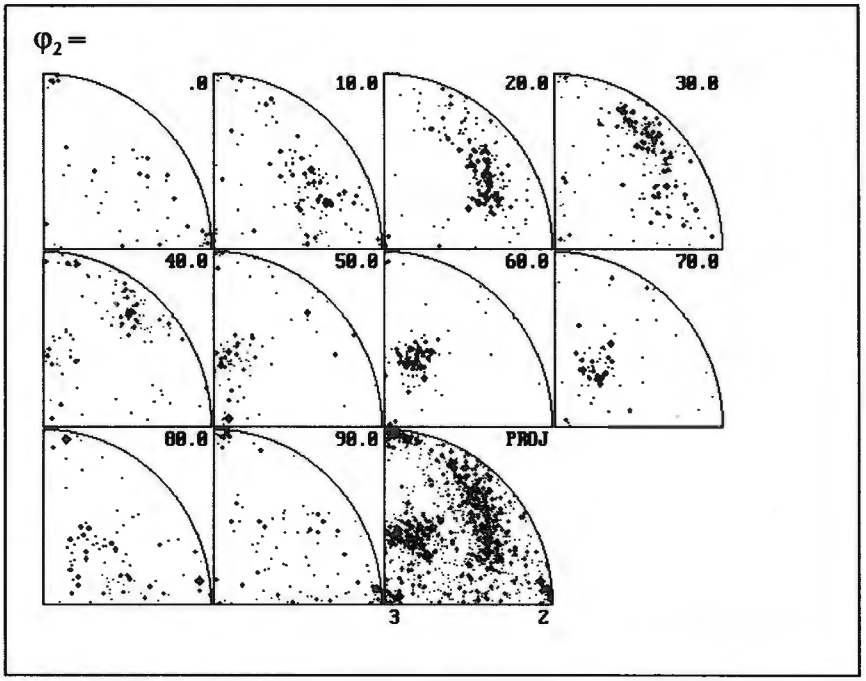

Figure 6.16: Polar plot of orientations representative of the ALU2 transverse scan. The texture components are replicated in each window.

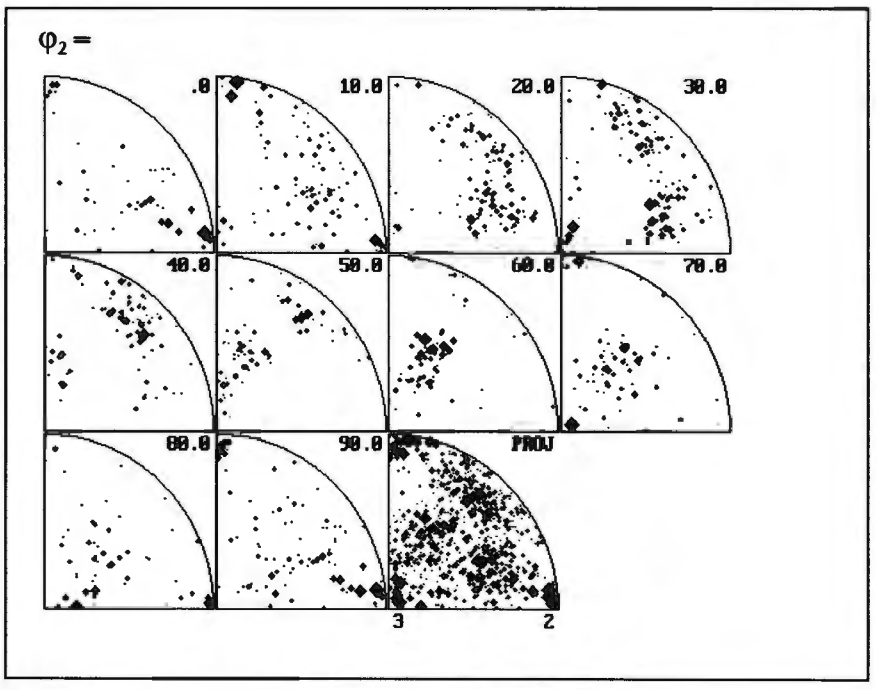

Figure 6.17: A typical polar plot of orientations from the ALU2 rolling plane scans.

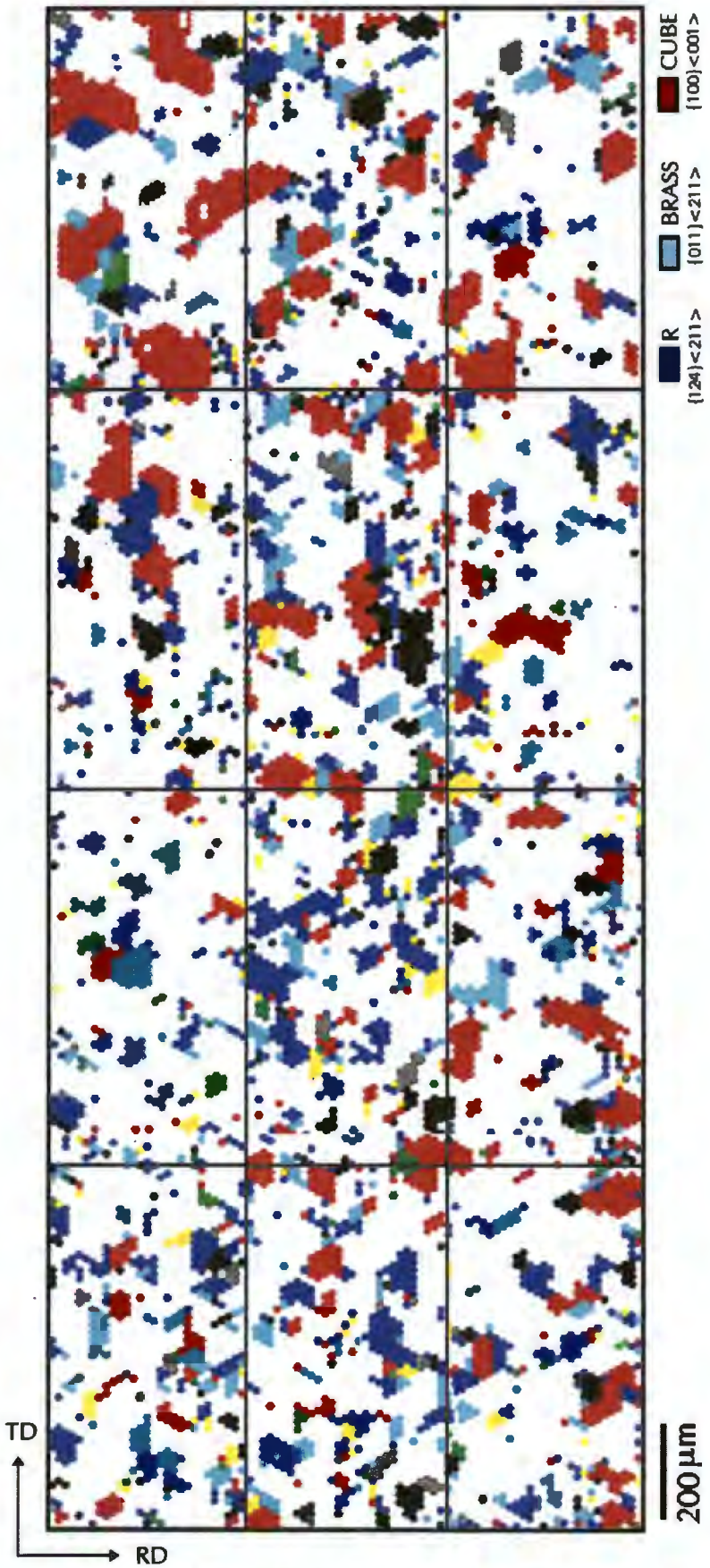

Figure 6.18: Texture map of rolling plane section of ALU2.

Sample ALU1 Transverse Section: The cube texture dominates the mid-section of this sample almost entirely (1/4-1/2 thickness). This is in contrast to the near surface regions (0-1/4 thickness) where cube, brass and R orientations are all present (figure 6.20). Approximately equal proportions of cube and non-cube textures are visible across the section and again the texture windows are considered to replicate each other in texture type and distribution (figure 6.19).

Sample ALU1 Rolling Plane (Mid-plane): In contrast to the homogeneous distribution of textures present in sample ALU2 , sample ALU1 shows distinct clustering or banding of the R texture component within a matrix dominated by cube orientations (figure 6.23). A continuous localised band of grains with an R texture extends in the rolling direction up to 2 mm in length and reaching dimensions of about 500 μm in the transverse direction. To provide confirmation of the texture clustering in sample ALU1, a similar texture map constructed using the **OIM** software is included in Appendix B. Secondary texture components include the brass texture and traces of Goss and RD rotated cube. An example of a polar plot for a cube dominated region is given in figure 6.21, while that for an R dominated region is given in figure 6.22.

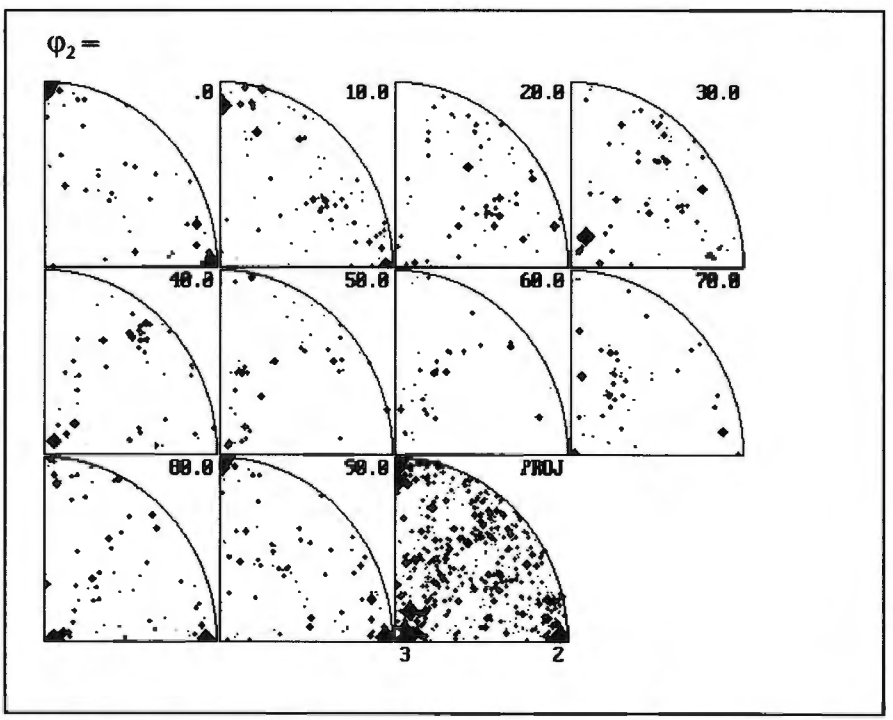

Figure 6.19: Polar plot of orientations representative of the ALU1 transverse scan. The texture components are replicated in each window.

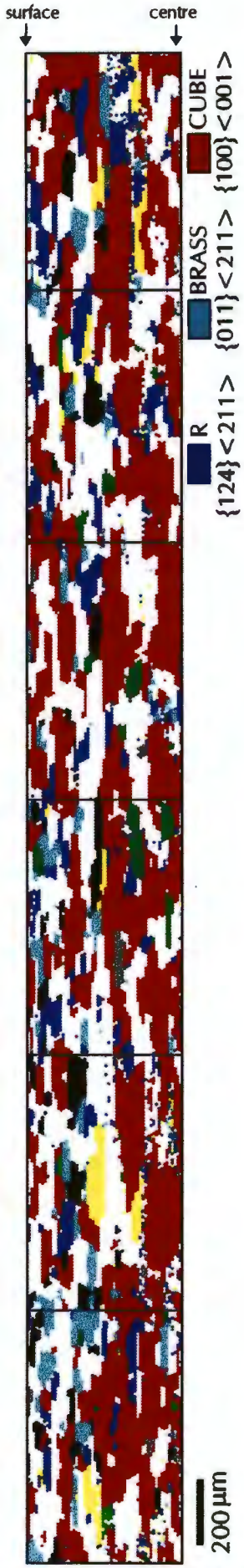

Figure 6.20: Texture map of the transverse section of ALU1.

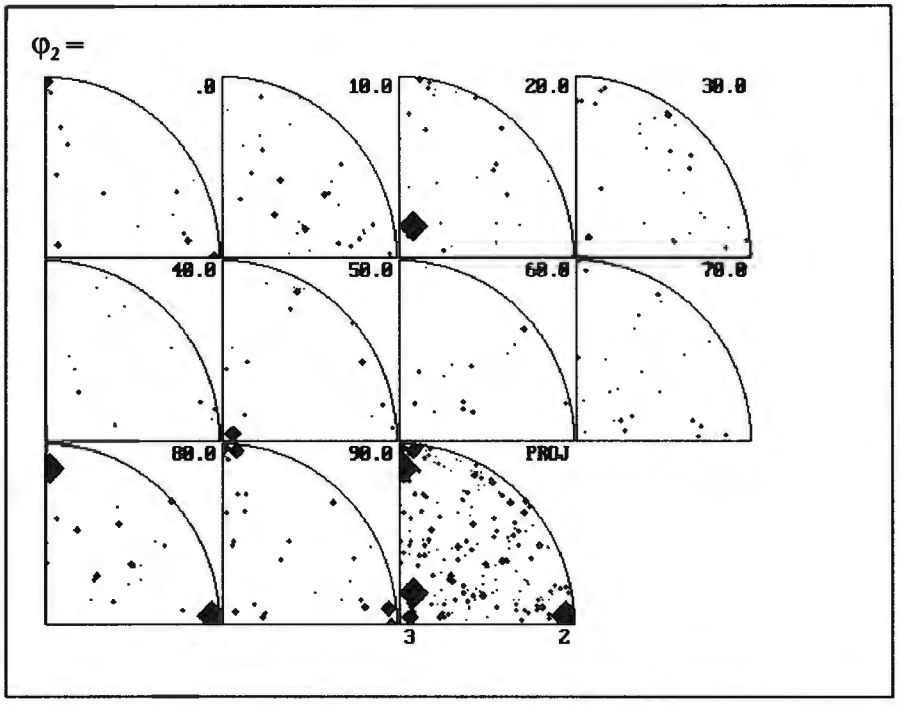

Figure 6.21: Polar plot of orientations from scan 4C which has a high percentage of cube texture (ALU1 rolling plane).

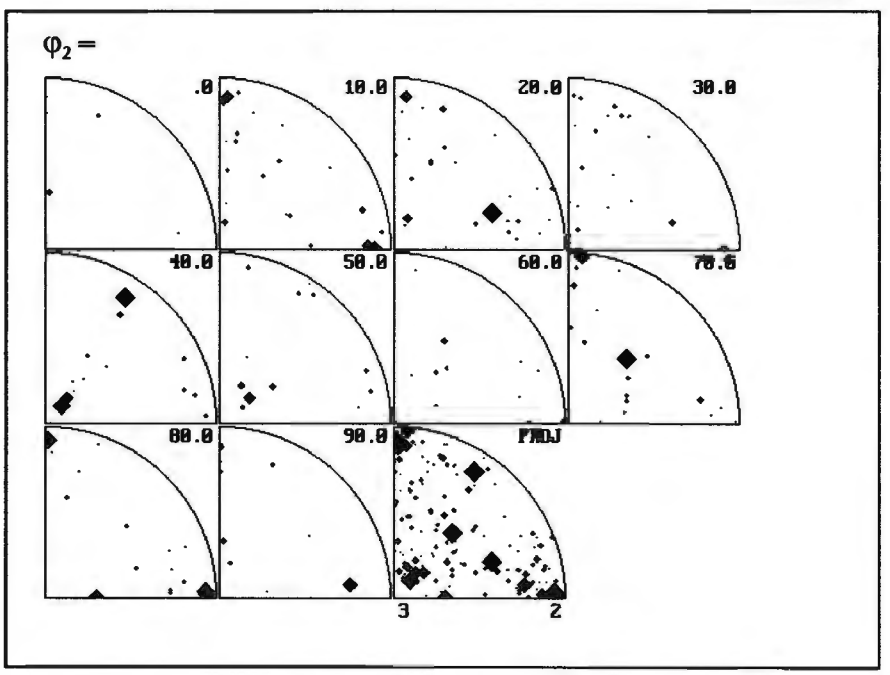

Figure 6.22: Polar plot of orientations from scan 4J which has a large percentage of R texture (ALU1 rolling plane).

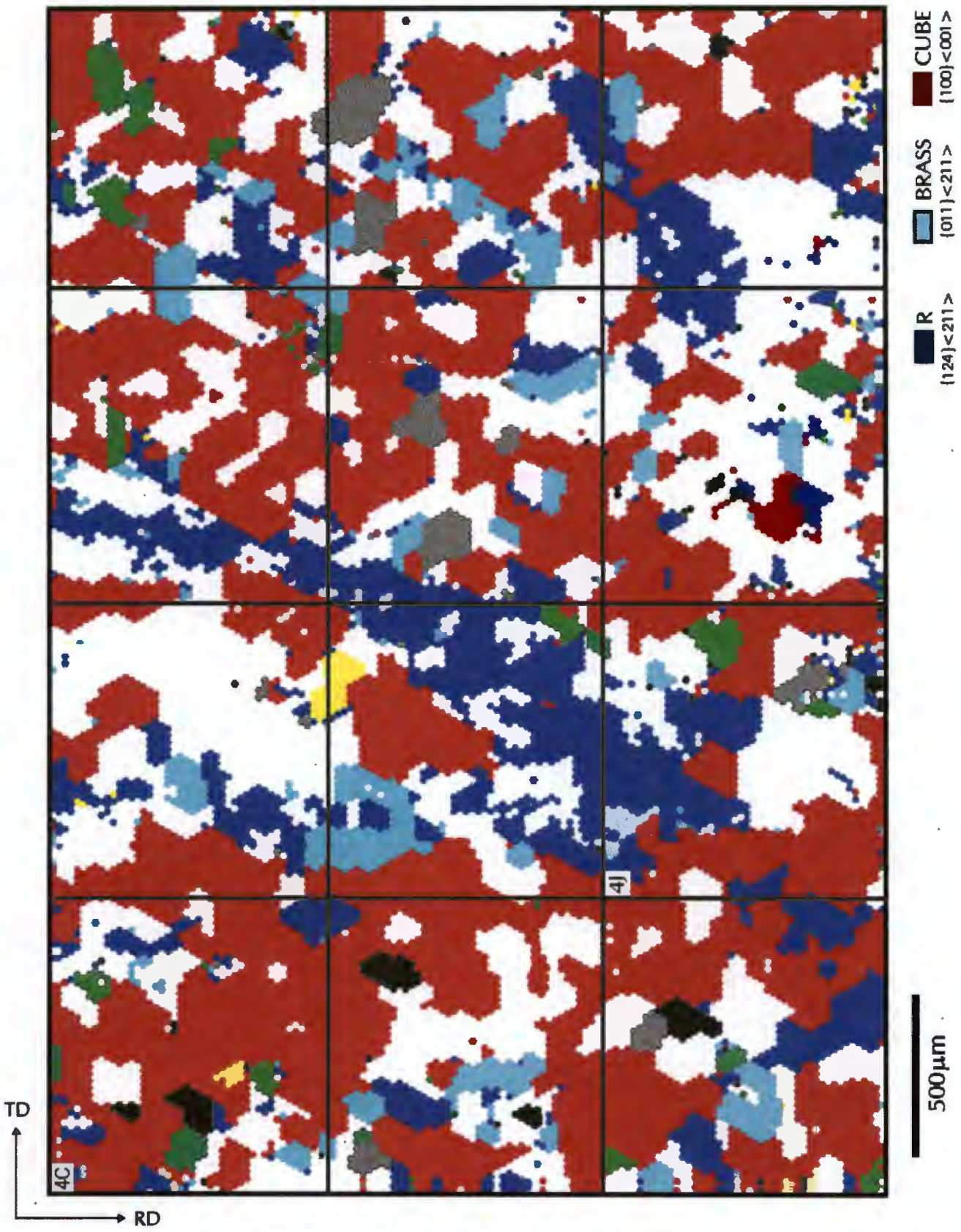

Figure 6.23: Texture Map of rolling plane section of ALU1.

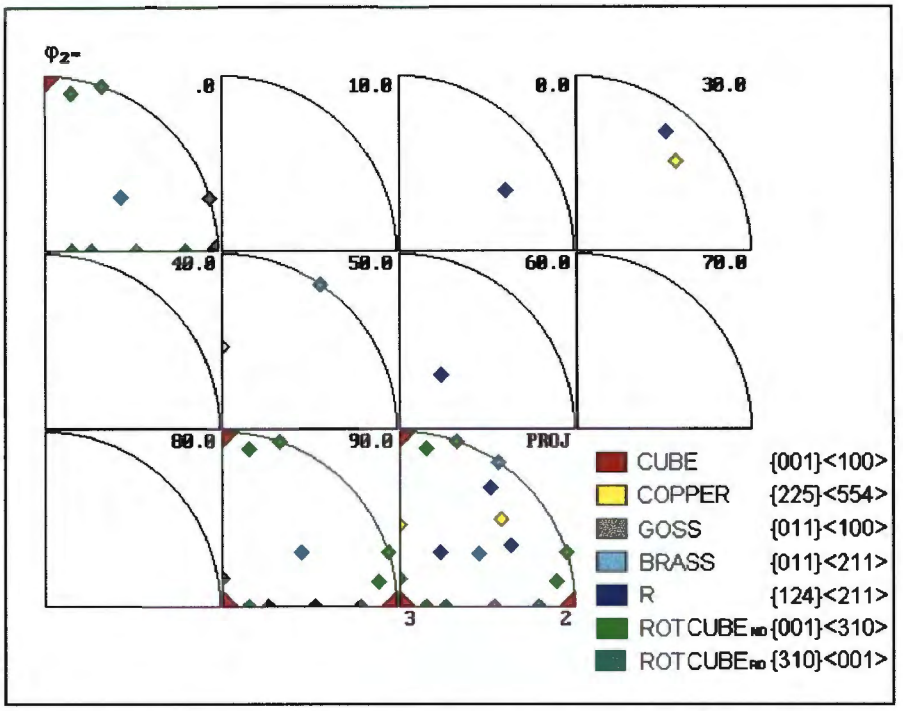

Figure 6.24: Polar plot of common textures found in FCC materials.

6.5 Plasticity Analysis

In order to gain more quantitative information on the yield behaviour of the aluminium alloys, the yield surfaces and strain ratios for each texture window were calculated and analysed in a similar manner to the stainless steels.

The yield surfaces for the texture windows of the ALU2 transverse and rolling plane sections show very little variation from window to window. Figure 6.25 and 6.26 illustrate the yield surfaces from three texture windows, of the transverse and rolling plane sections respectively, which have been superimposed on one set of axes. Limited differences in overall shape, slope at the axis intercepts and intercept value are visible. This suggests little variation in predicted yield behaviour across both transverse and rolling plane sections for sample ALU2. In addition, similar yield surface gradients at the X and Y intercepts within each texture window are noticeable thereby implying similar strain ratios and thus isotropic plastic behaviour for uniaxial deformation in both the transverse and rolling directions. The calculated strain ratios presented in figure 6.27 for the transverse section and figure 6.28 for the rolling plane

section indicate a similar trend. There is little variation in r-value across both sections as well as within each texture window.

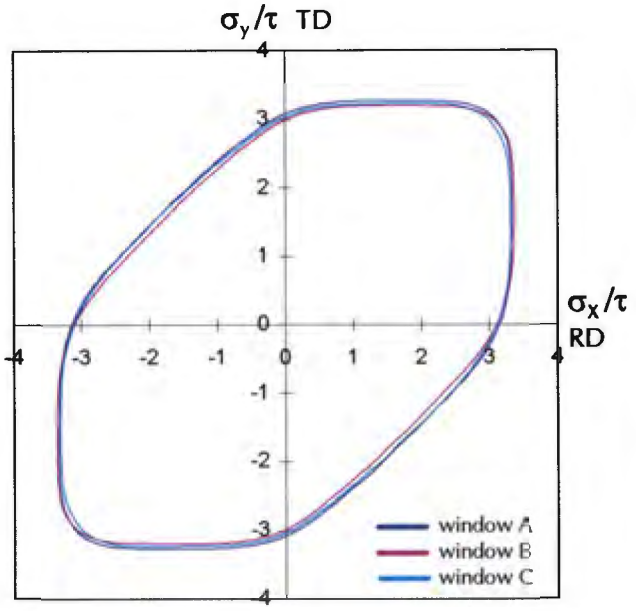

Figure 6.25: Yield surfaces for three texture windows across the transverse section of ALU2.

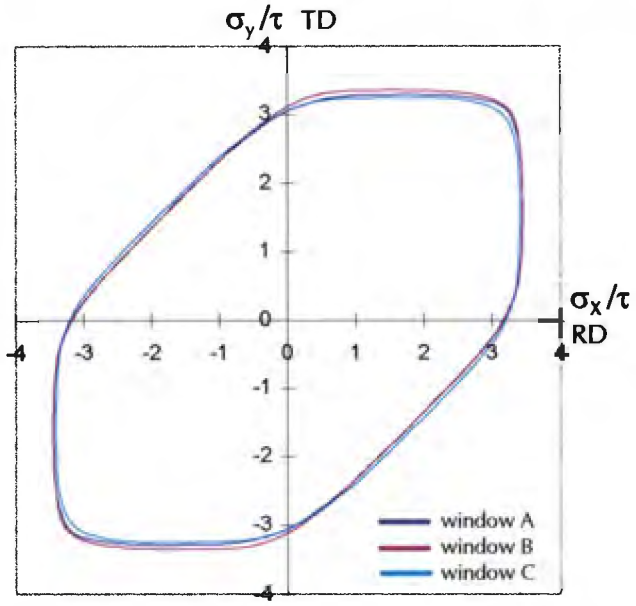

Figure 6.26: Yield surfaces for three texture windows across the rolling plane section of ALU2.

r_{RD} = 0.83 r_{TD} = 0.70	r_{RD} = 0.75 r_{TD} = 1.10	r_{RD} = 0.81 r_{TD} = 0.73	r_{RD} = 0.76 r_{TD} = 0.74	r_{RD} = 0.73 r_{TD} = 1.00	r_{RD} = 0.98 r_{TD} = 0.69

Figure 6.27: Strain ratios across the transverse section of ALU2.

$r_{RD} = 1.00$ $r_{TD} = 1.00$	$r_{RD} = 0.99$ $r_{TD} = 1.13$	$r_{RD} = 0.86$ $r_{TD} = 1.23$	$r_{RD} = 0.90$ $r_{TD} = 0.89$
$r_{RD} = 1.00$ $r_{TD} = 0.95$	$r_{RD} = 1.00$ $r_{TD} = 1.30$	$r_{RD} = 1.17$ $r_{TD} = 0.71$	$r_{RD} = 1.00$ $r_{TD} = 1.00$
$r_{RD} = 0.93$ $r_{TD} = 0.97$	$r_{RD} = 0.82$ $r_{TD} = 0.82$	$r_{RD} = 1.00$ $r_{TD} = 0.92$	$r_{RD} = 1.27$ $r_{TD} = 0.84$

Figure 6.28: Strain ratios across the rolling plane section of ALU2.

Yield surfaces across the transverse section of ALU1 also show very little variation in form. Figure 6.29 indicates the yield surfaces from three texture windows across the transverse plane. The shape of the yield surfaces are duplicated in each texture window with only slight differences in intercept gradient or intercept value, which means little variation in strain ratio or Taylor factor across the section. Furthermore, the strain ratios and Taylor factors for uniaxial tensile straining in the TD and RD are similar (figure 6.30). In the same way as that for ALU2, this implies isotropic yield behaviour during uniaxial tensile deformation in the transverse and rolling directions. These results suggest that there is little or no variation in through-thickness average properties across the transverse plane of sample ALU1.

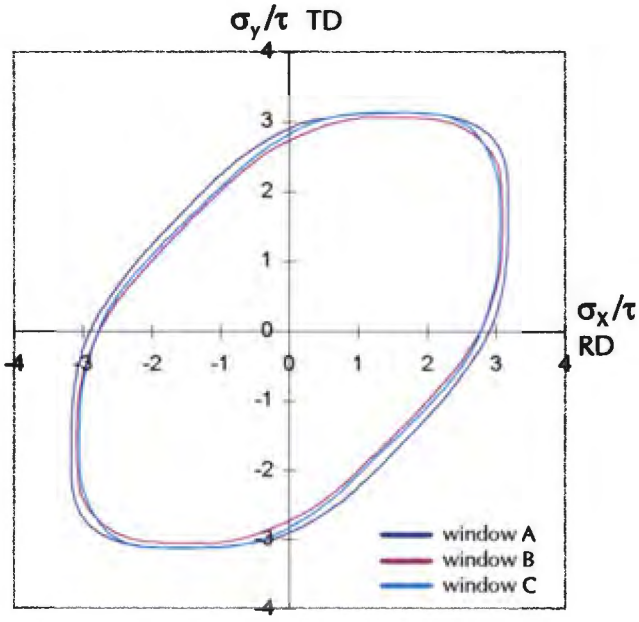

Figure 6.29: Yield surfaces for three texture windows across the transverse section of ALU1.

$r_{RD} = 1.13$ $r_{TD} = 0.81$	$r_{RD} = 0.74$ $r_{TD} = 0.92$	$r_{RD} = 1.27$ $r_{TD} = 0.72$	$r_{RD} = 0.92$ $r_{TD} = 1.00$	$r_{RD} = 0.72$ $r_{TD} = 1.02$	$r_{RD} = 1.00$ $r_{TD} = 1.28$

Figure 6.30: Strain ratios across the transverse section of AL1.

Conversely, across the rolling plane of alloy ALU1 a significant variation in yield surface morphology is evident. Not only are there differences in intercept value, but the slope of the yield surfaces at the intercepts differ, which means a variation in yield stress or Taylor factor as well as a variation in strain ratio across the section. Figure 6.31 shows the differences in yield surface shape for three texture windows across the rolling plane section. (Window A possesses a large percentage of cube texture, window B a large percentage of R texture while window C contains grains of both orientations). These trends can also be identified from figure 6.32 which illustrates the calculated strain ratios for deformation in the RD and TD. A greater range of strain ratios is evident across this section relative to the ALU2 rolling plane, as well as relative to the transverse section of both alloys. Furthermore, for certain windows a large difference in r-value for deformation in the TD and RD is visible, which implies anisotropic yield properties for these regions of sample ALU1.

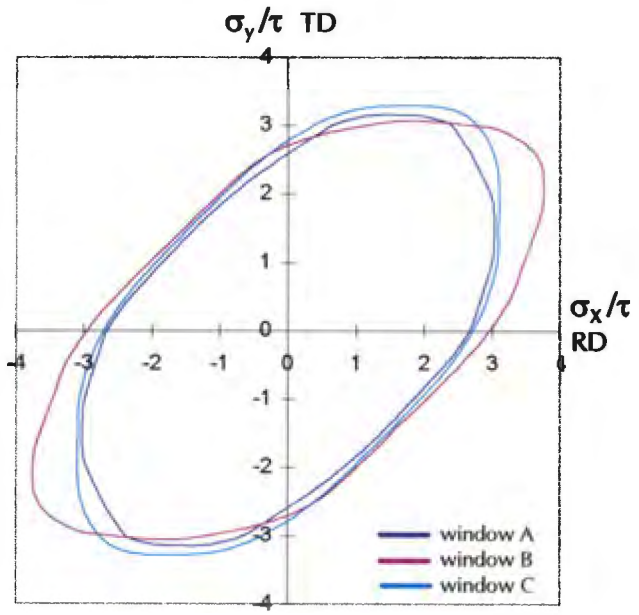

Figure 6.31: Yield surfaces from three texture windows across the rolling plane section of ALU1.

$r_{RD} = 1.87$ $r_{TD} = 1.51$	$r_{RD} = 1.11$ $r_{TD} = 2.80$	$r_{RD} = 1.56$ $r_{TD} = 2.30$	$r_{RD} = 2.02$ $r_{TD} = 1.53$
$r_{RD} = 2.24$ $r_{TD} = 1.46$	$r_{RD} = 0.72$ $r_{TD} = 2.91$	$r_{RD} = 2.77$ $r_{TD} = 1.73$	$r_{RD} = 1.64$ $r_{TD} = 1.17$
$r_{RD} = 1.05$ $r_{TD} = 1.34$	$r_{RD} = 1.58$ $r_{TD} = 2.27$	$r_{RD} = 2.18$ $r_{TD} = 1.31$	$r_{RD} = 1.93$ $r_{TD} = 1.08$

Figure 6.32: Strain ratios across the rolling plane section of ALU1.

In an attempt to correlate yield surface shape with texture distribution, yield surfaces for two texture windows possessing predominately R texture and two windows with predominately cube texture are indicated on one set of axes in figure 6.33. Significant differences in yield surface morphology are evident between the two pairs of yield surfaces. The yield surfaces R1 and R2, which possess a large percentage of R texture, indicate a shallow slope or high strain ratio at the Y intercept, while surfaces C1 and C2 with a majority of cube texture, have steeper slopes or lower r-values at the Y intercept. Thus, there is a reasonable correlation between texture and predicted plastic behaviour for the rolling plane section of sample ALU2.

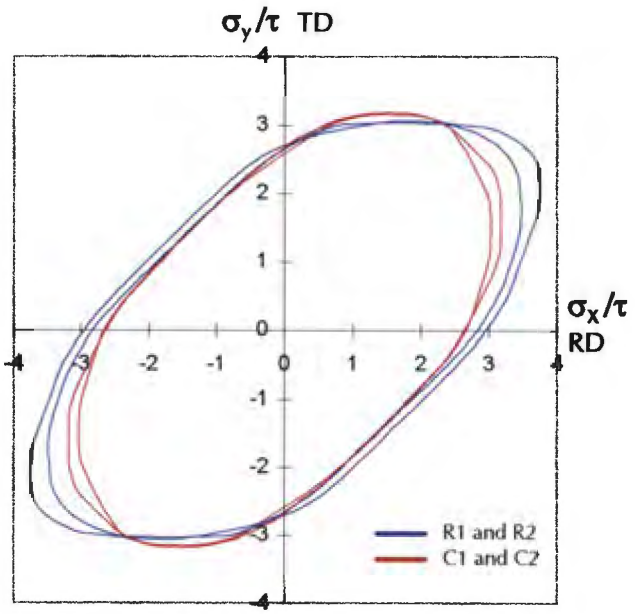

Figure 6.33: Yield surfaces from four texture windows from the rolling plane section of ALU1.

6.6 Discussion of Aluminium Results

Uniaxial tensile deformation has demonstrated considerable differences in surface roughening behaviour of the two AA3002 aluminium alloys. These differences are most obvious when the tensile axis is parallel to the sheet transverse direction, in which case specimen ALU1 forms characteristic surface ridges parallel to the rolling direction. Detailed analysis of these surface features indicates that the ridges are in fact not a result of a true corrugation effect, as found in the stainless steels, but rather form a ribbed profile as schematically illustrated in figure 6.34. This means that a distinct variation in sheet thickness develops across the transverse section of ALU1 to produce an alternating sequence of incipient necked regions. An explanation of this contrast in surface roughening behaviour lies in a comparison of the microstructural and textural properties of samples ALU1 and ALU2.

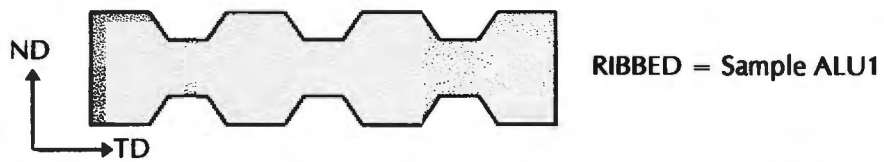

Figure 6.34: Ribbed through-thickness profile of ALU1 after elongation in the TD. (Amplitude of the ribs has been exaggerated).

The microstructural investigation of the ALU2 alloy indicates an approximately equiaxed homogeneous grain structure with an average grain size of 30 μm. In contrast, alloy ALU1 exhibits a larger average grain size (61 μm) with an aspect ratio of approximately 1:3 across the longitudinal and transverse sections. In addition, it is evident from polarised light microscopy analysis that the grain size in sample ALU1 is not homogeneous and many smaller non-cube grains are visible distributed within a matrix consisting of fewer large cube grains. As detailed in the literature review, the development of surface roughness of a metal during tensile deformation increases with grain size[1,6,7]. In addition, it has been established that an inhomogeneous distribution of texture components within a material can increase the rate of surface roughness development during deformation[2]. Therefore, based on grain size properties and texture

distribution, it is expected that alloy ALU1 would produce a rougher surface morphology during straining relative to alloy ALU2. The results of the tensile tests for the alloys indicate that this is indeed the case, in as much as the roughness of specimen ALU1 is significantly more severe after elongation in both the transverse and rolling directions compared to the same situation for ALU2.

Apart from the disparity in grain size and grain morphology between ALU1 and ALU2, a difference in material property for the two alloys is also evident from the bulk texture investigation. Sample ALU1 is dominated almost entirely by the cube texture, while the ALU2 alloy comprises of primary components of cube and R orientations. Microtexture measurements, recorded using automatic EBSD techniques, reveal a more or less homogeneous distribution of cube, brass and R texture components across the transverse and rolling plane sections of sample ALU2. It follows therefore that there is no variation in microtexture properties on a scale of the texture windows, across both the measured sections of the sample ALU2. An equivalent result is also manifest for the transverse plane of sample ALU1. Although a variation in orientation does exist from centre to surface in each window, a comparison of the texture components present reveals no differences in average microtexture across the transverse section on a scale of the window size. In contrast, the microtexture investigation of the rolling plane reveals distinct clustering of texture components in elongated bands in the RD. In particular, a 500 μm band of mostly R texture is visible extending for up to 2 mm in the RD (figure 6.20). These results suggest that the extent of clustering of the R texture in the rolling plane demonstrates that the microstructure could behave in a composite manner during deformation. Thus incompatible plastic flow of R and cube orientations during tensile deformation could help to explain the anisotropic flow behaviour or ribbed effect of specimen ALU1.

In order to gain more quantitative information regarding the texture properties of the two samples, the strain ratios and yield surfaces were calculated from the microtexture data. The results of the quantitative plasticity analysis mimic those of the interpretation of the microtexture analysis. As expected, little variation in

predicted plastic behaviour for the ALU2 samples is visible on a scale of the texture windows across both the transverse and rolling plane sections. The yield surfaces for the transverse section of sample ALU1 also provide little evidence for any differences in plastic flow behaviour across the section, as the overall shape of the yield surfaces, the calculated strain ratios and the Taylor factors are similar for each texture window. For the rolling plane however, a clear difference in yield surface shape is present from window to window. By comparing yield surfaces from texture windows dominated by different texture components, a good correlation between actual texture distribution and predicted plastic behaviour could be identified. The variation in plastic behaviour across the rolling plane implies that either the windows are relatively small compared to the grain size, or that grains of similar orientation exist in colonies on a scale similar or larger than the window size. From an inspection of the grain size it is clear that the latter situation applies.

Consideration must now be given to the relationship between the results of the texture plasticity analysis and the development of the ribbing effect in the ALU1 alloy. Two possibilities exist for the origin of the anisotropic plastic flow behaviour of sample ALU1 which causes the ribbed effect. Firstly, plastic instabilities could develop within the material which result in strain localisation and the initiation of necking in specific areas. Secondly, a variation in strain ratio or r-value could exist across the transverse plane on a scale similar to the ribbing profile.

The absence of through-thickness average property variation on scale of the texture windows, and therefore on a scale of the ribbing profile, identified from the plasticity analysis across the transverse plane of sample ALU1, rules out the latter possibility for the formation of the ribbed effect. This is in contrast to the conclusions of Bate[13], Wilson *et al*[2] and Wilson and Rodriques[3]. Each subscribe the origin of ribbing to the presence of a variation in through-thickness texture properties which leads to a variation in through-thickness plastic flow and ultimately necking in the regions of low average strain ratio. Therefore, for sample ALU1 it is necessary to investigate the first suggestion for

ribbing and identify what could cause the formation of plastic instabilities in the material which could lead to strain localisation.

If we examine the behaviour of the material during straining, a general surface roughening occurs during the early stages of plastic deformation (figure 6.35b below). If one considers the heterogeneous distribution of texture across the rolling plane of sample ALU1, then the shape changes on the surface will be influenced by the R texture colonies. Since the yield surface analysis has shown that the R dominated regions are more likely to thin in the ND direction when loaded in the TD, the R colonies will promote the formation of elongated depressions perpendicular to the applied stress. Progressive straining could lead to the coalescence of some of these depressions to form long shallow grooves (figure 6.35c). Analysis by Marciniak and Kuczynski (MK)[11] has shown that strain localisation leading to necking can occur when the separation of the grooves is greater than twice the sheet thickness. For the aluminium tensile samples the thickness is 1.0 mm and the average R_{max} value 40 μm. Therefore the defect coefficient, f, can be calculated from:

$$f = \frac{1000 - 40/2}{1000} = 0.98,$$

which is a reasonable upper limit for the MK analysis.

Since the formation of long grooves in sample ALU1 seems feasible when considering the development of surface roughening, the condition described by the MK analysis for strain localisation can arise. Continued straining will increase strain localisation and promote the development of the ribbing profile (figure 6.35d and 6.35e). Thus the ribbed profile of sample ALU1 can be characterised by a series of alternating necked regions which originates from the anisotropic flow occurring at the free surfaces.

(a)

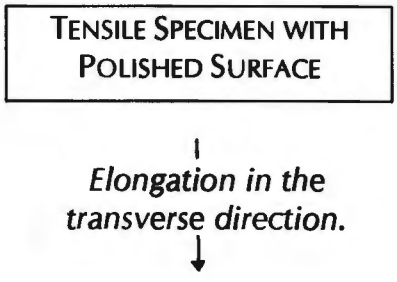

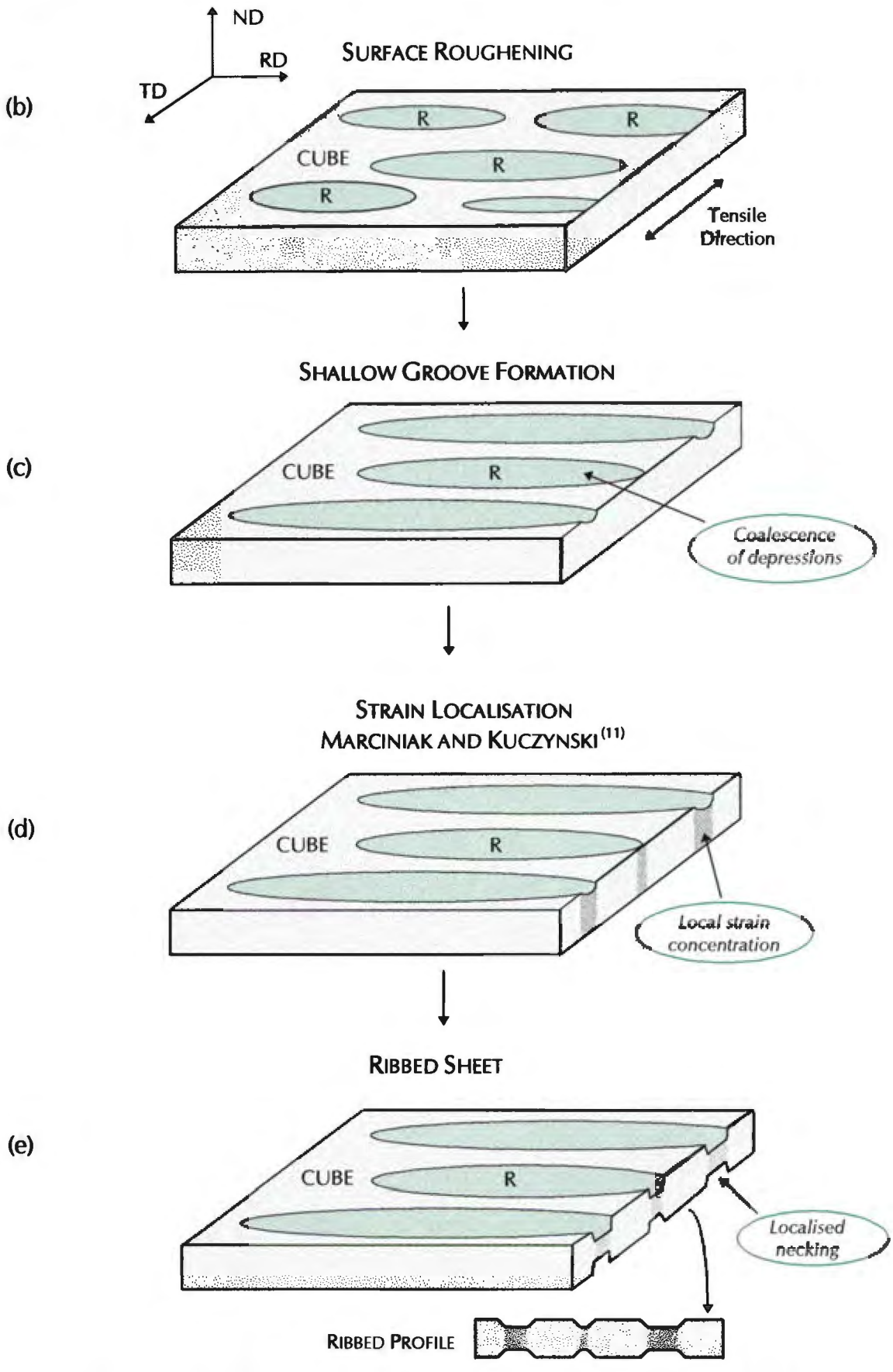

Figure 6.35: Schematic indicating the evolution of surface roughness to a ribbed profile.

This model will not be applicable when the material is subjected to uniaxial loading parallel to the rolling direction for two reasons. Firstly, the texture clusters are now elongated parallel to the tensile axis, and secondly, the r-ratio for the R texture under this tensile condition produces less relative thinning in the normal direction. The r-value for an ideal R texture is higher for uniaxial tensile deformation in the RD ($r = 1.707$) relative to tensile deformation in the TD ($r = 0.866$) which suggests less thinning in the normal direction when the tensile axis is parallel to the RD. Ribbing of course does not occur when the tensile axis is parallel to the RD, but general surface roughening still occurs which is consistent with the coarse grain size, grain shape and texture clustering.

CHAPTER 7

SUMMARY AND CONCLUSIONS

A comprehensive study on the surface roughening behaviour of ductile metals has included the examination of the microstructural, texture and plastic flow properties in a commercially produced AISI 430 stainless steel, a laboratory rolled steel of the same alloy, and two aluminium alloys of type AA3002. This chapter summarises the major findings and conclusions made in the current project.

7.1 Summary: Commercial Stainless Steel

The microstructural analysis of the commercial steel indicates a fine equiaxed grain structure with a decrease in grain size from the centre to the surface of the sheet. No grain size banding is visible across any section of the material. The principal textures of the steel lie along the γ-fibre, $<111>$//ND, including both the $\{111\}<112>$ component which is stronger near the surface, and the $\{111\}<110>$ component which dominates at the centre.

Tensile tests performed to 20% elongation, with the tensile axis aligned at 0° and 90° to the RD, provide critical information regarding the surface roughening behaviour of the commercial steel. Severe ridging, in the form of narrow continuous corrugations extending in the RD, occurs during elongation in the RD. Only minor surface roughening appears on a scale of the grain size. During elongation in the TD, no surface roughening is evident apart from a slight streaking in the RD. Removal of a ¼-thickness layer from each surface of the tensile specimen has the effect of increasing the frequency of the corrugations after elongation in the RD. Reducing the gauge length, however, causes a distinct decrease in the frequency and severity of the corrugations suggesting that ridging is caused by a summation of deformation events, as opposed to a plastic flow variation due to texture banding.

The microtexture of the commercial steel was examined across the transverse and rolling plane sections using an arrangement of discrete texture windows, where the window area was 0.3 mm^2 and 0.4 mm^2 respectively. The major components, which could be identified via polar plots and texture maps constructed in Euler space, include orientations from the α and γ fibres and the cube texture. Although a change in principal texture component is evident from the centre to the surface of the material, no texture clustering is visible across the transverse section on a scale of the texture windows. Across the rolling plane section, however, narrow elongated clusters of similar textures are visible extending for a few millimetres in the RD.

Plasticity calculations using the microtexture information demonstrate a similar lack of variation in plastic flow properties on a scale of the texture windows across the transverse and rolling plane sections. Division of the texture windows into four equal sections, however, results in a spatial variation in plastic flow properties on this reduced scale. The differences from section to section are demonstrated by a variation in yield surface morphology, strain ratio and Taylor factor.

Simulations of uniaxial deformation behaviour using a finite element approach were performed using the plasticity information calculated from the texture windows. Contour plots of the surface morphology after 10% elongation in the RD indicate the presence of longitudinal corrugations parallel to the RD when the arrangement of microstructural components is asymmetric about the mid-plane. It is proposed that the r-value fluctuation across the transverse section of the specimen causes a spatial variation in the rate of width change of the microstructural components which results in an inhomogeneous distribution of transverse strain about the mid-plane. During tensile deformation, differences in transverse strain experienced by the upper and lower regions of the sheet result in a series of localised bending events which generate a corrugated through-thickness profile.

The ridging mechanism can therefore be characterised as a summation of localised bending events due to an asymmetric distribution of texture components about the mid-plane of the material.

Using a mirrored arrangement about the centre plane produces a localised thinning effect caused by increased thinning at areas of low strain ratio. A layered homogeneous specimen leads to an even distribution of transverse strain and produces no surface distortion at all. Bending does not occur during uniaxial deformation in the transverse direction as the arrangement of microstructural components relative to the tensile axis does not favour the development of the necessary transverse strains distribution.

7.2 Summary: Laboratory Rolled Stainless Steel

A set of controlled rolled stainless steel samples (AISI 430) were produced with the objective of investigating the influence of thermomechanical process parameters on the surface roughening behaviour during uniaxial deformation. In particular, the hot roll finish temperature was varied systematically to produce three rolling schedules terminating at 920°C (1), 785°C (2) and 654°C (3).

A full microstructural and bulk texture analysis was conducted on the samples at each stage in the thermomechanical process. It was found that the variation in hot roll finish temperature dramatically altered the microstructural condition and the textures present in the samples. Sample B3, with a hot roll finish temperature of 654°C, possesses a fully recrystallised microstructure after the hot roll-anneal stage. Sample B1, on the other hand, did not undergo recrystallisation which is evident from the recovered microstructure after the same stage. After the final cold rolling and annealing stage all three samples recrystallised, and a decrease in average grain size is visible with a reduction in hot roll finish temperature. The grain size in each case is bimodal with bands of differing grain sizes extending in the RD.

The bulk texture analysis demonstrated a significant difference in principal texture component between the three heats, highlighting the effect of the hot roll finish temperature on the microstructure evolution. The centre of sample

D1 indicates a partial α-fibre and Goss texture, as opposed to sample D3 which possesses a strong γ-fibre texture. The surface textures of these two samples both demonstrate a γ-fibre as the main component and a Goss texture as the secondary component.

An analysis of the surface ridging behaviour, assessed via uniaxial tensile tests at 0°, 45° and 90° to the RD, indicates that surface roughening occurred in all three cold rolled-annealed samples. For elongation in the RD, a similar amplitude of corrugation is visible for each of the three specimens, but varying degrees of grain scale roughening are superimposed on the corrugations. Specimen D3 demonstrates regular continuous corrugations extending for a few millimetres in the RD, while specimen D1 exhibits more grain scale roughening to produce a much rougher effect. Elongation in the TD results in a significant change in deformation behaviour. The fine roughening effect remains identical in each specimen but the wavy undulations or corrugations are absent. The variation in specimen thickness across the transverse section after deformation could be confirmed via line scans measured on the upper and lower surfaces of each tensile specimen.

The microtexture across the transverse sections of samples D1 and D3 was examined via a similar arrangement of texture windows as used for the commercial steel. The texture maps and polar plots again allowed the identification of the major components. The texture map for sample D3 shows that the main components, namely $\{111\}<112>$ and $\{100\}<001>$, are not evenly distributed but instead have a tendency to be concentrated in bands of similar orientations. Textures $\{110\}<110>$ and $\{100\}<001>$, which are the main components present in sample D1, are also clustered in groups across the transverse section.

The inhomogeneous distribution of texture is also reflected in the results of the plasticity analysis. On a scale of the texture windows, sample D1 shows a significant variation in plastic properties, while for sample D3 a spatial variation in yield surface morphology is only visible after reduction of the texture windows into four equal sections. The strain ratios for each reduced section

also vary more across the transverse section for sample D1 compared to sample D3.

As in the case of the commercial steel, finite element modelling using the yield data from sample D1 and D3 demonstrates that the variation in plastic properties is sufficient to produce a variation of transverse strain within the specimen. The asymmetric distribution of transverse strain results in the development of longitudinal corrugations extending in the RD. The larger variation in predicted plastic properties for sample D1 results in a greater range of transverse strain values within the specimen and consequently a greater tendency for bending to occur.

7.3 Summary : Aluminium Alloys

Fully recrystallised samples of AA3002, which were sourced from two different suppliers, were employed in this investigation. Sample ALU1 demonstrates an elongated grain structure with clusters of large and small grains. Sample ALU2 on the other hand possesses an equiaxed grain structure with a smaller average grain size compared to ALU1. The bulk texture analysis of the two alloys also reveals a variation in properties. ALU1 shows a strong cube texture with a weaker R $\{124\}<211>$ texture, as opposed to sample ALU2 which possesses approximately equal intensities of R and cube textures, particular at the mid-plane region.

During uniaxial deformation in the RD and TD the surface roughening behaviour of the two alloys is distinctly different. Sample ALU2 reveals limited surface roughening on a scale of the grain size during elongation in both directions. In contrast, specimen ALU1 experiences severe surface roughening including continuous parallel ridges and a fine grain size roughening during elongation in the TD. An examination of the through-thickness profile indicates areas of thinning which means that the sheet produces a ribbed effect during deformation as opposed to a corrugated effect. During elongation in the RD, the ridges are absent but significant grain scale roughening still persists.

The microtexture was examined using discrete texture windows across both the transverse and rolling plane sections of the alloys. The orientation information was then used to construct polar plots and texture maps in order to identify the distribution of preferred orientation. The texture maps of sample ALU2 suggest a homogeneous distribution of preferred orientation across both sections. Preferred orientations present include cube, brass $\{011\}<211>$ and R textures. Across the transverse section of ALU1 a similar random distribution is evident. The texture windows, consisting of mostly cube, brass and R orientations, are considered to replicate each other in texture type and distribution. The texture map for the rolling plane section of ALU1, however, reveals a distinctly inhomogeneous distribution or clustering of the major texture components namely, cube and R texture. In particular, a band of mainly R texture measuring approximately 500 μm in the ND, extends for 2 mm in the RD. These results suggest that the extent of clustering of the R and cube textures could lead to incompatible plastic flow during deformation which could explain the ribbing effect.

To provide a more quantitative assessment of the plastic properties, the yield surfaces and strain ratios were calculated for each texture window. For sample ALU2, only small differences in yield surface morphology are found from window to window. This suggests little variation in predicted plastic behaviour across both the transverse and rolling plane sections for sample ALU2. Comparison of the yield surfaces for the individual texture windows for the transverse section of ALU1 also demonstrates little change in predicted plastic behaviour. For the rolling plane section of ALU1, however, the extensive texture clustering results in a significant variation in yield surface morphology from window to window. After a detailed examination it was concluded that a good correlation exists between yield surface morphology and preferred orientation.

The next stage was to investigate the relationship between the plasticity analysis and the development of the ribbed through-thickness profile. The consistency in through-thickness average properties on a scale of the texture windows rules out the possibility of a variation in average strain ratio resulting in the ribbing

profile. A second possibility is the presence of plastic instabilities within the material leading to strain localisation and necking in certain areas. Since the yield surface analysis has shown that the R dominated regions are more likely to thin in the ND direction when elongated in the TD, the R colonies at the specimen surface will promote the formation of elongated depressions perpendicular to the applied stress. Progressive straining could lead to the coalescence of some of these depressions to form long shallow grooves. Analysis by Marciniak and Kuczynski[11] has shown that strain localisation leading to necking can occur when the separation of the grooves is greater than twice the sheet thickness. Since the formation of long grooves in sample ALU1 seems feasible when considering the development of surface roughening, the condition described by the MK analysis for strain localisation can arise. Continued straining will increase strain localisation and promote the development of the ribbing profile.

7.4 Conclusions

Commercial Stainless Steel:

a) The commercial stainless steel has a fine equiaxed grain structure with no grain size banding, which suggests that the origin of ridging is not dependent on an inhomogeneous microstructure.

b) A decrease in ridging frequency and amplitude occurs with a reduction in gauge length of the tensile specimen, during elongation in the RD. Ridging is therefore far more likely to be the result of a series of deformation induced bending events, as opposed to a plastic flow variation on a scale of the texture clustering.

c) Ridging is most severe during elongation in the RD and decreases in amplitude as the tensile axis rotates away from the RD, until no ridging occurs during elongation in the TD. The streaking that appears on the surface of the specimen can be attributed to a variation in crystal rotation of the surface grains due the narrow texture clusters elongated in the RD.

d) Ridging frequency is increased by a reduction in thickness of the specimen which also supports a bending controlled deformation mechanism.

e) No texture clustering occurs across the transverse section on a scale of the texture windows. This means that ridging cannot arise due to a variation in plastic flow properties on a scale of the texture windows and therefore on a scale of the ridging profile.

f) Division of the texture windows into four equal sections through-the-thickness of the sheet reveals a variation in plastic property across the transverse section.

g) Finite element modelling simulations have shown that the variation in plastic flow properties within the commercial steel is sufficient to produce a fluctuation in transverse strain within the specimen. The asymmetric variation in transverse strain about the mid-plane of the specimen results in alternating bending events which produce longitudinal corrugations.

h) Narrow clusters of similar orientation are visible across the rolling plane section of the commercial stainless steel and contribute to the extension of the corrugations in the RD.

Laboratory Rolled Stainless Steel

(a) The variation in hot roll finish temperature influences the extent of recrystallisation and recovery experienced by the sheet, which affects the microstructure and texture properties of the alloy.

(b) The corrugated effect is most severe during uniaxial tensile deformation in the RD and reduces to a level where no corrugations form during deformation in the TD. However, the grain scale roughening occurs regardless of the alignment of the tensile axis and can be attributed to a variation in crystal rotation due to the clusters of preferred orientation and grain size.

(c) Microtextural analysis of the heats in the cold rolled annealed condition demonstrates an inhomogeneous distribution of texture components, which

leads to a spatial variation in predicted plastic behaviour on a scale greater than the grain size.

(d) Sample D1 reveals a more pronounced variation in plastic flow properties, including yield surface morphology and strain ratio, suggesting that the spatial variation in plastic properties increases with an increase in hot roll finish temperature.

(e) Finite element modelling incorporating the microtexture information, has shown that longitudinal corrugations can arise due to the transverse bending mechanism described for the commercial steel. The amplitude of the corrugations is larger for the laboratory rolled steel compared to the commercial steel as the variation in plastic properties is relatively greater within the alloy.

(f) Sample D1 exhibits an inhomogeneous distribution of preferred orientation and a greater variation in predicted plastic properties compared to sample D3. Indications are therefore that increased recrystallisation and grain refinement, via a reduction in the hot roll finish temperature, will reduce variations in yield behaviour and thereby reduce the level of ridging.

Aluminium Alloys

(a) After uniaxial tensile deformation in the transverse direction, specimen ALU1 demonstrates a ribbed through-thickness profile whereas ALU2 demonstrates no ribbing. Neither of the specimens display ribbing when the tensile axis is parallel to the rolling direction.

(b) The plasticity analysis revealed no variation in through-thickness average properties on a scale of the texture windows across the transverse sections of samples ALU1 and ALU2.

(c) Yield surface calculations from the rolling plane section suggest a good correlation between the distribution of predicted plastic properties and the clustering of preferred orientations within sample ALU1.

(d) To explain the occurrence of ribbing it was concluded that plastic instabilities in the form of elongated depressions arise due to a texture related surface roughening effect.

(e) The MK theory is employed to propose that ribbing during uniaxial tension is the result of the formation of a series of localised necks.

(f) Ribbing in an aluminium alloy AA3002 can be eliminated by preventing the development of texture colonies and ensuring a homogeneous texture distribution.

REFERENCES

1. C. Gvangnan, S. Huan, H. Shiguang and B. Baudelet, Mat. Sci. Eng., A128, p 33, 1990.
2. D.V. Wilson, W.T. Roberts and P.M.B. Rodrigues, Metall. Trans. A, Vol 12A, p 1603, September 1981.
3. D.V. Wilson and P.M.B. Rodrigues, Metall. Trans. A, Vol 17A, p 367, February 1986.
4. D.V. Wilson, W.T. Roberts and P.M.B. Rodrigues, Metall. Trans. A, Vol 12A, p 1595, September 1981.
5. A.K. Todros and D.B. Mellor, Int. J. Mech. Sci., Vol 20, p 121, 1978.
6. D.V. Wilson, A.R. Mirshams and W.T. Roberts, Int. J. Mech. Sci., Vol 12, p 859, 1983.
7. K. Yamaguchi and P.B. Mellor, Int. J. Mech. Sci., Vol 18, p 85, 1976.
8. K. Osakada and M. Oyane, Bull. JSME, Vol 14, p 171, 1971.
9. A. Parmar, P.B. Mellor and J. Chakrabarty, Int. J. Mech. Sci., Vol 19, p 389, 1977.
10. U.F. Kocks, Metall. Trans., Vol 1, p 1121, May 1970.
11. Z. Marciniak and K. Kuczynski, Int. J. Mech. Sci., Vol 9, p 609, 1967.
12. D.W. Lin, D. Daniel and J.J. Jonas, Metall. Trans. A, Vol 22A, p 2069, September 1991.
13. P. Bate, Int. J. Mech. Sci., Vol 26, No5, p 373, 1984.
14. J.Lion and D. Zhou, Mat. Sci. Eng., Alll, p 1, 1989.
15. *Mechanics of Sheet Metal Forming*, J.W. Hutchinson, K.W. Neale and A. Needleman, eds: D.P. Koistinen and N.M. Wang, Plenum press, New York/London, p 111, 1978.
16. H.W. Swift, J. Mech. Phys. Solids, Vol 1, p 1,1952.
17. R. Hill, J. Mech. Phys. Solids, Vol 1, p 19, 1952.
18. R. Sowerby and J.L. Duncan, Int. J. Mech. Sci., Vol 13, p 217, 1971.
19. Z. Marciniak, K. Kuczynski and T. Pokora, Int. J. Mech. Sci., Vol 15, p 789, 1973.
20. S. Storen and J.R. Rice, J. Mech. Phy. Solids, Vol 23, p 421,1975.
21. *Mechanics of Sheet Metal Forming*, J.W. Hutchinson and K.W. Neale, eds: D.P. Koistinen and N.M. Wang, Plenum, New York, p 27, 1978
22. *Mechanics of Sheet Metal Forming*, E.H. Lee, eds: D.P. Koistinen and N.M. Wang, Plenum, New York, p 401, 1978.
23. R. Hill, Proc. Royal Soc. London, A193, p 281, 1948.
24. P.S. Bate, Scripta Metall. Mater., Vol 27, p 515, 1992.
25. R. Davies and V. Randle, Mat. Char., Vol 37, p 131, 1996.
26. R. Becker, to appear in Acta Mater.

27. Y. Itoh, T. Okajima, H. Maede and K. Tashiro, Trans. ISIJ, Vol 22, p 223, 1982.
28. T. Sheppard and P. Richards, Mat. Sci. Tech., Vol 2, p 693, July 1986.
29. H. Miyaji and S. Watanabe, Trans. Nat. Research Inst. For Metals, Vol 20, No 5, p 281, 1978.
30. J.D. Defilippi and H-C. Chao, Metall. Trans., Vol 2, p 3209, November 1971.
31. K. Suzuki, S. Asami and K. Suzuki, Trans. ISIJ, Vol 23, 1983.
32. H-C. Chao, Trans. of ASM, Vol 60, p 37, 1967.
33. T. Shindo and T. Furukawa, in Proc. 6th Int. Conf. Textures of Materials, ICOTOM 6, ISIJ, Japan, eds: S. Nagashima, p 846, Sept/Oct 1981.
34. R.N. Wright, Metall. Trans, Vol 3, p 83, January,1972.
35. H.M. Kim and J.A. Szpunar, Mat. Sci. Forum, Vol 157-162, p 753, 1994.
36. K. Bethke, M. Hölscher and K. Lücke, Mat. Sci .Forum. Vol 157-162, p 37, 1994.
37. J. Harase, K. Ohta, T. Takashita and R. Shimizu, Mat. Forum, Vol 14, p 296, 1990.
38. H. Takechi, H. Kato. T. Sunami. and T. Nakayama, Trans J.I.M, Vol 8, p 233, 1967.
39. J.A. Salsgiver, J.M. Larsen and P.R. Borneman, in Proc. Int. Conf. Recrystallisation '90, ed: T. Chandra, The Minerals, Metals and Materials Society, TMS, 1990.
40. C.M. Vlad, M. Dahms, H.J. Bunge and M. Haase, in Proc. 8th Int. Conf. on Textures of Materials, ICOTOM 8, ed: J.S. Kallend and G. Gottstein, TMS, p 873, 1988.
41. D.J. Dingley, Scanning Electron Microscopy, Vol II, p 569, 1984.
42. B.L. Adams, S.I. Wright and K. Kunze, Metall. Trans. A, Vol 24A, p 819, 1993.
43. H-G. Appel and H. Becker, Z. Metall., Vol 54, p 724, 1963.
44. H-C. Chao, Metall. Trans. A, p 1183, April 1973.
45. H-C. Chao, Metall. Trans. A, p 1009, June 1977.
46. R.N. Wright, Metall. Trans. A, Vol 7A, p 1385, September 1976.
47. H-C. Chao, Metall. Trans. A, Vol 9A, p 509, April 1978.
48. M. Hamasaki, I. Gokyu and S. Okamura, Trans. JIM, Vol 13, p 238, 1972.
49. J. Harase, K. Ohta, T. Takeshita and Y. Kawamo, in Proc. Int. Conf. on Stainless Steel, Chiba, p 856, 1991.
50. D. Raabe, Mat. Sci. Tech. Vol 11, p 461, May 1995.
51. M. Hölscher and L. Staubuwasser, in Proc. Int. Conf. Innovation Stainless Steel, Firenze, p 2.339, 11-14 October 1993.
52. M. Koike, Y. Machara, K. Kaneko and H. Fujikawa, in Proc. Int. Conf. on Stainless Steel, Chiba, ISIJ, p 864, 1991.
53. R. Patton. Mat. Sci. Tech., Vol 10, p 604, July 1994.

54. T. Sawatani, M. Ishii and H. Yoshimura, T. Ashiura et al., Technical Report: Nippon Steel Corp. Hikari City. Japan.
55. Y.D. Lee, D.Y. Ryoo, Y.Y. Lee and S.H. Park, in Proc. Recrystallisation '90, ed: T. Chandra, TMS, p 435, 1990.
56. D. Raabe and K. Lücke, Mat. Tech., Steel Research 63, No 10, 1992.
57. *Steel: A Handbook for Materials Research and Engineering*, ed: Verein Deutscher Eisnhuttenluete, Verlag Stahleisen, Düsseldorf, 1993.
58. D. Raabe and M. Ylitalo, Metall. Mat. Trans. A, Vol 2A, p 49, January 1996
59. R.A.E. Hooper, D.T. Llewellyn and V.T. McNeely, Sheet Metal Industries, p 26, January 1972.
60. D. Raabe and K. Lücke, Scripta Metall., Vol 26, p 1221, 1992.
61. M. Hölscher, D. Raabe and K. Lücke, Acta Metall. Mater., Vol 42, No 3, p 879, 1994.
62. D. Raabe and K. Lücke, in Proc. Strip Casting, Hot and Cold Working of Stainless Steel, Quebec City, Quebec, Aug 29 - Sept 2, p 221, 1993.
63. M. Hölscher, D. Raabe and K. Lücke, Steel Research 62, No 12, p 567, 1991.
64. D. Raabe and K. Lücke, Steel Research 63, No 10, p 457, 1992.
65. D. Raabe and K. Lücke, Mat. Sci. Tech., Vol 9, p 302, April 1993.
66. D. Raabe and K. Lücke, Scripta Metall., Vol 27, p 1533, 1992.
67. D. Raabe, M. Hölscher, M. Dubke and K. Lücke, in Proc. Strip Casting, Hot and Cold Working of Stainless Steel, Quebec City, Quebec, Aug 29 - Sept 2, p 3, 1993.
68. D. Raabe, Phys. Stat. Sol., Vol 181, p 291, 1994.
69. K Lücke, Canad. Metal Quart., Vol 13, p 261, 1974.
70. T. Haratani, W.B. Hutchinson, I.L. Dillamore and P. Bate, Met. Science, Vol 18, p 57, 1984.
71. I. L. Dillamore and W.T. Roberts, Metall. Reviews, Vol 10, No 39, p 271, 1965.
72. *Recrystallisation, Grain Growth and Textures*, ASM, Metals Park, Ohio, p 393, 1966.
73. W.B. Hutchinson, Metal Science, Vol 8, p. 185, 1974.
74. K. Lücke, in Proc. 7th Int. Conf. Textures of Materials, ICOTOM 7, The Netherlands Society for Materials Science, Zwijndrecht, p 195, 1984.
75. K Lücke and J. Hirsch, Aluminium Tech., p 267, 1986.
76. J. C Blade, Metals Science, p 206, March-April 1979.
77. J. C. Blade, Technical Report, Alcan , Banbury, November 1963.
78. O. Engler, in Proc. Minerals and Materials '96, SAIMM, Cape Town, p 449, August 1996.
79. T. Ozturk and G.J. Davies, Mat. Sci. Tech., Vol 5, February 89.

80. C.S. da Costa Vianna, G.J. Davies and J.S. Kallend, in Proc. 5th Int. Conf. Textures of Materials, ICOTOM 7, p 447, 1978.
81. P.M.B. Rodriques and P.S. Bate, in Proc. Textures in Non-ferrous Metals and Alloys, AIME, Warrendale PA, p 173, 1985.
82. D.V. Wilson, Metall. Reviews, Vol 37, p 175, 1969.
83. R.D. Doherty, W.G. Fricke Jr and A.D. Rollett, Aluminium Tech., p 289, 1986.
84. S. Panchanadeeswaran and D.P. Field, Acta Metall. Mater., Vol 43, No 4, p 1683, 1995.
85. J.R. Hirsch, Mat. Sci. Tech., Vol 6, p 1048, 1990.
86. J. Hirsch, W. Mao and K. Lücke, Aluminium Tech., p 303, 1986.
87. A.L. Dons and E. Nes, Mat. Sci. Tech., Vol 2, p 8, 1986.
88. A.A. Ridha and W. B. Hutchinson, Acta Metall., Vol 30, p 129, 1982.
89. O. Engler, P. Yang and X.W. Kong, Acta Mater., Vol 44, No 8, p 3349, 1996.
90. *Physical Metallurgy*, R.W. Cahn and P. Haasen, 3rd ed., North-Holland Physics Publishing, Amsterdam, 1983.
91. I.L. Dillamore and Katoh, Metal Science, Vol 8, p 73, 1974.
92. T.O. Saetre, J. K. Solberg and N. Ryum, Metallography, Vol 19, p 345, 1986.
93. 93.as referenced in 63: H.J. Bunge, "Mathematische Methoden der Texturanalyse", Akademie-Verlag, Berlin, 1969.
94. S.I. Wright, Journal of Computer-Assisted Microscopy, Vol 5, No 3, p 207, 1993.
95. *Microtexture Determination and its Applications*, V. Randle, Inst. of Materials, London, 1992.
96. G.I. Taylor, J. Inst. Metals, Vol 62, p 307, 1938.
97. G.I. Taylor, Royal Soc. Proc. A., Vol 116, p 16, 1927.
98. J.F.W. Bishop and R. Hill, Phil. Mag., Vol 42, p 414, 1951.
99. J.F.W. Bishop and R. Hill, Phil. Mag., Vol 42, p 1298, 1951.
100. J. Lian and J. Chen, Acta Metall. Mater., Vol 39, No 10, p 2285, 1991.
101. H. Honneff and H. Mecking, in Proc. 5th Int. Conf. Textures of Materials, ICOTOM 5, Springer, Berlin, eds: G. Gottstein and K. Lücke, Vol 1, p 265, 1978.
102. S. Tiem, M. Berveiller and G.R. Canova, Acta Metall., Vol 34, No 11, p 2139, 1986.
103. Leffers, Scripta Metall., Vol 9, p 261, 1968.
104. G.R. Canova, U.F. Kocks and C.N. Tomé, J. Mech. Phys. Solids, Vol 33, No4, p 371, 1985.
105. *The Mechanics of Crystals and Textured Polycrystals*, W.F. Hosford, Oxford University Press, Oxford, 1993.
106. L.S. Tóth, J. Hirsch and P. Van Houtte, Int. J. Mech. Sci., Vol 38, No 10, p 1117, 1996.

107. M. Brochu, T. Yokota and S. Satoh, Int. ISIJ, Vol 37, No 9, p 872, 1997.

108. I. Samajdor and R.D. Doherty, Scripta Metall. Mater., Vol 32, No 6, p 845, 1995.

109. R.D. Doherty, K. Kashyao and S. Panchanadeeswaran, Acta Metall. Mater., Vol 14, No 10, p 3029, 1993.

110. J.A. Venables and C.J. Harland, Phil. Mag., Vol 27, p 1193, 1973.

111. S.I. Wright and B.L. Adams, Metall. Trans. A, Vol 23A, p 759, 1992.

112. R.A. Schwarzer, in Proc. Conf. Frontiers of Electron Microscopy in Materials Science, Oak Brook, Chicago, June 4-7, 1996.

113. S. Nagashima, M. Shiratori and K. Matsukawa, J. Soc. Mat. Sci. Japan, Vol 34, p 486, May 1985.

114. J.S. Kallend, U.F. Kocks, A.D. Rollett and H-R. Wenk, Mat. Sci. Eng., Vol A132, p 1, 1991.

115. N.J. Wittridge and R.D. Knutsen, in Proc. Int. Conf. Thermo-mechanical Processing in Theory, Modelling and Practice, The Swedish Society for Materials Technology, 4-6 September 1996, Stockholm, p 390.

116. N.J. Wittridge and R.D. Knutsen, Mat. Charac., Vol 37, p 31, 1996.

APPENDIX A

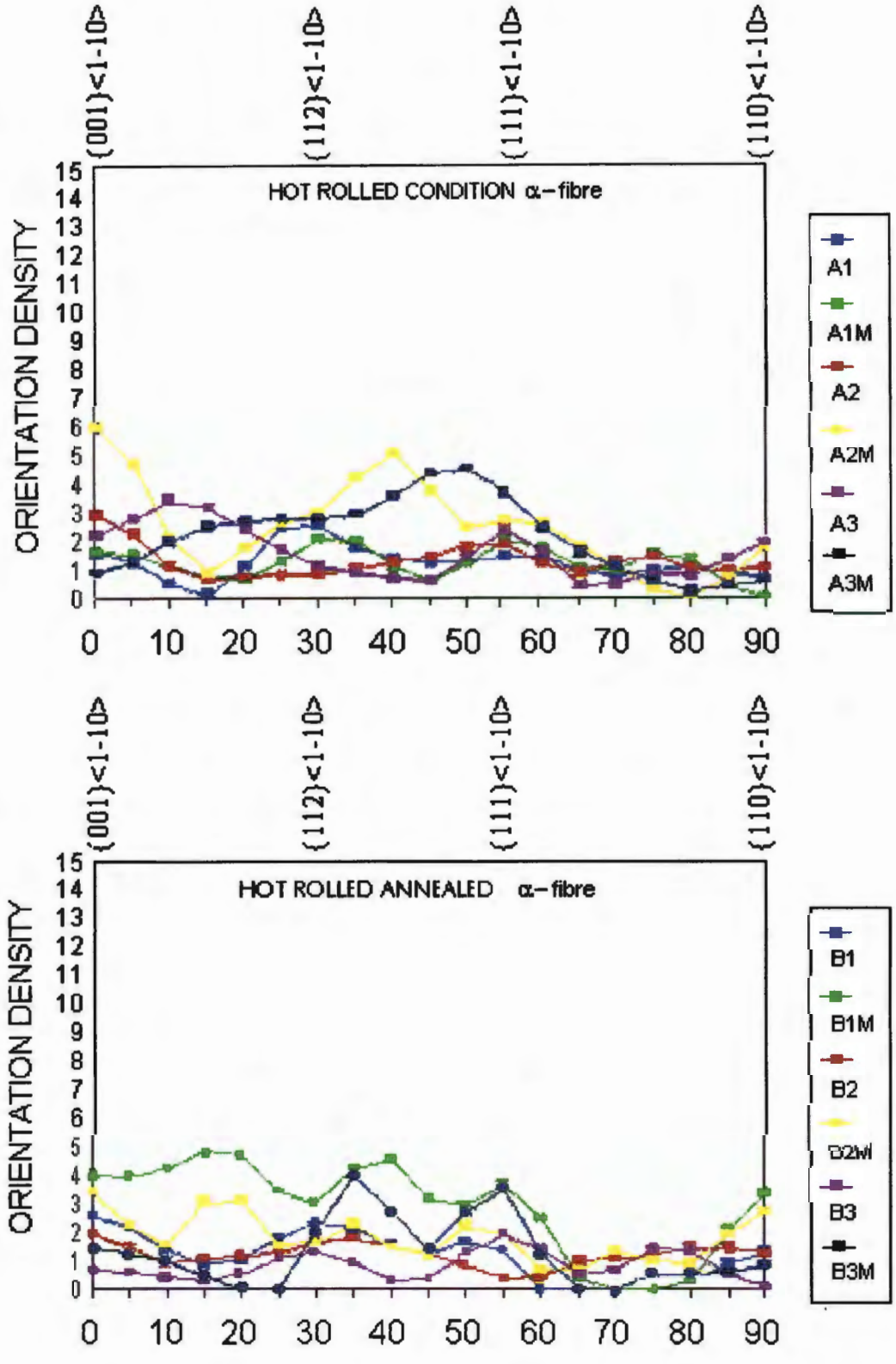

Figure A1: Diagram of the α-fibre for stages A (hot rolled) and B (hot rolled-annealed) M= Mid-plane.

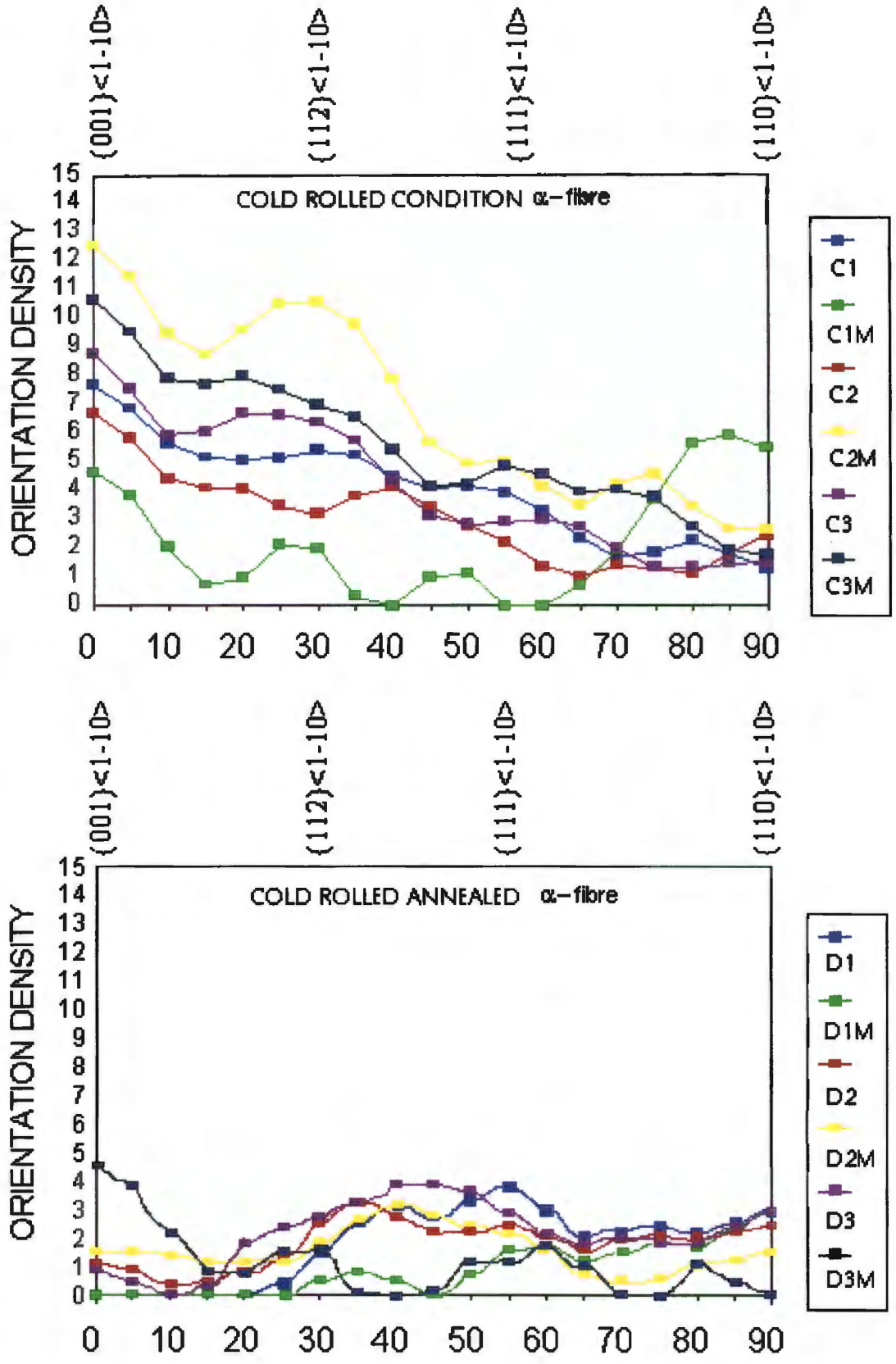

Figure A2: Diagram of the α-fibre for stages C (cold rolled) and D (cold rolled-annealed).

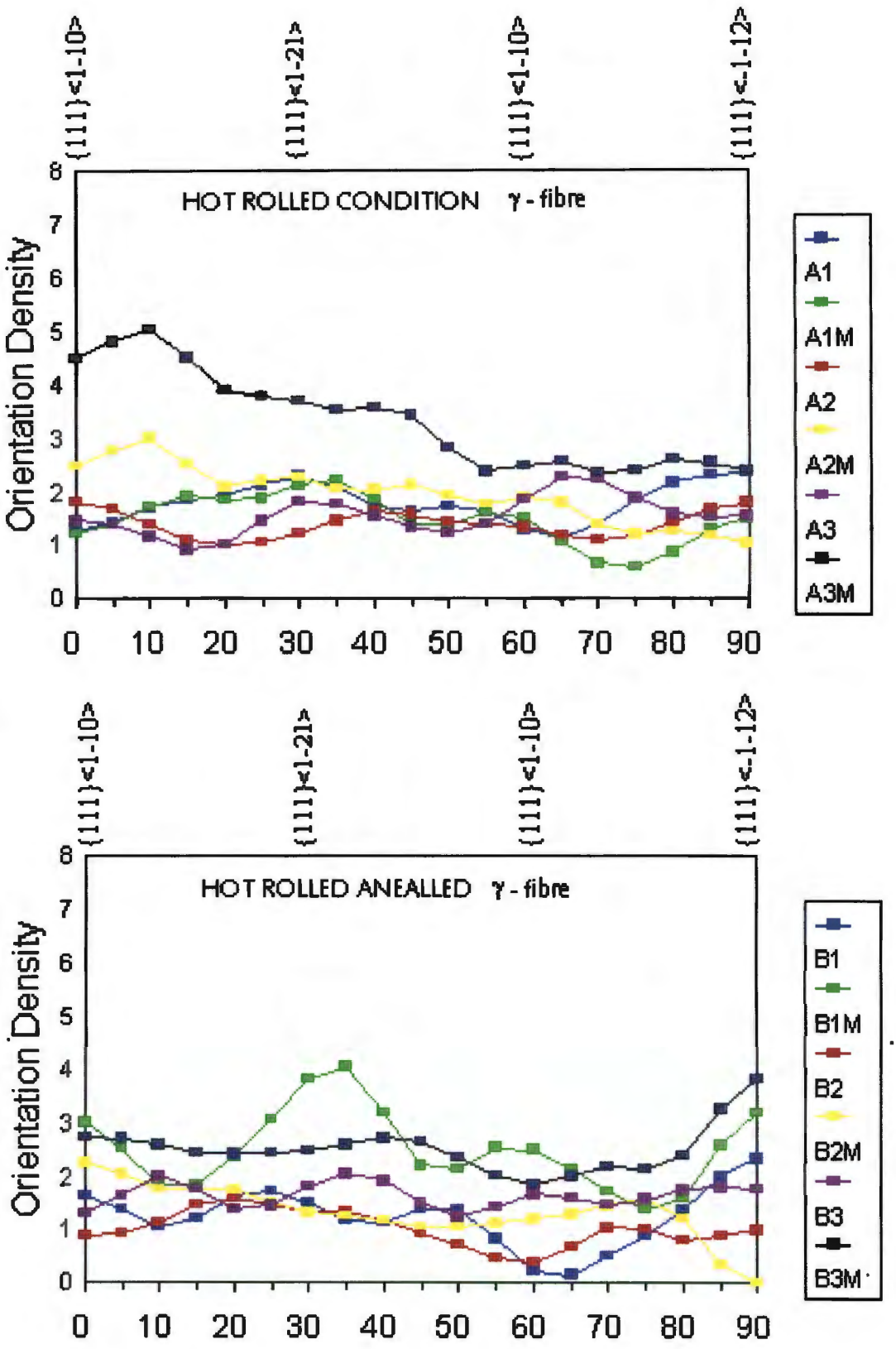

Figure A3: Diagram of the γ-fibre for stages A (hot rolled) and B (hot rolled-annealed).

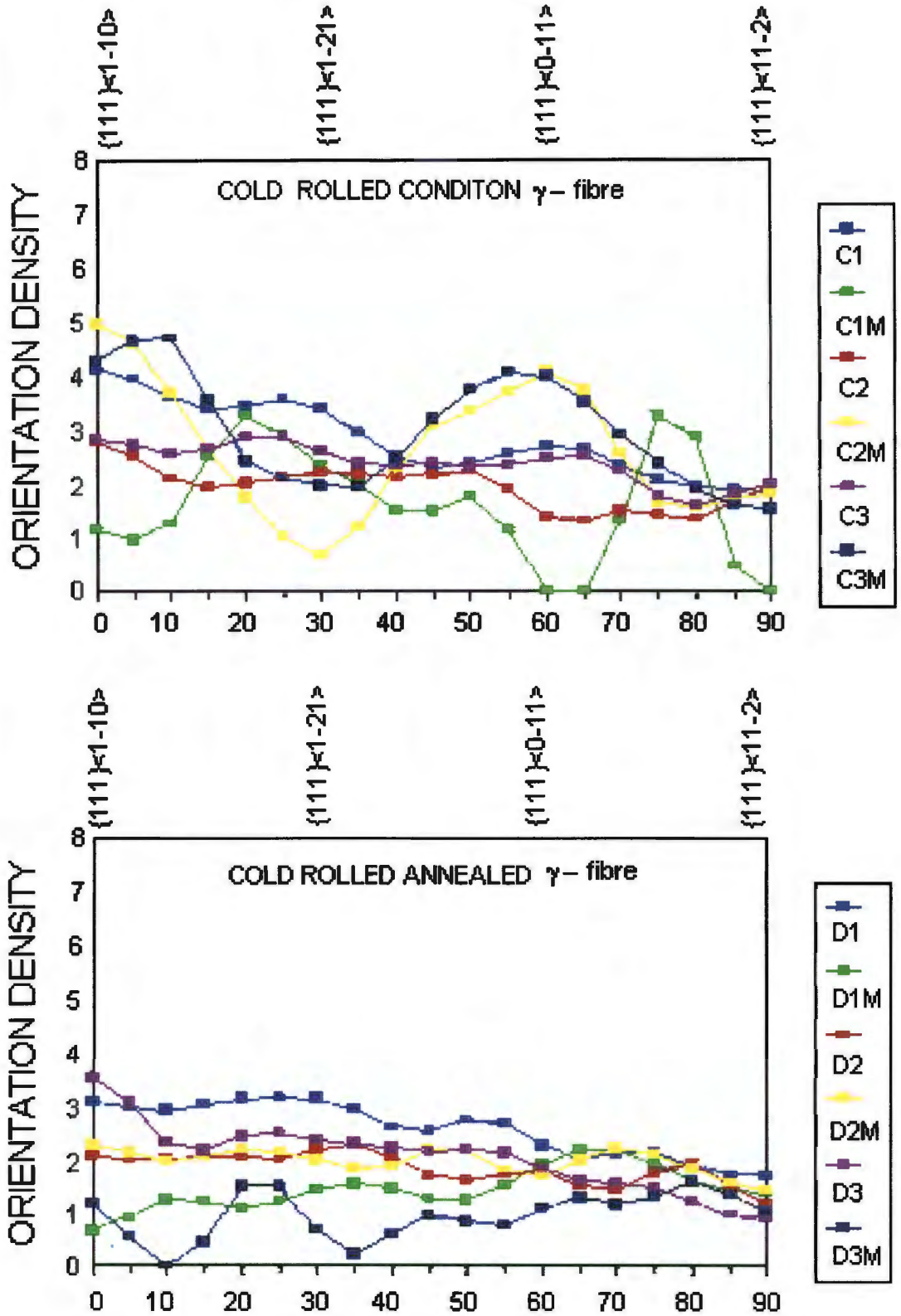

Figure A4: Diagram of the γ-fibre for stages C (cold rolled) and D (cold rolled-annealed).

APPENDIX B

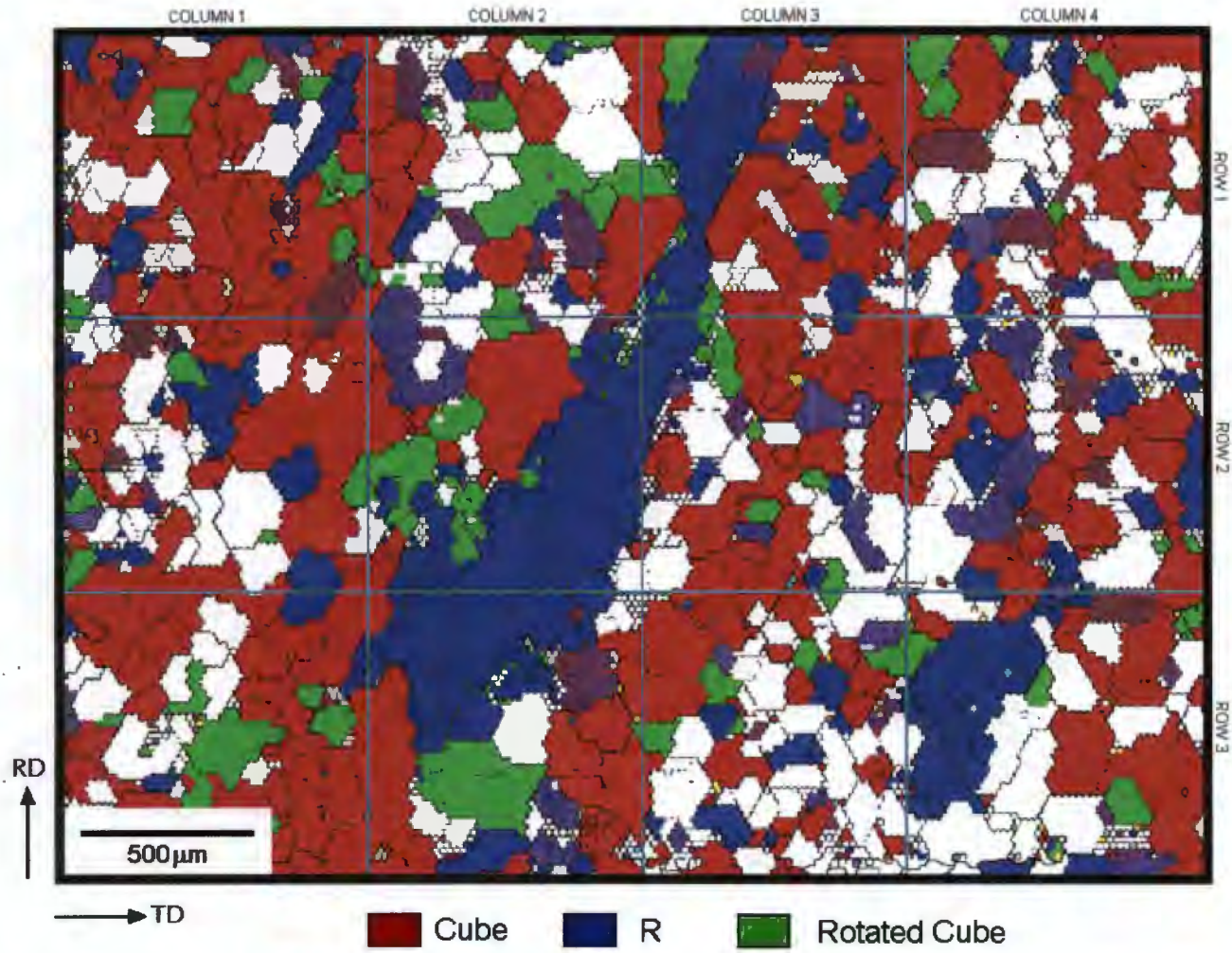

Figure B1: Texture map of sample ALU1 constructed using OIM software. (Clean-up level = 3).

APPENDIX C

Calculation of the Anisotropic Stress Ratios used in Hill's Potential Yield Function applied in the FEM Models:

Hill's potential function is a simple extension of the Mises function, which can be expressed in terms of rectangular Cartesian stress components as

$$f(\sigma)=\sqrt{F(\sigma_{22}-\sigma_{33})^2+G(\sigma_{33}-\sigma_{11})^2+H(\sigma_{11}-\sigma_{22})^2+2L\sigma_{23}{}^2+2M\sigma_{31}{}^2+2N\sigma_{12}{}^2}$$

where F, G, H, L, M and N are constants obtained by tests of the material in different orientations. They are defined as:

$$F=\frac{(\sigma^0)^2}{2}\left(\frac{1}{\bar{\sigma}_{22}^2}+\frac{1}{\bar{\sigma}_{33}^2}-\frac{1}{\bar{\sigma}_{11}^2}\right)=\frac{1}{2}\left(\frac{1}{R_{22}^2}+\frac{1}{R_{33}^2}-\frac{1}{R_{11}^2}\right),$$

$$G=\frac{(\sigma^0)^2}{2}\left(\frac{1}{\bar{\sigma}_{33}^2}+\frac{1}{\bar{\sigma}_{11}^2}-\frac{1}{\bar{\sigma}_{22}^2}\right)=\frac{1}{2}\left(\frac{1}{R_{33}^2}+\frac{1}{R_{11}^2}-\frac{1}{R_{22}^2}\right),$$

$$H=\frac{(\sigma^0)^2}{2}\left(\frac{1}{\bar{\sigma}_{11}^2}+\frac{1}{\bar{\sigma}_{22}^2}-\frac{1}{\bar{\sigma}_{33}^2}\right)=\frac{1}{2}\left(\frac{1}{R_{11}^2}+\frac{1}{R_{22}^2}-\frac{1}{R_{33}^2}\right),$$

$$L=\frac{3}{2}\frac{(\tau^0)^2}{\bar{\sigma}_{23}}=\frac{3}{2R_{23}^2},$$

$$M=\frac{3}{2}\frac{(\tau^0)^2}{\bar{\sigma}_{13}}=\frac{3}{2R_{13}^2},$$

$$N=\frac{3}{2}\frac{(\tau^0)^2}{\bar{\sigma}_{12}}=\frac{3}{2R_{12}^2},$$

where each $\bar{\sigma}_{ij}$ is the measured yield stress when σ_{ij} is applied as the only nonzero stress component. σ^0 is a specified reference yield stress. $R_{11}, R_{22}, R_{33}, R_{12}, R_{13}$ *and* R_{23} are anisotropic yield stress ratios, and $\tau^0=\sigma^0/\sqrt{3}$.

The six stress ratios are then defined as:

$$\frac{\bar{\sigma}_{11}}{\sigma^0},\ \frac{\bar{\sigma}_{22}}{\sigma^0},\ \frac{\bar{\sigma}_{33}}{\sigma^0},\ \frac{\bar{\sigma}_{12}}{\tau^0},\ \frac{\bar{\sigma}_{13}}{\tau^0},\ \frac{\bar{\sigma}_{23}}{\tau^0}.$$

In the present project the anisotropic material data is in the form of strain ratios r_0, r_{90} and r_{45}. The subscript is the angle between the applied tensile axis and the rolling direction. These values were calculated using the orientation

information (acquired on the OIM system) and software routines in the program LApp. The method to covert these strain ratios into the abovementioned yield stress ratios is described in the following paragraph.

In a simple tension test performed in the rolling direction in the plane of the sheet, the flow rule for Hill's potential function defines the incremental strain ratios as

$$d\varepsilon_{11}:d\varepsilon_{22}:d\varepsilon_{33} = G+H:-H-G$$

Therefore, the ratio of width to thickness strain, r_0 is: $\frac{d\varepsilon_{22}}{d\varepsilon_{33}} = \frac{H}{G}$.

Similarly, for a test performed at 90° to the rolling direction, r_{90} is $\frac{d\varepsilon_{11}}{d\varepsilon_{33}} = \frac{H}{F}$.

If the value of σ^0 is defined to equal $\bar{\sigma}_{11}$, then $R_{11} = 1$,

and using the above relationships:

$$R_{22} = \sqrt{\frac{r_{90}(r_0+1)}{r_0(r_{90}+1)}} \quad \text{and} \quad R_{33} = \sqrt{\frac{r_{90}(r_0+1)}{(r_0+r_{90})}}.$$

It is also possible to perform a test at 45° to the rolling direction in which case r_{45} is $\frac{2N-(F+G)}{2(F+G)}$ and $R_{12} = \sqrt{\frac{3r_{90}(r_0+1)}{(r_0+r_{90})(2r_{45}+1)}}$.

R_{23} and R_{13} in this case were assigned the value of 1 as no data was available for their calculation. The yield stress components in this format were used as input for the finite element simulation.

r-Values and Stress Ratios for Samples C430, D1 and D3

x,y,z = RD,TD,ND 0=RD=x, 90=TD=y

r-values **Stress Ratios**

Sample C430

6A	6B	6C	6D	6E
one	one	one	one	one
two	two	two	two	two
three	three	three	three	three
three	three	three	three	three
two	two	two	two	two
one	one	one	one	one

Repeated to produced 10 columns

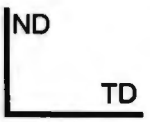

Transverse section of mirrored FEM Mesh

6A	r0	r45	r90	6A	R11	R22	R33	R12
one	2.014	0.849	1.091	one	1.000	0.884	1.029	1.085
two	2.337	0.864	1.017	two	1.000	0.849	1.006	1.055
three	1.597	1.582	0.906	three	1.000	0.879	0.970	0.823
four	1.568	1.344	1.000	four	1.000	0.905	1.000	0.902

6B	r0	r45	r90	6B	R11	R22	R33	R12
one	1.875	1.000	1.079	one	1.000	0.892	1.025	1.025
two	2.524	1.229	1.351	two	1.000	0.896	1.108	1.032
three	1.575	1.561	1.000	three	1.000	0.904	1.000	0.853
four	1.622	1.377	1.000	four	1.000	0.899	1.000	0.894

6C	r0	r45	r90	6C	R11	R22	R33	R12
one	2.240	0.813	1.243	one	1.000	0.895	1.075	1.149
two	1.496	1.182	0.646	two	1.000	0.809	0.868	0.819
three	1.446	1.586	0.756	three	1.000	0.853	0.916	0.777
four	1.309	1.000	0.716	four	1.000	0.858	0.904	0.904

6D	r0	r45	r90	6D	R11	R22	R33	R12
one	2.058	0.835	1.350	one	1.000	0.924	1.101	1.167
two	2.391	1.000	1.000	two	1.000	0.842	1.000	1.000
three	1.836	1.540	0.722	three	1.000	0.805	0.895	0.767
four	1.386	1.094	1.121	four	1.000	0.954	1.033	1.002

6E	r0	r45	r90	6E	R11	R22	R33	R12
one	2.242	0.793	1.240	one	1.000	0.895	1.074	1.157
two	2.121	0.791	1.000	two	1.000	0.858	1.000	1.078
three	1.833	1.493	1.000	three	1.000	0.879	1.000	0.868
four	1.612	1.147	1.172	four	1.000	0.935	1.049	1.001

Sample C430 Homogeneous Layers:

				R11	R22	R33	R12
Layer1	2.086	0.858	1.201	1.000	0.898	1.062	1.116
Layer2	2.192	1.013	1.003	1.000	0.854	1.001	0.997
Layer3	1.657	1.552	0.879	1.000	0.866	0.960	0.820

Sample D1

8A	8B	8C	8D	8E	8F
one	one	one	one	one	one
two	two	two	two	two	two
three	three	three	three	three	three
four	four	four	four	four	four

Repeated to produced 12 columns

Transverse section of FEM Mesh

ND

TD

8A	r0	r45	r90	8A	R11	R22	R33	R12
one	6.410	0.403	1.288		1.000	0.807	1.113	1.435
two	4.027	0.710	1.148		1.000	0.817	1.056	1.176
three	1.135	0.616	0.470		1.000	0.776	0.791	0.917
four	1.640	1.040	0.595		1.000	0.775	0.838	0.827

8B	r0	r45	r90	8B	R11	R22	R33	R12
one	1.670	0.262	0.922		1.000	0.876	0.975	1.367
two	0.808	0.345	0.808		1.000	1.000	0.951	1.267
three	1.638	1.000	0.620		1.000	0.785	0.851	0.851
four	1.000	0.598	1.518		1.000	1.098	1.098	1.283

8C	r0	r45	r90	8C	R11	R22	R33	R12
one	6.869	0.477	1.577		1.000	0.837	1.212	1.502
two	3.223	0.312	1.293		1.000	0.860	1.100	1.495
three	2.237	0.356	0.831		1.000	0.810	0.936	1.240
four	0.831	0.908	0.529		1.000	0.873	0.844	0.871

8D	r0	r45	r90	8D	R11	R22	R33	R12
one	4.822	0.485	1.904		1.000	0.890	1.284	1.584
two	3.814	0.538	1.000		1.000	0.794	1.000	1.202
three	2.138	0.703	1.318		1.000	0.914	1.094	1.222
four	3.488	0.636	1.178		1.000	0.834	1.064	1.223

8E	r0	r45	r90	8E	R11	R22	R33	R12
one	5.720	0.269	1.185		1.000	0.798	1.074	1.500
two	1.751	0.189	0.880		1.000	0.858	0.959	1.415
three	1.526	0.431	1.000		1.000	0.910	1.000	1.269
four	0.807	0.532	0.687		1.000	0.955	0.912	1.099

8F	r0	r45	r90	8F	R11	R22	R33	R12
one	9.321	0.354	1.396		1.000	0.803	1.159	1.537
two	4.856	0.541	1.316		1.000	0.828	1.117	1.341
three	3.702	0.311	1.000		1.000	0.797	1.000	1.360
four	1.778	0.325	1.035		1.000	0.891	1.011	1.363

Sample D3

7	7A	7B	7C	7D	7E
one	one	one	one	one	one
two	two	two	two	two	two
three	three	three	three	three	three
four	four	four	four	four	four

Repeated to produced 12 columns

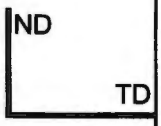

Transverse section of FEM Mesh

7	r0	r45	r90
one	2.143	1.000	1.405
two	2.010	0.725	1.258
three	1.000	0.342	1.123
four	3.789	1.033	2.935

7	R11	R22	R33	R12
	1.000	0.926	1.116	1.116
	1.000	0.913	1.076	1.191
	1.000	1.029	1.029	1.373
	1.000	0.971	1.446	1.430

7A	r0	r45	r90
one	1.994	1.000	1.380
two	1.653	0.725	1.256
three	2.043	0.885	1.193
four	3.619	1.242	2.736

7A	R11	R22	R33	R12
	1.000	0.933	1.107	1.107
	1.000	0.945	1.070	1.184
	1.000	0.900	1.059	1.102
	1.000	0.967	1.410	1.309

7B	r0	r45	r90
one	1.806	0.750	1.383
two	1.000	1.000	1.000
three	0.607	0.752	0.564
four	3.360	1.015	2.424

7B	R11	R22	R33	R12
	1.000	0.950	1.103	1.208
	1.000	1.000	1.000	1.000
	1.000	0.977	0.880	0.963
	1.000	0.958	1.352	1.345

7C	r0	r45	r90
one	2.818	0.925	1.408
two	1.804	0.490	1.393
three	1.278	0.277	1.833
four	1.751	0.791	1.413

7C	R11	R22	R33	R12
	1.000	0.890	1.128	1.157
	1.000	0.951	1.105	1.361
	1.000	1.074	1.159	1.610
	1.000	0.959	1.108	1.195

7D	r0	r45	r90
one	2.009	0.887	1.135
two	2.041	0.695	1.362
three	3.583	0.609	1.608
four	1.836	0.984	1.354

7D	R11	R22	R33	R12
	1.000	0.892	1.042	1.084
	1.000	0.927	1.103	1.236
	1.000	0.888	1.191	1.386
	1.000	0.943	1.097	1.103

7E	r0	r45	r90
one	1.269	0.807	1.219
two	2.023	0.622	1.297
three	6.219	0.773	2.056
four	2.844	0.661	2.163

7E	R11	R22	R33	R12
	1.000	0.991	1.054	1.130
	1.000	0.919	1.087	1.257
	1.000	0.884	1.339	1.454
	1.000	0.961	1.289	1.465